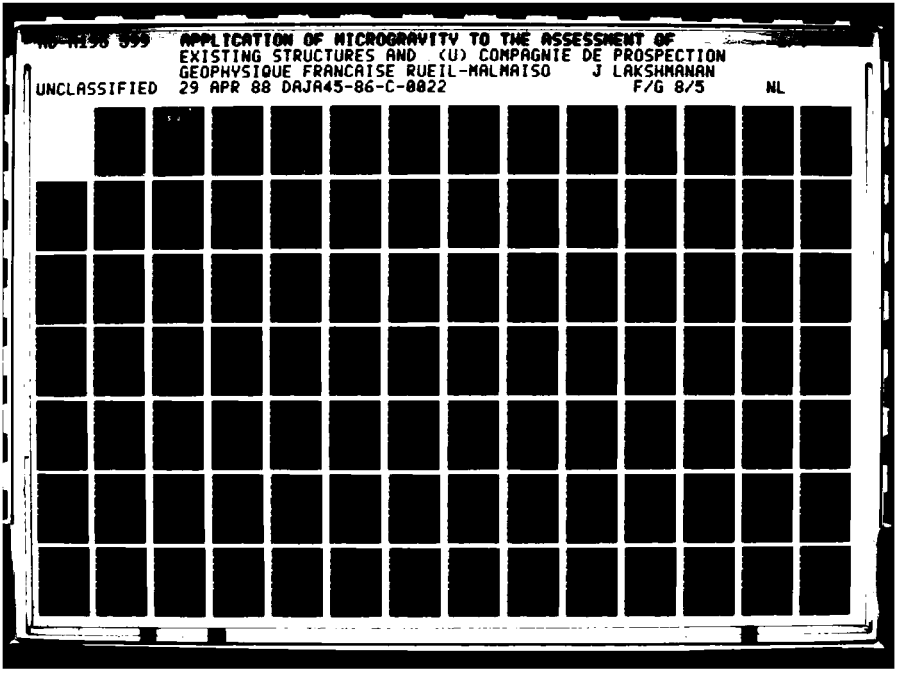
APPLICATION OF MICROGRAVITY TO THE ASSESSMENT OF
EXISTING STRUCTURES AND (U) COMPAGNIE DE PROSPECTION
GEOPHYSIQUE FRANCAISE RUEIL-MALMAISO J LAKSHMANAN
UNCLASSIFIED 29 APR 88 DAJA45-86-C-0022 F/G 8/5 NL

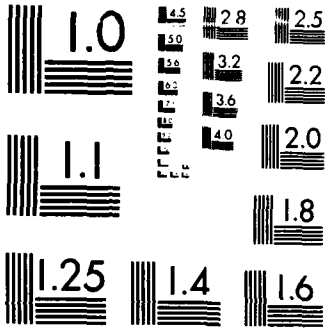
1.0
1.1
1.25
1.4
1.6
1.8
2.0
2.2
2.5
2.8
3.2
3.6
4.0
4.5
5.0
5.6

Unclassified
SECURITY CLASSIFICATION OF THIS PAC

AD-A195 599

DTIC FILE COPY (1)

REPORT DOCUMENTATION PAGE

Form Approved
OMB No 0704-0188
Exp. Date: Jun 30, 1986

1a. REPORT SECURITY CLASSIFICATION Unclassified	1b. RESTRICTIVE MARKINGS
2a. SECURITY CLASSIFICATION AUTHORITY	3. DISTRIBUTION/AVAILABILITY OF REPORT Approved for public release; distribution unlimited.
2b. DECLASSIFICATION/DOWNGRADING SCHEDULE	
4. PERFORMING ORGANIZATION REPORT NUMBER(S) 2893	5. MONITORING ORGANIZATION REPORT NUMBER(S) R&D 5395-EN-01
6a. NAME OF PERFORMING ORGANIZATION Compagnie de Prospection Geophysique Francaise	6b. OFFICE SYMBOL (If applicable)
6c. ADDRESS (City, State, and ZIP Code) 20, Rue des Pavillons 92800 Puteaux, France	7a. NAME OF MONITORING ORGANIZATION USARDSG-UK 7b. ADDRESS (City, State, and ZIP Code) Box 65 FPO NY 09510
8a. NAME OF FUNDING/SPONSORING ORGANIZATION USAE Waterways Experiment Station	8b. OFFICE SYMBOL (If applicable)
8c. ADDRESS (City, State, and ZIP Code) P.O. Box 631 Vicksburg, MS 39180-0631	9. PROCUREMENT INSTRUMENT IDENTIFICATION NUMBER DAJA45-86-C-0022

10. SOURCE OF FUNDING NUMBERS

PROGRAM ELEMENT NO.	PROJECT NO.	TASK NO.	WORK UNIT ACCESSION NO
61102A	1L161102BH57	01	

11. TITLE (Include Security Classification)

(U) APPLICATION OF MICROGRAVITY TO THE ASSESSMENT OF EXISTING STRUCTURES AND STRUCTURAL FOUNDATIONS

12. PERSONAL AUTHOR(S)
Jacques Lakshmanan

13a. TYPE OF REPORT	13b. TIME COVERED	14. DATE OF REPORT (Year, Month, Day)	15. PAGE COUNT
Final	FROM 4/1986 TO 4/1988	1988 April 29	251

16. SUPPLEMENTARY NOTATION

17. COSATI CODES		
FIELD	GROUP	SUB-GROUP
08	11	

18. SUBJECT TERMS (Continue on reverse if necessary and identify by block number)
Microgravity, geophysics, cavities, densities, existing structures, foundations

19. ABSTRACT (Continue on reverse if necessary and identify by block number)

The report evaluates microgravity and other geophysical techniques, applied to the detection of density anomalies in structures and in their foundations. Microgravity measurement and processing techniques, as well as in-situ density evaluation (including the Cheops pyramid) are described.
After a summary of microgravity practice in France, 21 case histories are developed. 71 references are followed by the English summaries of 7 selected papers and by the copies of 5 relevant papers.

20. DISTRIBUTION/AVAILABILITY OF ABSTRACT	21. ABSTRACT SECURITY CLASSIFICATION
☒ UNCLASSIFIED/UNLIMITED ☐ SAME AS RPT. ☒ DTIC USERS	Unclassified

22a. NAME OF RESPONSIBLE INDIVIDUAL	22b. TELEPHONE (Include Area Code)	22c. OFFICE SYMBOL
Jerry C. Comati	+441-4[illegible]-7331	AMXSN-UK-RE

DD FORM 1473, 84 MAR — 83 APR edition may be used until exhausted. All other editions are obsolete.

SECURITY CLASSIFICATION OF THIS PAGE
Unclassified

DISCLAIMER NOTICE

THIS DOCUMENT IS BEST QUALITY PRACTICABLE. THE COPY FURNISHED TO DTIC CONTAINED A SIGNIFICANT NUMBER OF PAGES WHICH DO NOT REPRODUCE LEGIBLY.

SUMMARY

The contracted research aimed at evaluating different geophysical techniques, and particulary microgravity applied to the detection of density anomalies in earth and rock structures, as well as in their foundation. The work consisted in collecting data and information from the work done on the subject at CPGF since 1962 and in developing certain aspects of interpretational techniques. On a railroad at Varangéville, France, a survey funded by the French Railways including repeat gravity measurements after grouting, was completed as part of the present contract. The results of an innovative survey of the Cheops Pyramid, funded by Electricité de France, were also partly included in the report.

The first and largest part of the report summarizes microgravity techniques. After a description of field techniques, the main interpretation techniques, both conventional and innovative, are described.

The second and the sixth parts of the report describe the application of microgravity to the direct in-situ measurements of embankment densities and to the assessment of foundations of existing structures, and includes the description of the Cheops survey. The third part of the report decribes the use of microgravity for grouting control and other repeat surveys. It includes the description of the above mentioned Varangéville survey.

The fourth part of the report compares microgravity with other geophysical methods in the fields of cavity detection and grout control. It describes the use of resistivity, electromagnetics, seismic methods and down-hole logging.

The fifth part compares current French practice in the field of cavity detection, with methods used in the rest of the world. The seventh part is a case history section, where 21 selected case histories are described.

The eighth section is a reference section, with 71 references, followed by 7 English summaries of selected references. Finally, an appendix contains copies of 5 papers published in English.

PREFACE

The present report was made under contract between the Department of the Army, Contracting Office, Hq. 47th Area Support Group, P.O. Box 160, Warrington, Cheshire, England, under the reference DAJA45-86-C-0022, and the Compagnie de Prospection Géophysique Française, 20 rue des Pavillons, 92800 Puteaux, France. The contract was issued on March 25, 1986. The contracting officer was Dennis P. Foley, while the work was supervised by Jerry C. Comati, Chief, Environmental Sciences Branch and by Dr. Dwain K. Butler, Waterways Experiment Station, Corps of Engineers, Vicksburg, Miss.

By letter dated August 3, 1987, CPGF sollicitated a delay for the submission of the draft final report, taking into account the work done at the Cheops Pyramid, Egypt, part of which was included in the report. Also by letter dated November 10, 9187, the Department of the Army authorized Mr. Lakshmanan to publish partially or in toto, the research material in his thesis which will be maintained at the University of Nancy, France, in June 1988.

The following CPGF personnel participated in the elaboration, the preparation and the edition of the report : Jacques Lakshmanan, ingénieur géologue E.N.S.G. Erkan Kutkan, geophysicist; Jean-Claude Erling, geophysicist; Ms Monique L'Huillier, for the typing in English; Ms Martine Hérisson, for the drafting and report preparation.

TABLE OF CONTENTS

List of tables

CONVERSION FACTORS, NON-SI TO SI (METRIC) UNITS OF MEASUREMENT

note : In microgravity surveys, the following NON-SI units are commonly used :

Length : meters (m)
Mass : tonnes (t)
Mass per unit volume : grammes per cubic centimeter, g/m^3 erroneously called "density".
Relative acceleration of gravity : microgals (µgal)

MULTIPLY	BY	TO OBTAIN
meters (m)	1	Meters (m).
Metric tons or tonnes	1	Metric tons or tonnes (t).
Grammes per cubic-centimeter (g/cm^3).	10^3	Kilogrammes per cubic meter (kg/m^3).
Microgals (µgal)	10^{-8}	m/s^{-2}

List of figures

APPLICATION OF MICROGRAVITY TO THE ASSESSMENT OF EXISTING STRUCTURES AND STRUCTURAL FOUNDATIONS

PART 1 : OVERVIEW OF THE MICROGRAVITY TECHNIQUE

Historical Background

1. The word "microgravity" was first coined by the late R. Neumann (1967) from Compagnie Générale de Géophysique (C.G.G.). However, the first commercial microgravity surveys in the world (to our knowledge) were carried out in France by Compagnie de Prospection Géophysique Française (C.P.G.F.) in 1962, and published the following year (J. Lakshmanan, 1963). In fact, the leadership of French geophysicists in the field of microgravity is a normal continuation of work by the great French physicists of the 18th and 19th centuries, Coullomb, Poisson and Bouguer and in the 20th century by Cagniard (1960). The important role of French scientists in the knowledge of gravity, after Newton, was recently recalled by Thomas LaFehr (1980).

2. However, if the theory was often French, gravity meter technology, after Eotvos (1986), is mainly American. Since the forties, field gravity meters regularly allow readings to 10^{-5} gals. In 1968 Lacoste and Romberg brought out the model D gravity meter, often called the "microgal", which can be read to the microgal (10^{-6} gals; 1 gal = $1 cm/s^2$ and $g \sim 980 cm/s^2$).

3. The introduction of the model D meter has really allowed gravity surveys for shallow features to add the prefix "micro" to the word "gravity". Just over a hundred of these D-meters have been built since 1968, and at least 12 of these are in commercial use in France.

4. According to the size and depth of suspected causes of density anomalies, and to corresponding spacings between gravity stations, we can classify gravity surveys in three main groups :

Table 1: Classification of gravity surveys

	Depth	Station Spacing	Amplitude of anomalies	Accuracy
Gravity surveys	2000-6000 m	1000-5000 m	5 to 30 mGal	0.1 mGal
"Minigravity" surveys (Mining-ground water)	200-1500 m	100-300 m	0.5 to 5 mGal	0.01 mGal
"Microgravity" surveys	0 to 50 m	2 to 40 m	0.02 to 0.40 mGal	0.001 mGal

5. C.P.G.F. is proud to be a pioneer and a leader in the field of microgravity and has carried out over 500 surveys in 9 countries. The most interesting of them will be analysed in chapter 7 of this report.

6. Salient features of development of microgravity in Europe are as follows :

a. A symposium of the International Association of Engineering Geologists was held in Hannover in 1973, on the theme of dissolution cavities (J. Lakshmanan, 1973). The French government financed a multicompany research program in 1977 on the theme of Cavity Detection. C.P.G.F. was in charge of appraising microgravity and a novel 3-D seismic technique, the Sismobloc-C.P.G.F. (J. Lakshmanan, M. Bichara, J.C. Erling, 1977). In 1979, a working committee of the French National Committe on Soil Mechanics established "Recommendations on the treatment (and the detection) of underground cavities". This committee included J.C. Erling and J. Lakshmanan from C.P.G.F. (P. Habib et al, 1979).

b. In the United States, interest in geophysical detection of caves seems more recent. Quite comprehensive research has been carried out by the U.S. Corps of Engineers for the last 15 years (Butler, 1977, 1984). Further details on published papers, either by C.P.G.F. geophysicists, or other experts, will be described in chapter 8.

c. The use of microgravity for density determinationin the structure itself is more recent and has been described in two papers by C.P.G.F. and French Railway geologists (M. Bichara and J. Lakshmanan, 1983, J.C. Erling and G. Roques, 1983). In this case, when the structure is located above the normal ground level, application of a generalized Nettleton processing technique can lead to direct absolute density measurement (when the anomaly is located below the average ground level, only relative densities can be computed). An important application of the generalized Nettleton processing technique is for embankment density monitoring.

Field Measurements and Data Reduction

7. Readings with the model D meter are made to the microgal (0.001 milligal). However, special procedures are necessary in order to achieve the best repeat accuracies which can be brought down to a few microgals. Some of these are described by McConnell, Hearty and Winter (1975). As for data reduction, the main reference is still Nettleton (1940).

Meter Control.

8. Every two months, the meter's instrument constant is checked on a test range. In France, the main contractors (C.P.G.F. and C.G.C.) use the Marly-Croissy test range near Paris. These two bases are separated by 3 kilometers and there is a difference in elevation of about 100 meters. The difference in gravity between these stations is 32.86 mGal. Usual check includes at least 3 alternate measurements at each base. The mean square difference (compared to average difference) is generally in the order of 5 microgals. Generally, no significant change of the instrument's constant is observed.

9. Before using the test range, the cross and longitudinal levels of the instrument are checked and, if necessary, adjusted according to the manufacturor's specifications. General revisions at the manufacturor's plant are only needed every 4 or 5 years. The "life" of each instrument is followed on a special notebook. A copy of 3 sheets of one of these notebooks is enclosed.

Daily checks.

10. The meters are kept under thermostatic heating permanently. One spare battery is therefore absolutely necessary when readings are started in the morning, several repeat readings are necessary at the first base, especially when outside temperatures are very different from room temperatures (either in very cold or very hot weather). When temperature contrasts are very high, "warm-ups" or "cool-downs" may need up to half an hour. Otherwise, measurements would start with heavy, erratic drift, which can also be related to the duration of previous clamping.

Return to base.

11. Returns to base are made every 20 to 30', in order to check whether abnormal drift is occuring, which can be due to a shock during transport, or irregular functioning of the thermostat (it should be reminded that D-meter's thermostatic temperature is generally in the order of 49.5°C).

HORIZONTALITE DES BULLES

HORIZONTALITY OF LEVELS

READINGS			Checks	Adjustments	Date	Operator	Job	Observations
1/4 grad left shift	0	1/4 grad. right shift.						
	OK		oui	non	07.12.83	DJ/Bi	Recal	reception au Gradient
	OK				20-9-84	DJ/Bi	Recal	
1/2 R. 100,627 B 100,628	l'e Horizon 100,629 elle vert. 100,620	1/2 raie 100,605 elle 100,630	x		1-7-85	AG.	Recal	avant départ Rif Tant.
1/2 102 512	Bulle Nord 102 505	1/2 102 498	x		12-7-85	AG	Rif Tant	
	Bulle Vert 102 505	102 511						
1/2 102 508	Bulle Nord 102 505	1/2 102 499		x	12-7-85	AG	Rif Tant	Légère oscillation en Bulle Nord. Pas de mouvement en Bulle Vert.
	Bulle Vert 102 514	102 518						
	102 513							
547 546	Bulle Nord 545 Bulle Vert 545	533 548	X	NON	7-5-86	SCE	EGYPTE	

Figure 1. Example of control sheet:
Control of level of horizontality

GALVANOMETRE

GALVANOMETER

Light beam check	Zero adjustment	Sensibility for one grad	Checks	Adjustments	Date	Operator	Job	Observations
2,7	bon	$5\ 10^{-2}$	oui	non	07.12.83	JJ/Bi	Ruil	
2.7		4.10^{-2}		oui (+Jumx4)	20.9.84	JJ/Bi		
		3.10^{-2}	x		1.7.85	AG	Ruil?	
		$3.4\ 10^{-2}$	x		12.7.85	AG	Rif Tnt	
		$2.7\ 10^{-2}$		x	12.7.85	AG	Rif Tnt	
2,7	OK	$4,5\ 10^{-2}$	x		2.6.86	TCE	EGYPTE	

Figure 2. Example of control sheet: galvanometer

SENSBILITE DE DEPLACEMENT (Butées : 2.0 - 3.4)

DISPLACEMENT SENSITIVITY (Limits 2.0; - 3.4)

READING FOR 10 GRAD. DISPL.		Checks	Adj.	Date	Operator	Job	Observations
Horizontal level	Cross level						
10 mgal	>1 gal ① >0,5 3 1,5	oui	non	07.12.83	JMPi	Ruil	
OK 10 -	Haut ② 1 à 1 mm (OK)		tri légèrement du côté horiz.	20.9.84	JMPi	Ruil	ligne de fracture vérifiée (OK)
0,5 grad/mgal		x		11/7/85	AG	Ruil	
8.5 grad/mgal		x		12.7.85	AG	R.f Tart	
10 grad/mgal			x	12.7.85	AG	R.f Tart	
8 → 12 grad/gal			oui	24.03.86	JMPi	Ruil.	
9,5 grad/mgal			oui	7.5.86	JCE	EGYPTE	

Figure 3. Example of control sheet: displacement sensitivity

Luni-solar corrections.

12. Before further corrections, the drift curve of a D-meter is very close to the luni-solar drift curve, i.e., it shows amplitudes of 150 to 300 microgals, with an approximately twelve hour period. Maximum gradient is about 50 microgals/hour. The following graphs are from Nettleton, 1940. It should be noted that at that time, for conventional gravity surveys, Dr Nettleton mentioned : "Since in most gravimeter operations, the instrument is returned to a subbase at intervals of at most a few hours, any tidal effect appears only as a slight modification of the drift curve and therefore does not affect the gravity difference determination.

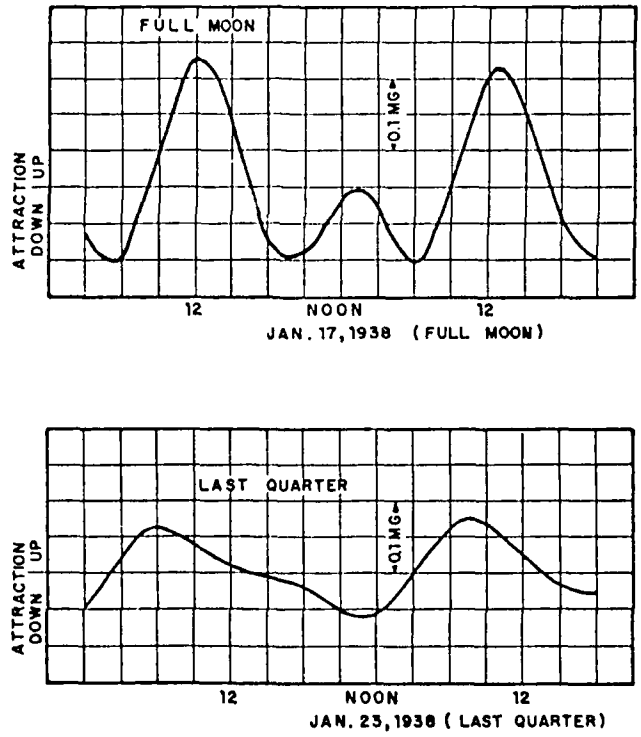

Fig. 4. Example of luni-solar drift (after Nettleton)

Consequently, in ordinary gravimeter operations no attention need be given to tidal effects. If an instrument were used for a period of 6 hr. or more without a drift reading, and if it were stable enough so that its drift could be interpolated reliably to 0.1 mg. or better over that period, and if gravity differences were being depended on to better than 0.1 mg., then it would be necessary to consider the tidal effects."

13. In microgravity, it is necessary to correct for luni-solar variations before any further processing. These corrections can be made with the tables published by Compagnie Générale de Géophysique and Service hydrographique de la Marine, and edited by Geophysical Prospecting. Alternatively (and preferably), the corresponding formulas can be programmed on a microcomputer.

Residual drift.

14. Once the luni-solar corrections are made, the residual drift should in theory, show out quite a regular curve, in fact something close to a straight line. The usual drift rate of a very good D-meter is in the order of 2 to 7 microgals/hour. For a less regular D meter, the drift can be in the order of 5 to 20 microgals/hour. An actual field example follows and is shown on figure 5.

15. The measurements were made along the circular freeway surrounding Paris, with severe traffic conditions, despite measuring at night. This example shows the "beat" often found in microgravity surveys, where pseudosine oscillations with an amplitude of 5 to 20 mGals and a period of an hour are found, superposed to the regular drift.

16. This "beat" has been described as being due to variations in the duration of clamping. Between stations, the instrument is clamped during a nearly constant interval, 2 minutes for example. If the meter is returned to the base, it may stay clamped for 5 or 7 minutes. This increase of clamping may contribute to the "beat" effect (the explanation being hysterisis of the spring).

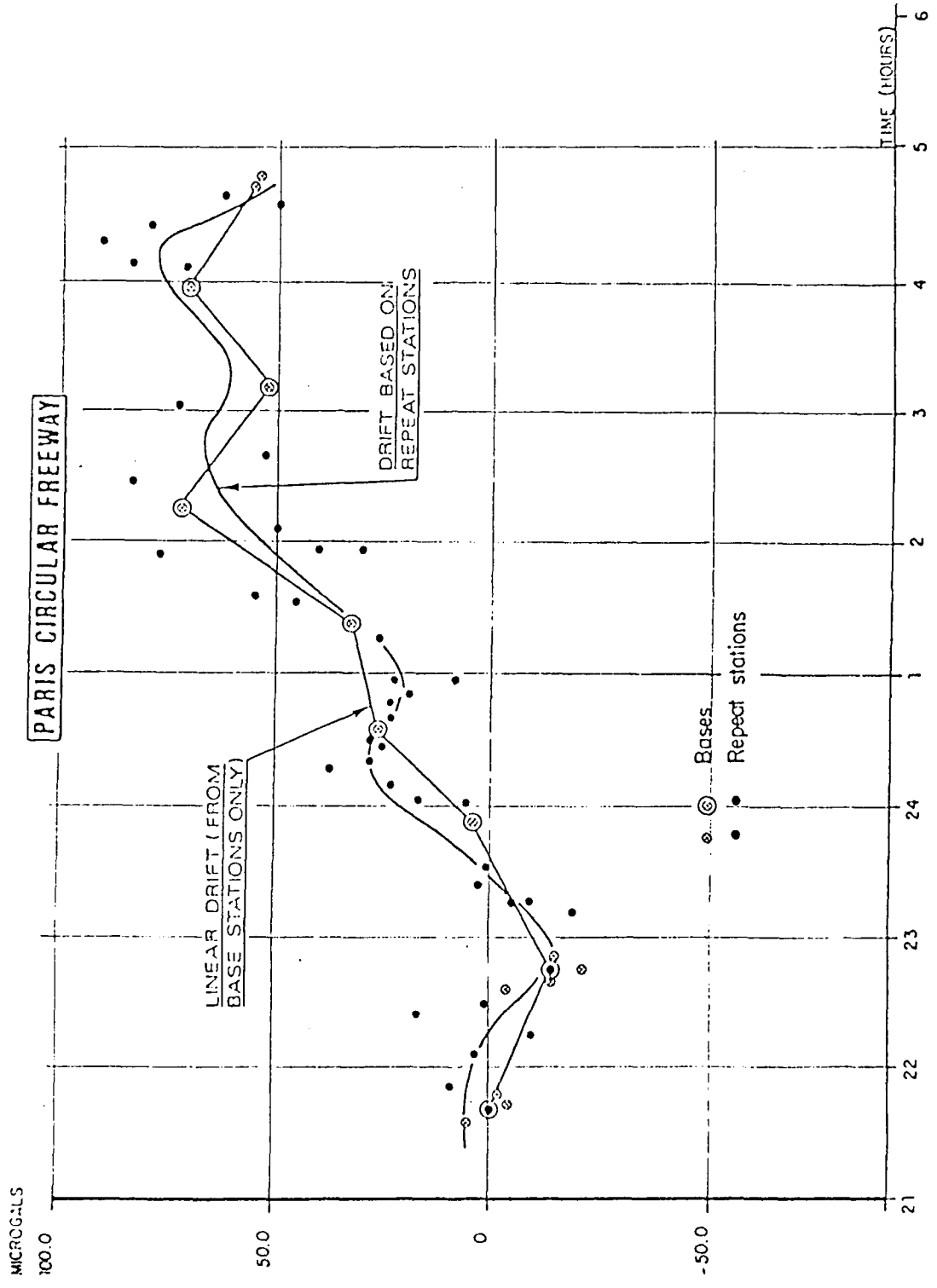

Fig. 5. Example of drift control

17. In certain conditions, and with certain less regular meters, residual drift can appear as a sine curve, with an apparent period of 20 to 40' and an amplitude of 10 to 15 microgals, as shown on the same enclosed graph. This means that an anomaly of this amplitude may either be spurious, or may be cancelled by a drift of opposite sign.

Semi-random field procedure.

18. In order to avoid this type of phenomenon, which leads to Bouguer maps showing anomalies lined up along the profile direction, C.P.G.F. has developed a drift control technique (see Bichara, Erling, Lakshmanan, 1981), which implies a semi-random field procedure. The spatial sequence should not be correlated with time. In other terms, each gravity station (supposing a regular grid) should be surrounded by points taken at dates differing as much as possible from the central station's date. In addition, the dates of the surrounding stations should also be the most variable possible. The processing technique is described in the above mentioned paper. The field technique procedure implies the corresponding processing.

19. In the same field sequence (between 2 returns to base), the 8 to 15 stations forming the program should be spatially as far as possible one from each other. In order to keep production to a reasonable level, measurements can be made according to the following principles;

- Base (time 0)
- Line 5: points A, D, G, J, M (times 3', 6', 9', 12', 15')
- Base (time 18')
- Line 8: points A, D, G, J, M (times 21', 24', 27', 30', 33')
- Base (time 36')
- Line 11: points A, D, G, J, M (times 39', 42', 45', 48, 51')
- Base (time 54')
- Line 6: points B, E, H, K, N (times 57', 60', 63', 66', 69')
- Base (time 72')
- Line 9: points B, E, H, K, N (times 75', 78', 81', 84', 87')
- Base (time 90')
- Line 12: points B, E, H, K, N (times 93', 96', 99', 102', 105')
- Base (time 108')
- Line 7: points C, F, I, L, O (times 111', 114', 117', 120', 123')

- Base (time 126')
- Line 10: points C, F, I, L, O (times 129', 132', 135', 138', 141')
- Base (time 144')
- Line 13: points C, F, I, L, O (times 147', 150', 153', 156', 159')
- Base (time 162')
- Line 5: points B, E, H, K, N (times 165', 168', 171', 174', 177)
- Base (time 180') ..... etc .....

20. In such a manner, a good decorrelation between time and space can be achieved. In the previous example, on line 9, points A to O will be read as follows:

Point	A	B	C	D	E	F	G	H	I	J	K	L	M	N	O
Time	396	75	237	399	78	240	402	81	243	405	84	246	408	87	249

Along each line, each point is surrounded by 2 points belonging to two different programs. Considering the grid, point 9-D will be surrounded as follows :

8-C	8-D	8-E
345'	24'	186'
9-C	9-D	9-E
237'	399'	78'
10-C	10-D	10-E
129'	291'	453'

Each of these 9 points belong to a different program.

Final drift evaluation.

21. Generally, however, the semi-random procedure is simplified by covering a grid four times :

- even lines, even stations
- odd lines, odd stations
- even lines, odd stations
- odd lines, even stations

In addition, at about 10 % of the stations, repeat readings are made.

If instrumental drift is sufficiently regular, linear interpolation between base stations is made. If not, a polynominal fit is made, taking into account (by order of weight) :

- base stations
- repeat stations
- differences between readings at the

station and at the four closest stations.

22. Readings made by a professional operator have an apparent accuracy of 1 or 2 microgals (difference between 2 readings made at 1 or 2 minutes intervals. In a survey made in normal environmental conditions (no great winds, not much traffic, no industrial vibrations) the mean square difference between repeat readings at different dates is about 5 to 15 microgals, or even less with the smallest grids. After adjustment of the drift curve, if anomalies in this curve or in repeats are observed, certain portions of the survey may be rerun.

23. The complete procedure as described in paragraph 19 slows down the field production from 80 to 50 stations per day, but it allows maximum reading accuracy. A residual anomaly of 10 micrograls seen on several adjacent points can be considered to have a very high degree of confidence.

Other field recommendations.

24. Some additional recommendations for microgravity survey field procedure are listed below :

a) The meter should be read, placed in the same direction in respect to the North.

b) The sequences should follow one another continuously : 1 eight hour sequence is better than 2 four hour sequences with a lunch break. When possible, with 2 operators, a meter can be read from dawn to dusk.

c) The ground surrounding the meter should be a flat as possible. When working in ploughed fields, a 1m by 1m area will be flattened out with a spade. Alternatively, if the weather is not windy, the base plate can be set on a 75 cm high tripod.

d) When elevation variations are large, points in the same program should be at altitudes as close as possible to one another. This fact has been studied by McConnel et al (1975).

Surveying

25. Usually, the area covered by a microgravity survey is quite small, and the surface is relatively flat. At least, this is the case for most building projects.

26. Starting from a bench mark supplied by the main contractor, and often by using a side of the building plot as one of the coordinate directions, stations are often located by chain. Each station is pegged, and the ground flattened, if necessary, at the foot of the peg. Using an automatic level (such as the Wild Nak-1) all the stations can often be measured with a single instrument station and a moving rod. This is the usual simple procedure for a survey on flat ground, with 50 to 200 stations with a station spacing of 5 m, for which a millimeter accuracy is no problem, at least if the ground is sufficiently compact, and not formed by ploughed land.

27. When station spacing is greater (20 to 40 m) and when the area is large, it may be necessary to use a high precision theodolite (Wild T2, for example) coupled with a distance meter (such as Wild Distomat with a T2 theodolite). Instead of using the gravity operator to do the surveying, a large area will need a professional surveyor.

28. The largest microgravity survey we ever carried out included 6,000 stations on a 10 by 50 m grid, in an area of quite severe topography in the Alps (Rif Tort hydroelectric project, owner Electricité de France ; the survey was carried out by C.G.G., associated with C.P.G.F.). This survey needed a series of topographic control points, along a 200 by 200 m grid, which were set up by a separate surveying company. Between these points, the infilling was done using a Distomat.

Corrections

Altimetric correction.

29. Variations of elevation create variations of g between 2 stations due to (Z in meters, ΔG in microgals) :

- Change in distance from the centre of the earth ("free air correction"). The free air correction is $\Delta G1 = 308.6\ (Z_2 - Z_1)$ (at a latitude of 45°).
- Theoretical attraction of the horizontal infinite slab, having a density of σ, and located between elevations Z_2 and Z_1 (in meters) of stations 2 and 1 : it is called the Bouguer correction : $\Delta G2 = -\frac{40\pi}{3}\,\sigma\,(Z_2 - Z_1)$.

These two corrections related to elevations, in microgals, are generally combined : $\Delta G = (308.6 - 41.9\sigma)\ (Z_2 - Z_1)$.

At other latitudes, a more sophisticated evaluation of the free air correction may be necessary : $\gamma = \frac{9.780318}{a(1-f\cos^2\varphi)}\ [1+0.0053024\ \sin^2\varphi\ -\ 0.0000059\sin^2 2\varphi]$

where φ is the latitude, $f = 3.35282.10^{-3}$ (earth's flattening) and $a = 6.378139.10^{6}$ m (earth's equatorial radius). The Bouguer coefficient may then be taken to be 41.9214.

For $\sigma = 0$ $\quad \Delta G = 308.8\ (Z_2-Z_1)$ (free air correction)

For $\sigma = 2.0$ $\quad \Delta G = 225.0\ (Z_2-Z_1)$

For $\sigma = 2.5$ $\quad \Delta G = 204.0\ (Z_2-Z_1)$

Latitude correction.

30. The latitude correction is due to the flattening of the earth and to its rotation, which reduces g when moving from the poles to the equator. The correction is given by $L = \pm k \Delta X$, where k is the gradient and ΔX is the north-south distance of a station from a reference station.

The average gradient of this correction is given in table 2 (due to Nettleton, 1939). This correction is added when a gravity station is south of a site reference station and subtracted when a station is north of the reference station.

Table 2 : latitude corrections

Latitude in degrees	k mgal/mile	k mgal/km.
0	0	0
10	0.447	0.278
20	0.840	0.522
30	1.132	0.703
40	1.287	0.800
50	1.287	0.800
60	1.132	0.703
70	0.840	0.522
80	0.447	0.278
90	0	0

Plate height corrections.

31. The meter may be at a certain height H above the ground; if this height varies from one station to the other, an additional free air correction PHC should be added : $PHC = 308.6\ (H_2-H_1)$.

Usually $H_2 = H_1$, and this correction becomes constant in each point and is therefore neglected.

Basis of terrain corrections.

32. In Paragraph 29, we suppose that the correction due to elevation is related to density and to the difference of elevation between two stations supposing that each station is located on an absolutely flat ground, as illustred in Figure 6.

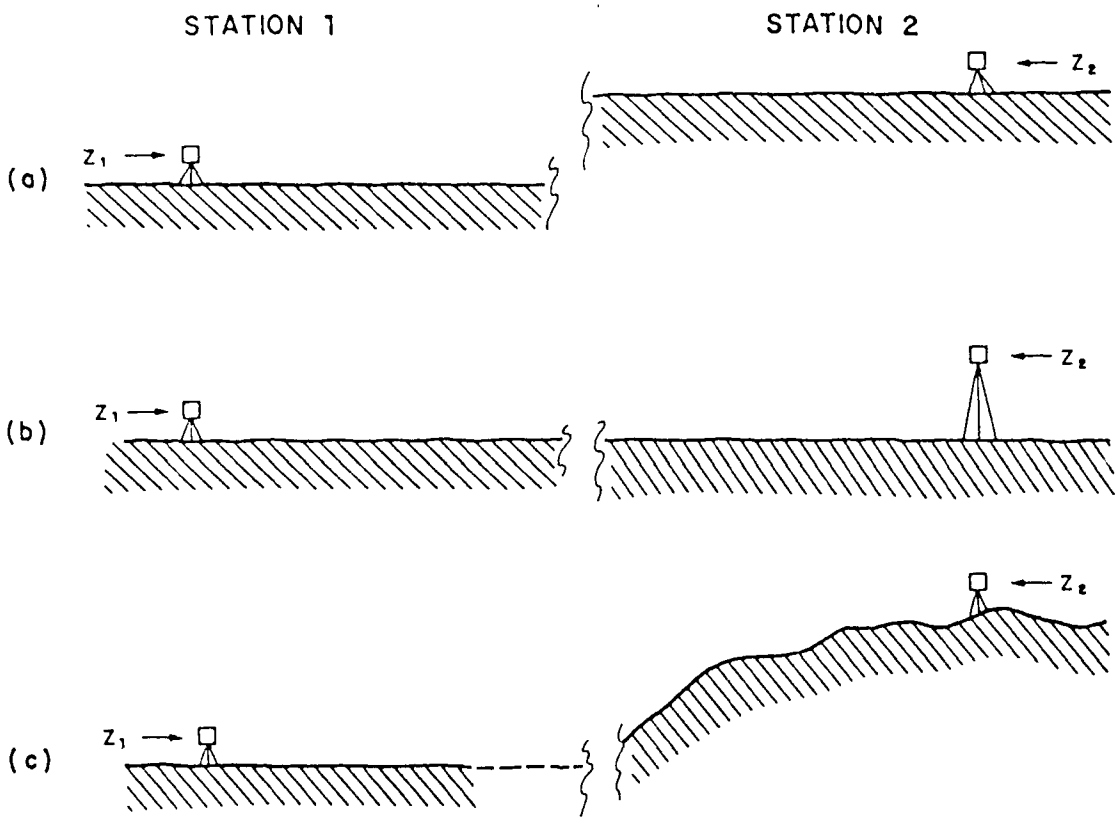

Figure 6. Basis of terrain corrections

In the theoretical case(a), the total altimetric correction will be (Z in meters, ΔG in microgals) ;

$$\Delta G = (308.6 - 41.9\sigma)(Z_2 - Z_1)$$

for $\sigma = 2.0$ gm/cc

$$\Delta G = 225.0\ (Z_2 - Z_1)$$

In case (b), supposing a very high tripod at station 2 (or a fictitious thin pinnacle $Z_2 - Z_1$ meters high), with the ground elevations the same at stations 1 and 2 :

$$\Delta G = 308.6\ (Z_2 - Z_1)$$

33. In the real case (c), lateral masses must be taken into account. The valley to the left of station 2 will have an influence on the reading at station 2 ; it will reduce the value of g at 2 (we suppose here that base station 1 is in an absolutely horizontal area). The necessary terrain corrections, TC, will be positive, and the equivalent coefficient B will be intermediate between 225.0 and 308.8, as if the density were lower than $\sigma = 2.0$.

$$\Delta G = 225.0\ (Z_2-Z_1) + TC$$

$$\Delta G = B(Z_2-Z_1)$$

For example, for $\sigma = 2$, $Z_2 = 110$m, $Z_1 = 100$ m and

TC = 120 microgals at station 2 :

$$\Delta G = 237.0\ (Z_2-Z_1)$$

The equivalent density $\sigma' = 1.71$ is intermediate between case (a) : $\sigma = 2.0$, and case (b): $\sigma = 0.0$.

34. Alternatively, we can consider that the correction is equivalent to the effect of a fictitious elevation Z'_2 at station 2. Considering the total correction:

$$\Delta G = 225.0(110.53-100.0)$$

$Z'_2 = 110.53$ instead of $Z_2 = 110.0$

Considering the Bouguer correction only :

$$\Delta G2 = -41.9\sigma(Z_2-Z_1 - TC(o).\frac{\sigma}{\sigma_0}$$

(TC(o) is the terrain correction for an arbitrary density σ_0).

$$\Delta G2 = -41.9(Z_2-Z_1 - \frac{TC}{41.9\sigma_0})\,\sigma .$$

$Z_2 - \frac{TC}{\sigma_0}$ can be considered to be a fictitious equivalent altitude :

$$Z_3 = Z_2 - \frac{TC}{\sigma_0}$$

with the previous example $Z_3 = 110 - \frac{120}{83.8} = 108.57$.

(Note : If station 2 were at the bottom of a valley, the terrain correction due to lateral hills would also be positive.)

Terrain correction program used in microgravity.

35. Many years ago, Hammer (1939) published detailed tables, allowing computation of terrain corrections. These tables are based on the use of a template applied on a topographic map and centered at the point where terrain correction is to be computed. These tables were made for large scale gravity surveys, and are not applicable for microgravity.

In fact, Hammer's first zone ranges from a radius of 2 m to a radius of 16.6 m, the second zone reaching 53.3 m. Apart from the scale effect, microgravity surveys are often conducted in urban environment, and severe corrections (and gradients of corrections) are to be made due to:

- masses of buildings
- cellars
- open pits

Corrections can frequently reach 200 to 300 microgals, while the anomalies we are looking for may only be of 30 to 50 microgals.

36. Accurate computerized corrections are absolutely necessary. Various programs have been developed at C.P.G.F. For example, Tercor program is mainly used for measurements made inside an open pit (such as a building project under construction). The enclosed fig. 7 illustrates the procedure used. Inside a first window F1 surrounding the considered point M, the ground is divided into prisms, following the grid at which elevations have been measured (often, a 2 x 2 m, or a 5 x 5 m grid is used). Each prism is divided into elementary prisms 0.50 m high. The attraction of each prism is the integration of the effect of the elementary prism, using the formulas given by P. Vallabh Sharma (1967) or by Nagy (1966). Alternatively, the formula given by Olivier and Simard (1981) which supposes that prisms have sloping tops can also be used.

37. Outside the moving window F1 and up to the limits of the grid (equivalent to a window F2), a simpler formula is used to compute the effect of each prism. It supposes that the effect of the prism is the same as that of a vertical cylinder (Parasnis, 1961). A third correction is applied to correct for the influence of masses outside window F2. In the usual version of the program used for measurements inside pits, the external elevation is supposed to be constant.

38. The second example, Figure 8, gives a pratical resul obtained for measurements made at Charleroi (Belgium) inside an open pit about 8 m deep. The station spacing is 4 m. The corrections vary from about 320 microgals at the corners of the pit to 250 along the sides of the pit, down to less than 150 microgals in the middle of the pit. We were looking for old, superficial coal mining works ; the corresponding anomalies only attained 50 microgals (Michel and Erling, 1975).

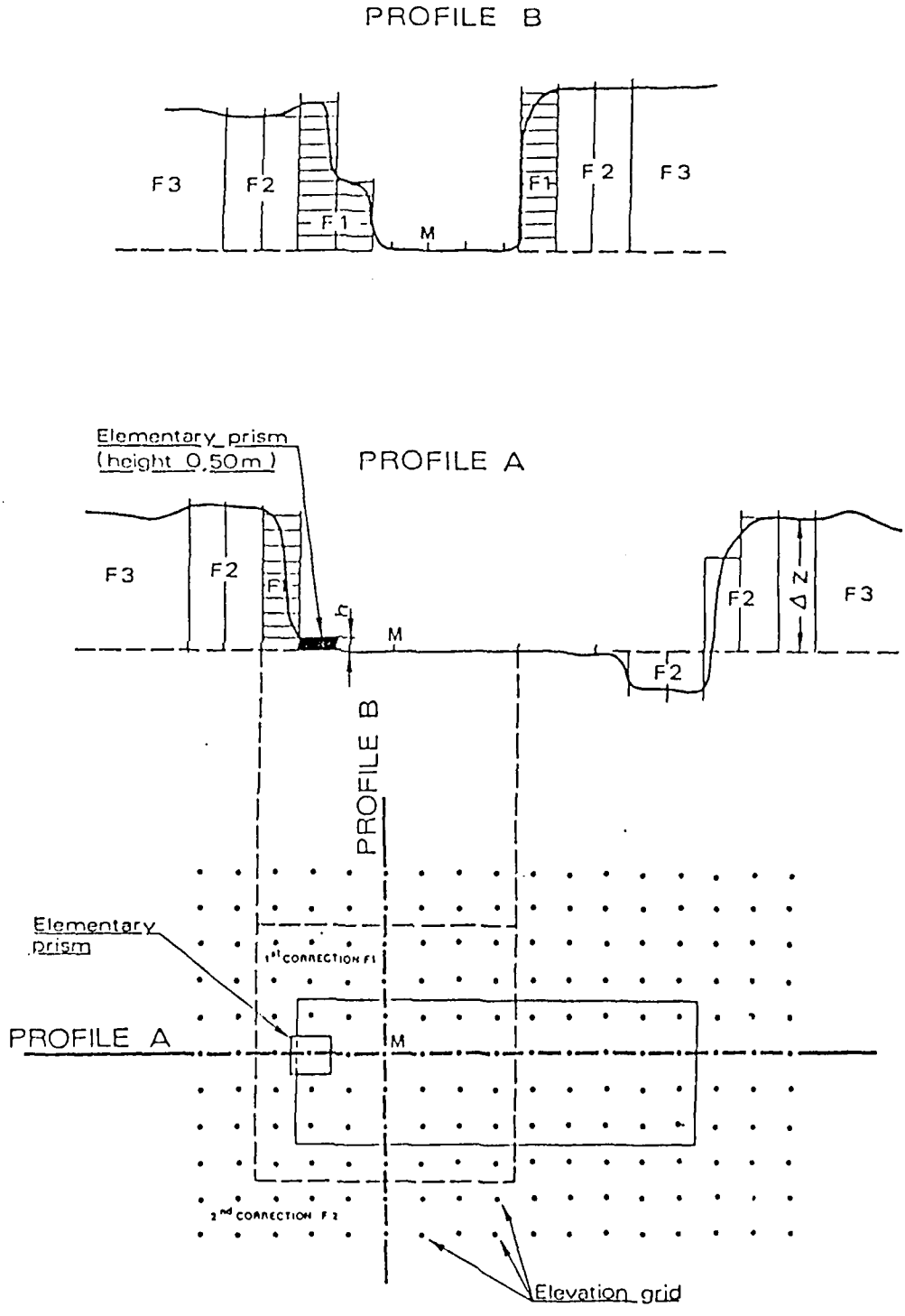

Figure 7. Terrain corrections, use of CPGF's Tercor program for measurement in an open pit

Generalized Nettleton corrections.

The Bouguer and the terrain corrections suppose that a density has been suitably selected. Usually, a constant value based on geology and soil mechanics is selected. However, an error on the evaluation of can create fictitious anomalies in zones of important elevation variations. An error on σ of $\Delta\sigma$ will make an error on g of :

$$\Delta g = - 41.9\ \Delta\sigma(Z_2-Z_1)$$

For Z_2-Z_1 = 10 m and $\Delta\sigma$= 0.3 gm/cc :

$$\Delta g = 125 \text{ microgals !}$$

Even for $\Delta\sigma$ = 0.1 gm/cc, Δg = 42 microgals. We can see that correct evaluation of density is very important as soon as elevation variations exceed a few meters. In 1939, Nettleton invented a procedure which since carries his name, the Nettleton profile (Nettleton, 1939). We shall cite his book :

> "This consists of taking a series of closely spaced stations over a local topographic irregularity, preferably a hill or valley or both. The gravity values are then reduced for different densities. The criterion for the actual density is that which gives the smoothest reduced gravity profile across the topographic irregularity. The method has the advantage that it samples a comparatively large mass of material. It has the disadvantage that very accurate gravity differences are needed, especially if the topographic relief is small. However, this latter disadvantage is compensated to a certain extent because, where the relief is small, a larger error of density is tolerable and, where the relief is large, a more accurate measurement of the density can be made. In regions where a gravity survey extends across outcrops of rocks of different density, it may be necessary to use variable densities for the reduction of different parts of the survey. In such a case, if the reduction is properly made, it is necessary to make an estimate of the thicknesses of the different beds considered and reduce different elements of the topography with different elevation constants."

This fundamental description is illustrated by Figure 9, also due to Nettleton.

40. Among cases where remarkable terrain corrections were necessary, we mention in this report : the Cheops pyramid (see Paragraph 140 to 145) ; Blaisy Bas tunnel (see cas history 5) ; Porte Pouchet, Paris (see case history 9).

An interesting published case is a crypt identification survey inside St Venceslas church, Czechoslovakia (Blizkowsky 1979).

CHARLEROI (BELGIUM)

Figure 8. **MAP OF TERRAIN CORRECTIONS**
(hundredths of milligals)

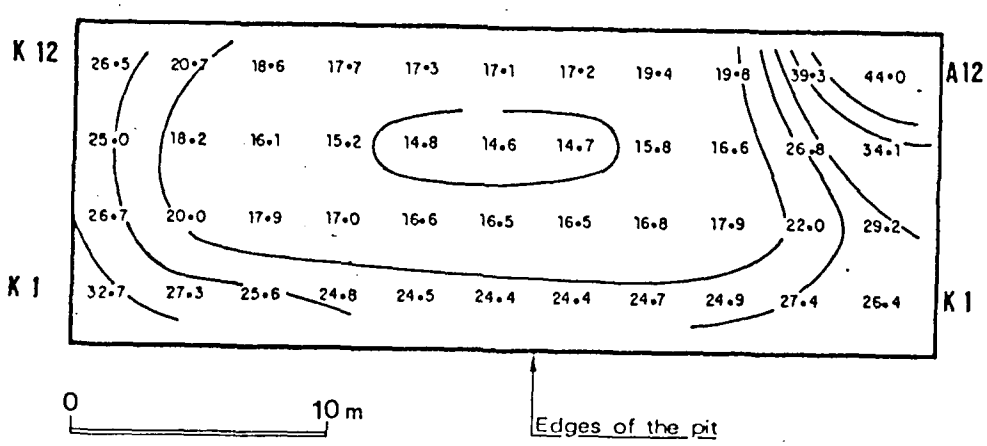

Figure 9. DENSITY PROFILE FOR MEASUREMENT OF SURFACE DENSITY WITH A GRAVIMETER
THIS PROFILE INDICATES A DENSITY OF 1.9.

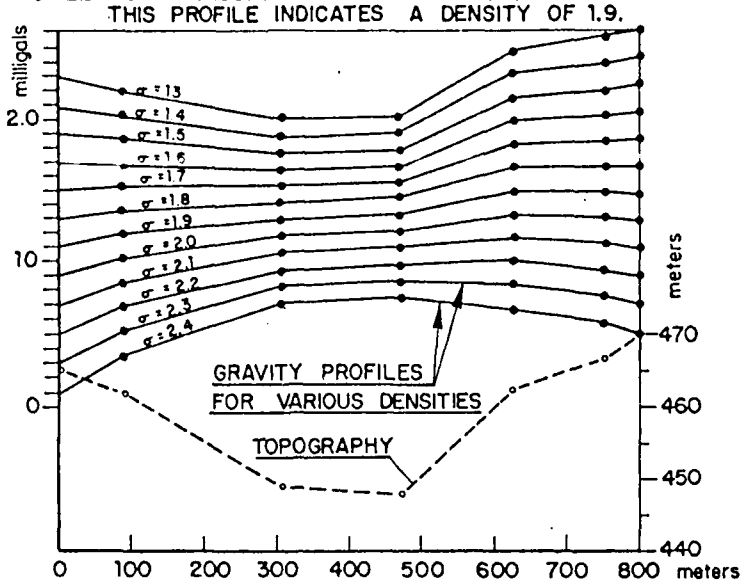

41. The use of computers has allowed generalization of Nettleton's principle, by trying to minimize correlation between elevation and the Bouguer anomaly (Parasnis, 1952). The innovations introduced by C.P.G.F. (Lakshmanan, 1982, F. Rimbert et al, 1984, Lakshmanan, 1985) have been:

a. the use of moving windows in order to compute a density at each point,

b. decorrelation of residual Bouguer and elevation with respect to regional datums, and not of absolute Bouguers and elevations, which leads to absurd values.

c. iterative computation.

42. Elevation Z and original Bouguer G are separated into regional (m) and residual (o) components :

$$Z = Z_m + Z_o$$
$$G = g_m + g_o$$

G is computed with a constant density σ_o.

Regionals are computed with the same operator so that they pass just below minimum points (such as valley bottoms for z).

The purpose of the procedure is to evaluate a new Bouguer GI computed with a variable density σ_1 above the variable datum, as shown in Figure 10.

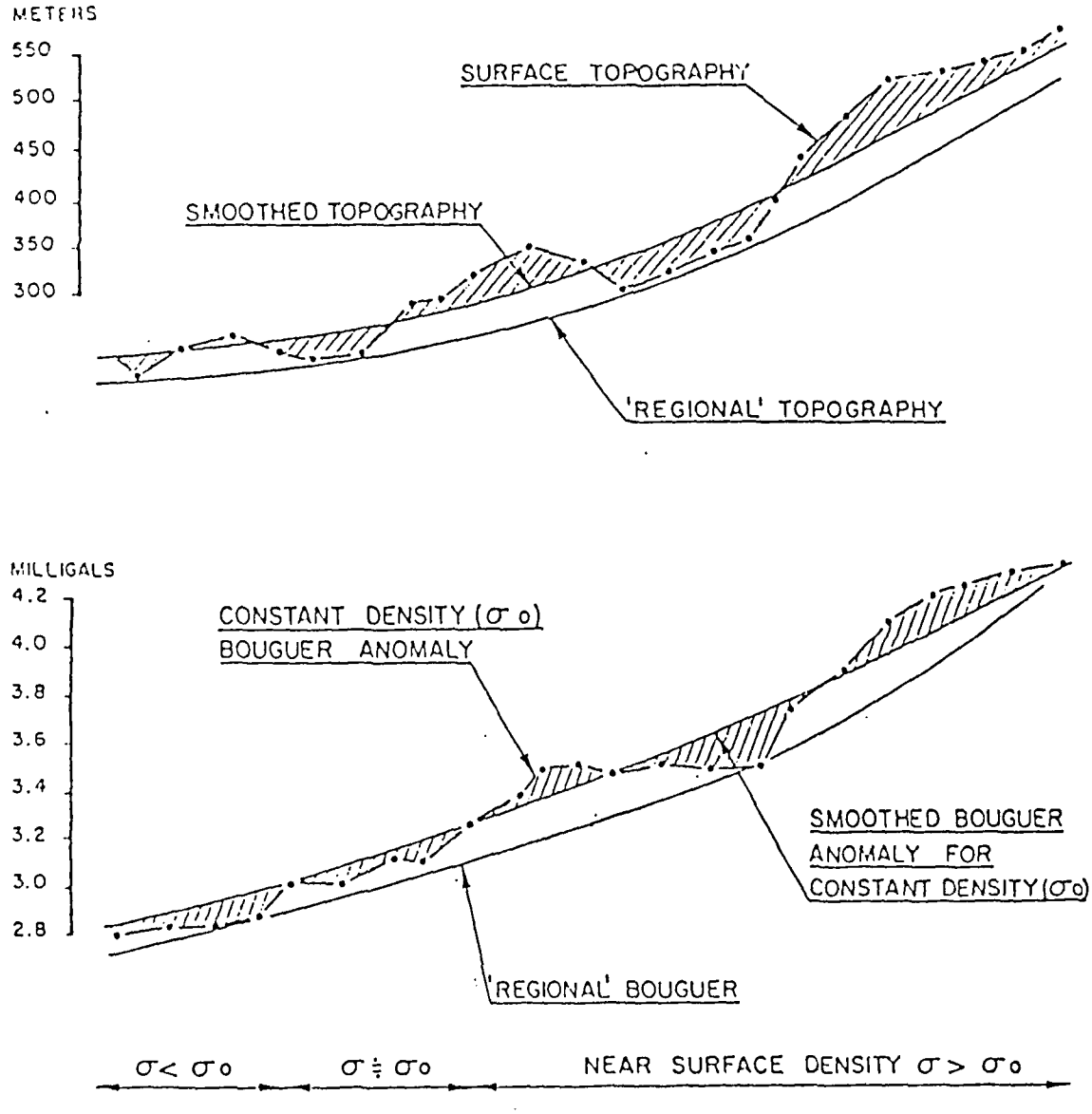

Figure 10. Principle of generalized Nettleton corrections

43. If F is the free air anomaly and C_o the terrain correction computed for σ_o, then :

$$g_m + g_o = F - \frac{40\Pi}{3} \left\{ \sigma_o Z_o + \sigma_o Z_m \right\} + C_o \qquad \text{for a constant density } \sigma_o$$

$$g_{1m} + g_{1o} = F - \frac{40\Pi}{3} \left\{ \sigma Z_o + \sigma_o Z_m \right\} + \frac{\sigma_1}{\sigma_o} C_o \qquad \text{for a constant density } \sigma_1$$

$$g_{1o} = g_o - (g_{1m} - g_m) - \frac{40\Pi}{3} (\sigma_1 - \sigma_o) \left\{ Z_o - \frac{3C_o}{40\Pi\sigma_o} \right\}$$

setting $\Delta r = g_{1m} - g_m$

and $Z_3 = Z_o - \frac{3C_o}{40\Pi\sigma_o}$

If g_o and Z_o are to be independant variables, we must have, setting

$$COV\ (x,y) = \frac{1}{n} \Sigma\ (x_i - \bar{x}) - (y_i - \bar{y})$$

$$Cov\ (g_o, Z_o) - Cov(\Delta r, Z_o) - \frac{40\Pi}{3} (\sigma_1 - \sigma_o)\ Cov(Z_3, Z_o) = 0$$

The new density σ_1 will be : $\sigma_1 = \sigma_o + \dfrac{Cov(g_o,Z_o) - Cov(\Delta r,Z_o)}{\frac{40\Pi}{3} Cov(Z_3,Z_o)}$

44. We will first suppose that $\Delta r \neq 0$ (this is experimentally correct); after one or two iterations Δr becomes very small compared to g_o . In addition, Δr and Z_o being practically independant variables, Cov $(\Delta r, Z_o)$ will be very small. The first evaluation of the new density σ_1 is then :

$$\sigma_1 = \sigma_o + \frac{Cov(g_o,Z_o)}{\frac{40\Pi}{3} Cov(Z_3,Z_o)}$$

45. When terrain corrections can be neglected, we get :

$$\sigma_1 = \sigma_o + \frac{Cov(g_o,Z_o)}{\frac{40\Pi}{3}(var\ Z_o)}$$

as written by Legatt (1984). This generalized Nettleton technique "rubs out" anomalies strongly correlated with elevation variations, and has to be used very carefully. It supplies an interesting by-product, the densities of the hills. In a further chapter, its use for density evaluation of embankments (Bichara and Lakshmanan, 1983) and other finite structures, such as the pyramid of Cheops (Lakshmanan and Montluçon, 1987) will be described.

Accuracy of microgravity surveys

46. The various corrections leading to the Bouguer anomaly add up as follows:

$$B = K\,R + D\,T + M + (308.8 - 41.9\sigma)(Z-Z_o) + \frac{C_o\sigma}{\sigma_o} + L$$

B : Bouguer anomaly

K : instrumental coefficient

R : reading

D : drift

T : time

M : luni-solar correction

σ : density

$Z-Z_o$: difference of elevation compared to base

C_o : terrain corrections for an initial density σ_o

L : latitude correction

Accuracy ΔB is given by:

$$\Delta B = \Delta K\,R + K\Delta R + T\Delta D + D\Delta T + \Delta M + (308.8 - 41.9\sigma)\Delta Z + 41.9\Delta\sigma(Z-Z_o) + \Delta C_o\frac{\sigma}{\sigma_o} + \frac{C_o\Delta\sigma}{\sigma_o} + \Delta L$$

For K = 1.1636 (gravity meter D7)

ΔK = 0.003 (following tests on standard bases)

R = 100 microgals

ΔR = 5 microgals

D = (maximum) 5 microgals/hour

ΔD = 2 microgals/hour (?)

T = (maximum) 0.75 hour

ΔT = 0.05 hour

ΔM = $\leq$ 1 microgal (?)

$\sigma_o = \sigma$ = 2.0 gm/cc

$\Delta\sigma$ = 0.2 gm/cc

$Z-Z_o$ = 1 meter (in a flat area)

ΔZ = 0.01 m

C_o = 30 microgals

ΔC_o = 3 microgals

ΔL = 10 microgals/kilometer ; therefore negligeable for a microgravity survey

47. Separating errors on reading, surveying and densities :

$\Delta B = 0.3 + 1.16\Delta R + 1.5 + 0.2 + 1.0 + 224.8\ \Delta Z$

$+ 41.9\Delta\sigma + 3.0 + 15\Delta\sigma$

$\Delta B = 6.0 + 1.16\ \Delta R + 224.8\ \Delta Z + 56.9\ \Delta\sigma$

This equation gives an idea of the relative weights of the different causes of error.

For ΔR = 5 microgals

ΔZ = 0.005 meters

$\Delta\sigma$ = 0.2

48. The errors are summarized as follows :

- Error related to drift, etc ... : 6 microgals } 11.8
- Error related to reading : 5.8 "
- Error related to elevation : 2.2 "
- Error related to density : 11.4 "

49. The first two errors, once combined, are controlled by repeat readings, at the same station, at different dates or hours. In fact, practical experience show rather better results, as shown below. The selected example is a microgravity survey at Cambrai (northern France), planned for locating ancient underground chalk quarries. The survey included 250 stations, among which 25 were double repeats. 3 different gravity meters were used (in order to compare them together). Among the 25 absolute differences :

- 8 were lower than 4 microgals (32 %)
- 23 " " " 8 " (92 %)
- 25 " " " 10 " (100 %)

The 3 gravity meters compared as follows:

Table 3: example of repeat measurements

Gravity meter	Number of repeats	Absolute differences					
		Less than 4 µgals		Less than 8 µgals		Less than 10 µgals	
		Number	%	Number	%	Number	%
D7	3	0	0	3	100	-	-
D11	7	2	28	7	100	-	-
D94	15	6	40	13	87	15	100

STATION	DATE		GRAVITY METER	BOUGUER IN MICROGALS			AVERAGE DIFFER.
	DAY	TIME		1ST MEASURE	2ND MEASURE	3RD MEASURE	
AB 25	9-17-86 "	9.35 9.59	D94 "	-30	-33		3
AB 24	9-17-86 9-18-86	9.38 9.59	D94 "	19 9			10
Y 20	9-17-86 9-18-86	10.08 10.15	D94 "	18	19		1
Y 19	9-17-86 9-18-86	11.26 10.15	D94 "	27	27		0
Y 11	9-10-86 9-10-86	13.05 14.55	D11 "	-30	-31		1
X 5	9-17-86 9-17-86 9-17-86	12.14 14.18 16.05	D94 " "	2	-1	-7	6
W 11	9-10-86 9-10-86	15.03 15.45	D11 "	-35	-35		0
V 10	9-10-86 9-10-86	17.09 17.20	D11 "	-47	-53		6
U 7	9-11-86 9-12-86	11.20 9.30	D11 "	-37	-31		6
U 13	9-10-86 9-15-86 9-16-86	11.03 15.30 13.38	D11 D94 "	21	20	14	4
T 14	9-10-86 9-16-86	16.25 11.52	D11 D94	14	10		4
R 10	9-10-86 9-16-86	10.15 9.21	D11 D94	22	15		7
R 13	9-10-86 9-12-86	9.58 11.04	D11 "	21	17		4
G 21	9-16-86 9-16-86	9.50 9.46	D94 "	50	55		5
Q 20	9-16-86 9-16-86	10.59 9.46	D94 "	50	55		5

STATION	DATE		GRAVITY METER	BOUGUER IN MICROGALS			AVERAGE DIFFER.
	DAY	TIME		1ST MEASURE	2ND MEASURE	3RD MEASURE	
Q 19	9-16-86 9-16-86	9.46 11.37	D94 "	50	45		8
N 26	9-4-86 9-4-86	11.05 11.21	D7 "	162	167		5
N 21	9-3-86 9-4-86	17.08 10.30	D7 "	20	27		7
N 19	9-16-86 9-18-86	10.02 8.50	D94 "	29	26		3
M 18	9-15-86 9-18-86	16.31 18.48	D94 "	33	33		0
M 19	9-15-86 9-18-86	16.25 8.59	D94 3	12	16		4
L 17	9-15-86 9-16-86	16.18 8.25	D94 "	34	32		2
K 17	9-15-86 9-15-86	14.41 16.14	D94 "	24	19		5
E 24	9-4-86 9-11-86 9-12-86	14.47 15.04 8.13	D7 " D11	113	123	118	7
R 10	9-12-86 9-15-86 9-18-86	8.21 15.50 9.21	D11 " D94	17	22	15	5

50. The third error, related to elevation, shows the importance of accurate surveying. The station position has to be flattened, so that the base plate will actually be positioned at the point where the base of the rod will be placed (the rod should not be put on the top of the peg, as often done).

51. Surprisingly, the weight of the errors due to bad evaluation of surface densities is very high. The case is of course worsened in hilly areas. However, in a microgravity survey, we do not often know how to separate surface anomalies, related to topography, from deeper ones. If we do not try to separate them, then in fact the inaccuracy related to $\Delta\sigma$ is not an inaccuracy, but rather something related to what we are looking for.

52. On the whole, the error on the Bouguer can be considered - in microgravity - to be in the order of 5 to 15 microgals without taking into account the influence of surface variations of density.

Conventional interpretation

General

53. For the mathematician, interpretation of gravity data has the intrinsic beauty of simplicity, everything being held in a single line, Newton's law. In microgravity units (microgals, tons and meters), the vertical component of a sphere (or a similar concentrated mass m located at a distance r and a depth z, will be $G = \frac{20}{3} \frac{mz}{r^3}$

54. For the geophysicist unfamiliar with gravity, such as the petroleum seismologist, gravity is synonymous with ambiguity. To suppress ambiguity, we need to input constraints, which are given by geology :

- density ranges
- depths
- sizes
- shapes

55. We can illustrate the fundamental ambiguity of gravity by the following example :

a horizontal earth G (x,y,o) is due to variations of thickness (t(x,y)) of a very thin, superficial slab, as shown below.

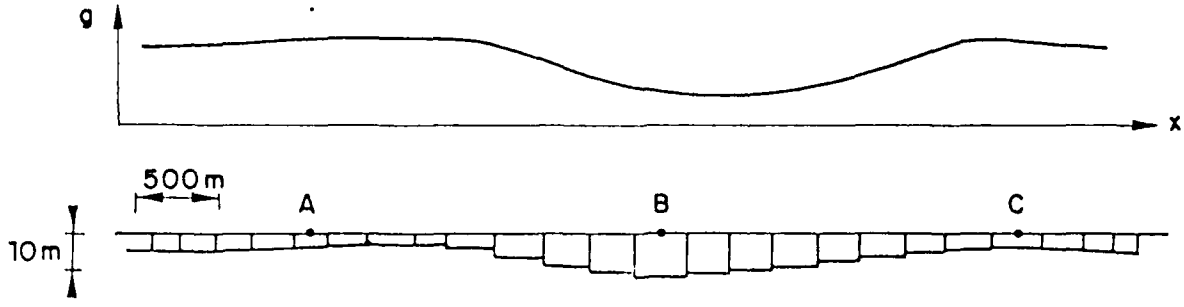

Figure 11. Effect of surface variations

The gravity anomaly at a given point I,J will be

$$G(I,J) = \frac{20}{3} \sum_K \sum_L \frac{m(K,L)z(K,L)}{r^3(I,J,K,L)}$$

K,L is a running point moving from $-\infty$ to $+\infty$.

Thicknesses being very small compared to horizontal distances, it can be shown that the anomaly will be very close to $G(I,J) \simeq \frac{20}{3}.2\Pi.\sigma(I,J).t(I,J)$, $\sigma(I,J)$ being the density of the slab and $t(I,J)$ its thickness.

If $\sigma(I,J) = \sigma$ = constant, $t(I,J) = \frac{3}{40\Pi} \frac{G(I,J)}{\sigma}$

Now if we suppose that $G(I,J)$ was in fact due to a sphere of 10,000,000 T centered at a depth of 1,000 m below the surface, we would have

$$G(I,J) = \frac{20}{3}.10^7. \frac{z}{(x^2+z^2)^{3/2}}$$

Selecting the origin of coordinates vertically above the center of the sphere, we could have the following values of G, and equivalent values of t (supposing $\sigma = 2.0$ g/cm^3).

Table 4 : thicknesses of a superficial layer equivalent to a deep sphere

x	G(μgals)	t(m)
-5000	0.5	0.01
-2000	6.0	0.07
-1000	23.6	0.28
0	66.7	0.80

A layer less than a meter thick, and very slowly thinning away to each side could in theory create an anomaly similar to that due to a ten million ton sphere, 1,000 m deep!! One of the aims of the rest of this report, both in its mathematical section and in its field case history section, will be to illustrate practical ways to resolve this paradox.

56. Regional and residual components of the Bouguer anomaly.

The terms "regional" and "residual" anomalies are quite misleading. What the gravity interpreter needs, whether he is looking for deep oil-bearing structures or for caves, is rejecting low frequency and high frequency variations in order to focus on the depth of interest. The methods generally used are :

- graphical
- mathematical (polynomial functions, for example)

57. In microgravity (and particularly at CPGF) it is usual practice to keep the "regional" high, so that nearly all the "residuals" are negative.

Figure 12. Separation of Bouguer anomaly into regional and residual components

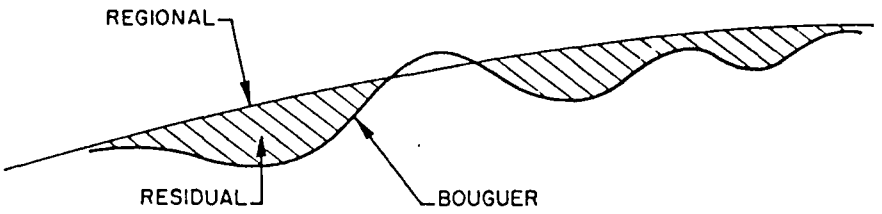

58. Considering the empirical rule "the higher the frequency, the shallower the depth", it should be kept in mind that the regional should not include causes which are of interest, and the interpreter should always carefully examine and interpret the regional.

59. A good way of checking the validity of a regional is the evaluation of its average gradient. Supposing a planer regional over a total distance of ΔL, and with a gravity variation of Δg ; if the regional is due to a thick elongated slab, as shown below, we can suppose that the plane regional corresponds to the steepest gradient of the complete curve.

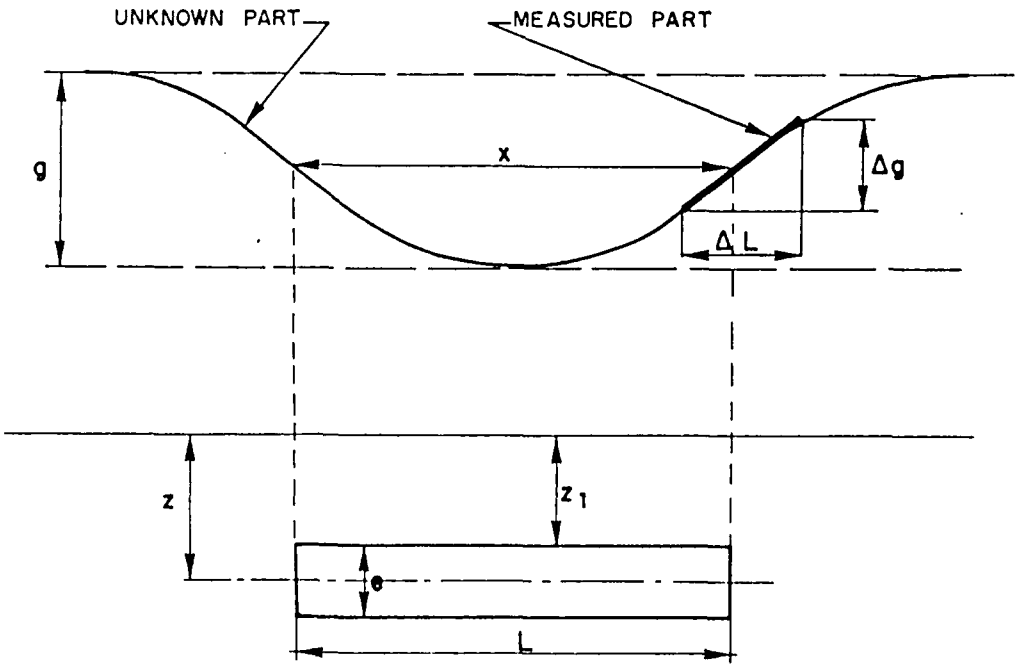

Figure 13. Validity of a regional anomaly

The anomaly due to such a slab is examined in a later section, where it is shown that the normalized depth $\frac{Z}{L}$ can be computed from normalized relative gradient $U = \frac{1}{X} \frac{g}{dg/dx}$ (with $X \neq L$). In our case, we can admit that the unknown maximum amplitude g is

$$g \geqslant 2\Delta g$$

and the unknown maximum width L is

$$L \geqslant 2\Delta L$$

In that case $U \sim \frac{1}{2\Delta L} \cdot \frac{2\Delta g}{\Delta g/\Delta L} \sim 1.0$

In fact, our experience shows that $0.4 < U < 1.0$. For these limits and for a thin wide slab, we have (see paragraph 85) :

$0.15 < \frac{z}{L} < 0.5$
or $0.3\Delta L < z < \Delta L$.

Our nomogram (see paragraph 85) also gives the tickness-density product $t\Delta\sigma$. For the above limits,

$$0.029 < \frac{t\Delta\sigma}{g} < 0.050$$

Supposing $\Delta\sigma = 0.3$, and with $g \sim 2\Delta g$

$$0.193 < \frac{t}{\Delta g} < 0.333$$

Depth to the top of the slab will be :

$$0.3.\Delta L - \frac{0.193}{2} \Delta g < z_1 < \Delta L - \frac{0.333}{2} \Delta g$$

For various values of ΔL and $\frac{\Delta g}{\Delta L}$, values of z_1 are given by the following table :

Table 5 : depths to a wide slab as a function of $\Delta g/\Delta L$

$\frac{\Delta g}{\Delta L}$ (microgals/m or milligals/km)	z_1 (depth to top of slab)		
	ΔL = 100 m	ΔL = 200 m	ΔL = 500 m
0.5	25.2 to 91.7	50.3 to 183.3	125.9 to 458.4
1.0	20.3 to 83.3	40.6 to 166.7	101.7 to 416.7
2.0	10.7 to 66.7	21.3 to 133.3	53.3 to 333.3
3.0	1.0 to 50.0	2.0 to 100.0	5.0 to 205.0
$z_1/\Delta L$ for $\frac{\Delta g}{\Delta L}$ = 2.0	0.11 to 0.67	0.21 to 1.33	0.53 to 3.33

60. This table shows that the regional gradient should not exceed 2 milligals per kilometer, particularly when the survey area is small. Typically, microgravity field surveys yield regional anomalies of 0.2 to 1.5 milligals/kilometer, which correspond to causes deeper than 50-100 m.

61. A confirmation of these values can be obtained from Bott and Smith's (1958) formulas, which compute maximum depth of anomalies.

For an elongated body, Bott and Smith's formula is :

$$\frac{Z_1+Z_2}{2} \leq 0.6495 \frac{g_{max}}{\left(\frac{dg}{dx}\right)_{max}}$$

Supposing g max > $2\Delta_3$ as on the previous page,

$$\frac{Z_1+Z_2}{2} \lesssim 0.65 \frac{2\Delta g}{\Delta g/\Delta L}$$

$$\frac{Z_1+Z_2}{2} \lesssim 1.30\ \Delta\ L$$

We get figures of the same order as from the above table. For a body of arbitrary shape, Bott and Smith's formula is:

$$\frac{Z_1+Z_2}{2} \leq 0.86 \frac{g_{max}}{\left(\frac{dg}{dx}\right)_{max}}$$

therefore, $\frac{Z_1+Z_2}{2} < 1.72\ \Delta\ L$

62. To summarize regional selection techniques, and considering that in microgravity surveys, targets are generally located at depths of less than a hundred meters, the regional anomaly should have :

- a gradient of less than 2 milligals/km
- been observed on distances exceeding 200 m in both x and y directions.

63. Quite often, a very small microgravity survey, for example a grid of 7 x 7 stations, 5 meters apart, will therefore have to be extended by 4 "regional" profiles, as shown on the following sketch.

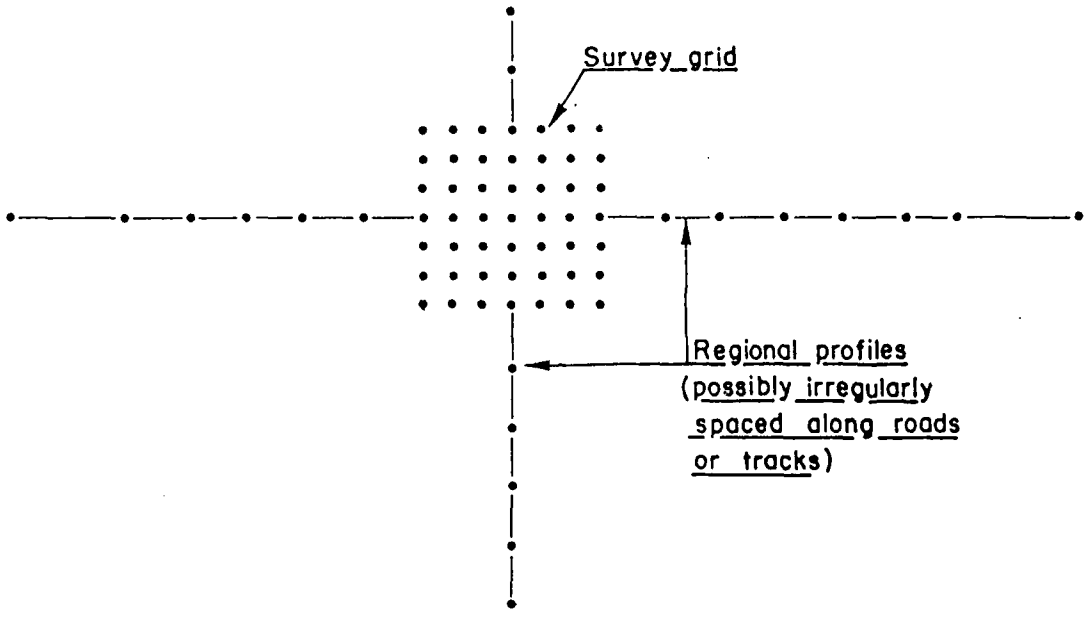

Figure 14. Typical "regional" profiles in microgravity

64. High frequency filtering. When the target is medium deep, for example dissolution lenses in gypsum, North of Paris, at depths of 50 m, it can be suitable to filter "noise" related to anomalies in the first few meters of the soil. These anomalies are usually visible on a single gravity point, with station spacings ranging from Δx = 15 to 40 m. Using Bott and Smith's formula for an arbitrary shaped body :

$$z_1 \leqslant 0{,}86 \frac{g\ max}{\left(\frac{dg}{dx}\right) max}$$

For an anomaly gv only visible on a single point, we can arbitrarily suppose that :

$$g\ max \sim 1.2\ gv$$

and that $\left(\frac{dg}{dx}\right) max. \sim 2.0 \frac{gv}{\Delta x}$

Therefore :

$$z_1 \leq 0{,}86 \frac{1.2\ gv}{2.0\ \frac{gv}{\Delta x}}$$

$$z \leq 0{,}52\ \Delta x$$

Anomalies visible on a single point along a profile with a station spacing of Δx, are approximately situated at depths less than $\Delta x/2$. Simple smoothing, based on a moving window technique (average on 3 adjacent points for a single profile, or 5 for a grid) will quite well reject phenomena located at depths less than half the grid spacing, for example, variations in thickness of top soil or loose fill. A more accurate proof of this empirical rule would need a detailed geostatic analysis, taking into account the shape of the superficial anomaly to be filtered out, and the size of the grid. Figure 15 shows an example of such a smoothing.

65. Other methods, such a spectral analysis or linear inversion, can be used for procession the Bouguer anomaly itself, and will then implicitly carry out the low and high frequency filtering described above and in paragraph 56. They will be described in later sections.

66. Use of set curves. One of the main techniques in preliminary interpretation of gravity data is the use of standard or set curves, computed for bodies of simple geometrical shapes. These set curves are compared to selected field profiles, carefully chosen so that they intersect the anomaly's maximum. Of course, more sophisticated inversion techniques are often used for final interpretation, but conventional interpretation methods still hold their place, particularly in the cases of field interpretation, and of survey feasibility studies (when one has to reply to the question "can a cavity be detected or not?").

67. The following bodies are the most useful in the analysis of microgravity anomalies, either alone, or using a combination of several bodies to simulate an underground quarry or karst :

- sphere
- horizontal cylinder
- semi-infinite slab or fault

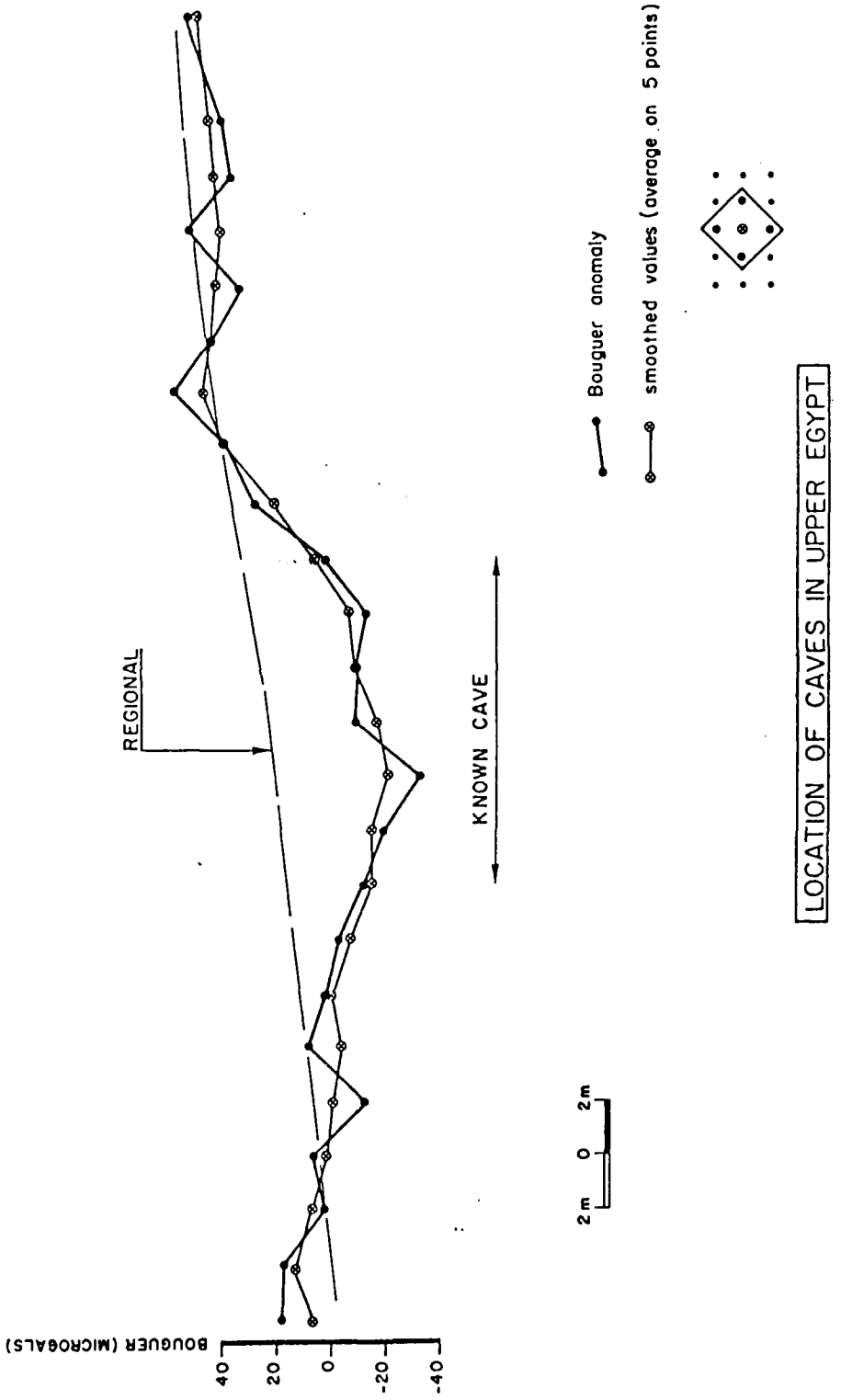

Figure 15. Example of high frequency filtering

- infinite strip { wide / narrow
- vertical cylinder { wide (flat disc) / narrow (vertical tube)
- right prisms

68. Sphere. $$g(\mu gal) = \frac{20\,m}{3}\,\frac{z}{(x^2 + z^2)^{3/2}}$$

$$g\ max. = \frac{20\,m}{3}\,\frac{1}{z^2}$$

$$\left(\frac{dg}{dx}\right) max = \frac{20\,m}{3}\,\frac{0{,}85685}{z^3}$$

$$\frac{g\ max}{\left(\frac{dg}{dx}\right) max} = \frac{z}{0{,}85685}$$

$$\text{and}\quad Z = 0.85685\,\frac{g\ max}{\left(\frac{dg}{dx}\right) max}$$

69. The maximum gradient is for $x = \pm 0.50\ z$. For this value $g\ (\frac{z}{2}) = 0.7155\ g\ max$. Half value of g max is reached for $x = 0.766\ z$. Depth to center is equal to the separation between inflexion points (which should be at 0.72 g max) as shown in Figure 16.

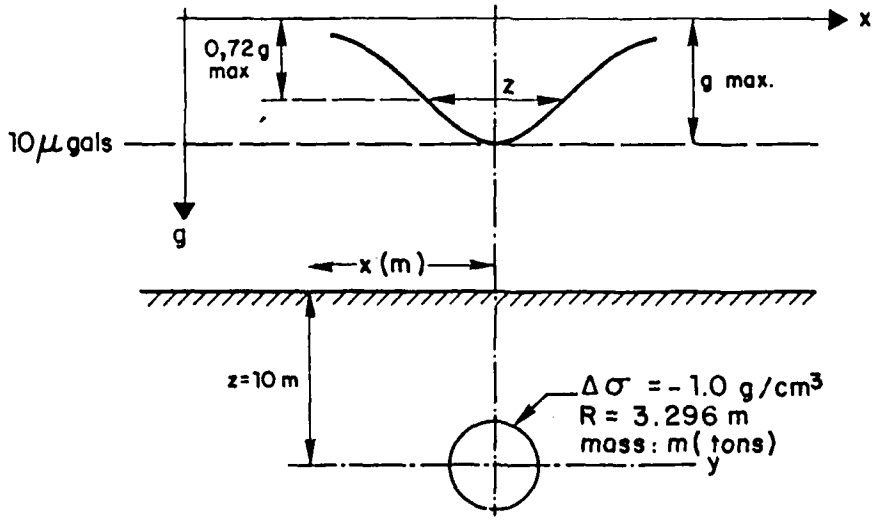

Figure 16. Example of anomaly due to a sphere.

Once z is determined by the above formula, mass m of the sphere is given by:

$$m = \frac{3 z^2 \, g_{max}}{20}$$

70. The following table summarizes the main results of the set curves enclosed (for depths of z = 2, 3, 5, 10 and 20 m) :

Table 6 : Sphere, maximum anomaly

			Maximum anomaly (microgals)				
Weight	Volume for σ = 2.0	Radius	z=2 m	z=3 m	z=5 m	z=10 m	z=20 m
8.4	4.19	1	14.0	6.2	2.2	0.6	0.1
67.0	33.5	2	111.7	49.6	10.7	2.7	0.7
226.2	113.1	3	-	167.6	60.3	15.1	3.8
1047.2	523.6	5	-	-	279	69.8	17.5
8378	4189	10	-	-	-	558.5	139.6
67021	33510	20	-	-	-	-	1117.0

The set curves (Fig. 17-21) at calculated for radii of R = 1, 2 3, 4, 5, 6 7, 8, 10, 15 and 20 m.

71. Figure 22 gives the maximum anomaly for spheres located at center depths ranging from 1 to 12 m, with radii ranging from R = 1 m to R = 30 m. The family of curves is limited by a straight line corresponding to z = R (spheres tangent to the soil surface). This straight line's equation is

$$\frac{g}{\Delta \sigma} = \frac{20}{3} z$$

In all cases of spheres

$$\frac{g}{\sigma} \leq \frac{20}{3} z$$

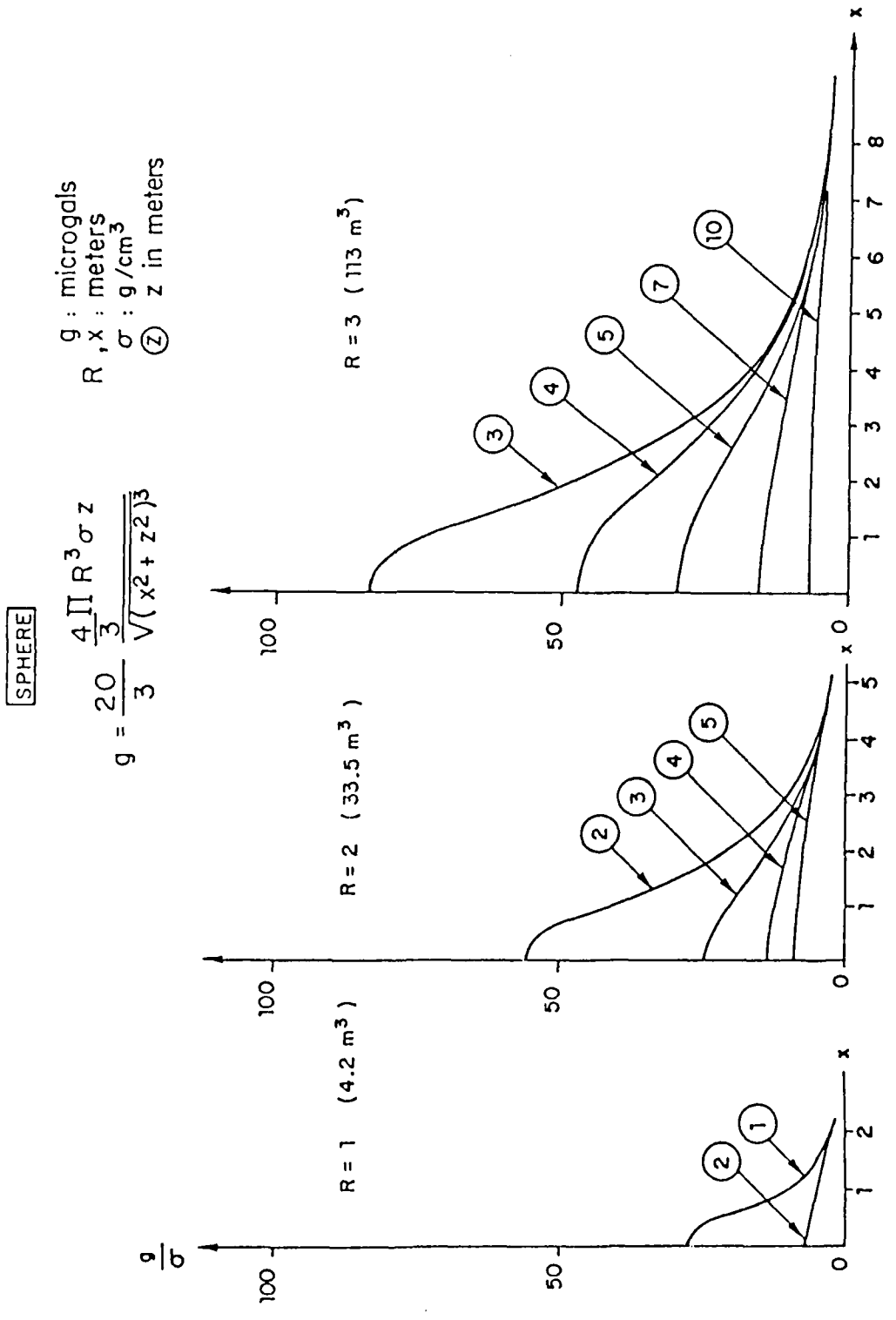

Figure 17. Anomaly due to a sphere (radius: 1, 2, 3 m)

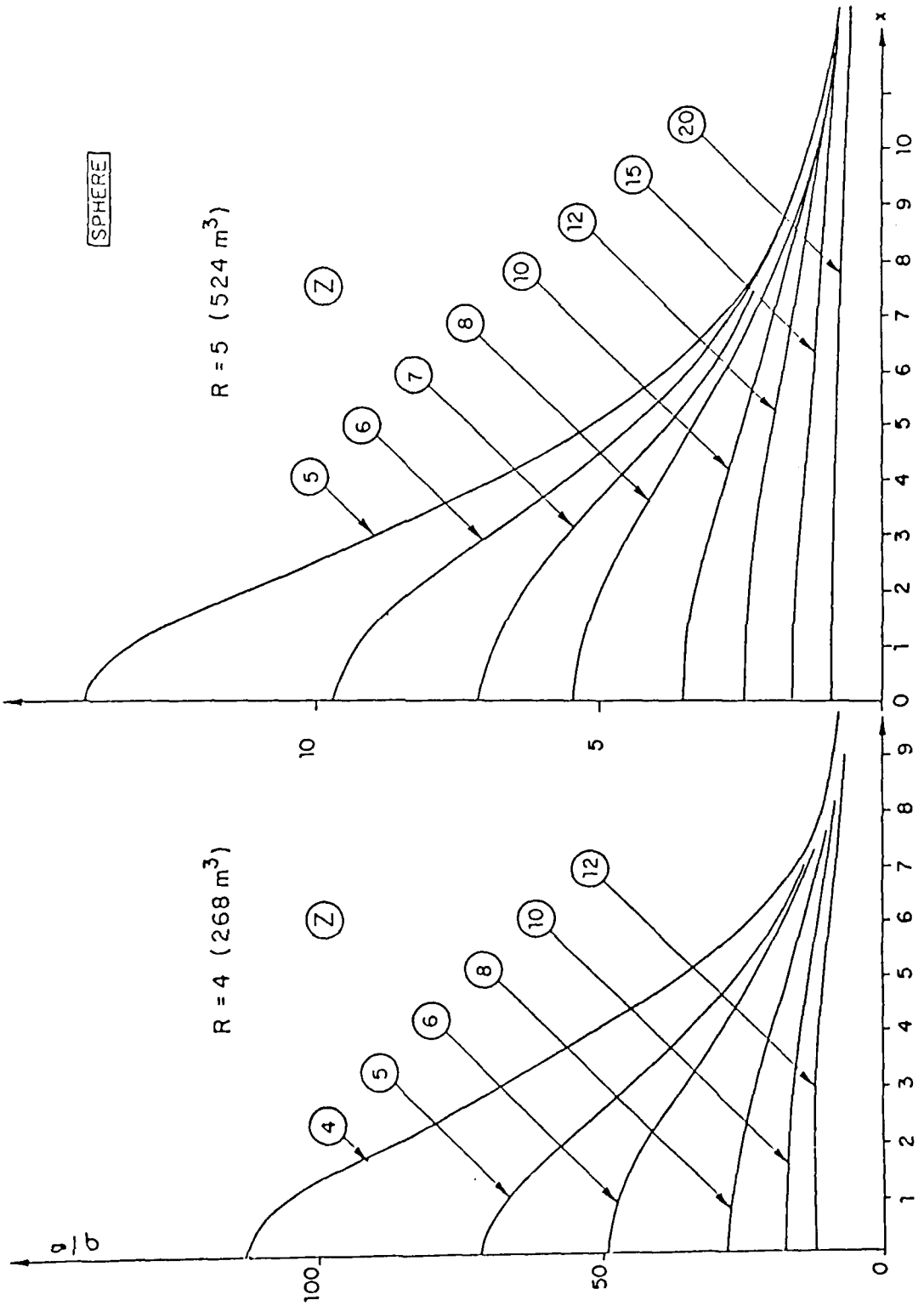

Figure 18. Anomaly due to a sphere
(radius: 4, 5 m)

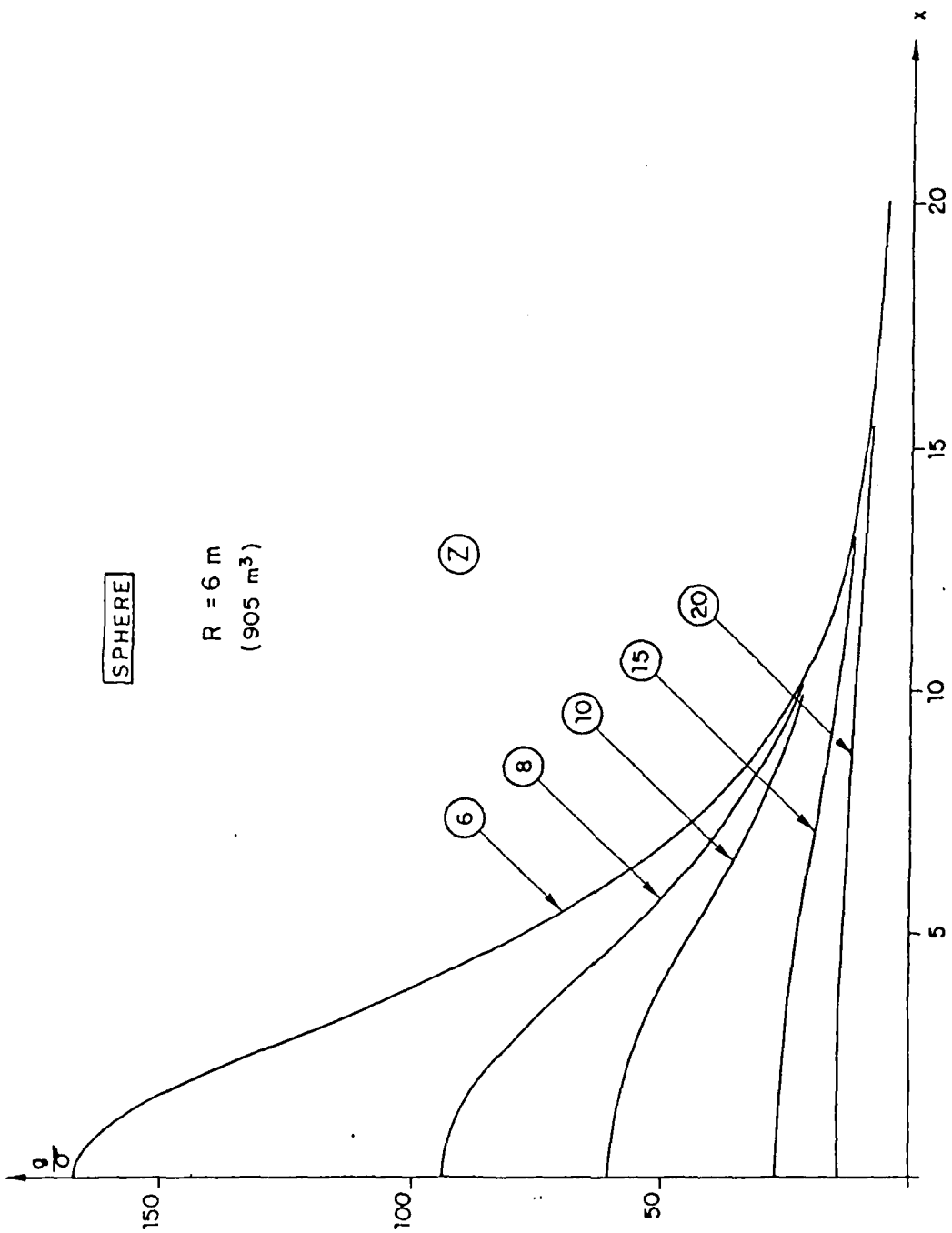

Figure 19. Anomaly due to a sphere (radius: 6 m)

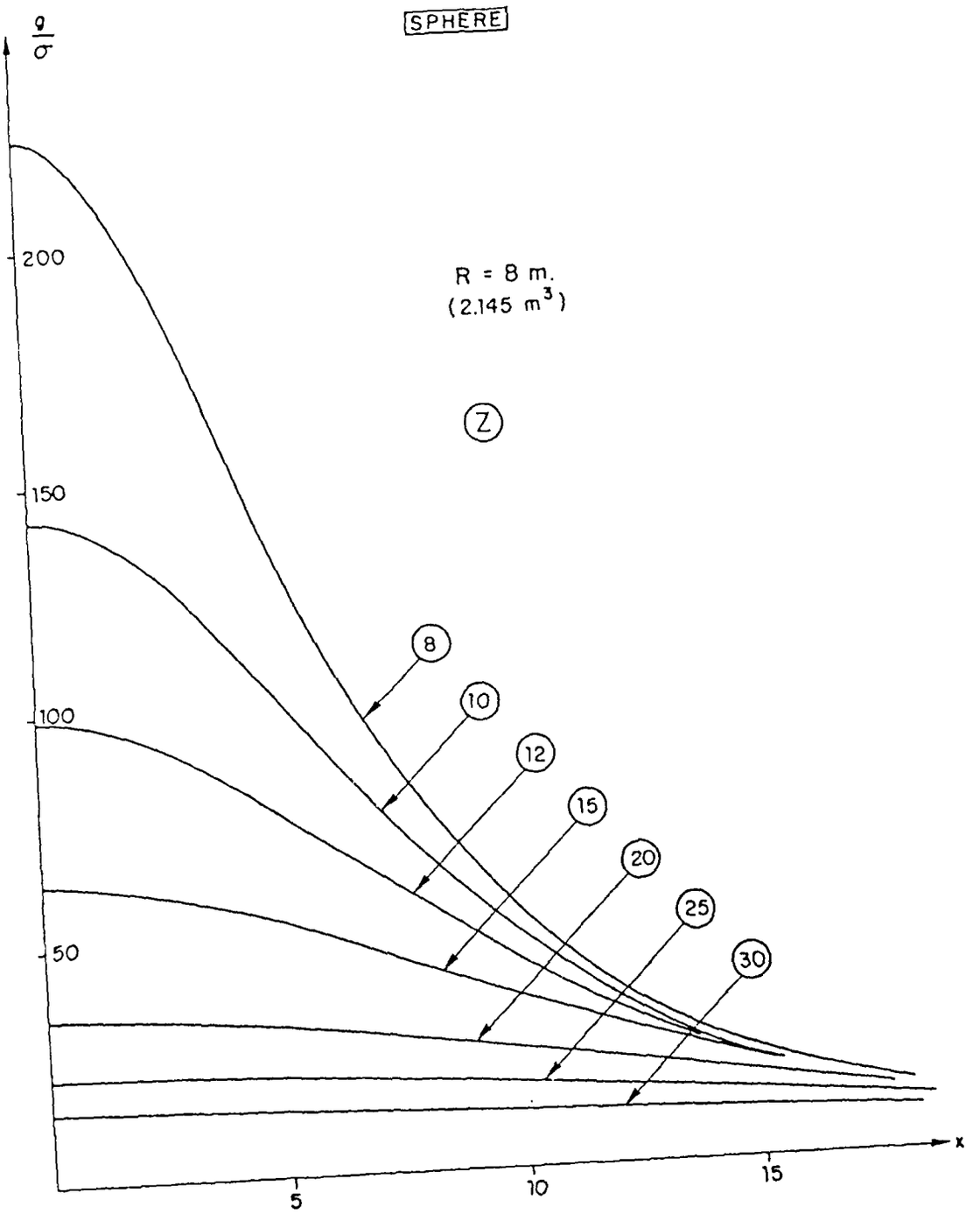

Figure 20. Anomaly due to a sphere (radius: 8 m)

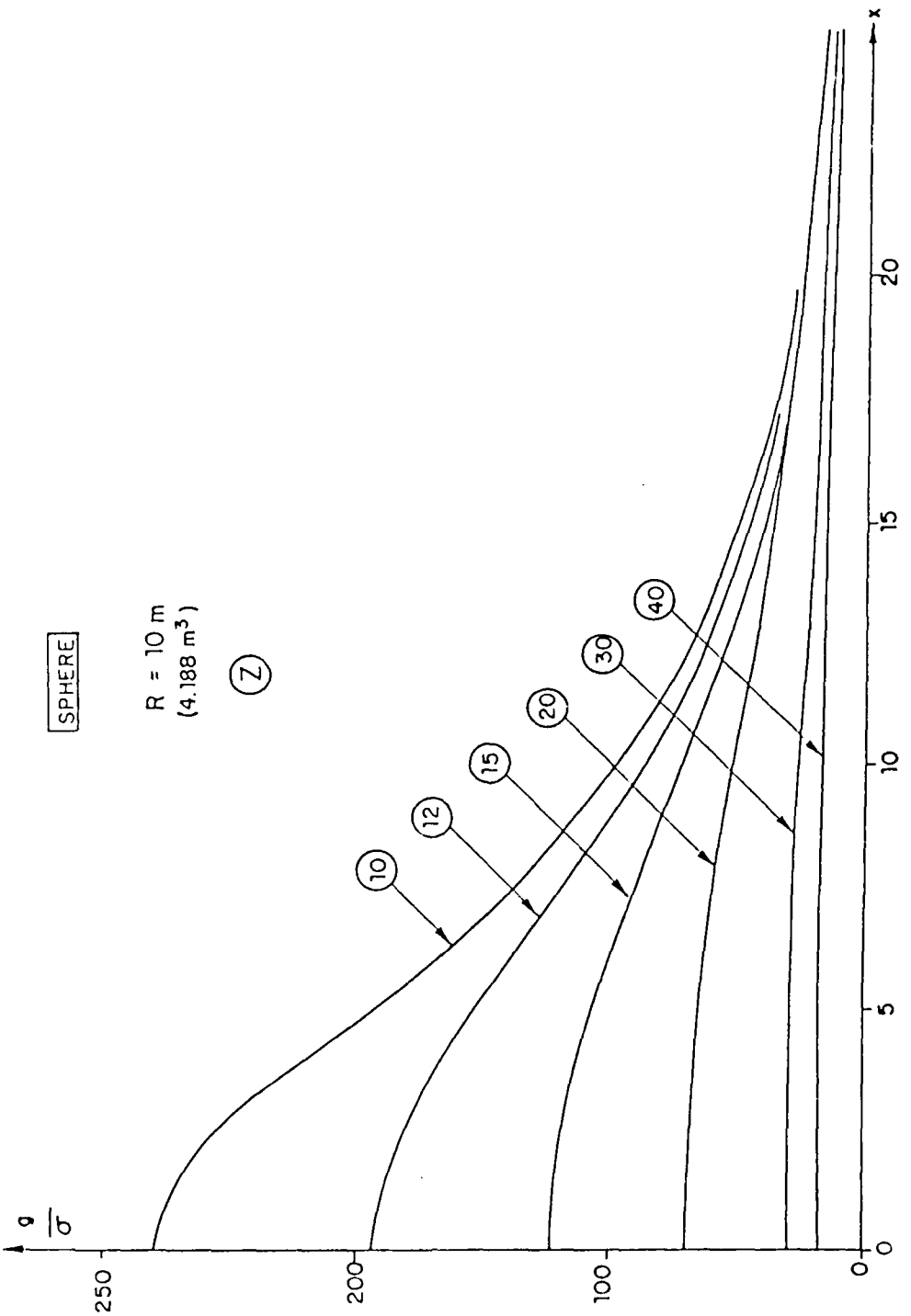

Figure 21. Anomaly due to a sphere (radius: 10 m)

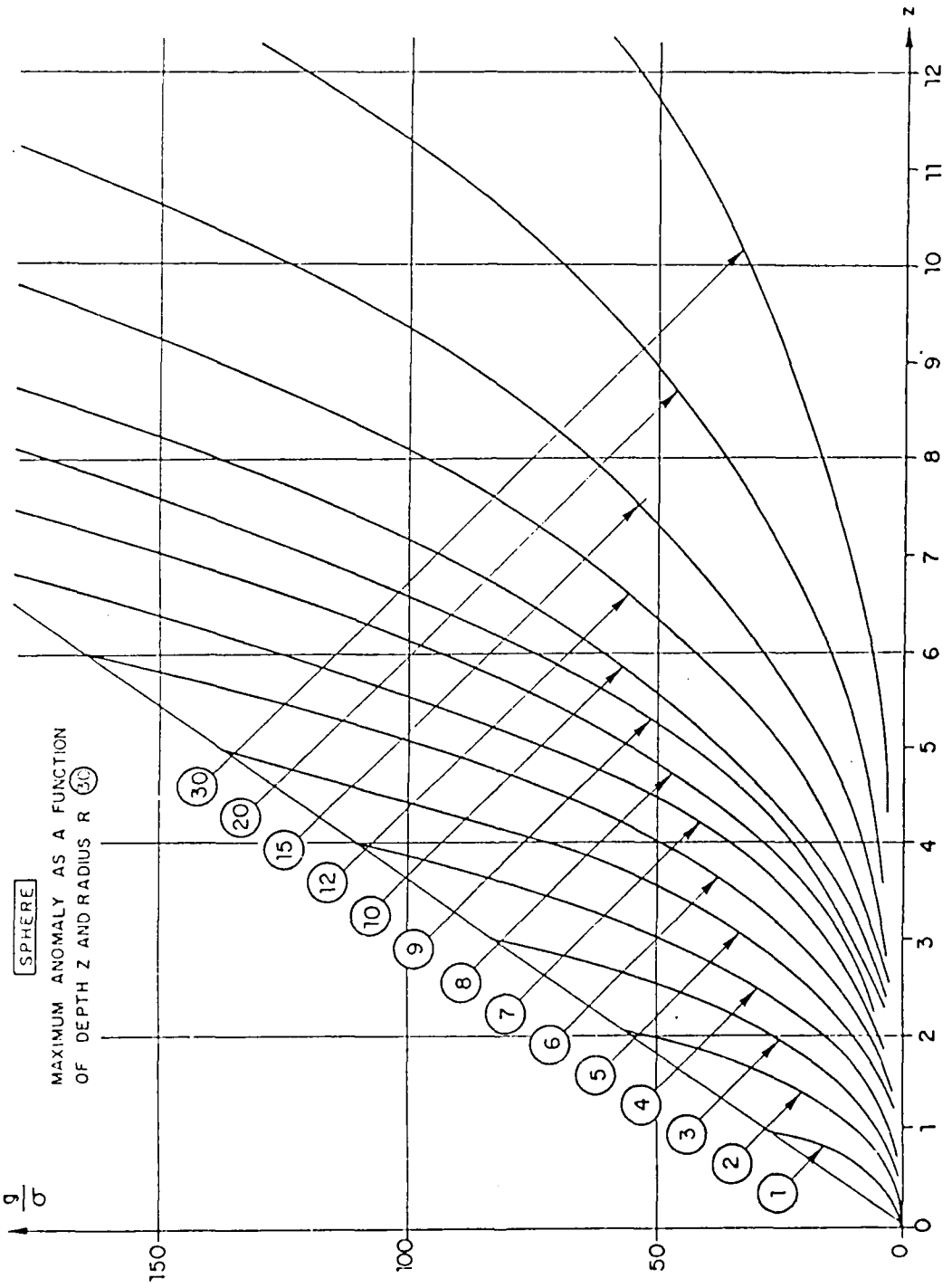

Figure 22. Maximum anomalies due to spheres at various depths

72. Horizontal cylinder (radius R in meters, depth z in meters, $\Delta\sigma$ in T/m^3, g in μgal.

$$g = \frac{40}{3} \cdot \Delta\sigma \cdot \frac{\pi R^2 z}{x^2 + z^2}$$

$$\frac{dg}{dx} = -\frac{80}{3} \frac{\Delta\sigma \cdot \pi R^2 z \cdot x}{(x^2 + z^2)^2}$$

$$g\ max = \frac{40}{3} \cdot \Delta\sigma \frac{\pi R^2}{z}$$

or if P is the mass per unit length ($P = \Delta\sigma \cdot \pi R^2$)

$$g\ max = \frac{40P}{3z}$$

$$\left(\frac{dg}{dx}\right)\ max = \frac{40}{3} \cdot \Delta\sigma \cdot \frac{\pi R^2}{\frac{8\sqrt{3}}{9} z^2} = 27.207 \frac{\Delta\sigma\ R^2}{z^2}$$

$$\frac{g\ max}{\left(\frac{dg}{dx}\right) max.} = \frac{z}{0.6495}$$

The maximum gradient is for $x = \pm \frac{z}{\sqrt{3}} = \pm\ 0.577\ z$, and for this value $g\ \left(\frac{z}{\sqrt{3}}\right) = 0.750\ g.max$;

half value of g max is reached for x = z and quarter value for $x = \sqrt{3}\ z$.

73. For a same value of g max, the anomaly due to a cylinder is less sharp than the one due to a sphere. (see Figure 24).

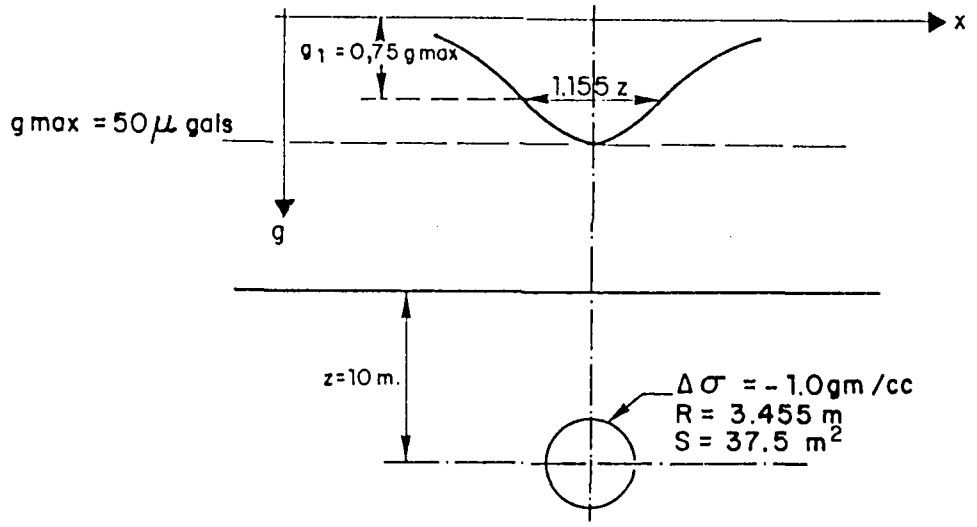

Figure 24. Example of anomaly due to a cylinder.

The mass per unit length of the cylinder will be given by :

$$P = \Delta\sigma . S = \Delta\sigma . \Pi R^2 = \frac{3z\ g_{max}}{40}$$

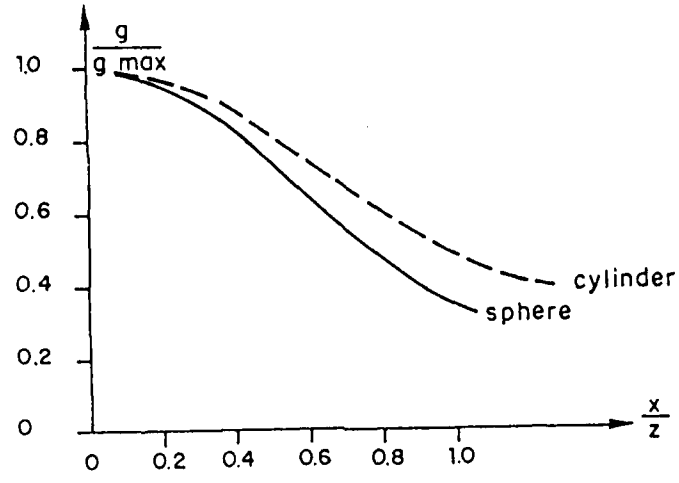

Figure 23. Comparison of anomalies due to a sphere and to a cylinder

74. The following set curves (figures 25-26) are enclosed:

- Radius R : 1, 2, 3 and 5 m
- Depth Z : 1, 2, 3, 5, 10, 20 and 30 m.

Figure 27 shows the maximum anomaly created by cylinders of radii ranging from 1 to 8 m at depths of 1, 3, 5, 9, 15 and 30 m. A density contrast of $\Delta\sigma = -2.0\ g/cm^3$ is supposed (void in a chalk environment, for example).

75. Horizontal slabs. An horizontal slab, of thickness t and with a density contrast $\Delta\sigma$, infinite in the x and y directions, gives an anomaly independent of its depth below the surface : $g = \frac{40\ \Pi}{3} \Delta\sigma t$ (μgal, when t is in m and $\Delta\sigma$ in g/cm^3).

In the following paragraphs, we will examine the adjustments to be made when the slab is not infinite in the x direction :

$$g = \frac{40\Pi}{3} \Delta\sigma t \left\{ 1 - f(t, z, x) \right\}$$

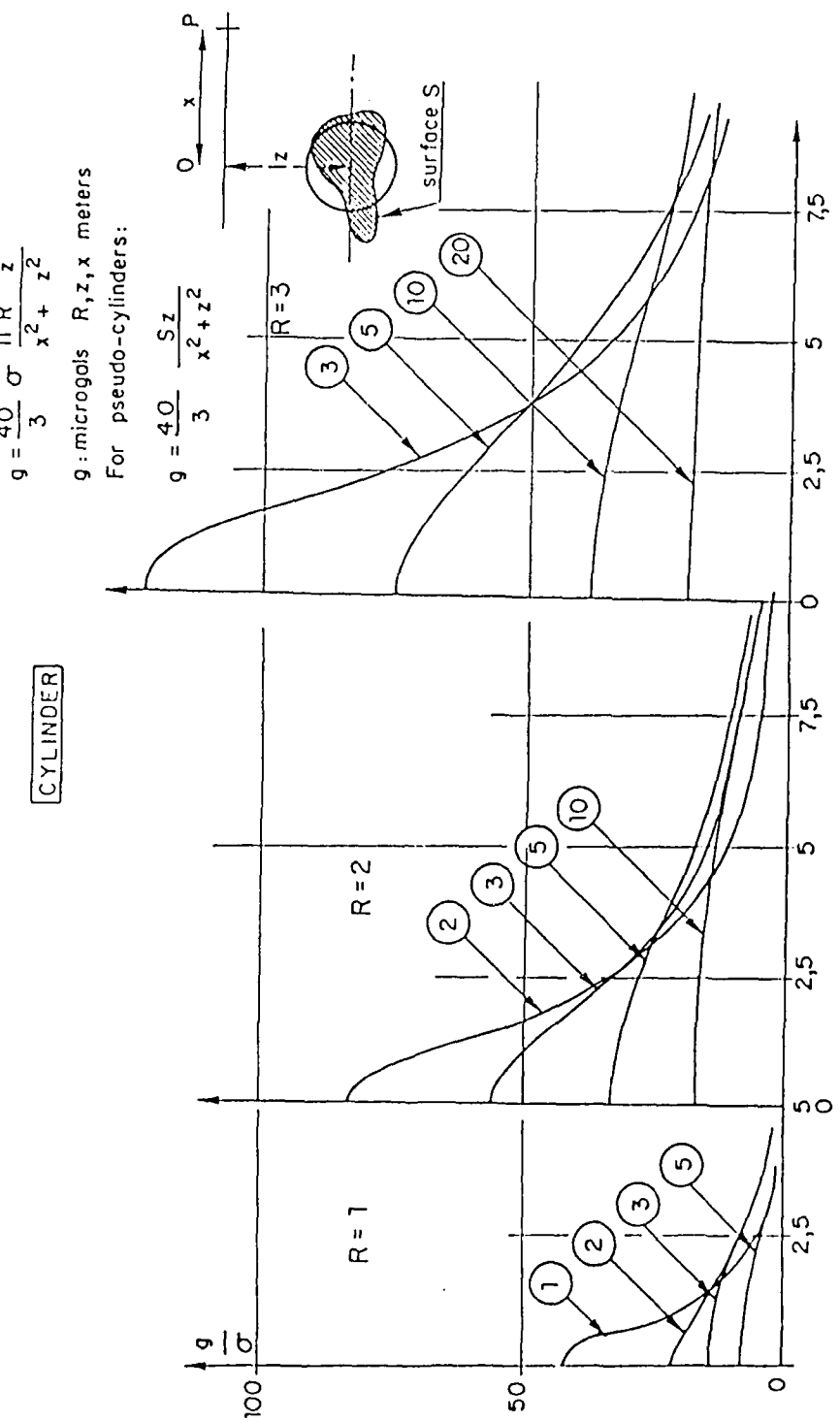

Figure 25. Anomaly due to a cylinder (radius: 1, 2, 3 m)

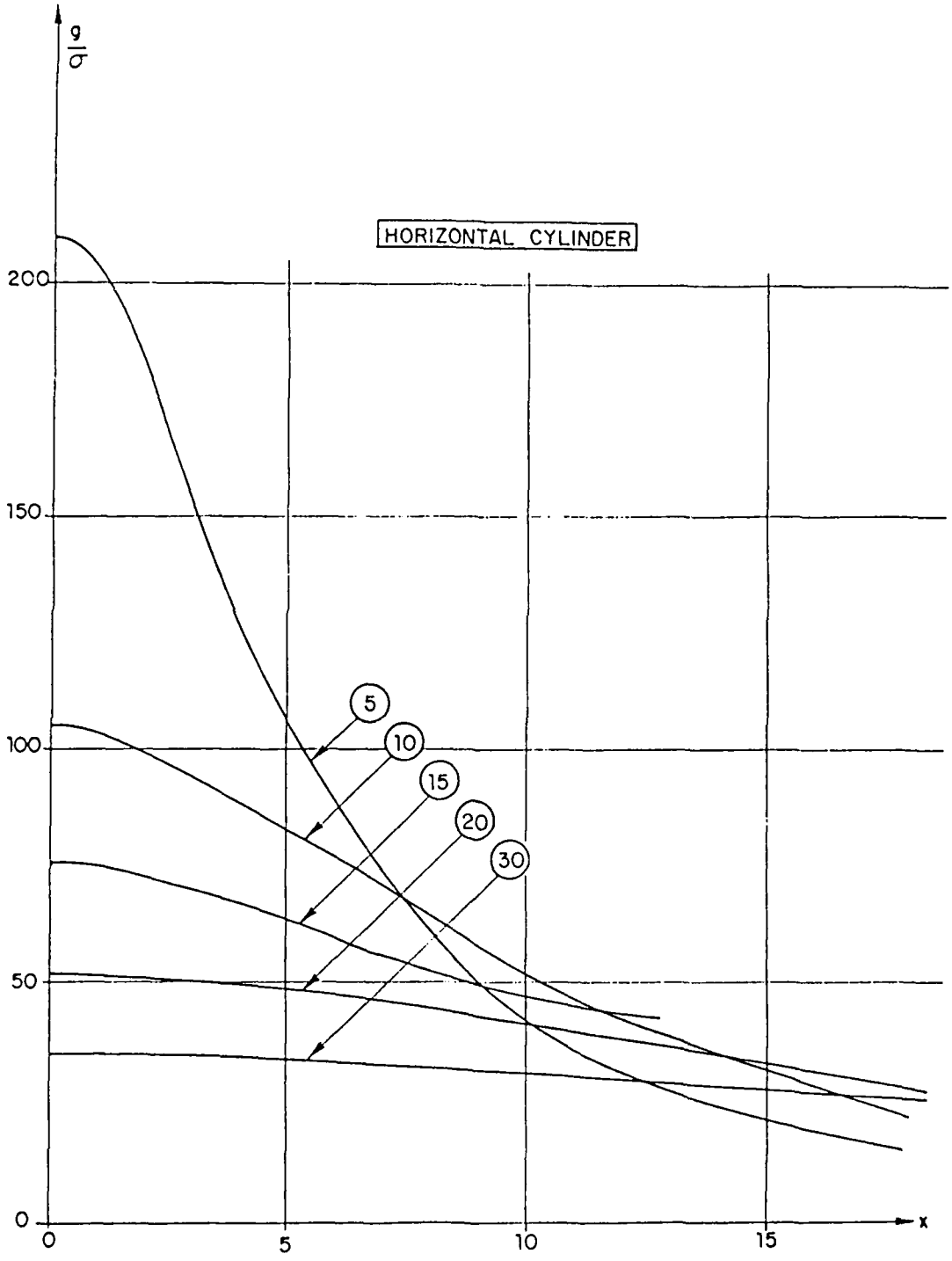

Figure 26. Anomaly due to a cylinder (radius: 5 m)

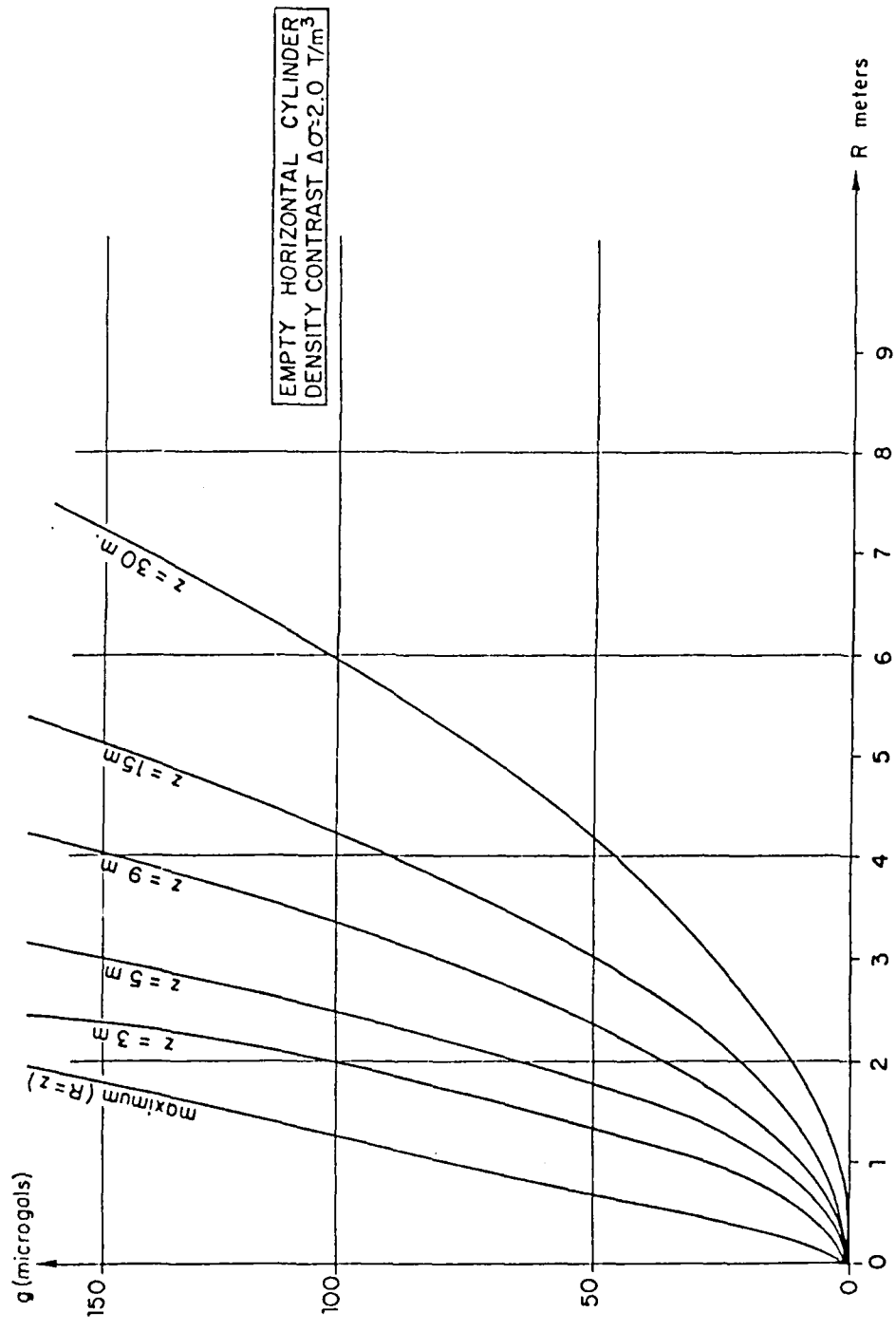

Figure 27. Maximum anomalies due to horizontal cylinders

76. Thick infinite horizontal slab.

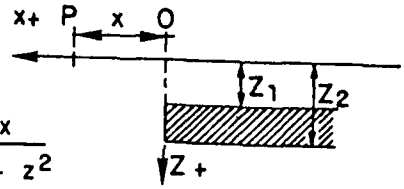

Integration in the x direction :

$$g = \frac{40\sigma}{3} \; z \; dz \int_x^{\infty} \frac{dx}{x^2 + z^2}$$

$$g = \frac{40}{3} \; \sigma \; dz \left[\tan^{-1} \frac{x}{z} \right]_x^{\infty} = \frac{40}{3} \; \sigma \; dz \left[\frac{\pi}{2} - \tan^{-1} \frac{x}{z} \right]$$

Integration from Z_1 to Z_2 yields :

$$g = \frac{40\sigma}{3} \int_{Z_1}^{Z_2} \left(\frac{\pi}{2} - \tan^{-1} \frac{x}{z} \right) dz$$

$$g = \frac{40\sigma}{3} \left\{ \frac{\pi}{2} (Z_2 - Z_1) - \int_{Z_1}^{Z_2} \tan^{-1} \frac{x}{z} \; dz \right\}$$

$$g = \frac{40\sigma}{3} \left\{ \frac{\pi}{2} (Z_2 - Z_1) - \int_{Z_1}^{Z_2} \operatorname{ctn}^{-1} \frac{z}{x} \; dz \right\}$$

$$g = \frac{40\sigma}{3} \left\{ \frac{\pi}{2} (Z_2 - Z_1) - \left[z \operatorname{ctn}^{-1} \frac{z}{x} + \frac{x}{2} \ln (z^2 + x^2) \right]_{Z_1}^{Z_2} \right\}$$

$$g = \frac{40\sigma}{3} \left\{ \frac{\pi}{2} (Z_2 - Z_1) - Z_2 \tan^{-1} \frac{x}{z_2} + Z_1 \tan^{-1} \frac{x}{Z_1} - \frac{x}{2} \ln \frac{Z_2^2 + x^2}{Z_1^2 + x^2} \right\}$$

Limits

If $x \longrightarrow -\infty$ $\quad g_{max} \longrightarrow \frac{40\pi\sigma}{3} (Z_2 - Z_1)$

If $x \longrightarrow +\infty$ $\quad g \longrightarrow 0$

If $x = 0$ $\quad g = \frac{20}{3} \pi\sigma (Z_2 - Z_1)$

Horizontal gradient

$$\frac{dg}{dx} = -\frac{20\sigma}{3} \ln \frac{x^2 + Z_2^2}{x^2 + Z_1^2}$$

maximum for $x = 0$, $\left(\frac{dg}{dx}\right)_{max} = \frac{-40\sigma}{3} \ln \frac{Z_2}{Z_1}$

$$\frac{g_{max}}{\left(\frac{dg}{dx}\right)_{max}} = \frac{-\pi (Z_2 - Z_1)}{\ln (Z_2 / Z_1)}$$

If $Z_2 - Z_1 = t$ and $\frac{Z_2 + Z_1}{2} = z$

$$\frac{g_{max}}{\left(\frac{dg}{dx}\right)_{max}} = \frac{-\pi t}{\ln \frac{1 + \frac{t}{2z}}{1 - \frac{t}{2z}}}$$

77. The following table shows that as soon as z exceeds t, the function $U = \frac{g\,max}{\left(\frac{dg}{dx}\right)max}$ is close to πz.

Table 7 : Function $\left(\frac{U}{\pi z}\right)$ as a function of thickness t and depth z. (thick infinite slab)

z \ t	10	20	30	50	100
10	0.91	0	-	-	-
20	0.98	0.91	0.77	-	-
30	0.99	0.96	0.91	0.70	-
50	1.00	0.99	0.97	0.91	0
100	1.00	1.00	0.99	0.98	0.91
200	1.00	1.00	1.00	0.99	0.98

Therefore : $$\frac{g\,max}{\left(\frac{dg}{dx}\right)max} \leqslant \pi z$$

The approximation is correct (error of 9 % or less) when $t \leqslant z$.

78. Figure 28 gives the half anomalies (outside the slab, the other half is symetrical) due to semi-infinite slabs located between the following depth :

5 m slab : 10-15 m, 20-25 m, 50-55 m

10 m slab : 10-20 m, 20-30 m, 50-60 m

50 m slab : 10-60 m, 20-70 m, 50-100 m

100 m slab : 10-110 m, 20-120 m, 50-150 m

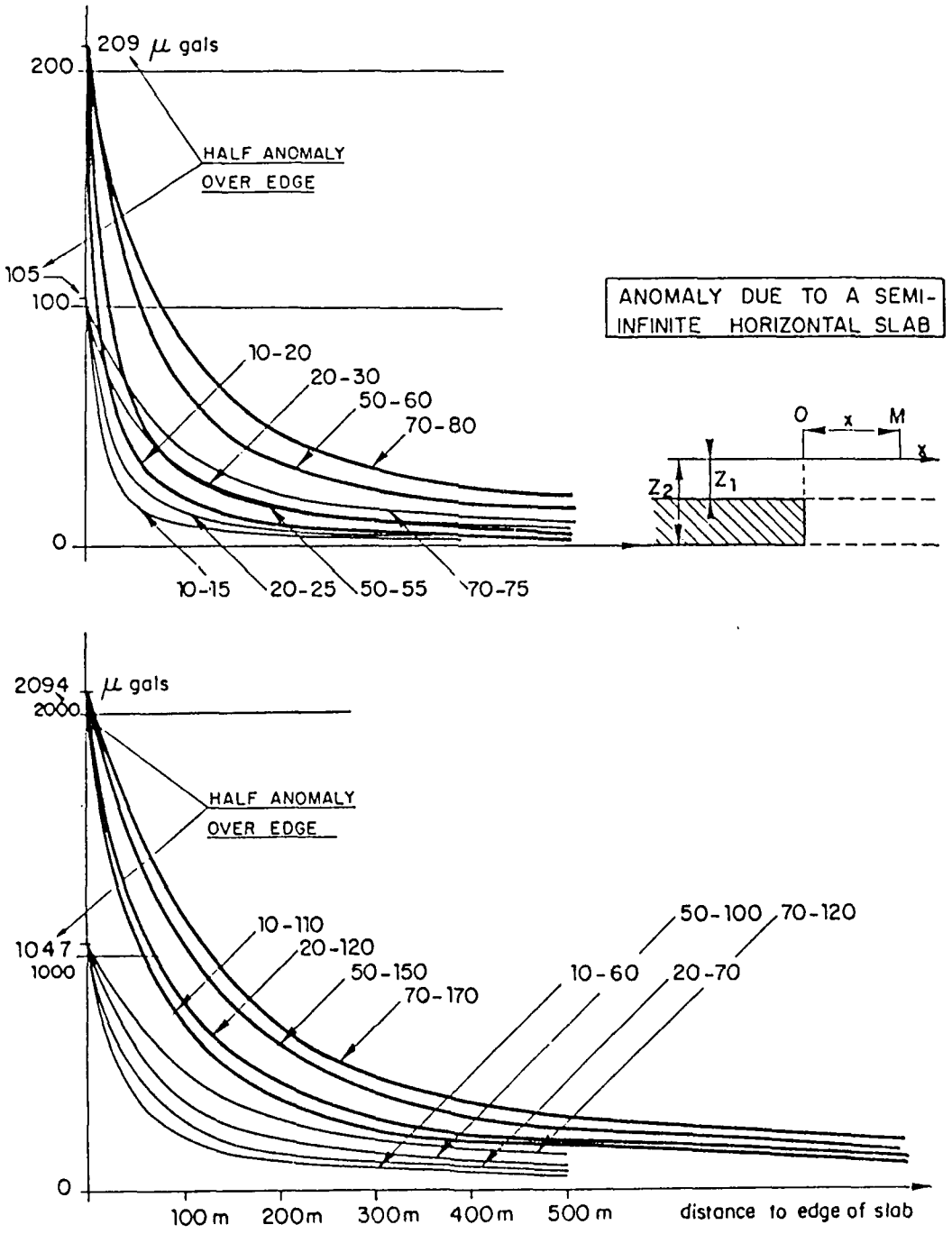

Figure 28. Anomaly due to a semi-infinite horizontal slab

It can be noted that the anomaly drops to 10 % of the maximum value (20 % of the half-anomaly) at the following distances D from the slab edge :

10-15 m : 45 m	10-20 m : 50 m	10-60 m : 100 m	10-110 m : 180 m
20-25 m : 70 m	20-30 m : 80 m	20-70 m : 150 m	20-120 m : 215 m
50-55 m : 160 m	50-60 m : 170 m	50-100 m : 210 m	50-150 m : 295 m
70-75 m : 205 m	70-80 m : 230 m	70-120 m : 280 m	70-170 m : 350 m

The distance D is approximately

$$D \# 3 \frac{(Z_1 + Z_2)}{2}$$

where Z_1 is the top of the slab and Z_2 the bottom of the slab as shown on Figure 29.

79. Thick finite horizontal strip.

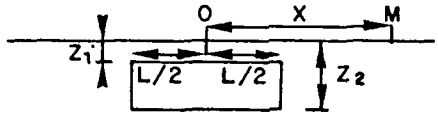

The slab is supposed to be infinite in the y direction.. Integration from $y \to -\infty$ to $y \to +\infty$:

$$g = 2 \cdot \frac{20}{3} \int_{y=0}^{y \to +\infty} \frac{z \, dx \, dy \, dz}{(x^2 + y^2 + z^2)^{3/2}}$$

$$g = \frac{40 \sigma z \, dz \, dx}{3 (x^2 + z^2)} \left[\frac{y}{(x^2 + y^2 + z^2)^{1/2}} \right]_0^{\infty}$$

$$g = \frac{40 \sigma z \, dz \, dx}{3 (x^2 + z^2)}$$

Integration from $x = X - \frac{L}{2}$ to $x = X + \frac{L}{2}$:

$$g = \frac{40}{3} \sigma z \, dz \int_{x=X-L/2}^{x=X+L/2} \frac{dx}{x^2 + z^2}$$

$$g = \frac{40 \sigma}{3} dz \left[\tan^{-1} \frac{X + L/2}{z} - \tan^{-1} \frac{X - L/2}{z} \right]$$

THICK SEMI - INFINITE HORIZONTAL SLAB

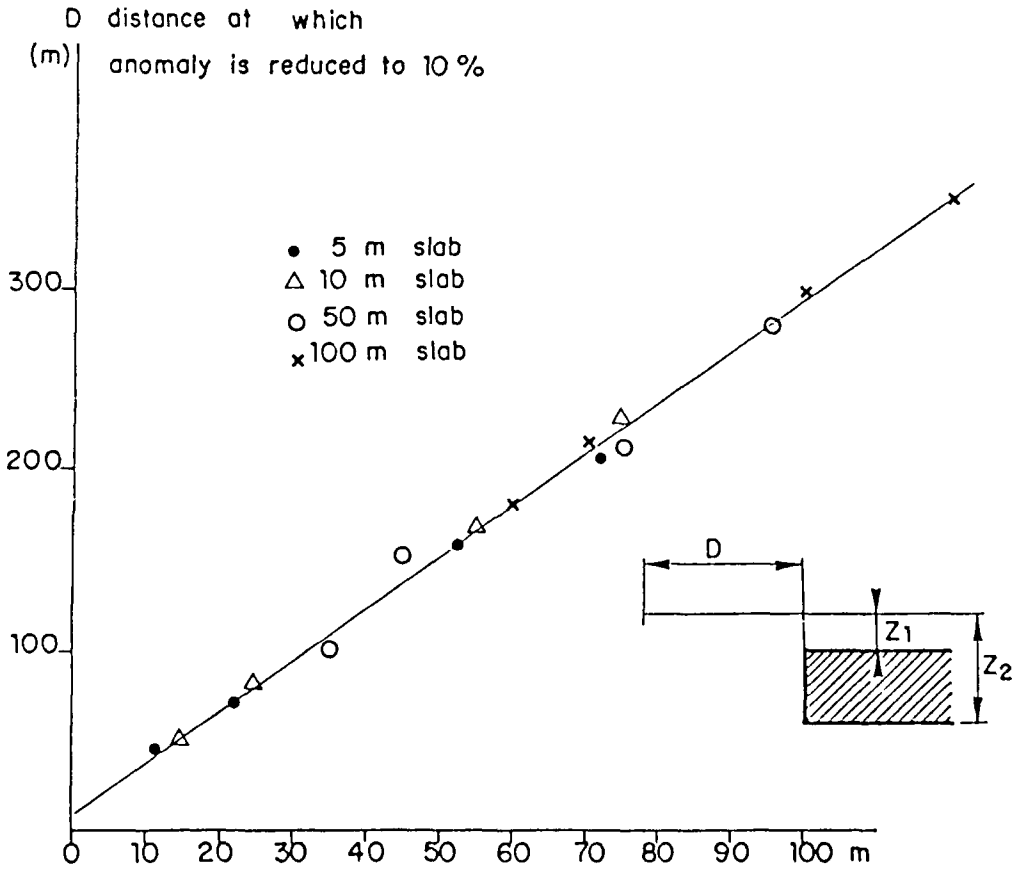

$$Z = \frac{1}{2}(Z_1 + Z_2)$$

Figure 29. Thick semi-infinite horizontal slab; distance at which anomaly is reduced to 10 % of maximum

Integration from $Z = Z_1$ to $Z = Z_2$:

$$g = \frac{40\sigma}{3}\int_{Z_1}^{Z_2} \tan^{-1}\frac{X+L/2}{z}\,dz - \frac{40\sigma}{3}\int_{Z_1}^{Z_2} \tan^{-1}\frac{X-L/2}{z}$$

$$g = \frac{40\sigma}{3}\left[z\tan^{-1}\frac{X+L/2}{z} + \frac{X+L/2}{2}\ln\left(\left(X+\frac{L}{2}\right)^2+z^2\right)\right]_{Z_1}^{Z_2}$$

$$-\frac{40\sigma}{3}\left[z\tan^{-1}\frac{X-L/2}{z} + \frac{X-L/2}{2}\ln\left(\left(X-\frac{L}{2}\right)^2+z^2\right)\right]_{Z_1}^{Z_2}$$

$$g=\frac{40\sigma}{3}\left\{ Z_2\left[\tan^{-1}\frac{X+L/2}{Z_2}-\tan^{-1}\frac{X-L/2}{Z_2}\right]-Z_1\left[\tan^{-1}\frac{X+L/2}{Z_1}-\tan^{-1}\frac{X-L/2}{Z_1}\right]\right.$$

$$\left. +\frac{X+L/2}{2}\ln\frac{(X+L/2)^2+Z_2^2}{(X+L/2)+Z_1^2}-\frac{X-L/2}{2}\ln\frac{(X-L/2)^2+Z_2^2}{(X-L/2)^2+Z_1^2}\right\}$$

The maximum value (for $X = 0$) is given by :

$$g_{max} = \frac{80\sigma}{3}\left\{ Z_2\tan^{-1}\frac{L}{2Z_2} - Z_1\tan^{-1}\frac{L}{2Z_1}+\frac{L}{4}\ln\frac{L^2+4Z_2^2}{L^2+4Z_1^2}\right\}$$

Above the edges, for $X = \pm\frac{L}{2}$

$$g\,(L/2) = \frac{40\sigma}{3}\left\{ Z_2\tan^{-1}\frac{L}{Z_2} - Z_1\tan^{-1}\frac{L}{Z_1}+\frac{L}{2}\ln\frac{L^2+Z_2^2}{L^2+Z_1^2}\right\}$$

Horizontal gradient is given by :

$$\frac{dg}{dx} = \frac{20\sigma}{3}\ln\left\{\frac{(X+L/2)^2+Z_2^2}{(X+L/2)^2+Z_1^2}\cdot\frac{(X-L/2)^2+Z_1^2}{(X-L/2)^2+Z_2^2}\right\}$$

Maximum value of $\frac{dg}{dx}$ is attained for :

$$X = \pm \sqrt{\frac{L^2}{4} + \frac{-(L^2 + Z_1^2 + Z_2^2) + (\sqrt{(L^2 + Z_1^2 + Z_2^2) + 12 Z_1^2 Z_2^2}}{6}}$$

Or, setting $\frac{Z_1 + Z_2}{2} = Z$ and $Z_2 - Z_1 = t$:

$$X = \pm \sqrt{\frac{L^2}{4} - \frac{2Z^2 + t^2/2}{6} + \frac{1}{6}\sqrt{L^4 + 16Z^4 + t^4 + 4L^2Z^2 + L^2t^2 - 4Z^2t^2}}$$

The next tables give the values of the parameters defined in Figure 30 :

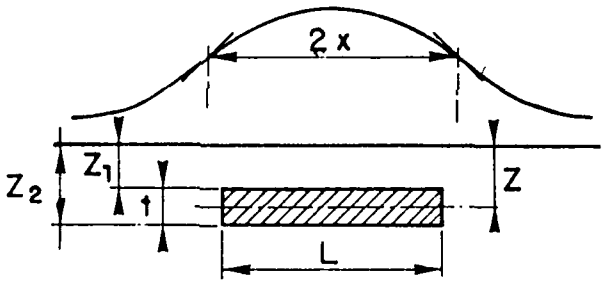

Figure 30. Bases of anomaly to a thick horizontal strip

$$\left.\begin{array}{l} \frac{X}{z} \\ A = \frac{3}{40\sigma}\left(\frac{dg}{dx}\right)_{max} \\ B = \frac{3}{40\sigma}\,\frac{g\ max}{z} \\ \frac{t\sigma}{g} = \frac{3}{40}\,\frac{C}{B} \\ U = \frac{g\ max}{z\left(\frac{dg}{dx}\right)_{max}} = \frac{B}{A} \end{array}\right\} \text{as functions of } C = t/z \text{ and of } L/z$$

Table 8 : Anomaly and horizontal gradient due to a finite horizontal strip.

t/z	L/z	0	0.1	0.2	0.5	1	2	5	10	∞
0.0	x/z	.577	.579	.583	.613	.717	1.075	2.507	5.001	∞/2
	A	.000	.000	.000	.000	.000	.000	.000	.000	.000
	B	.000	.000	.000	.000	.000	.000	.000	.000	.000
	tσ/g	∞	.751	.376	.153	.081	.048	.032	.027	.024
	U	1.540	1.541	1.546	1.578	1.680	1.949	2.476	2.774	3.142
0.1	x/z	.576	.577	.582	.612	.716	1.074	2.507	5.001	∞/2
	A	.000	.006	.013	.031	.055	.081	.096	.099	.100
	B	.000	.010	.020	.049	.093	.157	.238	.275	.314
	tσ/g	∞	.750	.375	.153	.081	.048	.032	.027	.024
	U	1.538	1.540	1.544	1.577	1.678	1.947	2.473	2.772	3.139
0.2	x/z	.572	.573	.577	.608	.713	1.073	2.507	5.001	∞/2
	A	.000	.013	.026	.063	.111	.162	.193	.199	.201
	B	.000	.020	.040	.098	.186	.314	.476	.549	.628
	tσ/g	∞	.748	.375	.153	.081	.048	.032	.027	.024
	U	1.532	1.534	1.540	1.572	1.674	1.943	2.467	2.765	3.131
0.5	x/z	.541	.543	.547	.580	0.693	1.065	2.506	5.001	∞/2
	A	.000	.034	.068	.162	.287	.414	.492	.506	.511
	B	.000	.051	.102	.250	.470	.791	1.191	1.374	1.571
	tσ/g	∞	.735	.368	.150	.080	.047	.031	.027	.024
	U	1.497	1.500	1.505	1.538	1.641	1.908	2.423	2.715	3.075
1.0	x/z	.429	.432	.438	.484	.627	1.041	2.504	5.001	∞/2
	A	.000	.081	.161	.380	.651	.909	1.061	1.089	1.099
	B	.000	.110	.219	.532	.985	1.612	2.388	2.748	3.142
	tσ/g	∞	.684	.343	.140	.076	.047	.031	.027	0.024
	U	1.350	1.355	1.361	1.400	1.512	1.774	2.252	2.524	2.860
1.5	x/z	0.241	.246	.260	.342	.543	1.013	2.501	5.000	∞/2
	A	.000	.191	.373	.828	1.290	1.671	1.889	1.931	1.946
	B	.000	.194	.384	.909	1.601	2.495	3.597	4.124	4.712
	tσ/g	∞	.580	.293	.124	.070	.045	.031	.027	.024
	U	1.014	1.017	1.029	1.098	1.241	1.493	1.904	2.136	2.422

T/z	L/z	0	0.1	0.2	0.5	1	2	5	10	∞
1.8	x/z	.099	.111	.141	.268	.508	1.001	2.500	5.000	∞/2
	A	.000	.478	.874	1.611	2.188	2.624	2.877	2.927	2.944
	B	.000	.291	.563	1.240	2.052	3.065	4.329	4.951	5.655
	tσ/g	∞	.465	.240	.109	.068	.044	.031	.027	.024
	U	.558	.608	.644	.770	.938	1.168	1.505	1.692	1.921
1.9	x/z	.050	.071	.112	.255	.502	1.001	2.500	5.000	∞/2
	A	.000	.880	1.438	2.280	2.881	3.329	3.593	3.645	3.664
	B	.000	.353	.661	1.381	2.220	3.263	4.575	5.227	5.969
	tσ/g	∞	.403	.216	.103	.064	.044	.031	.027	.024
	U	.366	.402	.460	.606	.770	.980	1.273	1.434	1.629
1.95	x/z	.025	.056	.103	.251	.500	1.000	2.500	5.000	∞/2
	A	.000	1.442	2.089	2.967	3.575	4.029	4.297	4.350	4.369
	B	.000	.401	.724	1.459	2.307	3.363	4.698	5.365	6.126
	tσ/g	∞	.365	.202	.100	.063	.043	.031	.027	.024
	U	.219	.278	.347	.492	.645	.834	1.093	1.233	1.402
2.00	x/z	0.000	.050	.100	.250	.500	1.000	2.500	5.000	∞/2
	A	0.000	∞	∞	∞	∞	∞	∞	∞	∞
	B	.000	.469	.799	1.541	2.397	3.464	4.821	5.503	6.283
	tσ/g	∞	.320	.188	.097	.063	.043	.031	.027	.024
	U	0	0	0	0	0	0	0	0	0

80. The above Table 8 is computed for various values of t/z, ranging from $\frac{t}{z} = 0$ (infinitely thin strip, equivalent to the case described later in 1613) to $\frac{t}{z} = 2.0$ (z being the average depth $z = \frac{Z_1 + Z_2}{2}$, t cannot exceed 2 z when $Z_1 = 0$). For each value of t/z, the parameters A, B, $\frac{t}{g}$ and U, as defined above, are computed for various values of L/z, ranging from L/z = 0 (infinitely narrow strip, as described later in 1617) to L/z = ∞ (for an infinitely wide, thick strip).

81. It can be noted that x (distance from center to point of maximum gradient) is close to $\frac{L}{2}$ (half width of strip), as soon as $\frac{L}{z} > 2$, with an accuracy better than 7.5 %.

1610. Nomogram for the interpretation of a finite thick horizontal strip.

As in 169, the strip is supposed to be infinite in the y direction. Thickness, depth and width can vary freely. From the formulas and tables derived in 169, we have developed the following procedure using parameters defined in Figure 31 and the nomogram in Figure 32 (where the procedure is illustrated with a specific example).

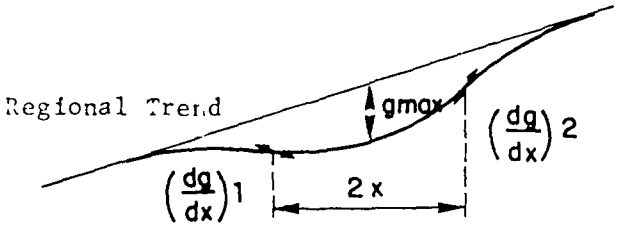

Figure 31. Example of parameters used in nomographic interpretation

1. Evaluate $\frac{dg}{dx}\ max = \frac{1}{2}\left\{\left(\frac{dg}{dx}\right)_1 + \left(\frac{dg}{dx}\right)_2\right\} = 20$ µgals/meter

   g max = 445 µgals

   2 X = 40 m

2. Compute $U = \frac{1}{2X}\frac{gmax}{\left(\frac{dg}{dx}\right)max} = 0.556 \sim 0.56$

3. Select a first value of t/z : 0.5

4. Starting from ordinate 0.56, move horizontally until curve $\frac{t}{z} = 0.5$ (on main set of curves)

5. Read abscissa: $\frac{z}{2x} = 0.235 \rightarrow z = 40 \times 0.235 = 9.4$ m

6. From point A (0.56, 0.235), move downwards to point B on curve $\frac{t\sigma}{g}$ (for $\frac{t}{z} = 0.5$)

7. Read ordinate: $\frac{t\sigma}{g} = 0.034$

8. Supposing $\sigma = 1.0$, compute t = 15.10 m and $\frac{t}{z} = \frac{15.10}{9.4} = 1.606$

9. Select a second and then a third value of $\frac{t}{z}$

10. Plot computed $\left(\frac{t}{z}\right)c$ as a function of selected $\left(\frac{t}{z}\right)s$

11. Point where $\left(\frac{t}{z}\right)c = \left(\frac{t}{z}\right)s$ is the best choice for the supposed value of density σ.

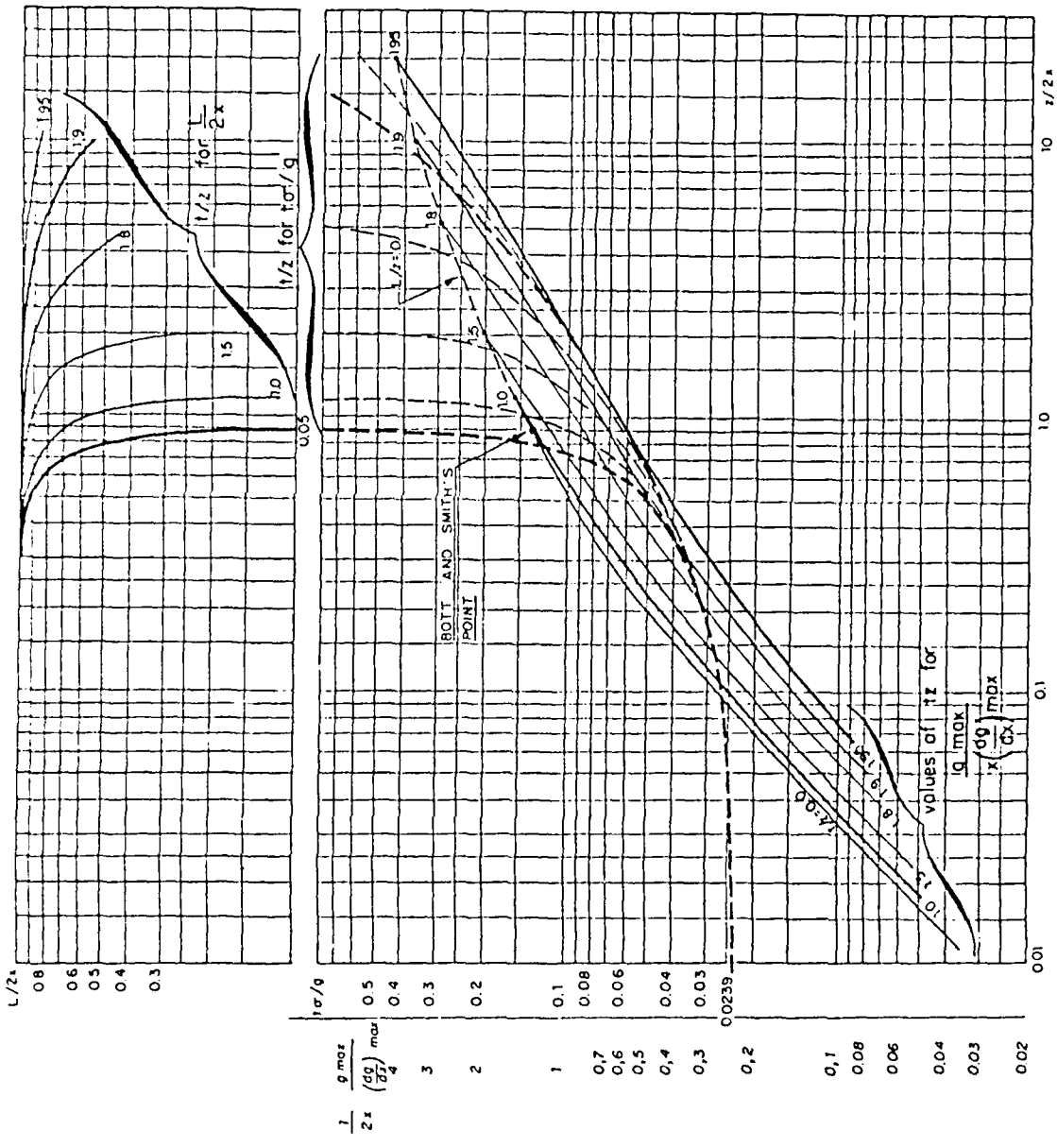

Figure 32. Nomogram for interpretation of thick horizontal strip

	$\left(\frac{t}{z}\right)$ s	z	t	$\left(\frac{t}{z}\right)$ c
	0.5	9.4	15.	1.6
	1.0	10.8	15.6	1.44
	1.25	12.0	16.2	1.35
	1.5	13.0	16.4	1.26
Interpolation	1.30	12.2	16.25	1.30

12. From interpolated point A (0.56, 0.31), move upwards to curves $\frac{L}{2x} = f\left(\frac{z}{2x}\right)$.

Interpolating t/z = 1.3 between curves $\frac{t}{z}$ = 1.0 and 1.5 for the same ordinate $\frac{z}{2x}$ = 0.31, read:

$$\frac{L}{2x} = 0.99 \text{ to } 1.00 \rightarrow L = 40 \text{ m.}$$

This example was derived from the following theoretical case :

L = 40 m

z = 12 m

t = 16 m

yielding X = 20.0788 m rounded to 20.0

g max = 446.76 µgals rounded to 445

$\left(\frac{dg}{dx}\right)$ max = 20.04038 µgals rounded to 20.

Of course, if density σ is not known, the iterative technique described above cannot be used. In that case, each selected $\frac{t}{z}$ curve will yield :

1. the same depth z as above

2. $t = \left(\frac{t}{z}\right)_s z$

3. $\sigma = \left(\frac{t\sigma}{g}\right) g \frac{1}{t}$

For the above example, we get :

	$\left(\frac{t}{z}\right)$ s	z	t	σ
	0.5	9.4	4.7	3.266
	1.0	10.8	9.4	1.442
	1.25	12.0	15.0	1.053
	1.5	13.0	19.5	0.821
real :	(1.333)	(12)	(16)	(1.000)

Using geological limits for maximum density contrast, certain solutions can be rejected.

83. Semi-infinite thin slab. The slab is supposed to be infinite in the y direction as well as in the x + direction.

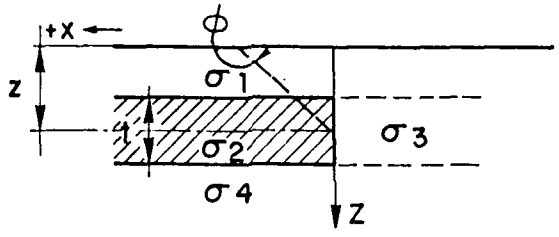

σ_1, σ_4 arbitrary $\quad \Delta\sigma = \sigma_2 - \sigma_3$

The first formula given in Paragraph 76 simplifies as follows, when the slab is thin. The approximation is quite acceptable when $t < z$.

$$g = \frac{40}{3} \Delta\sigma t \left[\frac{\pi}{2} + \tan^{-1}\frac{x}{z} \right] \qquad (z > 0)$$

This can also be written : $\quad g = \frac{40}{3} \Delta\sigma t \phi$

Limits:

To the left $g \longrightarrow \frac{40\pi}{3} \Delta\sigma t.$

For $x = 0$, $\quad g = \frac{40}{3}\frac{\pi}{2}\Delta\sigma t$ (half of the maximum anomaly)

To the right $g \to 0$.

Note : a quarter of the maximum anomaly is reached for $x = -z$.

First derivative $\quad \frac{dg}{dx} = \frac{40}{3} \Delta\sigma t \frac{z}{x^2 + z^2}$

Maximum for $x = 0$.

$$\left(\frac{dg}{dx}\right) \max = \frac{40}{3} \Delta\sigma \frac{t}{z}$$

$$\frac{g\,max}{\left(\frac{dg}{dx}\right)max} = \frac{\frac{40\pi}{3} \Delta\sigma . t}{\frac{40}{3} \Delta\sigma . \frac{t}{z}}$$

$$\frac{g\,max}{\left(\frac{dg}{dx}\right)max} = \pi z = \frac{z}{0.31831}$$

The enclosed fig.33 gives a normalized set curve for L $\Delta\sigma$ t = 10.0.

84. Thin finite horizontal strip.

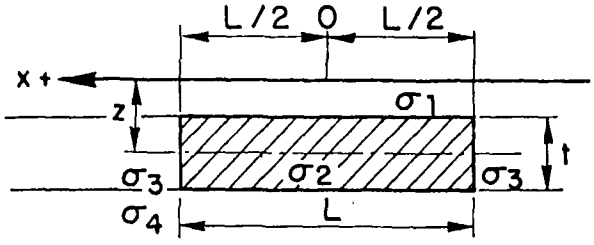

σ_1, σ_4 indifferent. $\Delta\sigma = \sigma_2 - \sigma_3$.

a. First formulas :

The formulas given in 79 simplify as follows when t < 0.5 z :

$$g = \frac{40}{3} \Delta\sigma\, t \left\{ \tan^{-1} \frac{x + L/2}{z} - \tan^{-1} \frac{x - L/2}{z} \right\}$$

Horizontal gradient : $$\frac{dg}{dx} = -\frac{80}{3} \frac{\Delta\sigma . t . L . x}{[(x + L/2)^2 + z^2][(x - L/2)^2 + z^2]}$$

g maximum for x = 0.

$$g \max = \frac{80}{3} \Delta\sigma . t . \tan^{-1} \frac{L}{2z}$$

Maximum horizontal gradient is reached for :

$$x_1 = \pm \sqrt{\frac{1}{3} \left\{ \frac{L^2}{4} - z^2 + 2\sqrt{z^4 + \frac{L^2 z^2}{4} + \frac{L^4}{16}} \right.}$$

b. Second formulas :

When L > 2z, these formulas can be further approximated.

$$g \max \# \frac{80}{3} \Delta\sigma . t \left(\frac{\pi}{2} - \frac{2z}{L} \right)$$

$$\left(\frac{dg}{dx} \right) \max \# -\frac{40}{3} \frac{\Delta\sigma t . L^2}{L^2 + z^2} \left\{ 1 - \frac{8}{3} \frac{z^4}{L^4} \frac{L^2 - z^2}{L^2 + z^2} \right\}$$

reached for $$x_1 \# \frac{L}{2} \left(1 + \frac{8}{3} \frac{z^4}{L^4} \right)$$

for which $$g_1 \# \frac{40}{3} \Delta\sigma\, t \left\{ \tan^{-1} \frac{L}{z} - \frac{4}{3} \frac{z^3}{L(L^2 + z^2)} \right\}$$

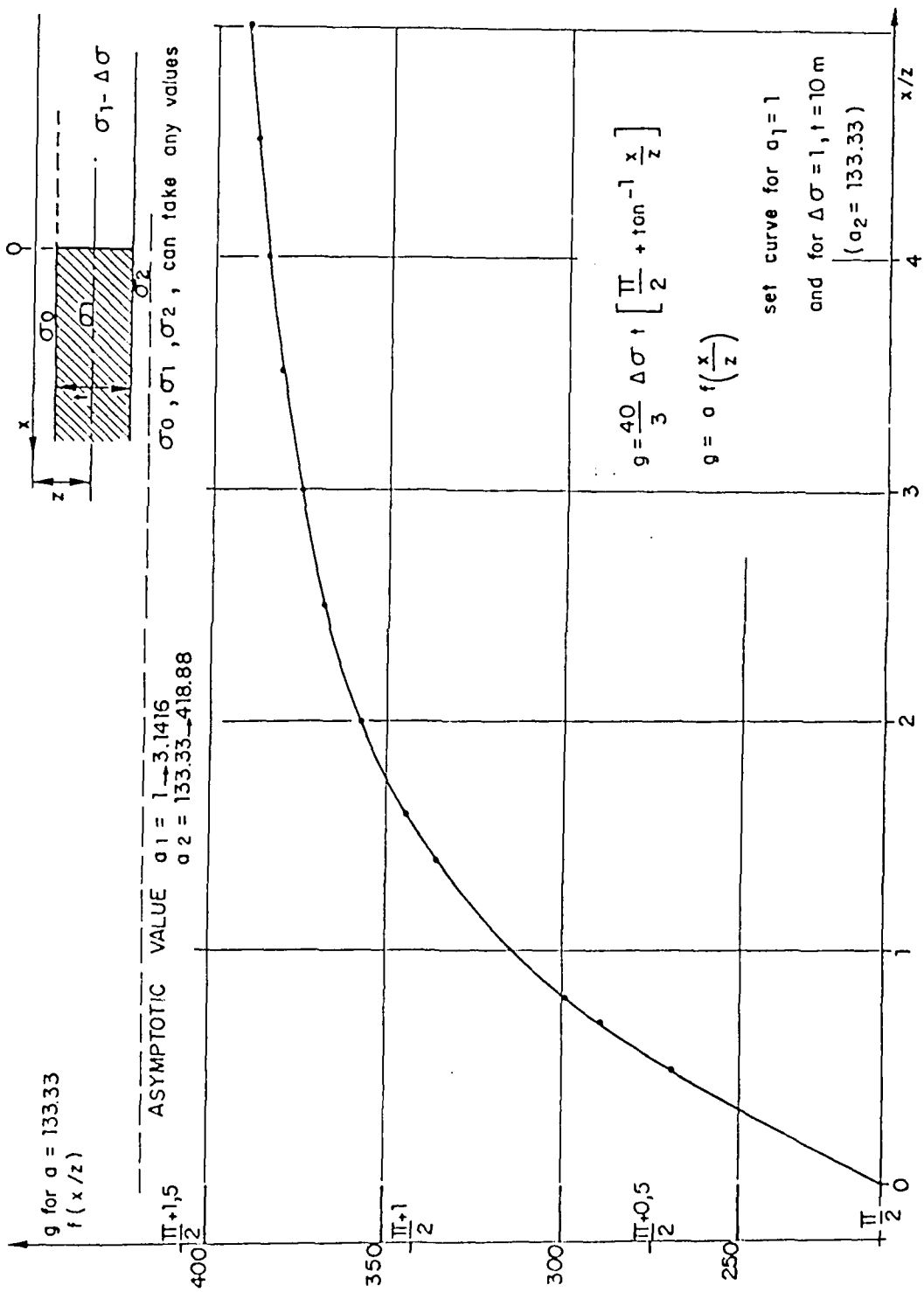

Figure 33. Anomaly due to a semi-infinite thin slab

c. Third formulas.

Further simplifications are possible when $L >> z$:

$$g_{max} \sim \frac{40}{3} \pi \Delta\sigma t$$

$$\text{and } \left(\frac{dg}{dx}\right)_{max} \sim^{+} \frac{40}{3} \frac{\Delta\sigma t . L^2}{z(L^2 + z^2)}$$

reached for $x_1 \simeq L/2$

and $g_1 \simeq \frac{40}{3} \Delta\sigma t \left(\frac{\pi}{2} - \frac{z}{L}\right)$

or $g_1 \sim \frac{20}{3} \pi \Delta\sigma t \quad \left(\frac{g_1}{g_{max}} \sim 0.500\right)$

d. Depth evaluation.

The ratio $\frac{g_{max}}{\left(\frac{dg}{dx}\right)_{max}}$ can be written as follows :

$$U = \frac{g_{max}}{\left(\frac{dg}{dx}\right)_{max}} \simeq z\left(\pi - \frac{4z}{L}\right) \times \left(1 + \frac{z^2}{L^2}\right)$$ (for the second group of formulas)

For : $z = 0.2\,L$: $U = 2.365$ (with exact formula $U = 2.476$)

$z = 0.1\,L$ $U = 2.769$ (with exact formula $U = 2.774$)

For the third set of formulas $U = \frac{g_{max}}{(dg/dx)_{max}} \sim \pi z$

Generally, when comparing with paragraph 79 for a thick plate, it can be noted that :

- the first simplified formulas are accurate to less than 1 % if $t/z \leq 0.2$, whatever L/z.
- the second, more simplified formulas, can be considered when $\frac{L}{z} > 2/0$ and $\frac{t}{z} \leq 0.5$.
- The third, even more simplified formulas, can be considered as limits, valid when $\frac{L}{z} > 20$ and $\frac{t}{z} \leq 0.5$.

85 . Interpretation of a wide strip. Taking into account the following simplified formulas, valid when $z < L/2$ and for $t < z/2$,

$$g_{max} \simeq \frac{80}{3} \Delta\sigma . t \quad \tan^{-1} \frac{L}{2z}$$

and $$\frac{dg}{dx}_{max} \simeq \frac{40}{3} \frac{\Delta\sigma . t . L^2}{z(L^2 + z^2)}$$

leading to : $$U = \frac{g_{max}}{\left(\frac{dg}{dx}\right)_{max}} = 2. \left(\tan^{-1}\frac{L}{2z}\right) \frac{z(L^2 + z^2)}{L^2}$$

we have developed an interpretation technique for wide slabs (see Figure 34).

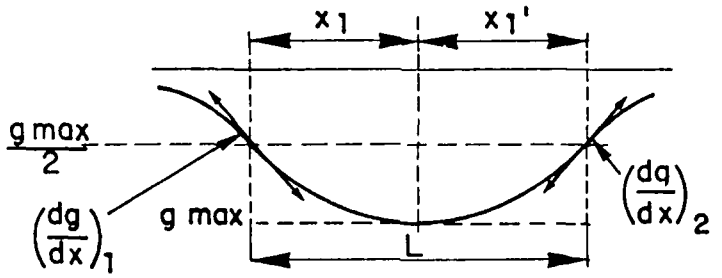

Note : this method can be used even in the case of a tilted regional.

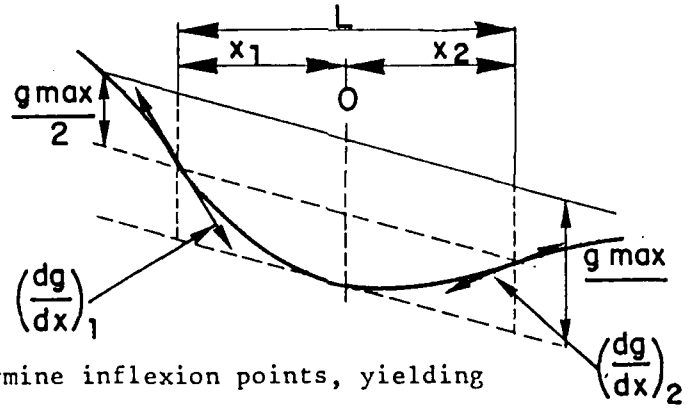

1st step : determine inflexion points, yielding

$$L \simeq x_1 + x_2$$

$$U = \frac{g_{max}}{\frac{1}{2}\left(\left(\frac{dg}{dx}\right)_1 + \left(\frac{dg}{dx}\right)_2\right)}$$

$$V = -\frac{1}{L} . U$$

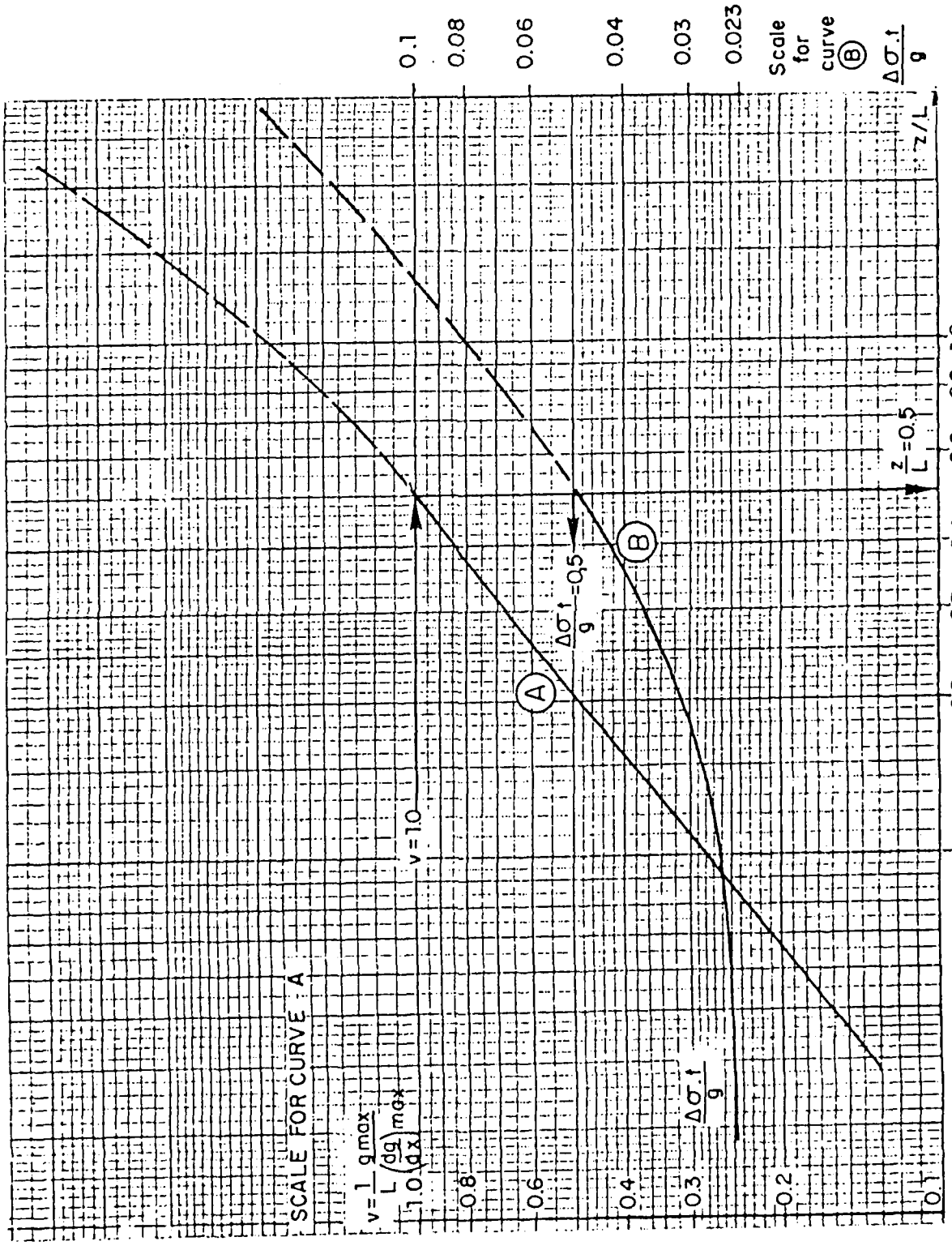

Figure 34. Nomogram for interpretation of a wide strip

2nd step : plot on curve (A), which is $v = f(\frac{z}{L})$, computed value of V as ordinate, find $\frac{z}{L}$ as abscissa, hence z.

3rd step : for the same abscissa, read ordinate w of curve (B), which yields

$$\frac{\Delta\sigma\ t}{g\ max} = w$$

Hence, $\Delta\sigma\ t = g\ max\ \ F(w)$

As an example : $g\ max = 80\ \mu gals$

$$(\frac{dg}{dx})\ max = 4.0\ \mu gals/meter$$

$$L = 20\ m$$

$$v = \frac{1}{20} \cdot \frac{80}{4} = 1.00$$

One reads $\frac{z}{L} = 0.50$; $z = 0.50 \times 20 = 10\ m$

and $\frac{\Delta\sigma\ t}{g\ max} = 0.50$; $\Delta\sigma\ t = 80 \times 0.50 = 40$

If $\Delta\sigma = 2.0$, $t = 20$ m. This means that the strip is located between depths :

$$z_1 = 10 - \frac{20}{2} = 0$$

$$\text{and } z_2 = 10 + \frac{20}{2} = 20\ m.$$

Compared to the set curves of Paragraph 76, it is clear that this simplified procedure is only valid when $L/z > 2.0$ and when $\frac{t}{z} < 0.1$ or 0.2.

86. Thick outcropping infinite slab. When $z_1 \to 0$, the integration in 76 becomes :

$$g = \frac{40\sigma}{3}\left\{\frac{\pi}{2}\ Z_2 - Z_2\ \tan^{-1}\frac{X}{Z_2} - \frac{X}{2}\ \ln\ (Z_2^2+X^2) + X\ \ln X\right\}$$

and horizontal gradient $\frac{dg}{dx} = -\frac{20\sigma}{3}\ \ln\ \frac{X^2+Z_2^2}{X^2}$

If $X \longrightarrow -\infty$; $gmax \longrightarrow \frac{40}{3}.\pi\sigma.\ Z_2$

If $X \longrightarrow +\infty$; $gmin \longrightarrow 0$

If $X = 0$ $g = \frac{20}{3}\ \pi\sigma\ Z_2$

If X = 0, horizontal gradient becomes infinite, except if Z_2 is very small but not nil (see table 6) $\frac{dg}{dx} \longrightarrow \frac{-40\sigma}{3}\ (\ln Z_2 - \ln Z_1)$

The usual depth criteria $\frac{g\,max}{(dg/dx)max}$ leads to :

$$\frac{g\,max}{\left(\frac{dg}{dx}\right)max} = \frac{\pi Z}{\ln(Z_2/Z_1)}$$

Table 9 : Horizontal gradient for semi-outcropping infinite slab.

Z_2	Z_1	$(\frac{dg}{dx})$ max (for σ = 1)	$\frac{1}{z}\frac{g\,max}{(\frac{dg}{dx})\,max}$
10 m	1 m	30.70	$\pi/2.30 = 1.364$
10 m	0.1 m	61.40	$\pi/4.61 = 0.682$
10 m	0.01 m	92.10	$\pi/6.91 = 0.455$
10 m	0.001 m	122.80	$\pi/9.21 = 0.341$
10 m	0.0001 m	153.51	$\pi/11.51 = 0.273$

87 . Thick outcropping finite strip. ($Z_1 = 0$)

$$g = \frac{40\sigma}{3}\left\{Z_2\left[\tan^{-1}\frac{X+L/2}{Z_2} - \tan^{-1}\frac{X-L/2}{Z_2}\right] + \frac{X+L/2}{2}\ln\frac{(X+L/2)^2+Z_2^2}{(X+L/2)^2} - \frac{X-\frac{L}{2}}{2}\ln\frac{(X-L/2)^2+Z_2^2}{(X-L/2)^2}\right\}$$

$$g\,max = \frac{80\sigma}{3}\left\{Z_2\tan^{-1}\frac{L}{2Z_2} + \frac{L}{4}\ln\frac{L^2+4Z_2^2}{L^2}\right\}$$

If Z_2 is small : $g\,max = \frac{80\pi}{3}\left\{\frac{\pi}{2}Z_2 + \frac{Z^2}{L}\right\} \# \frac{40\sigma}{3}\pi . Z_2$

$$\frac{dg}{dx} = \frac{20\sigma}{3}\ln\left\{\frac{(X+L/2)+Z_2^2}{(X+L/2)^2} \times \frac{(X-L/2)^2}{(X-L/2)^2+Z^2}\right\}$$ (horizontal gradient)

Maximum (infinite) value of $\frac{dg}{dx}$ is attained above the edges : $X = \pm \frac{L}{2}$.

At these points :

$$g(L/2) = \frac{40\sigma}{3}\left\{Z_2\tan^{-1}\frac{L}{Z_2} + \frac{L}{2}\ln\frac{L+Z_2^2}{L^2}\right\}$$

Figure 35 gives values of $\frac{G}{\sigma L}$ as a function of $\frac{X}{L}$, for various values of $\frac{Z_2}{L}$.

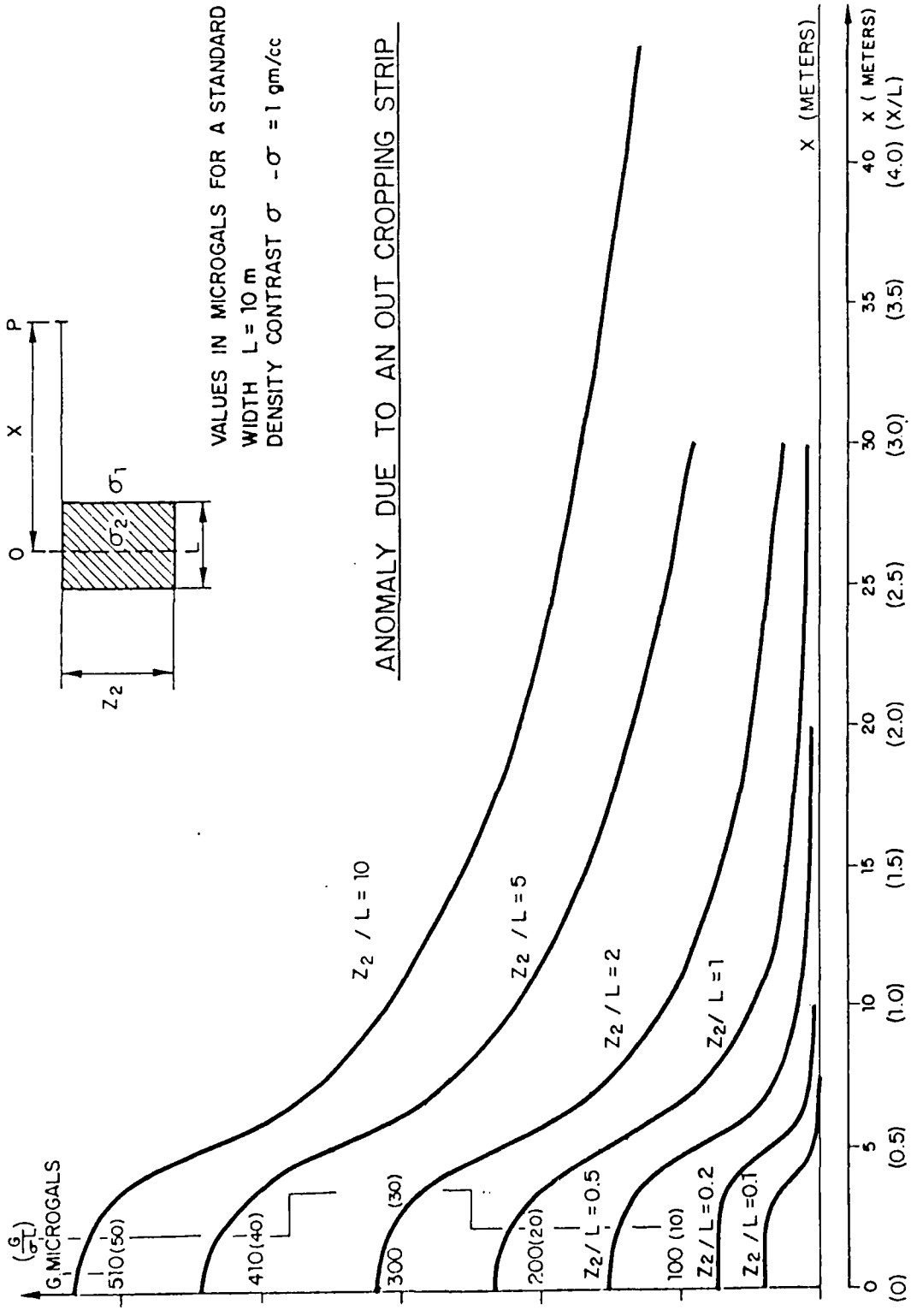

Figure 35. Anomaly due to an outcroppping strip

When the slab is only semi-outcropping, with Z ≈ 0, values of g max and g (L/2) are practically unchanged. Maximum gradient is attained for :

$$X \# \pm \frac{L}{2} \left\{1 + \frac{2 Z_1^2 Z_2^2}{L^2 (L^2 + Z_2^2)}\right\} = \pm \left(\frac{L}{2} + \epsilon\right), \text{ with } \epsilon = \frac{Z_1^2 Z_2^2}{L(L^2 + Z_2^2)}$$

or $x \sim \pm \frac{L}{2}$

$$\left(\frac{dg}{dx}\right) \max = \frac{20\sigma}{3} \ln \frac{(L+\epsilon)^2 + Z_2^2}{(L+\epsilon)^2} \frac{\epsilon^2}{\epsilon^2 + Z_2^2}$$

$$\left(\frac{dg}{dx}\right) \max \# \frac{40\sigma}{3} \ln \frac{Z_1}{L}$$

88. Narrow strip.

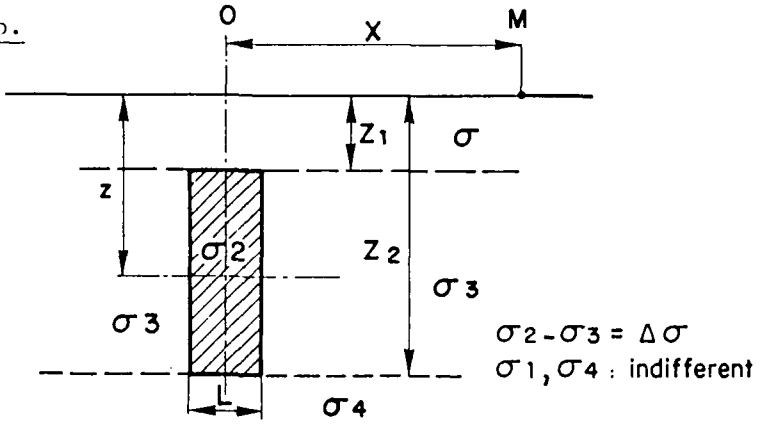

When L is small compared to Z_1 , Z_2 , the integral to be considered is :

$$g = \frac{40\sigma}{3} L \int_{Z_1}^{Z_2} \frac{z\,dz}{x^2 + z^2}$$

$$g = \frac{20\sigma}{3} L \left[\ln (x^2 + z^2)\right]_{Z_1}^{Z_2}$$

$$g = \frac{20\sigma}{3} L \ln \frac{x^2 + Z_2^2}{x^2 + Z_1^2}$$

setting $t = Z_2 - Z_1$;

$$G = \frac{20\Delta\sigma}{3} L \ln \frac{X^2 + (Z_1 + t/2)^2}{X^2 + (Z_1 - t/2)^2} \qquad (1)$$

and $$Gmax = \frac{20\Delta\sigma}{3} L \ln \frac{(Z_1 + t/2)^2}{(Z_1 - t/2)^2}$$

Vertical gradient is

$$\frac{\delta g}{\delta z} = \frac{40 \Delta \sigma . L . t}{3} \quad \frac{(X^2 - Z^2 + t^2/4)}{(X^2 + (Z + t/2)^2)(X^2 + (Z - t/2)^2)}$$

and horizontal gradient

$$\frac{\delta G}{\delta x} = \frac{80 \Delta \sigma L t \times Z}{(X^2 + (Z + t/2)^2)(X^2 + (Z - t/2)^2)}$$

Maximum for

$$X = \pm \sqrt{\frac{Z_1 + Z_2 + \sqrt{(Z_1^2 + Z_2^2) + 12 Z_1^2 Z_2^2}}{6}}$$

Formula (1) given above simplifies as follows when z > t :

$$g \simeq \frac{40}{3} \Delta \sigma t \frac{L z}{X^2 + z^2}$$

$$\text{or } g \max \simeq \frac{40}{3} \frac{\Delta \sigma . t . L}{z}$$

$$g \max = \frac{40}{3} \Delta \sigma \frac{t L}{\frac{t}{2} + z_1} \qquad (2)$$

The maximum horizontal gradient is :

$$\left(\frac{dg}{dx}\right) \max \simeq 5 \sqrt{3} \Delta \sigma \frac{t . L}{z^2}$$

reached for $x_1 \simeq \frac{z}{\sqrt{3}}$ or $x \simeq 0.577\ z$ as for a horizontal cylinder. For this value :

$$g_1 \simeq 10 \Delta \sigma . t . L / z$$

and $\frac{g_1}{g \max} = 0.750$ (as for a horizontal cylinder).

The ratio u is given by

$$U = \frac{g \max}{\left(\frac{dg}{dx}\right) \max} \simeq \frac{z}{0.64952} \qquad \text{(as for a horizontal cylinder)}$$

Tables given in paragraph 76 show that the above approximations of x_1 and of u are correct (accuracy better than 5 %) if both following conditions exist : $L < 0.7\ z$ and $t < 0.7\ z$. They are also valid if $L \simeq t$.

89 . Horizontal, cylindrical body of narrow cross-section. Considering a narrow prismatic body, infinite in the y direction, and of cross-section S = t.L, having a mass per unit length of

$$P = \Delta\sigma \; t \; L = \Delta\sigma \; S$$

The above formula (2) gives :

$$P = \frac{3z \; g \; max}{40}$$

90. It can be seen that the formulas giving g max, $(\frac{dg}{dx})$ max and corresponding values g_1 and x_1 for maximum gradient are exactly the same for a horizontal cylinder as for a a narrow buried strip. In fact, any narrow elongated body (of reduced height), continuous in the y direction, of mass per unit length P will give the same values :

$$g \; max = \frac{40 P}{3 z}$$

$$\left(\frac{dg}{dx}\right) max \simeq 5\sqrt{3} \; \frac{P}{z^2}$$

reached for $g_1 \simeq 10 \frac{P}{z}$

and for $x_1 = \pm 0.577 \; z$

z being the depth to the center of gravity of the body. The following ratios will hold :

$$\frac{g \; max}{\left(\frac{dg}{dx}\right) max} = \frac{z}{0.64952}$$

and $$\frac{g}{g \; max} = 0.750$$

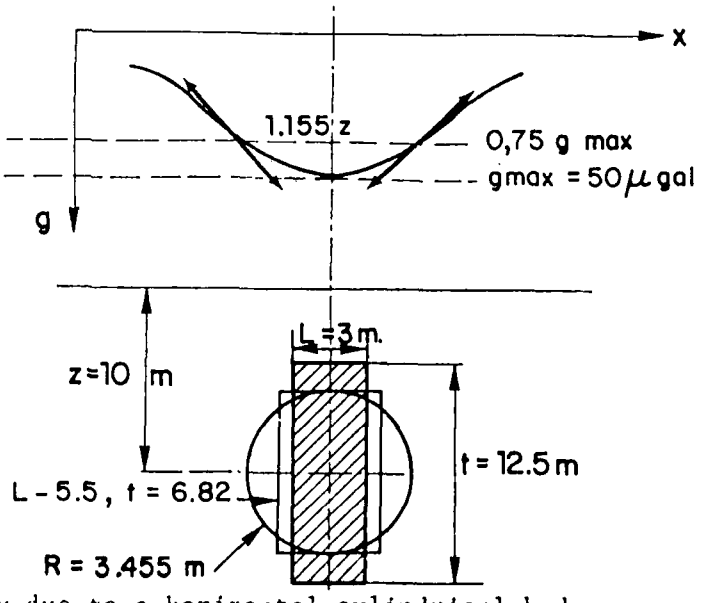

Figure 36. Bases of anomaly due to a horizontal cylindrical body

91. Comparison with tables given in paragraph 79 shows that the above approximations hold (with an accuracy of 5 %) if both the following conditions exist : $L/z \leqslant 0.7$ and $t/z \leqslant 0.7$ and also if $t \simeq L$. In the above sketch, the very narrow body (3 x 12.5) will only be equivalent to the cylinder if its middle depth z is greater than 17.8 m. In the case of a thin prismatic strip of feeble height, the same general formula as for a cylinder is found:

$$g = \frac{40\sigma}{3} \frac{\Delta x \, \Delta z . z}{x^2 + z^2}$$

or $$g = \frac{40}{3} \frac{Pz}{x^2 + z^2}$$

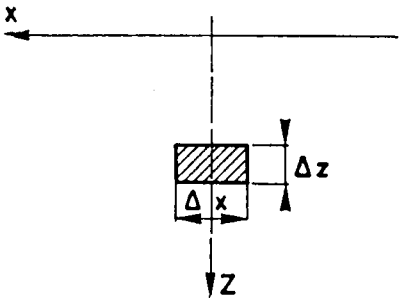

$$\frac{dg}{dx} = \frac{80P}{3} \frac{xz}{(x^2+z^2)^2}$$

$$g_{max} = \frac{40}{3} \frac{P}{z}$$

$$\left(\frac{dg}{dx}\right)_{max} = \frac{40P}{3} \frac{9}{8\sqrt{3}z^2}$$

$$x = \frac{z}{\sqrt{3}}$$

and $$\frac{g_{max}}{\left(\frac{dg}{dx}\right)_{max}} = \frac{8\sqrt{3}z}{9} = \frac{z}{0.6495}$$

These formulas are exactly the same as for a horizontal cylinder.

92. Vertical, limited bodies. These bodies are useful in microgravity, particularly for computing the influence of mine shafts. We will consider:

- the vertical cylinder of infinitely small horizontal section
- the vertical cylinder of circular section
- the right rectangular prism
- the right prism of any polygonal section

93. Weighted line (vertical cylinder of infinitely small horizontal section)

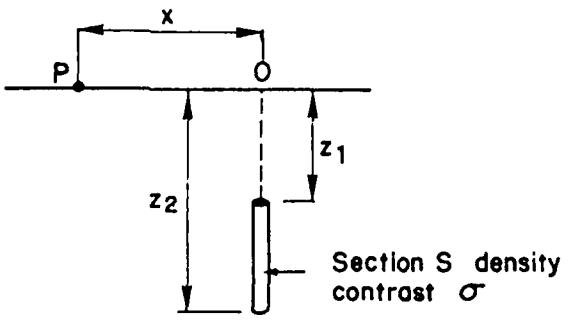

Figure 37. Bases of anomaly due to a weighted line

The vertical component of gravity is given by :

$$g = \frac{20\sigma S}{3} \int_{z_1}^{z_2} \frac{z\,dz}{(x^2+z^2)^{3/2}}$$

$$g = \frac{20\sigma S}{3} \left[-\frac{-1}{(x^2+z^2)^{1/2}} \right]_{z_1}^{z_2}$$

$$g = \frac{20\sigma S}{3} \left[\frac{1}{(x^2+z_1^2)^{1/2}} - \frac{1}{(x^2+z_2^2)^{1/2}} \right]$$

Limits :

When $x >> z_1, z_2$, $g \quad \frac{\sigma S}{3R^3} (z_2^2 - z_1^2)$

When $x = 0 \quad g = \frac{2\sigma S}{3} \left[\frac{1}{z_1} - \frac{1}{z_2} \right]$

Numerical example (case of mine shaft 2 m in diameter, $\sigma = -2.5$)

(a) $z_1 = 0.5$ m $\quad z_2 = 20$ m
(b) $z_1 = 5$ m $\quad z_2 = 20$ m
(c) $z_1 = 0.5$ m $\quad z_2 = 50$ m
(d) $z_1 = 5$ m $\quad z_2 = 50$ m

Table 10:anomalies (in microgals) due to a vertical cylinder of small section

Cases \ x	0	1	2	5	10	20	50
(a)	-102.1	-44.2	-22.8	-7.9	-2.9	-0.8	-0.1
(b)	- 7.9	- 7.7	- 7.1	-4.9	-2.3	-0.7	-0.1
(c)	-103.7	-45.8	-24.4	-9.4	-4.2	-1.6	-0.3
(d)	- 9.4	- 9.2	-8.7	-6.4	-3.7	-1.6	-0.3

It can be noted that :

- the anomaly is very strong when the cylinder is outcropping, but in that case, it reduces very much at a short distance.
- the overall length does not change the anomaly very much.

94. Vertical cylinder of circular section

When the cylinder does not have a infinitely small section, its anomaly is given by the following integral

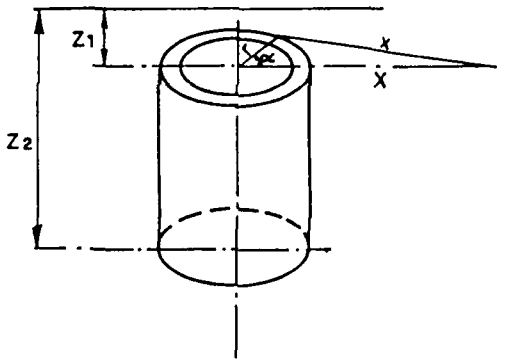

Figure 38. Bases of anomaly due to a vertical, circular cylinder

$$g = \frac{20\sigma}{3} \int_{\alpha=0}^{\alpha=2\Pi} d\alpha \int_{r=0}^{r=R} \frac{rdr}{(x^2+z_1^2)^{1/2}} - \frac{rdr}{(x^2+z_2^2)^{1/2}}$$

with $x = (r^2+X^2-2rX\cos\alpha)^{1/2}$

The integration in respect to R is possible :

$$\int_0^R \frac{rd^2}{(x^2+z_1^2)^2} = \left[(r^2+X^2+z_1^2-2rX\cos\sigma)^{1/2} + 2r + X\cos\alpha \ln \left| 2(r^2+X^2+z_1^2-2rX\cos\alpha)^{1/2} + 2r - 2X\cos\alpha \right| \right]_0^R$$

However, the integration in respect to α is a more complicated problem. Despite the efforts of several geophysicists and mathematicians (Parasnis, 1961 and Singh, 1977), the exact mathematical solution of this integral is not known and the analytical procedures long and tedious, leading to slowly converging series. The integration is however very easy along the axis of the cylinder, and leads to

$$g = \frac{40\Pi}{3}\,\sigma\left[z_2 - z_1 - \sqrt{R^2+z_2^2} + \sqrt{R^2+z_1^2}\right]$$

The exact anomalies for x = 0, for the 4 cases computed previously are the following:

	Simplified formula	Exact formula
(a)	-102.1	-62.1
(b)	-7.9	-7.8
(c)	-103.7	-63.7
(d)	-9.4	-9.3

It can be seen that as soon as the cylinder is slightly buried, the approximate formula becomes correct. Of course, if the cylinder was outcropping, the approximate formula becomes incorrect, giving, for $z_1 = 0$, g (at the center) $\to \infty$ instead of:

$$g(x=0,\ z_1=0) = \frac{40\Pi\sigma}{3}\left[R+z_2 - \sqrt{R^2+z_2^2}\right]$$

Outside the axis of the cylinder, the usual practice is to consider that at a certain distance, the appropriate formula is correct (which is correct especially when the overburden z_1 is thick) and for medium distances, to interpolate between the exact value on the axis and the values at long distances computed with the approximate formula.

Another procedure is to consider that the cylinder is in fact a right rectangular prism, and to use Nagy's formula (see par. 1619). Alternatively, the horizontal section of the cylinder can be assimilated to a polygon, and the procedure described in section 1620 be used.

95. Flat disc

When R > z, the equation giving the anomaly along the axis of a vertical cylinder has the following limit, writing

$$t = Z_2 - Z_1$$

$$Z = \frac{Z_2+Z_1}{2}$$

$$g = \frac{40}{3}\,\Pi\sigma t\left[1 - \frac{z}{R}\right]$$

It can be noted that as soon as R > 2z, the error becomes less than 5 %. When R >> z, we find the general formula for an infinite slab

$$g = \frac{40}{3}\,\Pi\sigma t$$

96. Right rectangular prism. Nagy (1966) has shown that the vertical component of the attraction of a right rectangular prism is given by:

$$Gz = \frac{20}{3}\sigma\left[\left[\left[x \ln(y+r)+y \ln(x+r)-Z \sin^{-1}\frac{Z^2+y^2+yr}{(y+r)\sqrt{y^2+z^2}}\right]_{Z_1}^{Z_2}\right]_{y_1}^{y_2}\right]_{x_1}^{x_2}$$

$$\text{or } G = \frac{20}{3}\sigma\left[\left[\left[F\right]_{Z_1}^{Z_2}\right]_{y_1}^{y_2}\right]_{x_1}^{x_2}$$

If x or y axes (or both) are crossed, the integration must be carried out separately from the lower limit to 0, then from the lower limit up to the upper limit. For example; if $y_1 < 0$, $y_2 > 0$ and x_1, $x_2 > 0$:

$$G = \frac{20}{3}\sigma\left[\left[\left[F\right]_{Z_1}^{Z_2}\right]_{y_1}^{0} + \left[\left[F\right]_{Z_1}^{Z_2}\right]_{0}^{y_2}\right]_{x_1}^{x_2}$$

These expressions, if written out completely as by Nagy in the general case, look very cumbersome. However, they are easy to program on a computer. The effects of the prisms of sections and lengths corresponding to the cylinders of the previous chapter follow (section of cylinder $S = \pi R^2 = \pi \times 1$, side of equivalent square prism = $\sqrt{\pi}$). The prism is symetrical in respect to x and y axes, and the anomalies are computed for y = 0

Table 11 : maximum anomalies for cylinder and prism

Cases	Weighted line	Vertical cylinder	Right square prism
(a)	-102.1	-62.1	-61.7
(b)	- 7.9	- 7.8	-7.7
(c)	-103.7	-63.7	-63.3
(d)	- 9.4	- 9.3	-9.3

It can be seen that the right square prism gives results very close to those of a vertical cylinder of same section, along its axis.

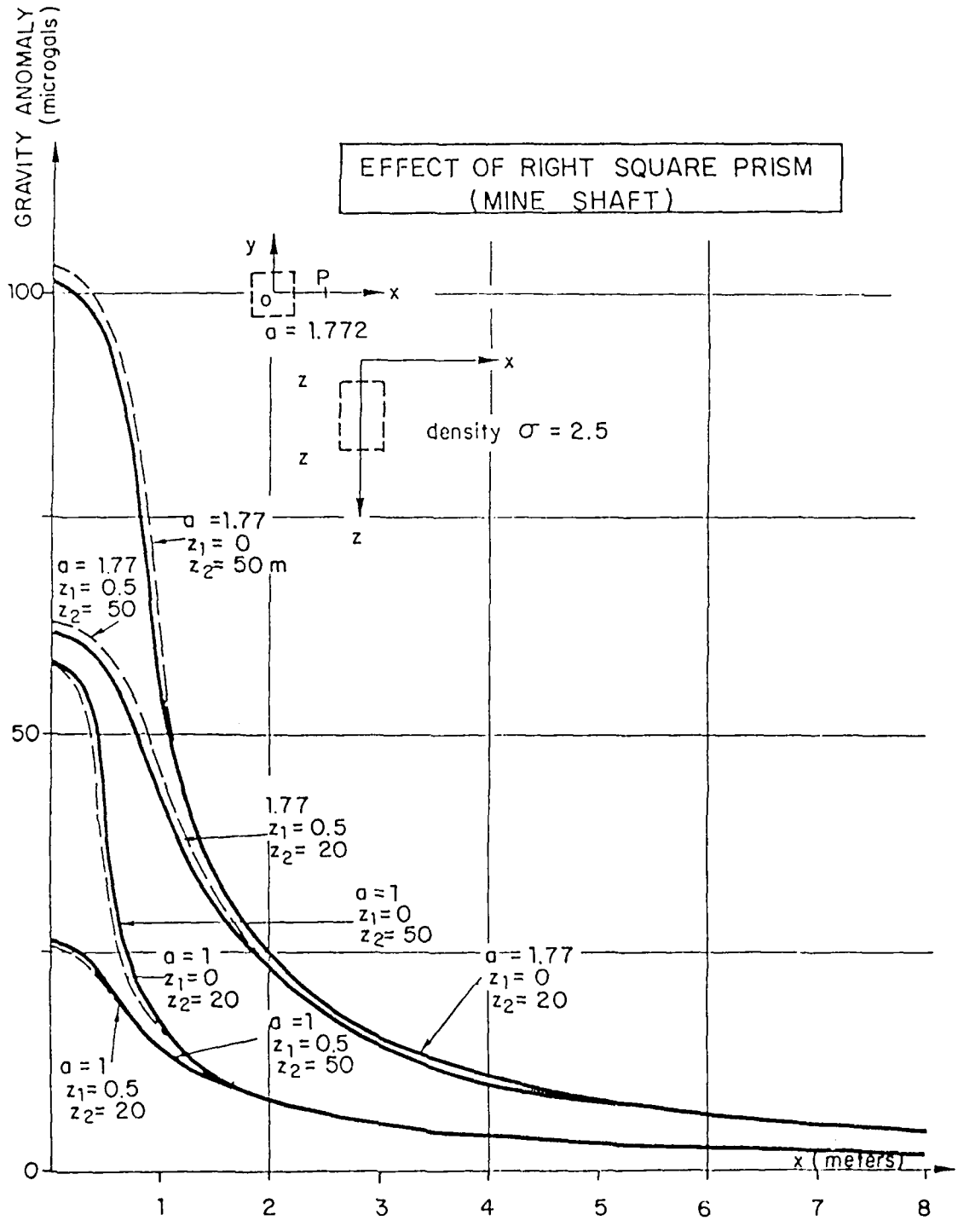

Figure 39. Effect of a right square prism (side = 1.77 m)

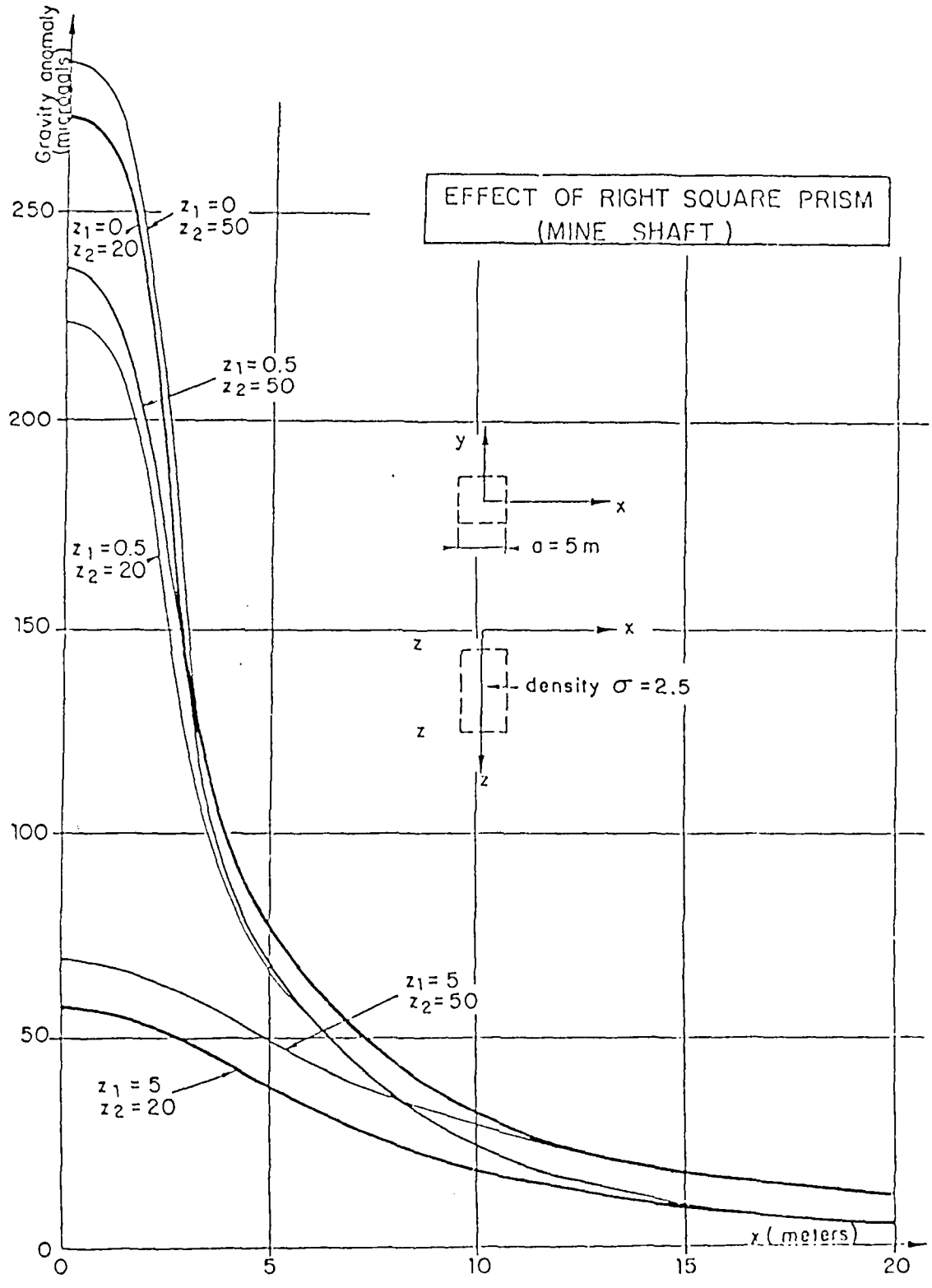

Figure 40. Effect of a right square prism (side = 5 m)

Table 12: anomaly (in microgals) due to a square right prism (side = 1.772 m)

Cases \ x	0	1	2	5	10	20	50
(a)	61.7	44.0	23.4	7.9	2.9	0.8	0.1
(b)	7.7	7.6	7.1	4.9	2.3	0.7	0.1
(c)	63.3	45.5	24.9	9.4	4.2	1.6	0.3
(d)	9.3	9.1	8.6	6.4	3.7	1.6	0.3

Case (a): z_1 = 0.5 m z_2 = 20 m

(b) z_1 = 5 m z_2 = 20 m

(c) z_1 = 0.5 m z_2 = 50 m

(d) z_1 = 5 m z_2 = 50 m

97. It should be noted that:

- the simplified formula for the weighted line gives very similar values to the right square prism, except for x < 1 m, and when, at the same time, overburden is very small (considering normalized parameters $\frac{x}{z}$ and $\frac{z_1}{z}$, with $z = (z_1+z_2)/2$, the limits are around $\frac{x}{z} < 0.01$ and $\frac{z_1}{z} < 0.01$).
- the very upper part of the prism creates the major part of the anomaly: for a same z_1 value, the anomalies for z_2 = 20 or 50 m are very similar.
- for $\frac{x}{z} \gtrsim 0.20$, the anomalies do not depend much on the normalized thickness of overburden $\frac{z_1}{z}$
- the major part of the anomaly is visible above the prism itself ; the anomaly drops out very quickly outside, especially when the overburden is thin (for $z_1 = 0$, the anomaly is reduced to half its maximum when $x > 1.2 \frac{a}{2}$, that is, just after the edge of the prism).

98. Effect of a horizontal thin polygon. Following Talwani (1960), and Moudressov et al (1979), the anomaly due to a thin horizontal polygonal lamina is given by:

$$\Delta G = \frac{20}{3} \sigma \Delta Z \sum_{i=1}^{i=n} W \cos^{-1} \left\{ \frac{x_i}{r_i} \frac{x_{i+1}}{r_{i+1}} + \frac{y_i}{r_i} \cdot \frac{y_{i+1}}{r_{i+1}} \right\} - \sin^{-1} \frac{Z q_i S}{(p_i+Z^2)^{1/2}} + \sin \frac{Z f_i S}{(p_i^2+Z^2)^{1/2}}$$

where σ : density

ΔZ : thickness of lamina, Z : depth of lamina

x_i, y_i } coordinates of successive vertices of the polygon,

x_{i+1}, y_{i+1} } i increasing counterclockwise

$$r_i = \left[(x_i^2+y_i^2)\right]^{1/2}$$

$$r_{i,i+1} = (x_i-x_{i+1})^2 + (y_i-y_{i+1})^2 \quad ^{1/2}$$

$S = +1$ if $p_i > 0$; $S = -1$ if $p_i < 0$

$W = +1$ if $m_i > 0$; $W = -1$ if $m_i < 0$

$$p_i = \frac{y_i-y_{i+1}}{r_{i,i+1}} x_i - \frac{x_i-x_{i+1}}{r_{i,i+1}} y_i$$

$$q_i = \frac{x_i-x_{i+1}}{r_{i,i+1}} \frac{x_i}{r_i} + \frac{y_i-y_{i+1}}{r_{,i+1}} \frac{y_i}{r_i}$$

$$f_i = \frac{x_i-x_{i+1}}{r_{i,i+1}} \frac{x_{i+1}}{r_i+1} + \frac{y_i-y_{i+1}}{r_{i,i+1}} \frac{y_{i+1}}{r_i+1}$$

$$m_i = \frac{y_i}{r_i} \frac{x_{i+1}}{r_i+1} - \frac{y_{i+1}}{r_i+1} \frac{x_i}{r_i}$$

For a right polygonal prism: $G = \int_{Z=Z^1}^{Z^2} \Delta G . \Delta Z$

This formula has proven very useful for computing the effect of the pyramid of Cheops which is not square. It is also used for computing terrain corrections, and for modelling dams.

99. Anomaly due to a sloping embankment.

Figure 41. Bases of anomaly due to a sloping embankment

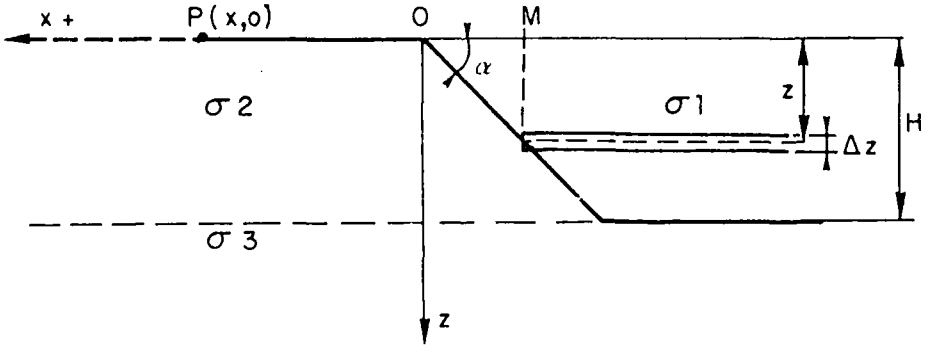

$\sigma 1 - \sigma 2 = \Delta\sigma$
$\sigma 3$ arbitrary

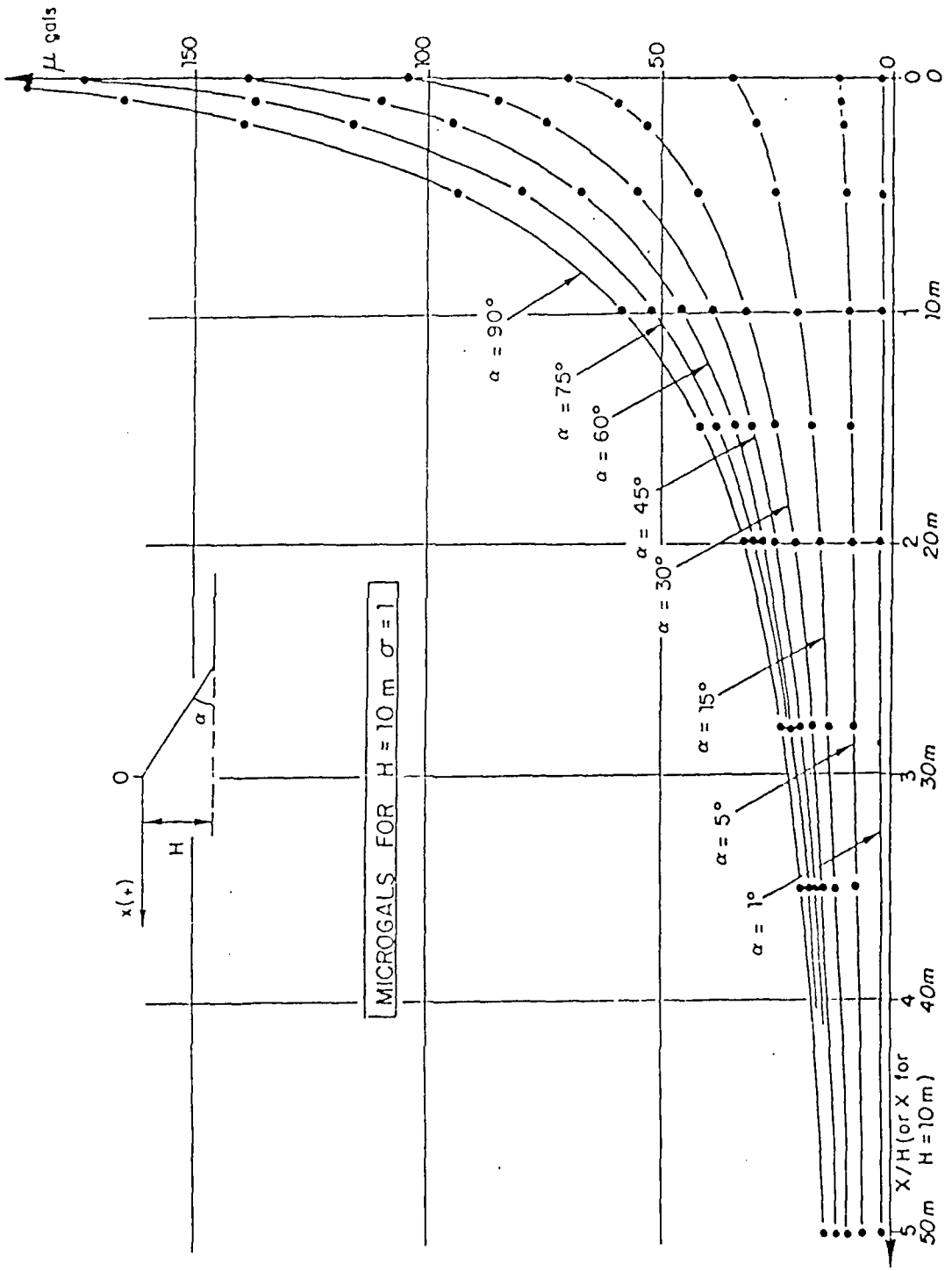

Figure 42. Anomalies due to sloping enbankments

The attraction of a thin slab is given by :

$$G = \frac{40}{3} \Delta\sigma.\Delta z \left\{ \frac{\Pi}{2} - \tan^{-1} \left[\frac{x + \frac{z}{\tan\alpha}}{z} \right] \right\}$$

Integration from z = 0 to z = H leads to :

$$G = \frac{40}{3} \Delta\sigma.H \left\{ \frac{\pi}{2} - \tan^{-1} \left(\frac{x}{H} + \frac{\cos\alpha}{\sin\alpha} \right) - \frac{x}{2H} \sin^2 \alpha \ln \left| \frac{H^2}{x^2 \sin^2\alpha} + \frac{2\cos\alpha}{\sin\alpha} \frac{H}{x} + 1 \right| \right.$$

$$\left. + \frac{x}{H} \sin\alpha \cos\alpha \left[\tan^{-1} \left(\frac{H}{x \sin^2\alpha} + \frac{\cos\alpha}{\sin\alpha} \right) - \frac{\Pi}{2} + \alpha \right] \right\}$$

Figure 42 gives values of G for a standard value of H = 10 m, as a function of the angle α and of the distance to the top of the embankment X. For other values, one can compute:

$$G(H,s) = G(10,1) \times \frac{Hs}{10}$$

and read as a fonction of $\frac{X}{H}$.

100. Special interpretation techniques. In the previous section (53to96) we examined various interpretation techniques, mainly based on the use of set curves, completed with depth evaluation with Bott and Smith's (1958) formulas and with the use of nomograms. We will now consider in this section a certain number of special interpretation techniques:

- second derivatives, very popular with petroleum geophysicists
- two-dimensional inversion and modelling
- three-dimensional inversion and modelling

101. Spectral analysis and Fourier transforms, also frequently used in petroleum gravity interpretation, often need large data sets. These techniques have not been used much in microgravity. In fact, at CPGF, we prefer spatial filtering, as described in section 174, even for oil exploration, rather than working in the frequency domain.

102. Second derivatives. Gravity being a Laplacian function, we have:

$$\frac{\delta^2 G}{\delta x^2} + \frac{\delta^2 G}{\delta y^2} + \frac{\delta^2 G}{\delta Z^2} = 0$$

Therefore, if we compute the horizontal second derivatives from field data,

the vertical second derivative is given by :

$$\frac{\delta^2 G}{\delta Z^2} = -\left(\frac{\delta^2 G}{\delta x^2} + \frac{\delta^2 G}{\delta y^2}\right)$$

The horizontal second derivatives can be computed in two manners :

(a) The Bouguer values G, inside a moving window surrounding the point where the second derivatives are to be computed, can be used to best fit a second degree polynominal, by minimizing

$$U = \sum\left[G-(ax^2+bx+cy^2+dy+e)\right]^2$$

The second derivatives will be:

$$\frac{\delta^2 G}{\delta x^2} = 2a$$

$$\frac{\delta^2 G}{\delta y^2} = 2c$$

The main problem is the selection of the size moving window, which will automatically influence the result.

(b) The second method is mainly useful in the case of gridded data. One computes the averages G(i) of the Bouguer values at various radi r(i) surrounding the considered point where the Bouguer is G(o). It can be shown that the second vertical derivative will be given by:

$$\frac{\delta^2 G}{\delta z^2} = a(o)G(o) + \sum_{i=1}^{i=n} ai\ G(i)$$

Suitable coefficients a(i) and radi (s) have been published by Henderson and Zeitz (1949), Elkins (1951) and Rosenbach (1953). Two formulas are given below:

$$\frac{\delta^2 G}{\delta Z^2} = \frac{4}{s^2}\left(G(o)-\overline{G}(s)\right)$$

$$\frac{\delta^2 G}{OZ^2} = \frac{1}{s^2}\left[4G(o) - 3\ G(s) - \frac{4}{3}\ G\ (S\sqrt{2}) + \frac{1}{3}\ G(S\sqrt{5})\right]$$

As in the first method, the result heavily depends on the radi selected. Once $\frac{\delta^2 G}{\delta Z^2}$ is computed, it can be used for depth evaluation and for filtering as follows:

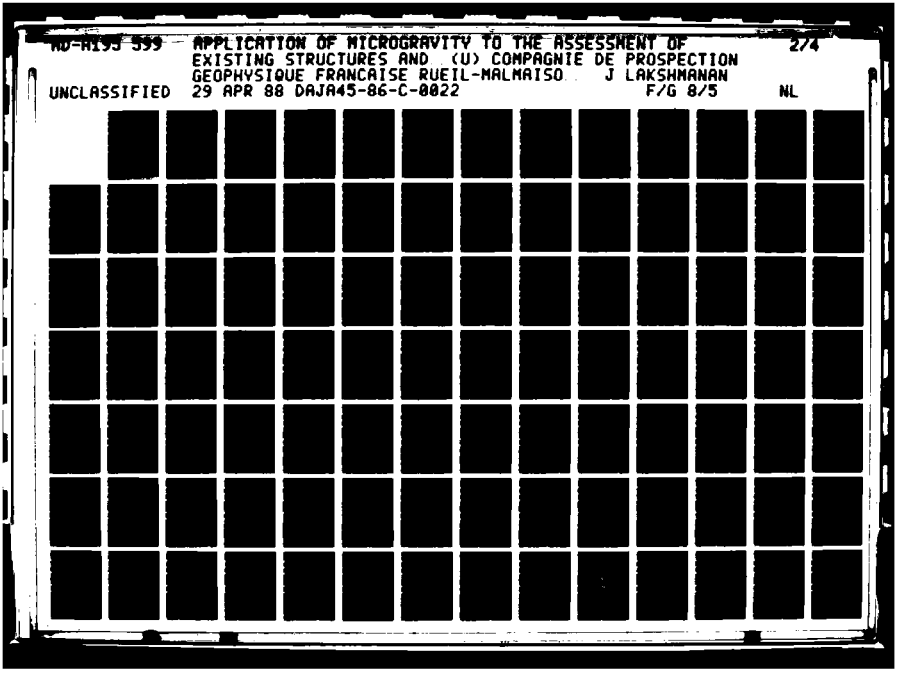

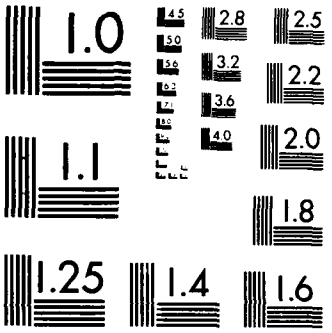
1.0
1.1
1.25
1.4
1.6
1.8
2.0
2.2
2.5
2.8
3.2
3.6
4.0
4.5
5.0
5.6

103. Sphere (volume V)

$$g = \frac{20}{3}\,\sigma\,V\,\frac{z}{(x^2+z^2)^{3/2}}$$

$$\frac{\delta^2 G}{\delta Z^2} = -\frac{60}{3}\,\sigma V\,zr^{-7}\,(3x^2-2z^2)$$

$$g\ max = \frac{20}{3}\,\sigma V\,z^{-2}$$

$$\frac{\delta^2 G}{\delta Z^2}\ max = \frac{120}{3}\,\sigma V\,z^{-4}$$

It results that depth z can be evaluated by:

$$z = 2.4495\sqrt{\frac{Gmax}{\frac{\delta^2 G}{\delta z^2 max}}}$$

104. Horizontal cylinder

$$g = \frac{40}{3}\,\Pi\sigma R^2\,\frac{z}{x^2+z^2}$$

$$\frac{\delta^2 G}{\delta Z^2} = \frac{80}{3}\,\Pi\sigma R\,z\,\frac{(z^2-3x^2)}{(x^2+z^2)^3}$$

For x = 0 : $g\ max = \frac{40}{3}\,\Pi\,\frac{R^2}{z}$

For x = 0 : $\frac{\delta^2 G}{\delta x^2}\ max = \frac{80}{3}\,\Pi\,\frac{R^2}{z^3}$

Depth z is given by:

$$z = 1.4142\sqrt{\frac{Cmax}{\frac{\delta^2 G}{\delta Z^2 max}}}$$

105. Semi-infinite plate

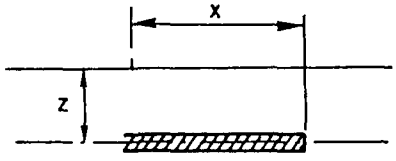

$$g = \frac{40}{3}\,\sigma t\left(\frac{\Pi}{2} + \tan^{-1}\frac{x}{z}\right)$$

$$\frac{\delta^2 G}{\delta z^2} = \frac{40}{3}\,\sigma t\,\frac{2xz}{(x^2+z^2)^2}$$

Maximum for $x = \frac{1}{2}z$

$$\left(\frac{\delta^2 G}{\delta z^2}\right)_{max} = \frac{20}{3}\frac{\sigma t}{z^2}$$

$$g_{max}\ (x \to \infty) = \frac{40}{3}\Pi\sigma t$$

$$\frac{g_{max}}{\left(\frac{\delta^2 G}{\delta z^2}\right)_{max}} = \frac{2\Pi}{z^2}$$

$$z = 0.3989\sqrt{\frac{g_{max}}{\left(\frac{\delta^2 G}{\delta z^2}\right)_{max}}}$$

106. Thin plate

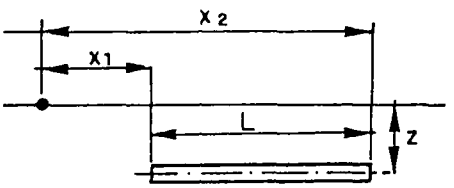

$$G = \frac{40}{3}\sigma t\left(\tan^{-1}\frac{x^2}{z} - \tan^{-1}\frac{x^1}{z}\right)$$

$$\frac{\delta^2 G}{\delta z^2} = \frac{40}{3}\sigma t.2z\left[\frac{x_2}{(x_2^2+z^2)} - \frac{x_1}{(x_1^2+z^2)^2}\right]$$

$$G_{max} = \frac{80}{3}\sigma t.\tan^{-1}\frac{L}{2z}$$

$$\frac{\delta^2 G}{\delta z^2}_{max} = \frac{80}{3}\sigma t\ \frac{zL}{\frac{L^2}{4}+z^2{}^2} \qquad \left(\text{for } x_2 = \frac{L}{2} \text{ and } x_1 = -\frac{L}{2}\right)$$

$$\frac{G_{max}}{\left(\frac{\delta^2 G}{\delta z^2}\right)_{max}} = z^2\tan^{-1}\frac{L}{2z}\cdot\frac{\left(\left(\frac{L}{2z}\right)^2+1\right)^2}{\frac{L}{z}}$$

$$\text{or } z = a\sqrt{\frac{G_{max}}{\left(\frac{\delta^2 G}{\delta z^2}\right)_{max}}}$$

a depends on the ratio $\frac{L}{z}$ as follows:

Table 13 : depth evaluation of a thin plate (second derivative).

$\frac{L}{z}$	0.1	0.2	0.5	1	2	5	10	20	100
a	1.411	1.402	1.344	1.175	0.798	0.283	0.104	0.0365	0.003

When $\frac{L}{z} \to 0$, $a \to 1.4142$ (as for the horizontal cylinder)

When $\frac{L}{z} \to \infty$, $a \to \sqrt{\frac{32}{\pi}} \left(\frac{z}{L}\right)^{3/2}$

Measured vertical gradient.

107. General. In microgravity, it is possible to actually measure the vertical gradient of g, using a tripod or, if necessary, a tower (Fajklewicz, 1976, Blizkovsky, 1979 and Butler, 1984). The general idea is to help determining depth to anomalies. If the anomaly is very shallow, repeating a station one meter higher will strongly filter it out.

We will give here a series of formulas, while in case history section II, Civaux nuclear power plant site survey is a good example of the practical use of this method.

108. Sphere

$$g = \frac{20}{3} m \frac{z}{r^3} \quad (\text{with } r^2 = x^2+z^2)$$

$$\frac{dg}{dz} = \frac{20}{3} m r^{-3} \left[\frac{x^2-2z^2}{r^2}\right]$$

$$u = \frac{\frac{dg}{dz}}{g} = \frac{1}{z} \frac{x^2-2z^2}{r^2}$$

For $x = 0$; $u = -\frac{2}{z}$

109. Horizontal cylinder (radius R)

$$g = \frac{40}{3} \pi\sigma R^2 \frac{z}{r^2}$$

$$\frac{dg}{dz} = \frac{40}{3} \pi\sigma R^2 \frac{x^2-z^2}{r^4}$$

$$u = \frac{\frac{dg}{dz}}{z} = \frac{1}{z} \frac{x^2-z^2}{r^2}$$

For $x = 0$; $u = -\frac{1}{z}$

110. Wide plate

Consider first three adjacent cylinders of radius R = az :

$$g_{max} = \frac{40}{3} \Pi\sigma \frac{R^2}{z} \frac{4a^2+3}{4a^2+1}$$

$$\text{and } \left(\frac{dg}{dz}\right)(x=0) = -\frac{40}{3} \Pi\sigma \frac{R^2}{z^2} \frac{16a^4+8a^2+3}{(4a^2+1)^2}$$

$$u = \frac{\frac{dg}{dz}}{g} = \frac{1}{z} \frac{16a^4+8a^2+3}{16a^4+16a^2+3}$$

$$\text{or } u = \frac{1}{z}\left[1 - \frac{8a^2}{16a^4+16a^2+3}\right]$$

$$u = \frac{\frac{dg}{dz}}{g} \equiv \frac{b}{z} \text{ and } z = \frac{bg}{\frac{dg}{dz}}$$

Table 14 : parameters for depth calculation from vertical gradient for 3 vertical cylinders.

Relative width = $\frac{6R}{z} = \frac{L}{z}$	0.6	1.2	2.4	3.6	4.8	6.0
$a = \frac{R}{z}$	0.1	0.2	0.4	0.6	0.8	1
b	0.9997	0.9127	0.7856	0.7342	0.7413	0.771

111. When the group of 3 cylinders is very deep, b → 1 (case of a unique cylinder). If one had considered more adjacent cylinders, the average value of 0.74 would be further reduced to 0.5, 0.3, etc ... In the case of an infinitely wide plate of thickness t, $g = \frac{40}{3} \Pi\sigma t$, which is independent of z, then b → 0.

112. To summarize, the ratio u of the vertical gradient above the center of the anomaly divided by the maximum value of the anomaly, varies as follows:

$$u = \frac{\frac{dg}{dz}}{g} = -\frac{b}{z}$$

. Point source (sphere) : b = 2.0

. Line source (horizontal cylinder, ratio $\frac{L}{z} < 1.0$) : b = 1.0

. Wider, 2 dimensional source : b < 1.0, depends on ratio $\frac{L}{z}$,
for $3 < \frac{L}{z} < 6$, b ∿ 0.75

. Very wide source: $b \to 0$.

113. Nomogram for the interpretation of vertical gradient. For a sphere or a horizontal cylinder, set curves can be computed, giving $\frac{dg}{dz}$ as a function of g, for various values of x, and not only above the center of the anomaly. The enclosed graph (figure 43) gives these curves for:

- spheres at a depth of 5 m (in detail for -100 and -200 Tons)
- spheres at a depth of 10 m (in detail for -1,000 Tons)
- spheres at a depth of 30 m (in detail for -10,000 Tons)
- spheres at a depth of 60 m (in detail for -100,000 Tons)
- single cylinders at a depth of 2.5 m
- single cylinders at a depth of 5 m
- single cylinders at a depth of 15 m
- single cylinders at a depth of 30 m (in detail for radius R = 6.2, 13.3 and 20 m)
- a group of 3 cylinders at a depth of 30 m (R = 7.68).

It can be seen that the group of 3 cylinders (R = 7.68) which has the same total section as the single cylinder of radius 13.3, gives a different curve, with lower vertical gradients.

114. The example comes from the Civaux nuclear plant site survey in France, designed to be built on Jurassic limestone. At a first (now abandoned) location, many gravity anomalies were found (see case history section 711). It can be seen on the chart that gravity anomalies are in 3 goups:

- shallow light ($\Delta < 0$) anomalies, located at depths of less than 20 m,
- deep, light ($\Delta\sigma < 0$) anomalies, located at depths of 30 to 60 m,
- shallow heavy ($\Delta\sigma > 0$) anomalies located at depths of about 5 m.

The use of this chart helps to confirm conventional depth evaluation.

115. To conclude, interpretation using both vertical gradient values and residual anomalies, along a profile crossing the structure, can help evaluate depths up to 50 m, even if the gradient is measured with a single vertical interval of only 1 m. But this needs the interpretation of several gradient measurements. A lone vertical gradient measurement is of no practical use. These remarks and the nomogram can be considered as completing the thorough evaluation of vertical gradients made by Butler (1984).

116. Vertical gradient measurements in tunnels. When gravity measurements are made inside a tunnel along a single profile, it is not possible to

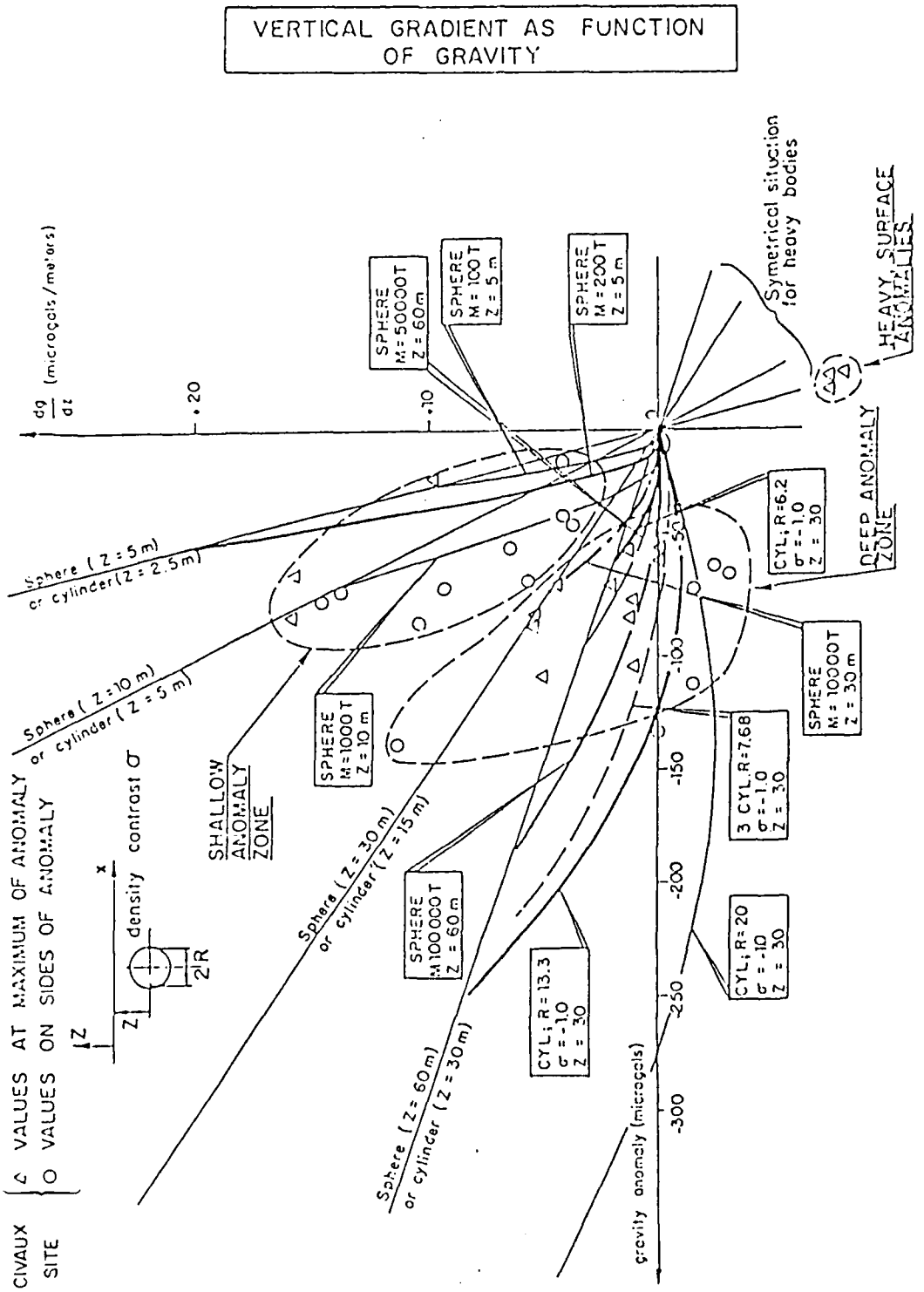

Figure 43. Vertical gradient as a function of gravity

separate a heavy cause above the tunnel from a light cause below the tunnel. This ambiguity disappears when measurements are made at two separate elevations. This is shown by considering the effect of a sphere (see Figure 44.) The results are summarized as follows :

$\frac{\Delta G}{\Delta Z}$	Δg		
>0	<0	light cause under the tunnel	($\Delta\sigma$ < 0)
>0	>0	" " over the tunnel	($\Delta\sigma$ < 0)
<0	<0	heavy cause over the tunnel	($\Delta\sigma$ > 0)
<0	>0	" " under the tunnel	
>0	≃0	" " on the side of the tunnel	
<0	≃0	light cause on the side of the tunnel	($\Delta\sigma$ < 0)

Intermedaite effects may be computed for anomalies not located in the same vertical plane as the measurements.

In case history section 5 describing Blaisy Bas railroad tunnel, most of the anomalies were due to low densities located below the tunnel, while a few of them were due to heavy causes above the tunnel.

117. To conclude, systematic vertical gradient measurements are absolutely necessary in gravity surveys made in tunnels. Otherwise, interpretations are completely ambiguous.

117. Two dimensional modelling. When detailed geological information is available, more detailed interpretation can be made, instead of simply trying to identify anomalous bodies as described previously. This is not often the case in microgravity surveys, while two dimensional modelling is a routine procedure in petroleum gravity surveys. One of these 2-D techniques, the MODCONG program used by CPGF, is described as follows. Two dimensional modelling is of course only valid if the structures are rather elongated.

a. The first step is to consider a certain structure, i.e., depth limits (z_1, z_2, z_3) separating 2, 3 or 4 layers, and suppose corresponding constant initial densities (σ_1, σ_2, σ_3, σ_4) and then compute gravity C(j) due to this model (using for each prism Nagy's (1966) formula).

$$C(j) = \sum_{i=1}^{i-n} \sigma(i,o)\ I(i,j)$$

I (i,j) being the influence of layer i on point j.

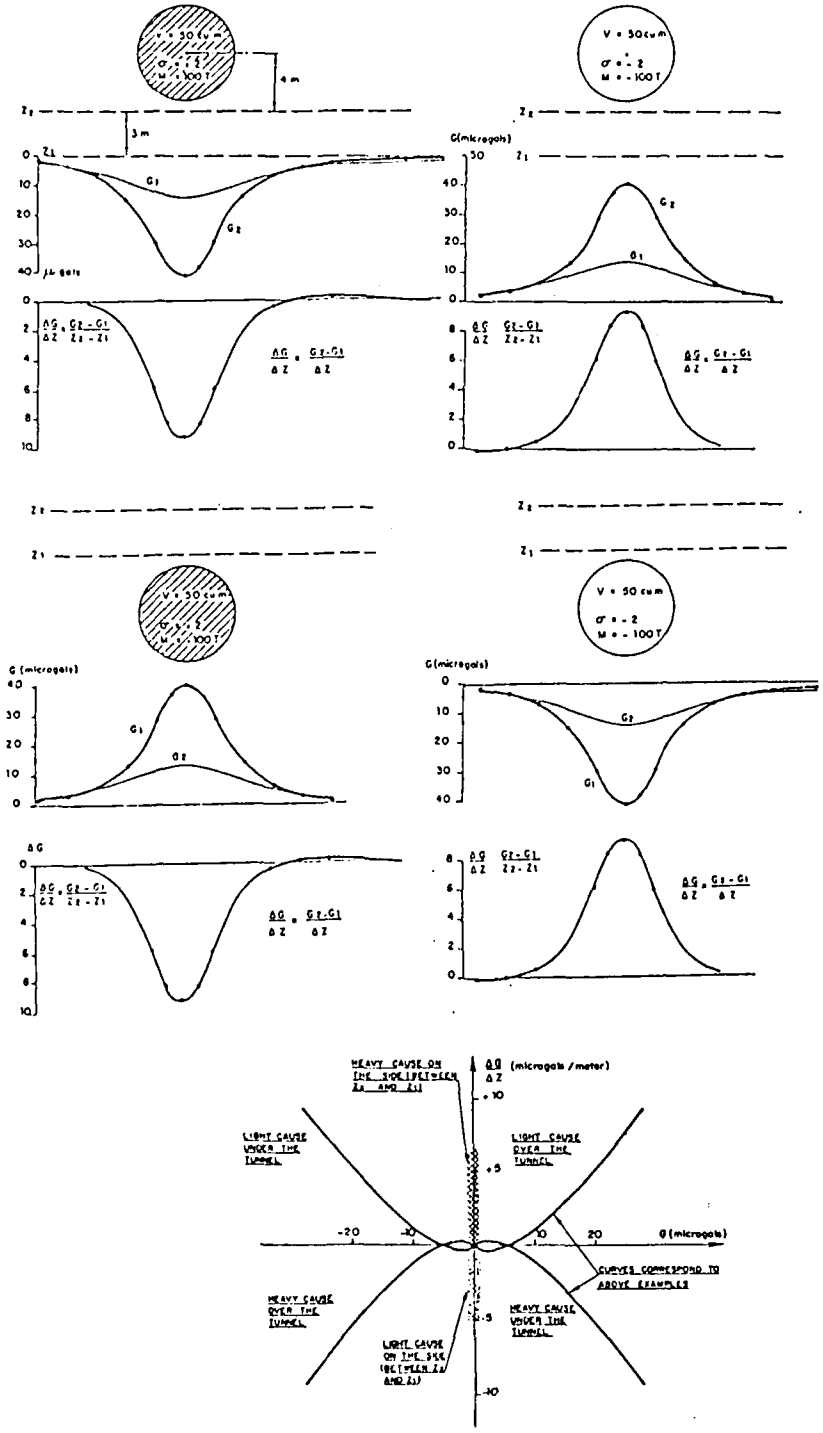

Figure 44. Vertical gradients in tunnels

b. The second step supposes that one of the parameters (depth Z(p,j) or density $\sigma(p,j)$) can be adjusted. The fastest procedure is the iterative adjustment of densities, supposing that along a given layer, densities may vary from one point to another.

Figure 45. "MODCONG" two-dimensional modelling

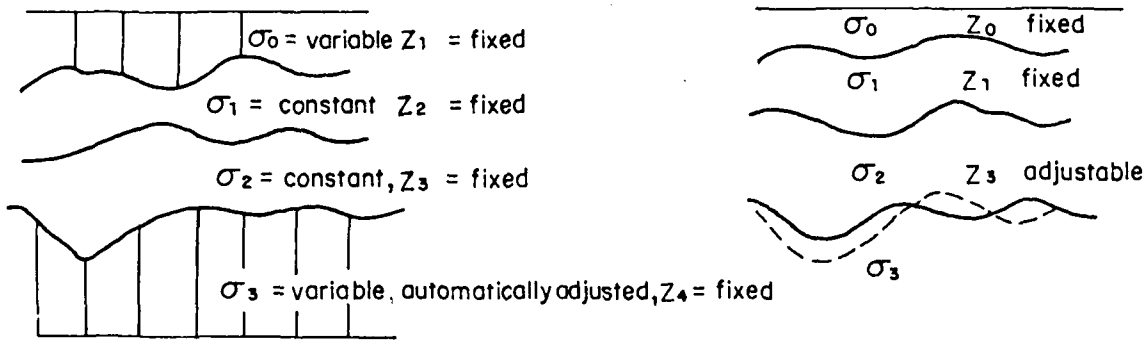

117. At the Civaux nuclear plant (general description in the case history section) this program was used on 3 main profiles. A four layer model was introduced as listed in Table 15.

Table 15 : densities at Civaux nuclear plant

Layer no.	Geology	Average thickness	Initial density contrast
1	Sand and gravel	10-25 m	-0.2
2	Fractured limestone	10-25 m	+0.1
3	Dolomitic sand	10-20 m	+0.3
4	Compact limestone	20-30 m	+0.2
5	Compact basement	∞	0.0

Variable initial depths were obtained from drill holes and from seismic refraction profiles. The main problem was the possibility of local low density lenses in layer 3 ; the model was first adjusted supposing that all the gravity anomalies were due to this layer. However, density DENS 3 was constrained to the interval -0.6 to -0.2. Figure 46 shows improvement of the correlation coefficient (between measured and computed gravity) after each of the 6 to 8 iterations.

118. After stabilization, the densities DENS 2 of layer 2 were allowed to vary between 0 and +0.2, and 5 to 11 iterations made. Moving up to the

first layer, a final iteration was made, allowing DENS 1 to vary. After these 3 phases, the initial correllation coefficients were improved from 0.816-0.899 to 0.9996-0-0.9999. Figure 47 shows the same procedure, using the mean square difference, expressed in centimilligals (1cmgal = 10 microgals). The adjusted model is shown on the cross-section on Figure 48.

120. To summarize this technique as used at Civaux, it consists in trying to adjust a model, mainly on an initial deep layer, and then working it up towards the surface. It yields the deepest possible structure, located above the top of the last fixed layer. Final results are shown on Figure 48. It should be noted that, to avoid edge effects, gravity should be known (or extrapolated) up to a distance of about 7 times maximum depth, at both ends of each profile.

121. Another remark concerns the transverse width of the model. CPGF's MONDCONG algorithm is in fact a 2.5 dimensional model, where a finite transverse width can be introduced. For infinitely extended horizontal bodies, of finite cross-section, Talwani's (1962) algorithm can be used, where the cross-section may be a polygon of any number of sides. This technique is convenient when a small number of bodies is considered. When one wants to adjust depths or densities of one or several layers, CPGF's MODCONC algorithm is preferable.

122. Three dimensional (3-D) inversion. Three main techniques can be used for 3-dimensions :

(1) - Processing in the frequency domain (not used at CPGF) ;

(2) - Inversion using spatial filtering (technique frequently used at CPGF) ;

(3) - 3-D iterative modelling (similar to the technique described in para.115)

Inversion using spatial filters is quite commonly used at CPGF in microgravity surveys, and is therefore described here. The mathematical bases were described in detail by Bichara and Lakshmanan (1979, see appendix 4), while the principles and an application to microgravity were described by Lakshmanan (1973 and 1977).

123. The basic assumption of CPGF's spatial filter supposes that, below a semi-horizontal surface (Z = 0) on which measurements are made, all causes of gravity anomalies are exclusively located between 2 horizontal planes Z_1 and Z_2 , and correspond to density variations and not to depth variations.

For this case, supposing in particular that measurements are made

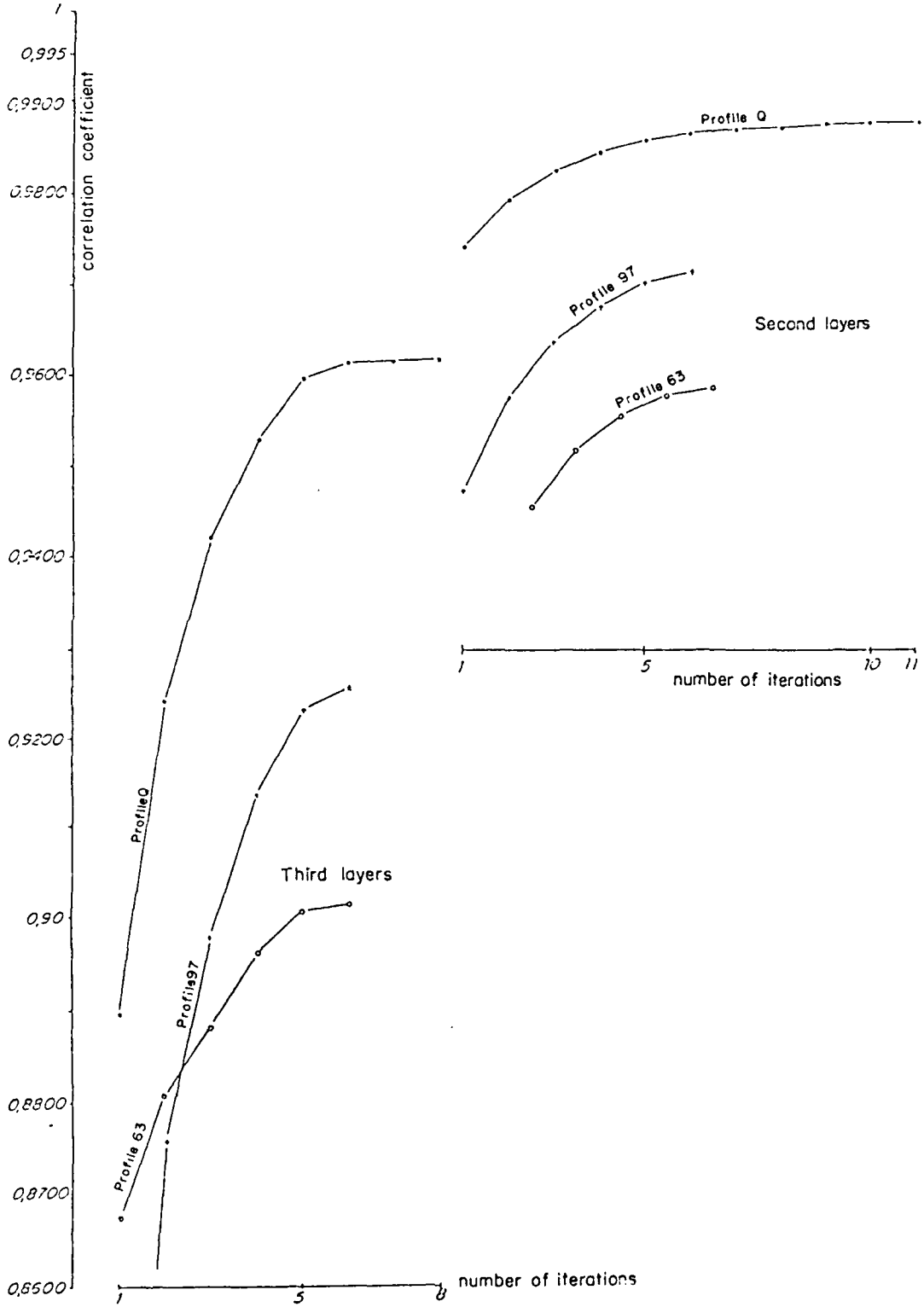

Figure 46. Civaux nuclear power plant, Modcong model, variation of correlation coefficient

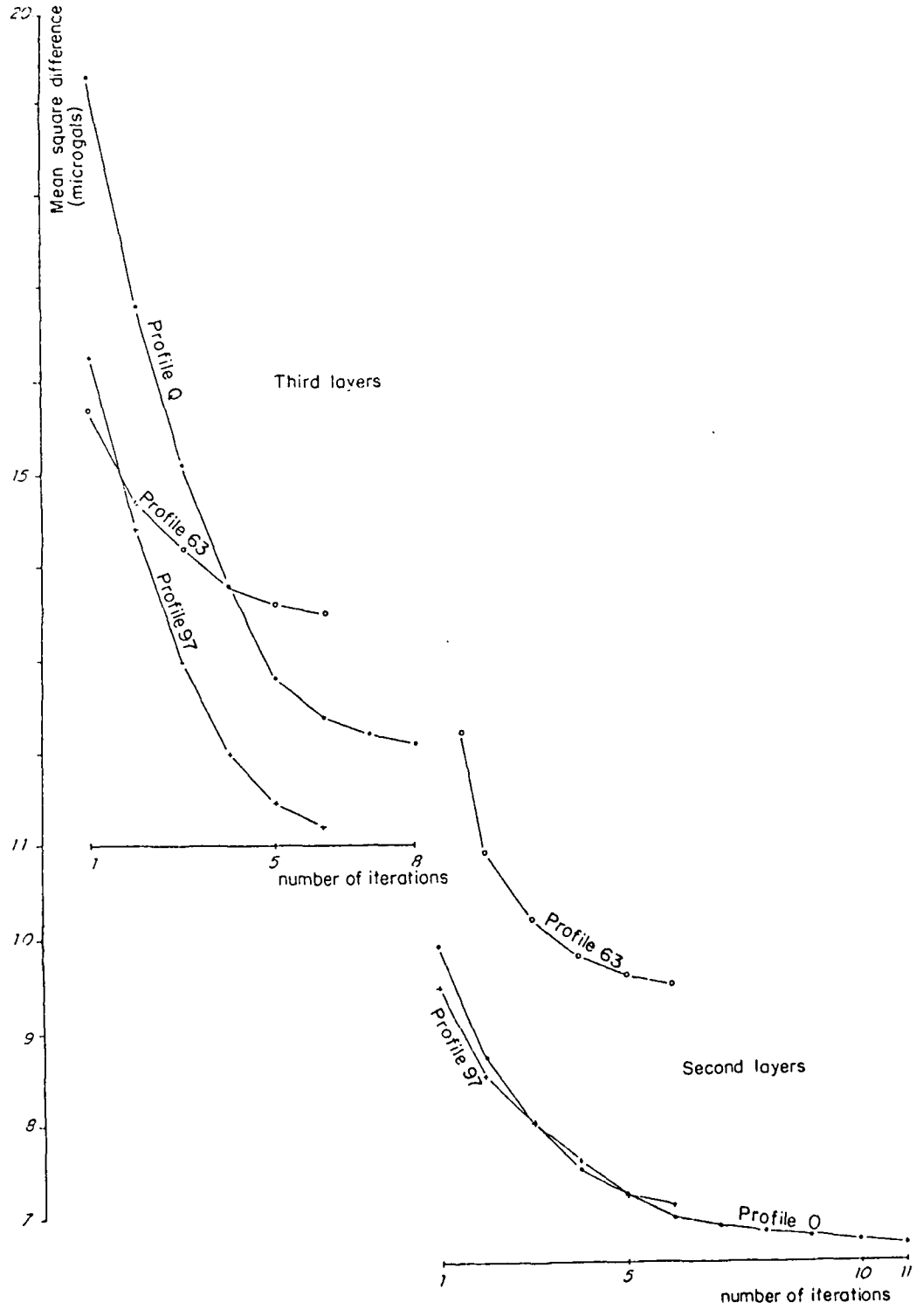

Figure 47. Civaux nuclear power plant, Modcong model, Variation of mean square difference

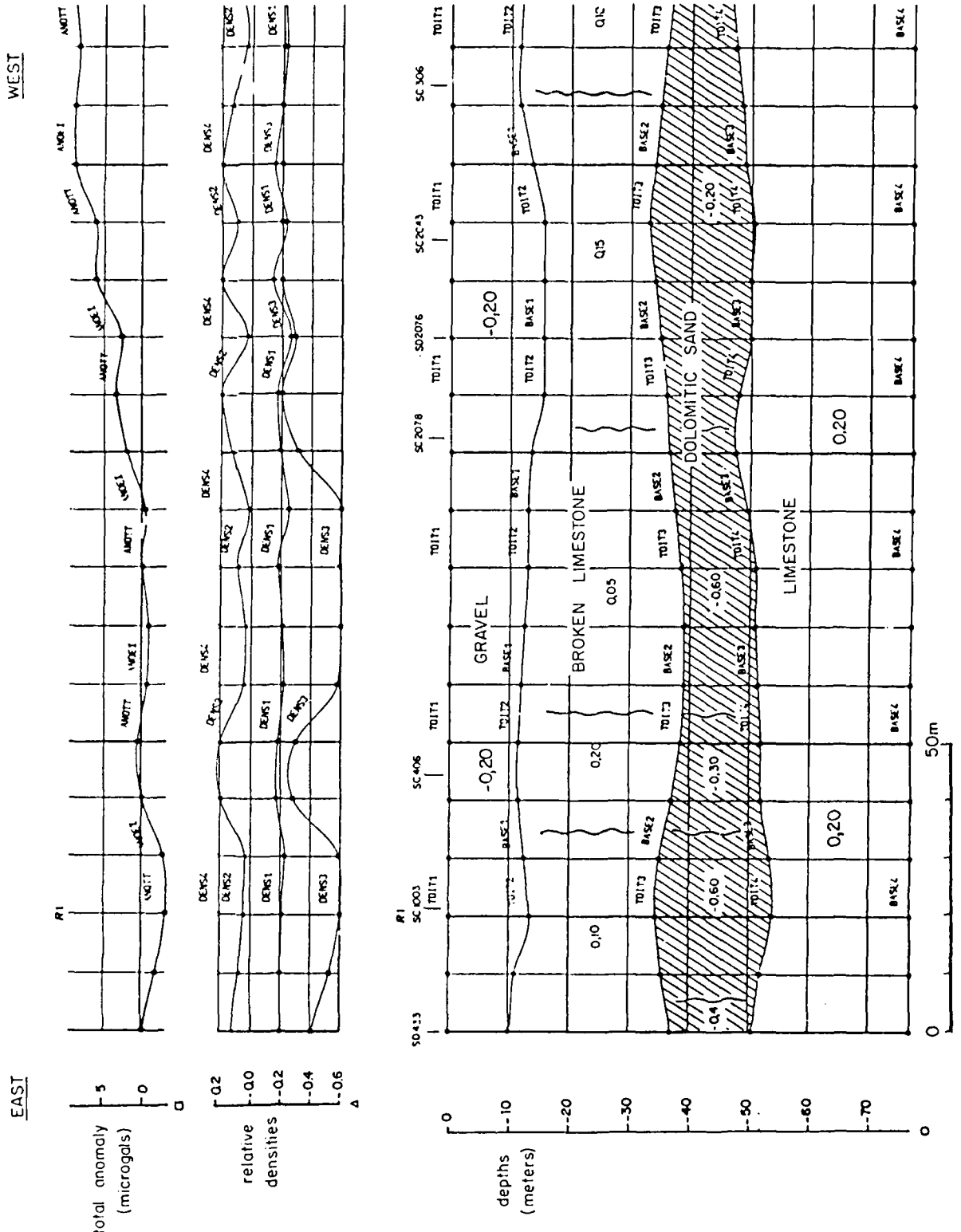

Figure 48. Civaux nuclear power plant-Modcong 2-D model

over a regular grid and that density variations follow the same grid, gravity G(i,j) at points (i,j) is a function of densities of prisms forming the layer Z_1, Z_2.

Figure 49. Schematic of "TESTFIL" 3-D inversion

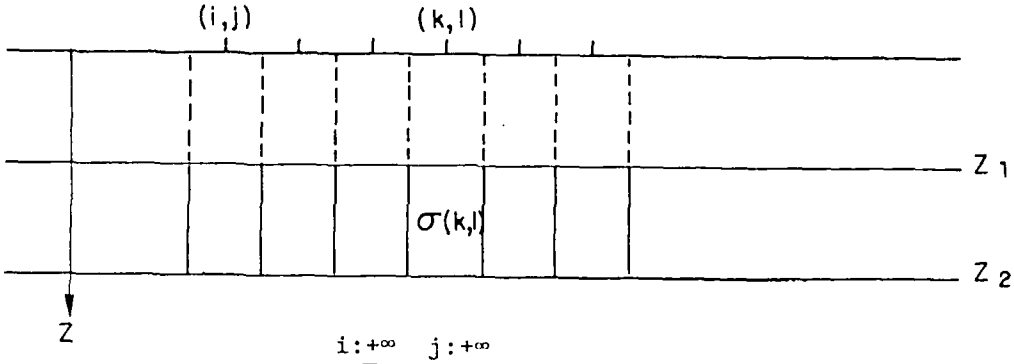

$$G(i,j) = \sum_{i:-\infty}^{i:+\infty} \sum_{j:-\infty}^{j:+\infty} \alpha(i,j,k,l)\ \sigma(k,l)$$

This equation can be inverted, leading to:

$$\sigma(k,l) = \sum_{k:-\infty}^{k:+\infty} \sum_{l:-\infty}^{l:+\infty} \beta(k,l,i,j)\ G(i,j)$$

The points being located along a regular grid and z_1 , z_2 being constant, the coefficients β will be the same for each point (k,l).

124. Empirically, if the summation is carried out inside a moving window, with the following sizes, a very good approximation is achieved :

$$x(k\ max) - x(k) = x(k) - x(k\ min)$$
$$= y(l\ max) - y(l) = y(l) - y(l\ min)$$
$$\geq 7\left(\frac{z_2+z_1}{2}\right)$$

It can be noted that when the moving window is large enough, the sum of coefficients β should be equal to:

$$\sum_{kmin}^{kmax} \sum_{lmin}^{lmax} \beta(k,l,i,j) = \frac{3}{4\pi(z_2-z_1)}$$

125. As an example, at the Cruas nuclear power plant, with a 10 x 10 meter grid, the following parameters were used :

+ Number of elements used: 7 x 7 = 49

+ Slab depth (Z_1, Z_2): 7 to 11 m

+ a = $\sum$filter coefficients = 0.0067

+ maximum filter coefficient = 0.066

+ b = a x (Z_2-Z_1) = 0.0268

+ Theoretical coefficient b = $\frac{3}{40\pi}$ = 0.0239
(the better the filter, the closer b is to 0.0239)

126. For this particular case, the numerical coefficients for computing density σ are:

$$\sigma = 0.0660g(0) - 0.0796\bar{g}(10) + 0.0098\bar{g}(10\sqrt{2}) + 0.0170\bar{g}(20) - 0.0019\bar{g}(10\sqrt{5}) - 0.0003\bar{g}(20\sqrt{2}) - 0.0037\bar{g}(30) - 0.0004\bar{g}(10\sqrt{10}) + 0.0003\bar{g}(10\sqrt{13}) - 0.0001\bar{g}(30\sqrt{2})$$

The normal procedure used at CPGF is to start the inversion with a very deep layer between Zn and Zn-1 and then work up towards the surface. The results include :

- initial residual (or Bouguer) map
- density map for each hypothesis of depths (Zn, Zn-1)
- gravity due to the model
- difference map (between measured and computed gravity)
- statistical map (correlation coefficient and mean square difference maps, the parameters being computed on a moving window).

127. We have shown that the filter should be extended laterally, so that the total radius of the area involved in the processing around each point should exceed 7 times maximum depth. However, it is preferable to limit (by suitable sampling) the number of values for each inversion to 9 x 9 = 81 (49 is usually used).

128. Case histories 711, 714 and 716 illustrate the use of spatial filters. They show the "sharpening" effect of this inversion technique. Even if the selected depth is not perfect, the very "soft" edges of a gravity anomaly clear up very well. This is also obtained by the second derivative transform, still in favour among petroleum geophysicists. The main and fundamental difference is that, if both methods have the "sharpening" effect needed for an effective interpretation, the spatial filter additionally yields a fundamental geological parameter, the relative density of the layer (for the supposed depth). As shown in appendix 4 , a maximum depth compatible with

logical densities can be deduced, which is a more limiting factor than purely mathematical criteria.

129. Three dimensional modelling. If one suspects that densities in the different layers of a 2, 3 or 4 layer model are constant but that depths limiting one of these layers can vary, the modelling technique used at CPGF is more complicated to carry out. Supposing a 3 layer model, with possible depth variations at the bottom of the 2nd layer, the following steps are made:

- 1st step: determine possible limits of variations of bottom depth Z_2, limiting the layer:

$$Z_2 \text{ min}, \; Z_2 \text{ max}$$

- 2nd step: determine Z_1 min, Z_1 max corresponding to the geological model
- 3rd step: make a 3-D inversion as in 174 for a horizontal layer limited by $Z_0 = Z_1$ min and $Z_0+t = Z$ max, compute densities $\sigma_2(i,j)$

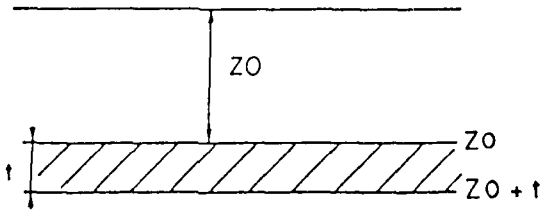

- 4th step: make a first evaluation of thickness ΔZ of second layer with fixed density

$$\Delta Z = (Z_2 \text{ max} - Z_1 \text{ max}) \times \frac{\sigma_2}{\sigma_2(i,j)}$$

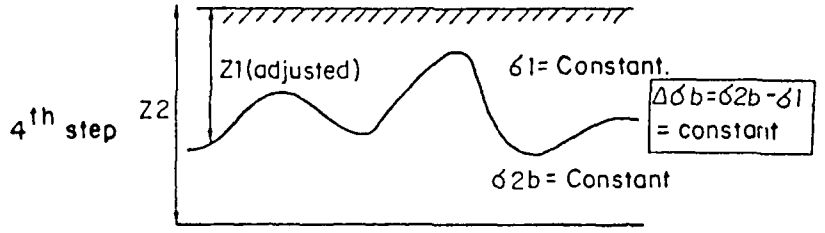

Figure 50. Bases of 3-dimensional modelling

- 5th step: compute new base (or top) of second layer $Z_2 = Z_1 + \Delta Z$ and new values of Z_2 min
- 6th step: compute gravity (GC) due to new model and compare with measured gravity (GM)

- 7th step: divide second layer into non-adjustable upper part, and adjustable lower part, with separation at $Z = Z_2$ min
- readjust layer between Z_2 min and Z_2 by going back to 3rd step and continuing as often as necessary (2 or 3 iterations are usually sufficient).

130. As for the density inversion procedure, the products include:

- initial and final gravity maps
- depth maps
- statistical maps

Various possibilities can be selected :

- fixed bottom or fixed top of a layer
- constraints for maximum variation
- variable density basement as sketched below (in this case Z_2 is taken to have an arbitrary, very large value):

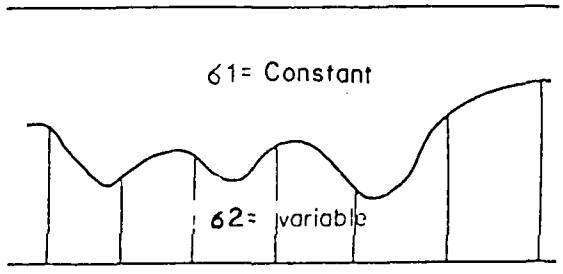

131. A three layer model can also be adjusted. After a certain number of iterations, the yet non explained residual can be transferred to another (usually superficial) layer and its thickness (or density) be in turn adjusted.

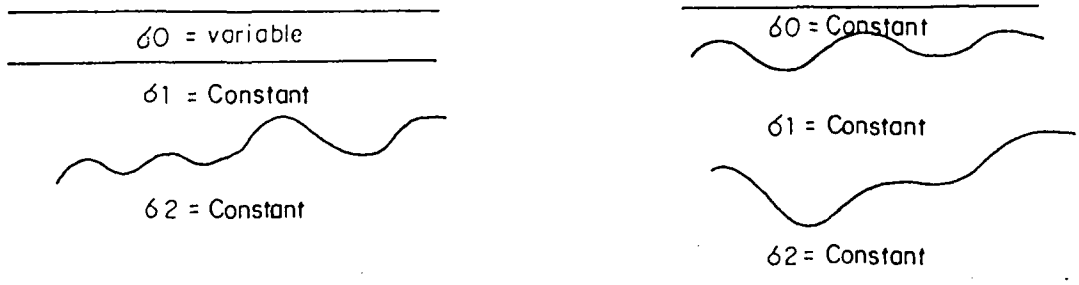

Figure 51. Techniques of 3-D modelling

The technique is described in detail by Alessandrello et al, 1983 (see APPENDIX 4).

132 . Direct evaluation of total mass. It can be shown, using Green's theorem (Schoeffler, 1978 and previous others) that the total mass M causing an anomaly is given by:

$$M = \frac{3}{40\Pi} \int_{-\infty}^{+\infty} \int_{-\infty}^{+\infty} g(x,y).dx.dy$$

(whatever the shape or depth of the cause). However, the main problem in the practical use of this integral is the selection of the radius inside which the integration is to be made efficiently. For example, in the case of a 1,500 Ton sphere, centered at a depth of 10 m, the integration with a AX = AY = 10 m grid, simplifies as follows:

$$M \quad \frac{3}{40\Pi} \sum_{k=i-m}^{k=i+m} \sum_{l=j-n}^{l=j+n} G(k,l).AX.AY$$

According to the size of the window -m, +m, -n, +n selected, the following approximations are achieved.

Table 16: Calculation of total mass by integration of gravity

m	Total size of the window / Depth	M approx. / M real
0	1.0	15.9 %
1	3.0	50.7 %
2	5.0	67.4 %
3	7.0	76.2 %
4	9.0	81.4 %
5	11.0	84.8 %
6	13.0	87.2 %
7	15.0	89.0 %

133. When the window is 15 times the depth (169 points used), the accuracy becomes nearly acceptable (but the error is still in the order of 10 %). The equivalent radius is 8.46 times the depth. If the anomaly were not spherical but more or less elongated, the ratio would have been greater.

134. In conclusion, this method is not presently very popular at CPGF, due to the fact that microgravity surveys are often not very extended, and

that integration of $\iint G.dx.dy$ over a limited area only yields 50 % to 75 % of the total mass. The method can however be used to make crude evaluations.

135 . Microgravity survey planning and design. Prior to carrying out a survey, it is absolutely necessary to carry out some preliminary modelling, in order to reply to the following questions:

- are the anomalies detectable or not?
- what is the most reasonable grid?

The two questions are in fact closely linked. Due to the known accuracy of microgravity measurements, one can consider that an anomaly exceeding 10 microgals on 3 adjacent stations, is very probably true (if the measurements were made during at least two different work programs). Without entering the field of probability analysis, and referring to set curves of section 16, this means that the following spherical voids can be detected (with a density contrast of -2 gm/cc).

Table 17: sphere: minimum spacing so that anomaly exceeds 10 µgals on adjacent points

Depth (m)	Radius of sphere (m)	Mass deficit	Maximum anomaly (µgals)	Minimum grid for 3 points > 10µgals
1	1	8.4 T	56	1.5 m
2	1	8.4 T	14	1.0 m
2	2	67 T	112	4.0 m
3	2	67 T	50	4.1 m
3	3	226 T	167	7.1 m
4	2	67 T	28	4.0 m
4	3	226 T	94	7.4 m
4	4	536 T	223	10.5 m
4	5	1048 T	437	13.5 m
5	2	67 T	18	3.4 m
5	3	226 T	60	7.6 m
5	4	536 T	143	11.1 m
5	5	1048 T	279	14.3 m

Depth (m)	Radius of sphere (m)	Mass deficit	Maximum anomaly (μgals)	Minimum grid for 3 points > 10μgals
7	2	67 T	(9)	Not achieved
7	3	226 T	31	7.4 m
7	4	536 T	73	11.6 m
7	5	1048 T	143	15.5 m
7	6	1810 T	246	19.1 m
10	3	226 T	15	5.6 m
10	4	536 T	36	11.6 m
10	5	1048 T	70	16.3 m
10	6	1810 T	121	20.6 m
10	8	4290 T	286	28.9 m
15	3	226 T	(7)	Not achieved
15	4	536 T	16	9.0 m
15	5	1048 T	31	15.9 m
15	6	1810 T	54	21.5 m
15	8	4290 T	127	31.6 m
20	4	536 T	(9)	Not achieved
20	5	1048 T	17	13.4 m
20	6	1810 T	30	20.9 m
20	8	4290 T	72	32.9 m
30	6	1810 T	13	13.9
	8	4290 T	32	32.3

136. This table, which is shown in graphical form in the enclosed figure 52, can be summarized by the following rules of thumb:

- optimum detection of spherical voids of mass M needs spacing of the same order of magnitude as depth
- maximum depth of detection $z < \sqrt{\frac{2}{3} |M|}$
- For a horizontal cylinder, with a density contrast of 2 gm/cc, the following table 13 gives the maximum anomaly and the minimum spacing so that three points (on a transverse profile) have an anomaly exceeding 10 μgals.

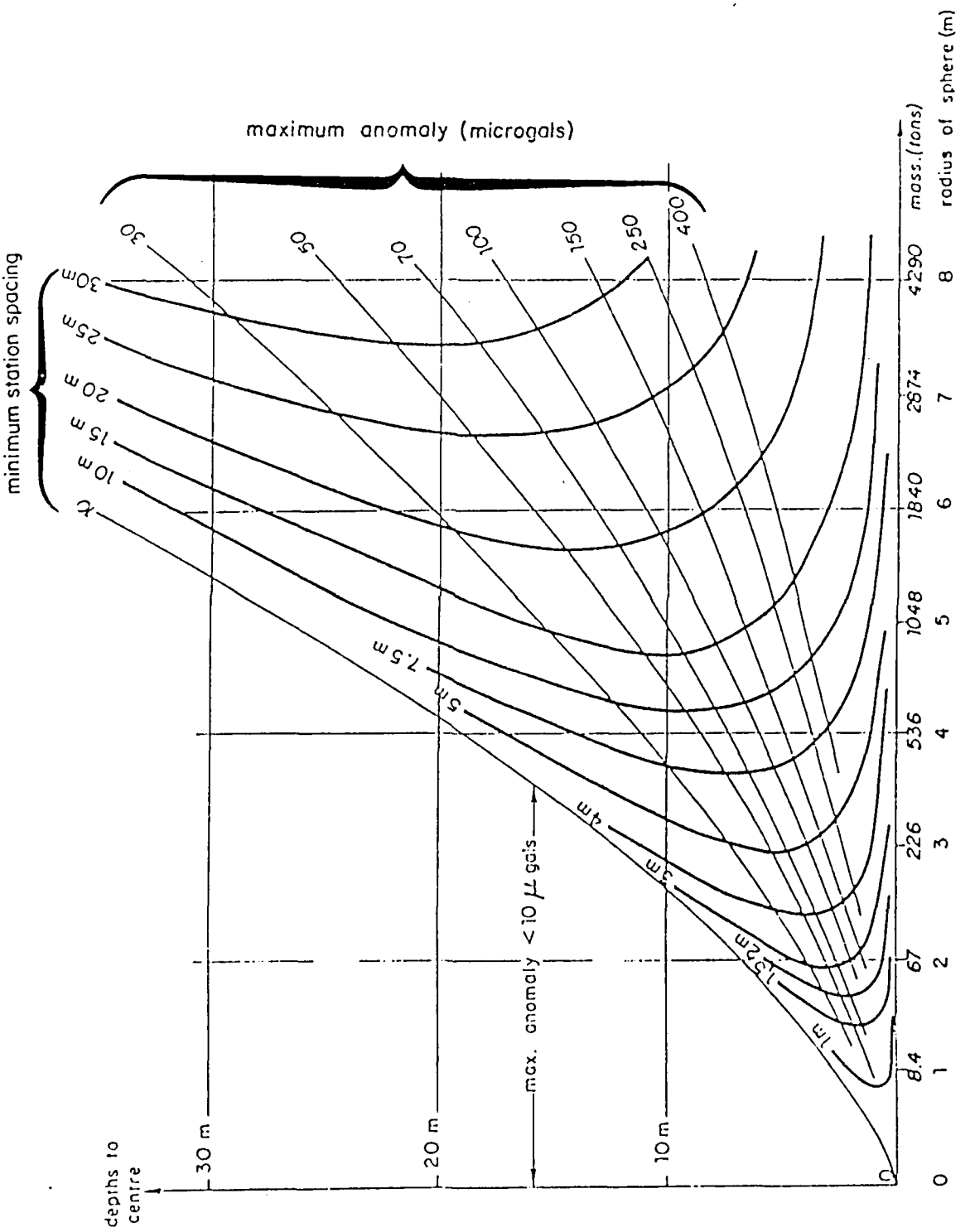

Figure 52. Anomaly due to a sphere - Minimum station spacing so that 3 adjacent points exceed 10 μgals

Table 18: cylinder, minimum spacing so that 3 adjacent points exceed 10 μgals

Depth (m)	Radius of cylinder (m)	Max. anomaly (for σ = 2) in microgals	Minimum spacing for 3 points > 10 μgals (m)
1	1	84	2.7
2	1	42	3.6
	2	168	7.9
3	1	28	4.0
	2	112	9.6
	3	251	14.7
	5	698	24.9
5	1	17	4.1
	2	67	11.9
	3	151	18.8
	5	419	32.0
	7	821	45.0
	10	1679	64.5
10	1	(8)	Not achieved
	2	34	15.3
	3	75	25.6
	5	209	41.7
	7	411	63.3
	10	838	91.0
20	2	17	16.4
	3	38	33.3
	4	67	47.8
	5	105	61.6
	7	205	88.4
	10	419	127.9
30	2	11	10.3
	3	25	36.9
	5	70	73.4
	7	137	106.8

Depth (m)	Radius of cylinder (m)	Max. anomaly (for σ = 2) in microgals	Minimum spacing for 3 points > 10 µgals (m)
40	3	19	37.6
	5	52	82.3
	7	103	121.7

137. Results concerning horizontal cylinders are shown in graphical form on figure 53. It should be noted that actual cavities are often easier to find than one could expect. This is due to a phenomenon of migration of voids towards the surface, by caving in.

In addition, it should be reminded that microgravity often detects karstic zones (groups of cavities, fractures, etc ...) and not just individual cavities. This has been particularly clearly shown by numerous surveys carried out in the northern part of Paris and its suburbs, as reported in the case history section (Porte Pouchet), as well as by Kutkan and Lakshmanan (1969) and Bolleli and Lakshmanan (1965).

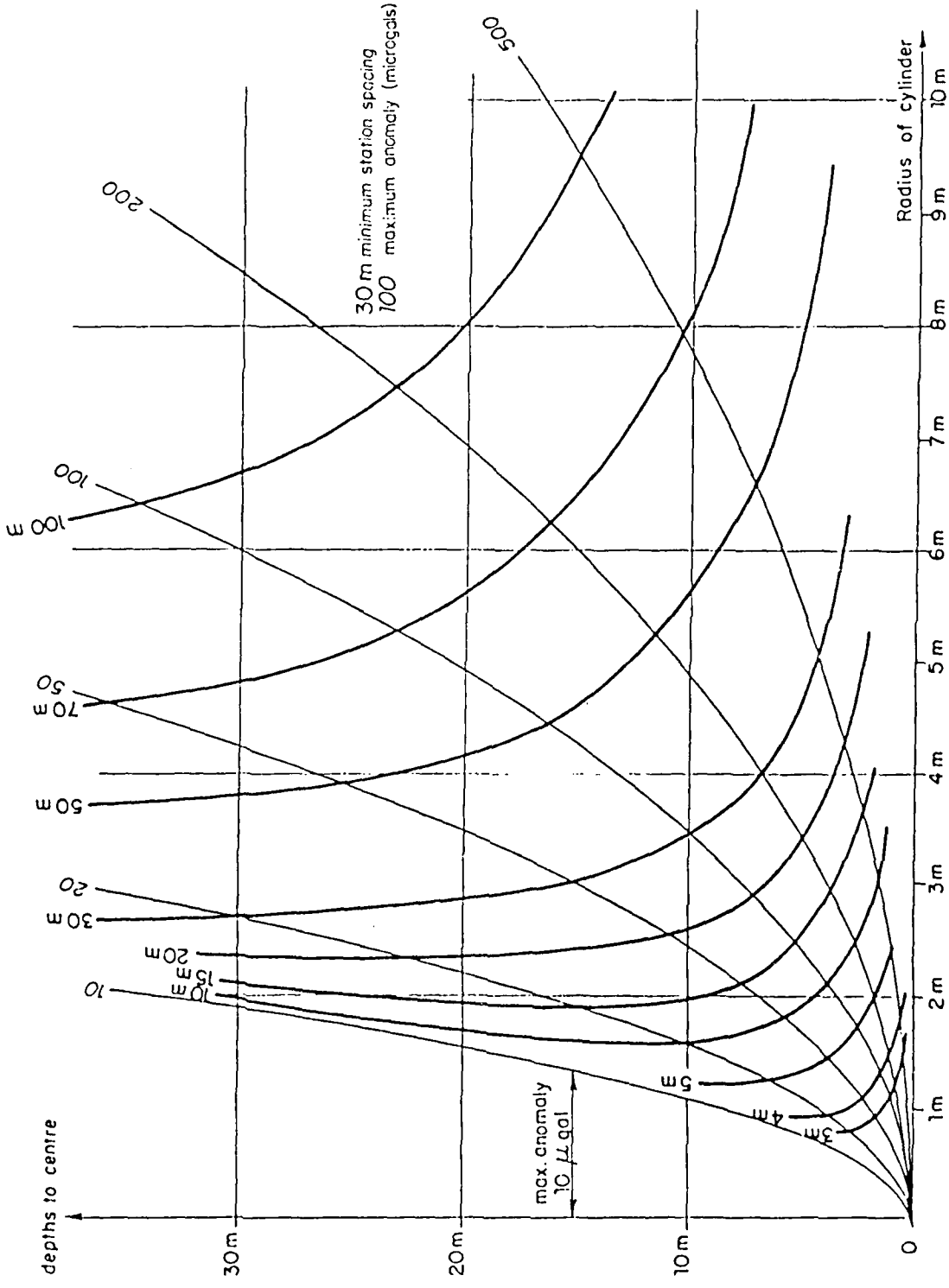

Figure 53. Anomaly due to a cylinder : minimum station spacing so that 3 points exceed 10 μgals

PART 2: APPLICATION OF MICROGRAVITY TO THE DIRECT IN-SITU MEASUREMENT OF EMBANKMENT DENSITIES

138. General. The generalized Nettleton technique described in 146 was first developed by CPGF in 1976 for microgravity surveys, in order to improve terrain corrections. We soon noticed that the procedure yielded an interesting by-product, the densities of the slice of ground located above a variable, smooth datum linking the lows (or relative lows) of the topographic surface. In the particular case of an embankment constructed on flat terrain, such as a railway embankment, a road embankment, or a river or canal levee, the datum can be a horizontal plane, which represent the ground surface before construction of the structure. In that case, the formulas given in the 39 can be written as follows, with h being the height of the embankment :

$$\sigma_1 = \sigma_0 + \frac{COV(g_0,h) - COV(\Delta r,h)}{\frac{4\pi}{3} COV(Z_3,h)}$$

g_0 is the initial residual computed with density σ_0,

$\Delta r = g_{1m-3m}$, difference between 2 successive values of the regional anomaly and $Z_3 = h - \frac{3C_0}{4\pi\sigma_0}$

C_0 being the terrain correction computed for density σ_0. After two iterations, a stable solution giving new values of embankment densities at each point is obtained.

139. Application to railway embankments. An example is given by Bichara and Lakshmanan (1983). It concerns the density evaluation of a railway embankment, 6 to 7 m high, in the south of France. A profile in a weak section gave an average density of 1.88 gm/cc, while in a section of good quality, a density of 2.15 gm/cc was computed. Another example concerning the Arles viaduct along the Arles-Marseilles railroad is described in the case history section.

140. Cheops pyramid microgravity survey. This method has been applied and largely improved during 1986 and 1987, during the processing of the gravity survey carried out by CPGF in the Great Pyramid of Cheops in Egypt.

The main results of the first two surveys (May and October 1986) are described in the enclosed paper "Microgravity probes the Great Pyramid", by J. Lakshmanan and J. Montluçon (1987) (see annexure 2). A third, more comprehensive survey was made in February 1987, during which the 4 sloping edges and a perimetric profile around the Pyramid were surveyed. A total of 608 stations were taken during the three surveys.

141. The interpretation procedure developed by CPGF includes a series of steps. Instead of computing, as usual, the Bouguer anomaly, gravity measurements on or in side a finite body are only corrected of the free air effect. The free air gravity (FA in microgals) is given by:

$$FA = kR + 308.8\ z - 0.7025\ x$$

R is the gravity reading corrected of luni-solar variations and of instrumental drift,

k is the instrumental coefficient

z is the elevation of the station and 308.8 the free air coefficient

z is the latitude (in meters) and 0.7025 the latitude correction (at Cairo's latitude).

In a first step, FA can be considered to be the sum of:

- the general attraction P of a homogeneous theoretical pyramid of density σP from which the effect C of known cavities is subtracted
- the attraction O of ground around the pyramid, computed from topographic maps at a scale of 1 to 5000th, up to a distance of 5 km
- long distance regional effects (RE = ax+by+cz) due to remote causes, supposed to be linear, and evaluated from the interpretation of a regional 1/1000000th gravity map (in fact, ax and by are very small and were added to the next linear coefficients Ax and By, while cz was used to correct FA).
- short distance regional effects Ax+By+C.

142. P and C having been calculated for an arbitrary density σ_0, a multivariate regression between FA, $\frac{(P-C)}{\sigma_0}$, x and y leads to the evaluation of the real average densities σP of the pyramid, σT of the ground around the pyramid, and of the linear coefficients A, B and C. Taking into account the effect GR due to heavy slabs of granite surrounding the King's chamber (density 2.70), the equation becomes:

$$FA-GR-cz = \sigma P\ \frac{P-C}{\sigma_0} + \sigma T.O + Ax + By + C + RE$$

143. It should be noted that Θ is not the usual terrain correction T used in normal gravity processing. Θ is the influence of the real terrain, while T is the usual correction made by "erasing" topographic features located above the station elevation z, and by "filling in" valleys located below z. The algorithms leading to O and to T are similar but differ in signs, as shown below:

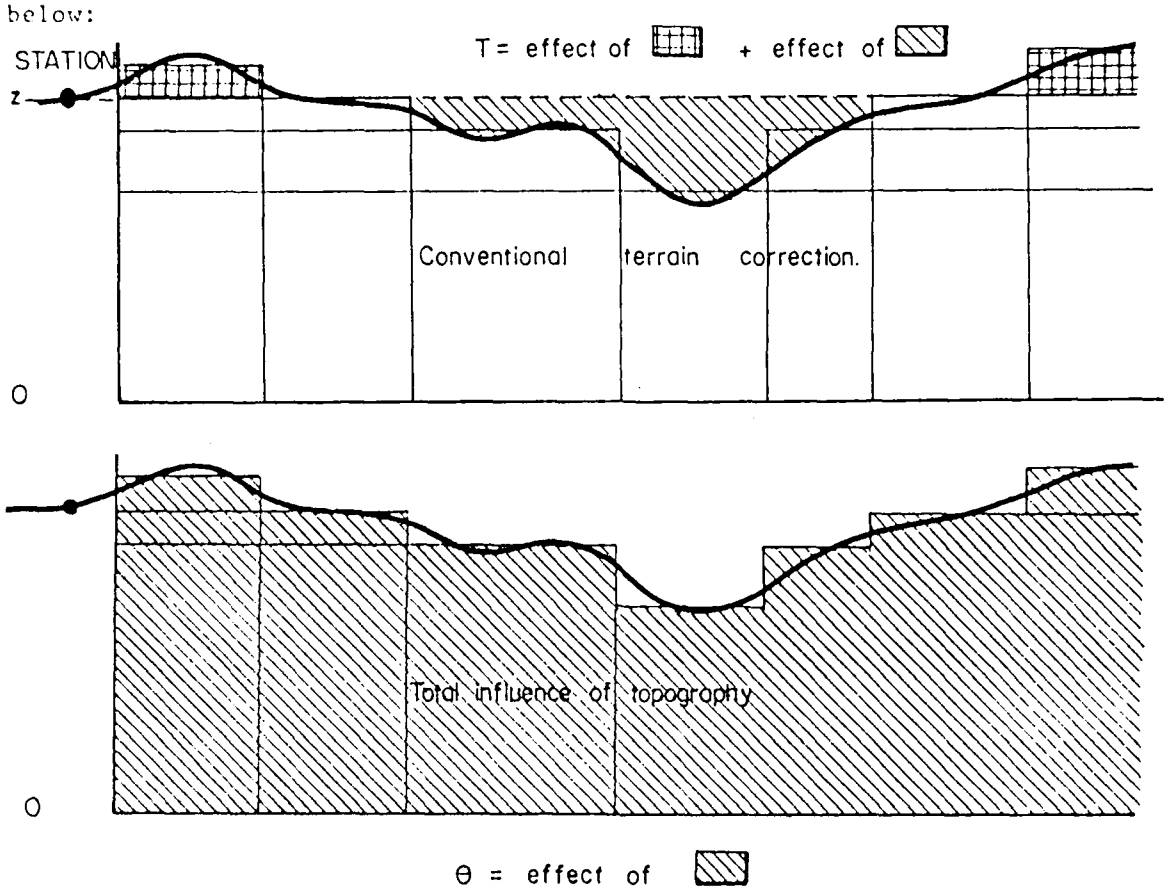

Figure 54. Difference between terrain corrections and influence of topography

After regression, a residual value of free air gravity was computed at each of the 608 stations. After examining the values of these residuals, the pyramid was divided into 21 blocks and the bedrock into 6 blocks, forming what we called the "macrostructure" of the pyramid. Multivariate regression yielded the absolute densities of these 27 blocks, shown on the following sketch. Central block 21 includes nearly all the accessible tunnels and chambers (see Figure 1 and 2 in enclosed paper).

Figure 55. Macrostructure of Cheops pyramid

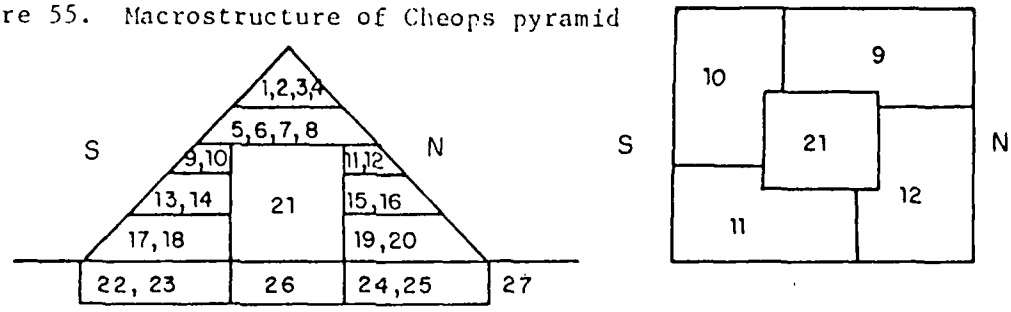

144. In a second step, in order to explain certain well organized residuals, 3 extra blocks were cut out of blocks 20 and 25, and the central block 21 was divided into 94 blocks, selected in order to take into account the organized residuals. This is the study of what we called the "mesostructure". The first degree residual obtained by the regression of the "macrostructure" replaced the Free Air gravity, and a second regression was made, yielding the relative densities of the new set of blocks (to be added or subtracted to density of block 21).

145. In a third step, a certain number of blocks of the "mesostructure" were redivided into blocks of "microstructures", and a third set of regressions made, using the second step residuals. Improvement in the knowledge of the densities is shown by the following mean square averages of residuals in microgals.

- Free air gravity (initial values)	1150
- Macrostructure (1 density for pyramid + bedrock):	32.9
- Macrostructure (1 density for the pyramid, 1 density for bedrock, neglecting effect of granite, neglecting Ax + By):	11.06
- Macrostructure (ditto with Ax + By):	5.93
- Macrostructure (ditto, with granite at 2.60 and Ax + By):	5.56
- Macrostructure (ditto, with granite at 2.75 and Ax + By):	5.53
- Macrostructure (25 blocks in pyramid, 7 in bedrock):	2.26
- Mesostructure (27 smaller blocks dividing block 21):	2.06
- Microstructure (with extra blocks around King's chamber and around Queen's gallery): presently in progress, should reach 1.5	

146. Application of the method to other structures. During the Cheops survey, we carried out at the same time:

- the development of a new technique for assessing densities of existing structures
- the survey of the pyramid itself.

If a new survey were to be carried out on another existing structure, a rock fill dam for example (1,000 m long, 50 m high, 200 m wide), the following procedure would be advisable:

1) Obtain topo maps surrounding the dam, at a scale of 1/10000th for example, covering an area of at least 3 x 2 km, and digitize at a 100 x 100 m grid.
2) Obtain a topo map of the structure and its surroundings, at a scale of 1/1000th, and digitize at a 20 x 20 m grid (the corresponding elevations have to be carefully checked and connected with those of the gravity survey points themselves).
3) Plan and carry out a gravity survey covering all accessible points on the structure and, if possible, inside it (along drainage tunnels, for example) with a station spacing of about 10 m.
4) Extend the gravity survey outside the dam with a 50 m grid close to the dam, and with a number of "regional" profiles extending to 2 km from the dam.
5) Compute free air gravity .
6) Divide the structure and the surrounding terrain into a very large set of prismatic blocks B(i) corresponding to the survey points and to all digitized points (i) (one or several blocks/point). For example, the number of blocks can be 1,000 for 200 measurements (see enclosed figure 56).
7) Compute the effect E(i,j) of each individual block on each survey point(j) for a standard density of 1.0 and store on tape.
8) Add effects of all blocks forming the structure ($SS(j)=\sum S(i,j)$) and of all blocks forming the terrain ($ST(j) = \sum T(i,j)$).
9) Compute global densities σ_S and σ_T of structure and of terrain by regression:

$$FA(j) = \sigma_S . SS(j) + \sigma_T\ ST(j) + ax + by + c$$

10) Compute first step "residuals" (differences between measured and computed values), examine carefully and regroup blocks B(i) accordingly, into a reduced set of macrostructure blocks B1(k), both in the s ure and in

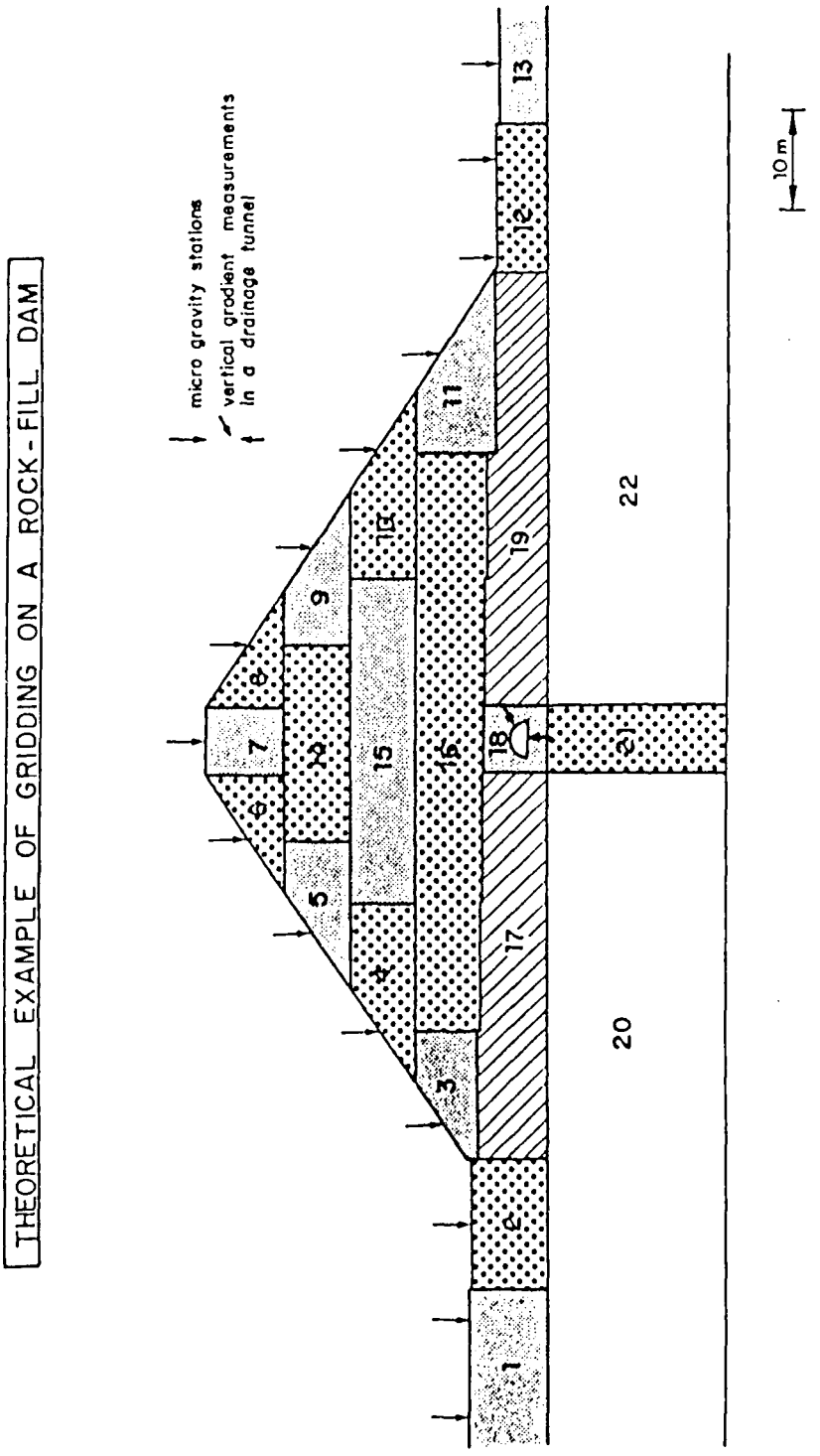

Figure 56. Theoretical example of gridding on a rock fill dam

the terrain (for example, 30 blocks.

11) Compute effect E1(k,j) of blocks B1(k) on survey points (j) by adding values computed in (7).

12) Compute densities $\sigma_1(k)$ of blocks B1(k) by regression.

13) If necessary, readjust by regrouping certain blocks and go to (11).

14) If necessary, divide important blocks of the structure, particularly in zones where sufficient data are available, into a mesostructure, and run steps similar to (11), (12), (13).

15) If necessary (and possible), create a (or several) microstructure(s) and run steps similar to (11), (12), (13) until mean square differences are less than 10 microgals and until residuals show no organized structure. The final product obtained is a model giving absolute 3-D densities of the structure and its foundation. We will show in the case history section 710 (example of Dowell-Schlumberger plant) that one of the main advantages of the regression technique is that it is not necessary to dispose of gravity data extending largely out of the survey area, as with the other inversion techniques.

147. Measurements during construction. M.L. Hadj-Aissa (1986) described a method of embankment monitoring by microgravity measurements, before, during and after construction (J. Lakshmanan was a member of the thesis jury). His method can be summarized as follows:

- a first set of measurements is made on the ground surface, before construction,
- a second set made at the end of the construction, on the top of the embankment, exactly at the same horizontal coordinates (x,y) as the previous set.
- the gradient between upper and lower measurements is a function of the density of the embankment, as with the borehole gravity meter, but with only a half coefficient (while the lower readings are made, the embankment does not yet exist).

148. Taking into account CPCF's techniques developed at Cheops pyramid, we have modified Hadj-Aissa's method as follows:

- we consider the free air anomaly and not the Bouguer
- we take into account the vertical gradient before construction (neglected by Hadj-Aissa).

Decomposing the dam into a set of prisms (j), whose gravity effect on measurement points (i) are P(j,i) for a standard density of 1, the 2 free anomalies are related as follows:

$$FA(top,i) = FA(bottom,i) + \sum_{j=1}^{j=n} P(j,i).\sigma j + \frac{\partial FA(bottom,i)}{\partial z} \Delta z(i)$$

Δz is the elevation difference between top and bottom points (i)

σj is the (unknown) density of prism j.

$\frac{\partial FA}{\partial z}$ is the vertical gradient obtained by interpretation of FA (bottom).

The above equation is linear with respect to unknowns σj. If the number of measurement points (i) is sufficiently large, compared to unknowns (n), a multivariate regression yields best fit values for σj.

The interpretation of FA (bottom) can be made before construction of the dam, by various means. Particularly, a separation of the foundation into "k" blocks of densities D(k) gives a set of j equations with the unknowns. A similar regression yields D(k) and an upward continuation is then easily made, using Newton's law, and from there $\frac{\partial F}{\partial z}$ can be evaluated.

149. The vertical gradient can also be computed by a linear filter, such as published by Schoeffler (1975):

$$\frac{\partial G}{\partial Z} = 2.24\ g(o) - 1.16\ \bar{g}(S) - 0.12\ \bar{g}(S\sqrt{2}) - 0.96\ \bar{g}(S\sqrt{5})$$

Hadj-Aissa has used a similar method on the Al Moustakbal dam in Algeria, as well as along several road embankments in Belgium. Some of these measurements were made at 3 levels (bottom, middle, top).

150. The borehole gravity meter. This tool, which is in fact a remotely operated gravity meter, is constructed by Lacoste and Romberg. The surface electronics have been strongly improved by EDCON, Denver, Co., who is the sole contractor supplying this service. This tool is primarily used in the oil industry for in-situ density measurements. The vertical gradient of "free air" corrected gravity is directly proportional to the density of a horizontal slab, in the case where other lateral sources of vertical gradient can be neglected. If readings R1 and R2 are made at two elevations Z_1 and Z_2, apparent density is given by:

$$\sigma = 3.683 + \frac{1}{83.8} \frac{R_1 - R_2}{Z_1 - Z_2}$$

The "radius of investigation" is about 50 to 100 meters (LaFehr, 1983).

151. Present applications to civil engineering have been limited to nuclear waste disposal sites (Bichara, Laurin, Black, LaFehr, 1981 and Lakshmanan and Kutkan, 1985) in Denmark and in Switzerland. Limitations are presently related to the required hole diameter (at least 5 1/2") and cost. Hoever, one can imagine a development of this tool for the evaluation of embankment densities, as described in chapter 24.

PART 3: APPLICATION OF MICROGRAVITY TO GROUTING CONTROL AND OTHER REPEAT SURVEYS

152. General. If the ground elevation is not modified by the works, the differences between measurements made before and after grouting are only due to the grout. Supposing that the ground is formed of zones of constant densities, plus an extra zone p+1, whose density can be modified by the grout, then before grouting:

$$G(0) = \sum_{i=1}^{i=p} \sigma i Ii + \sigma(0,p+1) Ip$$

Ii being the influence of the different bodies i on each measurement point, including terrain corrections, for a density $\sigma_0 = 1$

$$\text{After grouting} \quad G(1) = \sum_{i=1}^{i=p} \sigma i Ii + \sigma(1,p+1).Ip$$

Change in density will be given by:

$$\sigma(1,p+1) - \sigma(0,p+1) = \frac{G(1) - G(0)}{Ip}$$

Measurements need to be made very carefully, with stable and non movable (cemented) station positions.

The following case history was completed with the use of a small part of the funds made available to CPGF by the present contract. In the case history section, chapter 78 describes another case, the Nanterre reservoirs, where measurements were made before and after grouting.

Case history of Varangéville railroad

153. General. The Paris-Strasbourg railroad has been affected by sink-holes, near Varangéville (Lorraine) since nearly one hundred years. CPGF has carried out 4 surveys for SNCF (French railways):

Réf. 2220: microgravity survey in June-July 1981

Réf. 2311: microgravity modelling, December 1981

Réf. 2364: 4 drill holes with logging while drilling, June-July 1982

Réf. 3038: microgravity survey in December 1986

Réf. 3169: 2 drill holes with logging while drilling, August 1987

154. The average geological cross-section (with corresponding depths):

- 0 to 2-3 m : made ground and/or red dolomitic clay
- 2-3 to 7-9 m : Beaumont's bedded dolomite
- 7-9 to 17-19 m : sandstone (sandy clays, siltstone and silty clays)
- 17-19 to over 100 m: gray and red siltstone with gypsum lenses in the upper part
- Below 60-80 m : salt beds are interstratified.

The age of these formations is triasic. It should be noted that the hydrogeological conditions may be locally modified by the presence of a canal, which follows the railroad all along the surveyed section. These sink-holes have diameters reaching 2 to 4 m, and are mapped as black circles on enclosed Figure 57, left part), with corresponding dates of movements (example "année 1956"). Several geotechnical surveys and drilling have shown that the sink-holes could be related to karstic cavities in Beaumont's dolomite, and also in gypsum lenses located between depths of 20 and 40 m.

155. Another cause of the sink-holes is the old St Nicolas-Varangéville salt mines, located between depths of 100 to 150 m. An old (uncontrolled) map of these mines is produced on figure 57(b), with boundaries shown with dotted lines. If these boundaries are correct, it would seem that the mines are only related to the sink-holes between kilometer points 365.000 and 365.100. After the occurence of each of these sink-holes, SNCF has carried out many repairs : repairs :

- filling
- grouting (1978, 1980 and 1982)
- construction of rigid steel platforms ("tablier métallique" on the map).

156. The purpose of the first gravity survey (1981) was to check the existence and position of remanent voids and to help plan the next grouting campaign. It included two lines of microgravity stations (one along each track) with spacings of 7 or 14 meters, with a total of 183 stations in a section 760 m long. It should be noted that for maximum coverage, the stations on track 2 are located at mid point of stations on track 1. The second survey (1982) included 4 drill holes 27.5 m deep, with logging while drilling ("LWD") recording. These drill holes were equipped with "tubes à manchettes" for subsequent grouting.

The third survey (1986) was a repeat microgravity survey. 90 gravity stations (mainly along track i) were repeated in order to control the development of sink-hole phenomena for the last 5 years.

157. Results, 1981 microgravity survey. The microgravity results are plotted as follows:

- Bouguer values, plotted on figure 57
- Residual values on the left part of map 58, after subtraction of a graphical "regional" (it should be noted that this regional leads to maximum residuals of -40 microgals, while a higher regional between 364.700 and 364.900 would have doubled the residual).

The survey showed 4 main anomaly zones:

a) PK 364.400 to 364.550: several narrow anomalies with maximum negatives of -20 microgals. Modelling suggests causes at less than 10 m depth. These anomalies seem often related to a first set of sink-holes. Of course, previous grouting has strongly reduced the anomalies from their initial values (if measurements had been made). It is in this zone that a steel platform had previously been constructed ("tablier métallique").

b) PK 364 364.580 to 364.720: a set of anomalies attaining -40 microgals are strongly correlated with an impressive series of sink-holes and with the second steel platform. Maximum depth of causes can range from 0 to 10-20 m. It could appear that the eastern part of this anomaly has not been grouted sufficiently.

c) PK 364.750 to 364.920: a wide anomaly (-40 or -80 microgals, according to the choice of the regional curve) seems related to the old salt mines. The voids may have "moved up" a bit, but are still not at the surface, no sink-hole having been observed.

d) PK 365.300 to 365.140: a set of narrow anomalies reaching -20 microgals, related to 2 sink-holes. These anomalies probably have superficiel causes. In December 1981, modelling was made, using extensive drilling data (15 drill holes on each track, for a length of 80 m) made before 1980, prior to any grouting. The drill holes reached 20 m and a density interpretation was made, supposing the following densities:

Sound rock	: 2.1 gm/cc
Slightly open rock	: 1.95 gm/cc
Very open fractures	: 1.75 gm/cc
apparent "voids"	: 1.30 (water or mud filled)

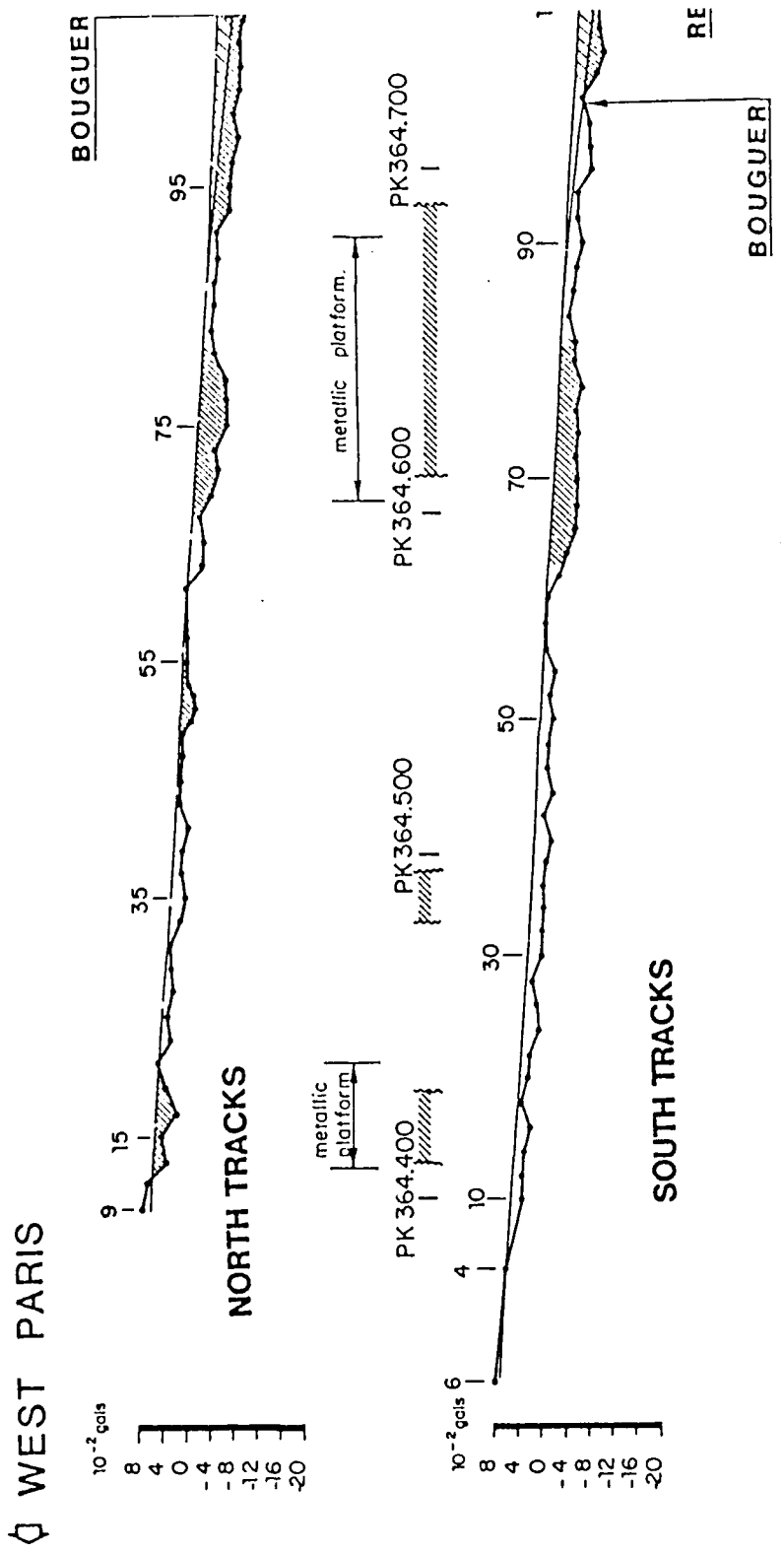

Figure 57. Varangéville railroad, 1981 and 1986: Bouguer profiles (a): western part

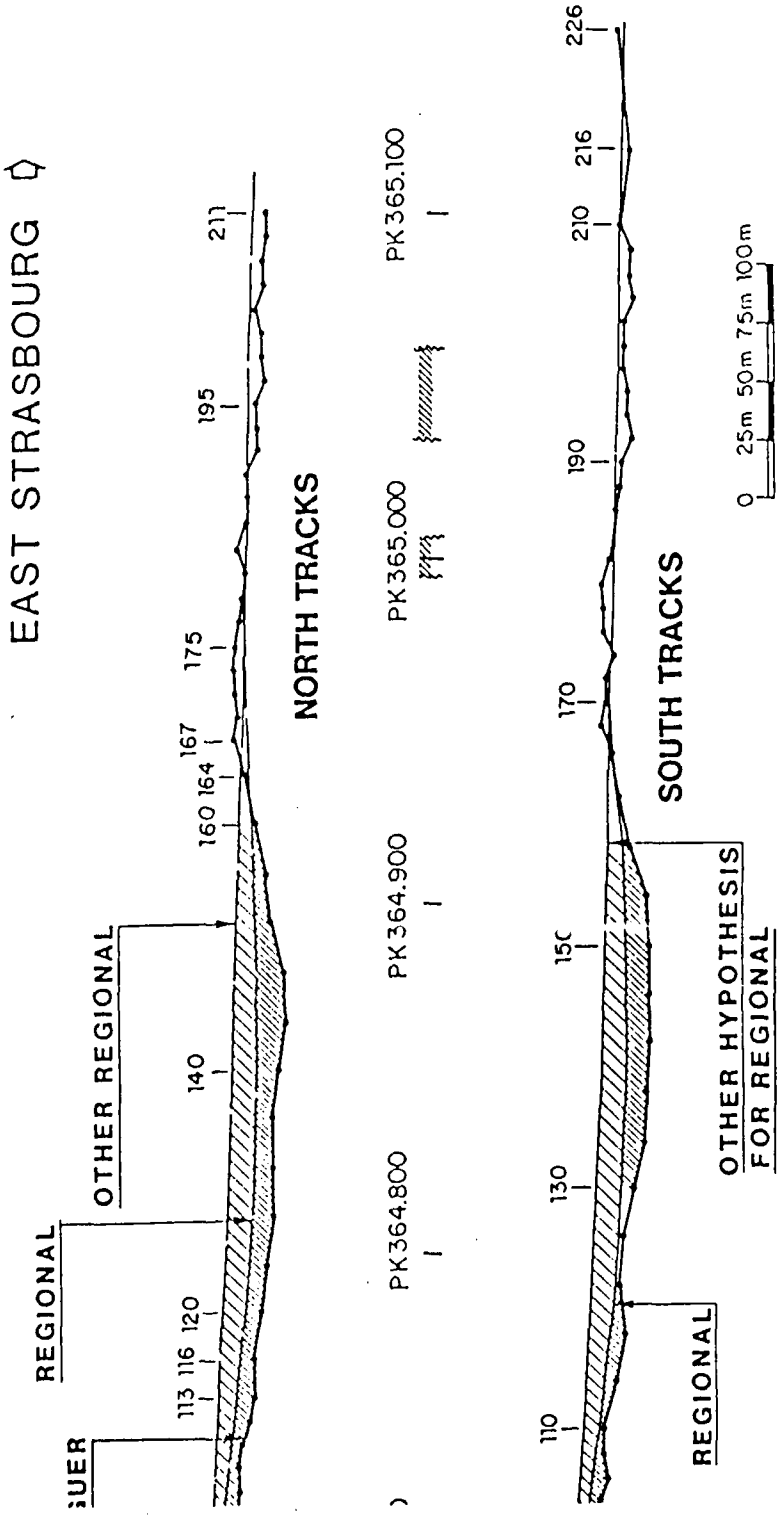

Figure 57. Varangéville railroad, 1981 and 1986: Bouguer profiles (b): eastern part

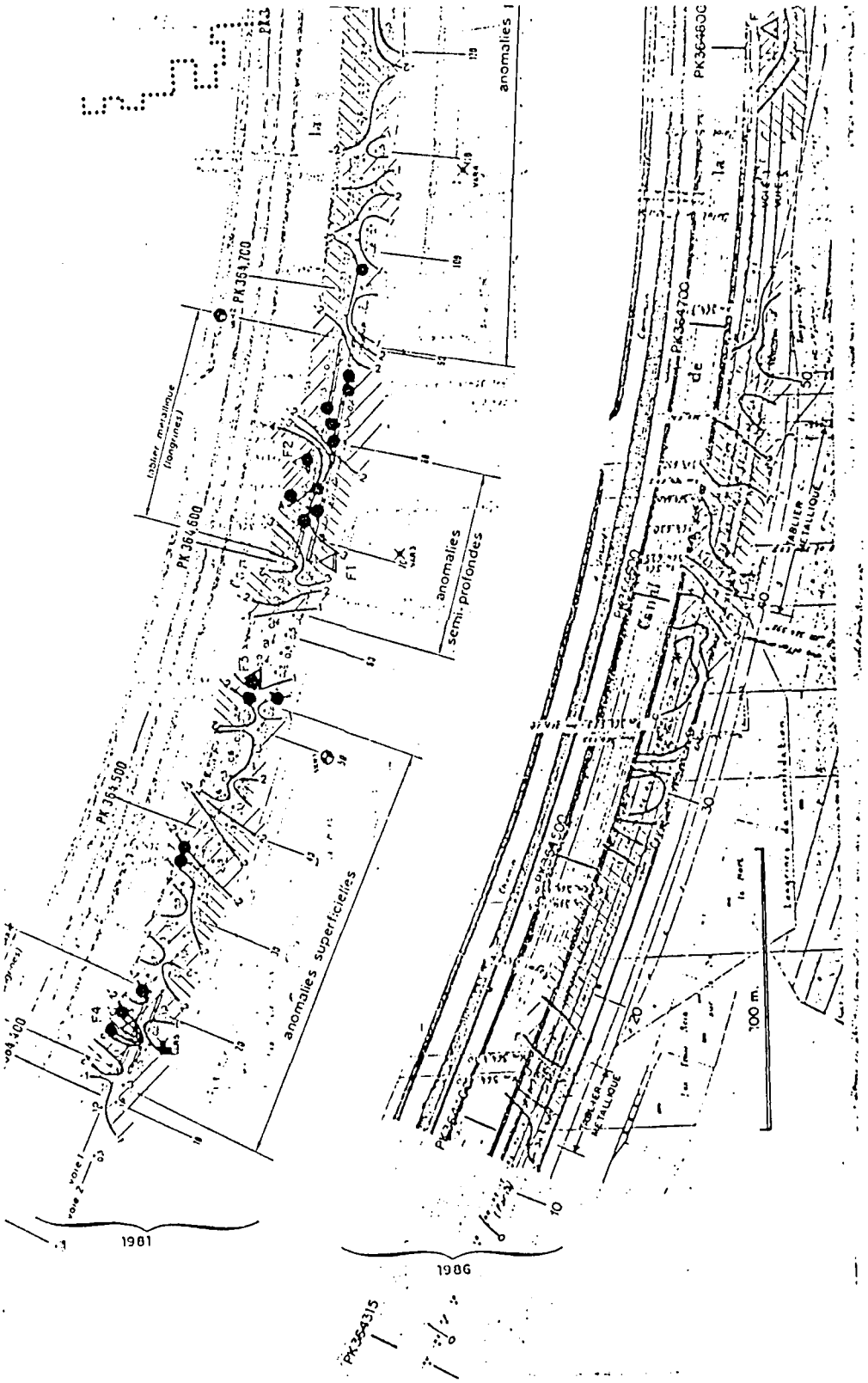

Figure 58. Varangéville railroad: 1981 and 1986 residual anomaly maps (a): western part (see legend on 58(b))

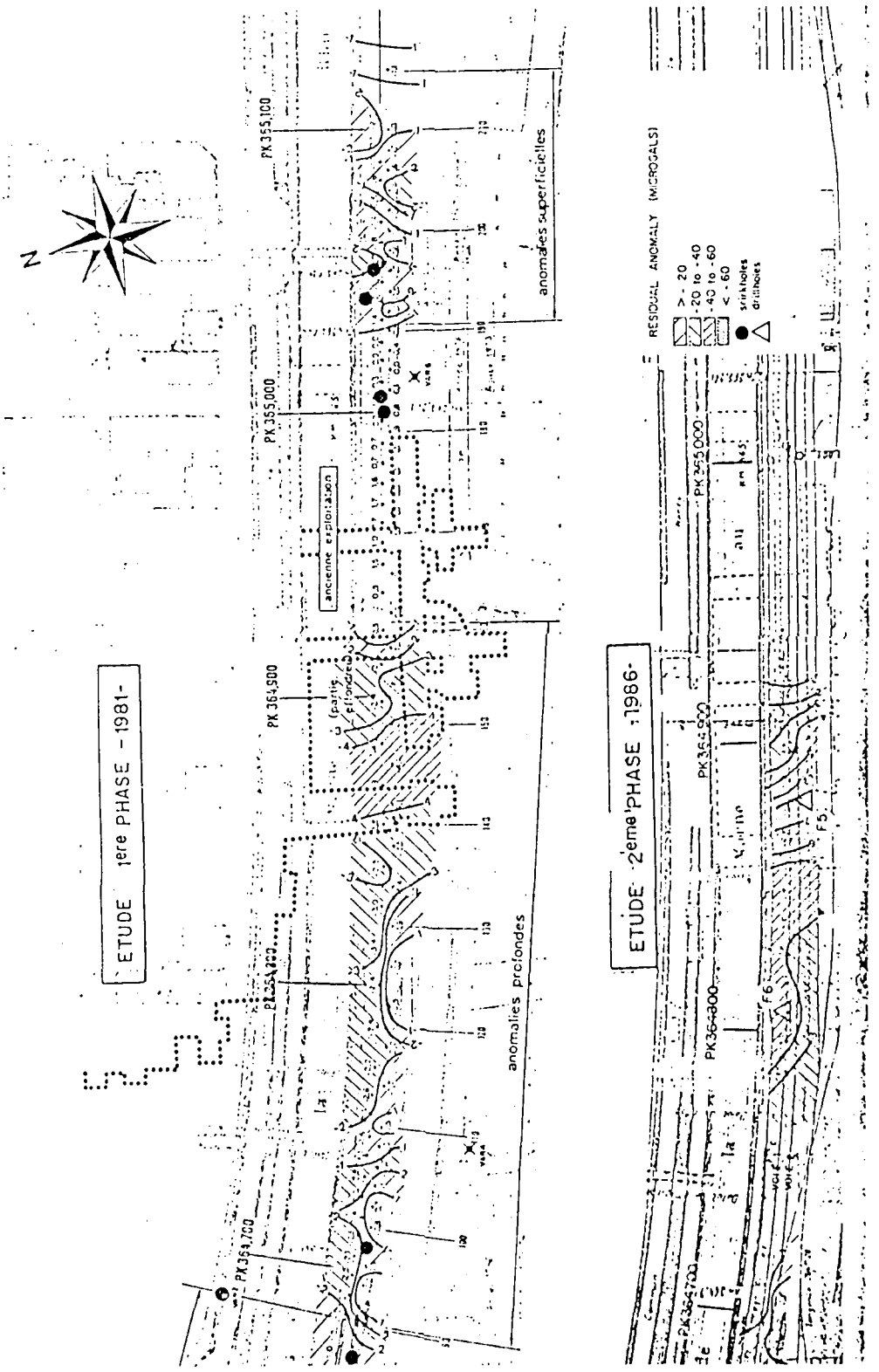

Figure 58. Varangéville railroad: 1981 and 1986 residual anomaly maps (b): eastern part

158. The corresponding gravity profile for the south track is shown at the top of the "difference" profile, figure 59, with anomalies reaching -100 to -120 microgals around the distance points 360.150 to 360.670. After the drilling which leads to this "initial" model, about 3,000 cu.m of cement grout were grouted in this section. The comparison between this theoretical profile and the one measured after grouting shows that :

+ the grouted zone probably extends on a transverse width of about 50 m
+ grouting is insufficient between 364.590 and 364.640, and that the lack of grout is in the order of 500 cu.m.

159. Results, 1982 drill holes.

Drill hole F4 is located in a critical part of anomaly (a) defined above.
Drill hole F3 is on the western edge of anomaly zone (a)
Drill holes F1 and F32 are in the main part of the anomaly zone (b).
These holes were drilled with a percussion up-hole hammer, with water flushing. Pressure on the tool was maintained constant and the following parameters were recorded during drilling (with a Lutz recorder) :

- instantaneous rate of drilling (in meters/hour)
- reflected percussion, as measured by an accelerometer fixed to the up-hole hammer.

160. After completion of drilling, a gamma ray was run. The Lutz parameters can generally be interpreted as follows:

Voids, open fractures, loose fill: high drilling rate (often over 500 m/h)
Clay filled fractures: high drilling rate, low reflected percussion
Slightly fractured or weathered rock: medium drilling rate (50-100 m/h), variable reflected percussion
Hard rock: low drilling rate (10-20 m/h), high reflected percussion
As an example, log of drill hole F1 is supplied (Figure 59(c)). The interpreted cross-section follows :

0 to 3.2 m	: fill (drilling rate is not significant, as a 94 mm casing was first installed, before pursuing with a 64 mm tool)
3.2 to 8.0 m	: weathered dolomite, with a very loose zone at the base. The gamma ray clearly shows the upper and lower limits of the dolomite

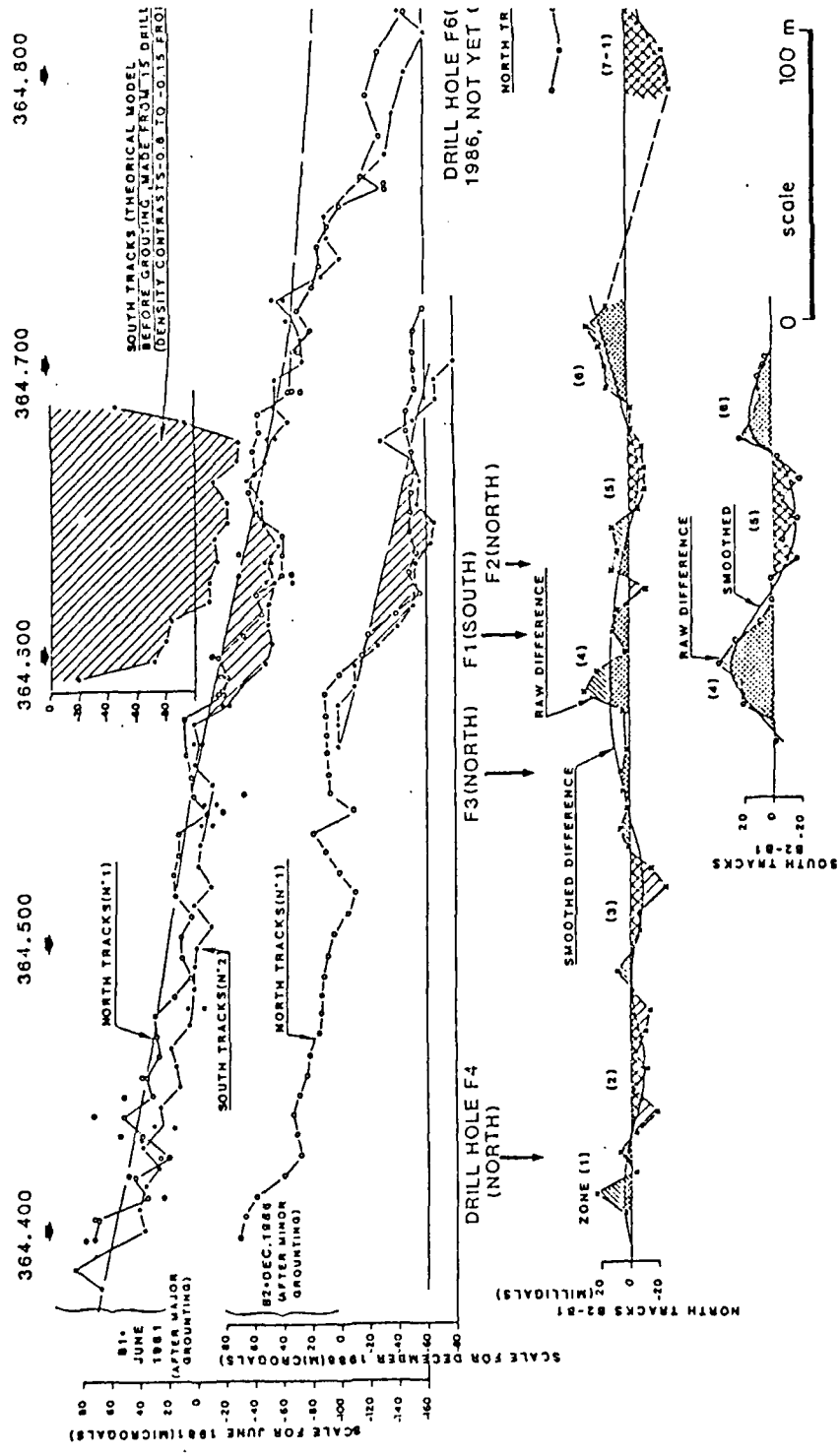

Figure 59. Varangéville railroad: 1981 and 1986 Bouguer and difference profiles
(a): western part

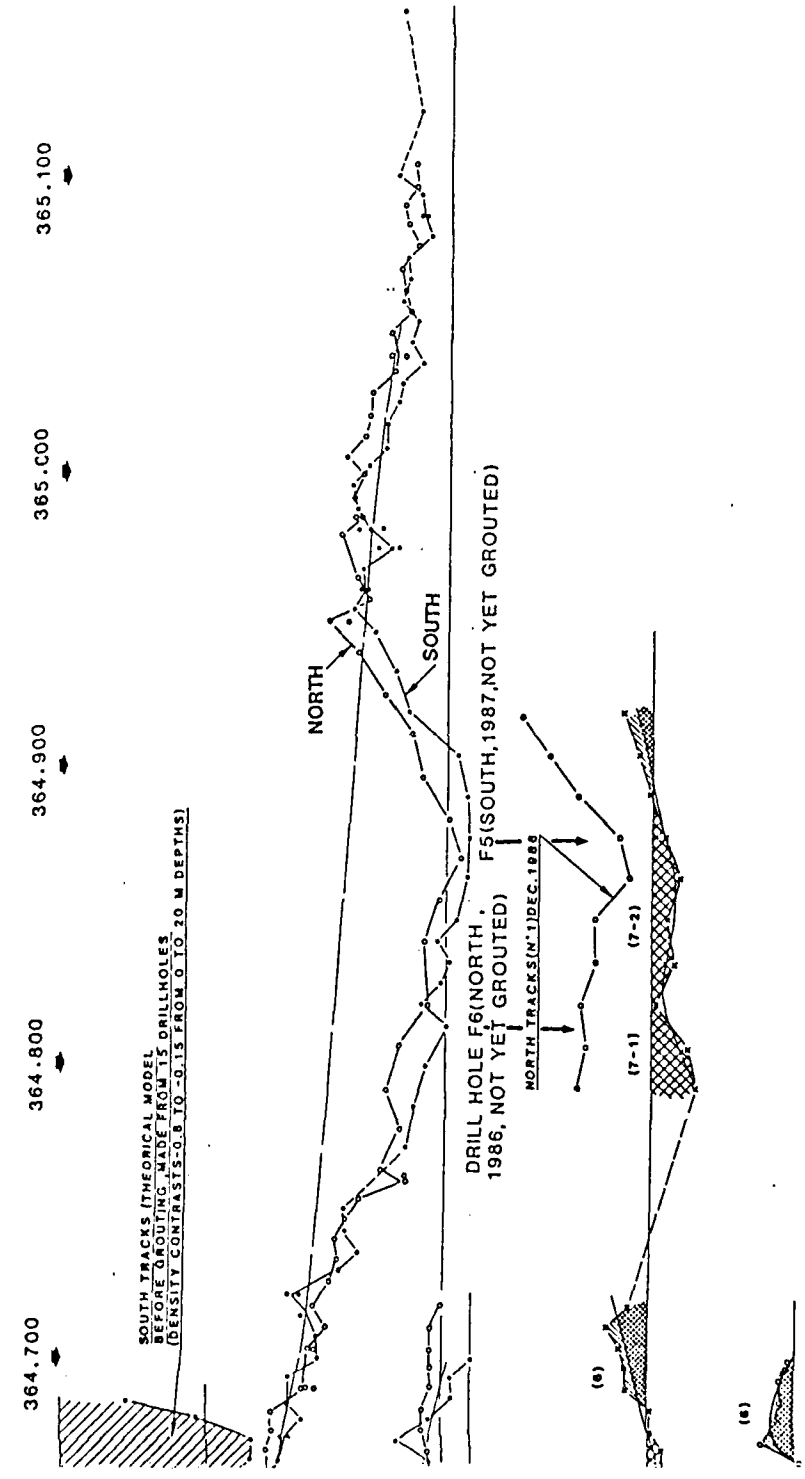

Figure 59. Varangéville railroad:981 and 1986 Bouguer and difference profiles
(b): eastern part

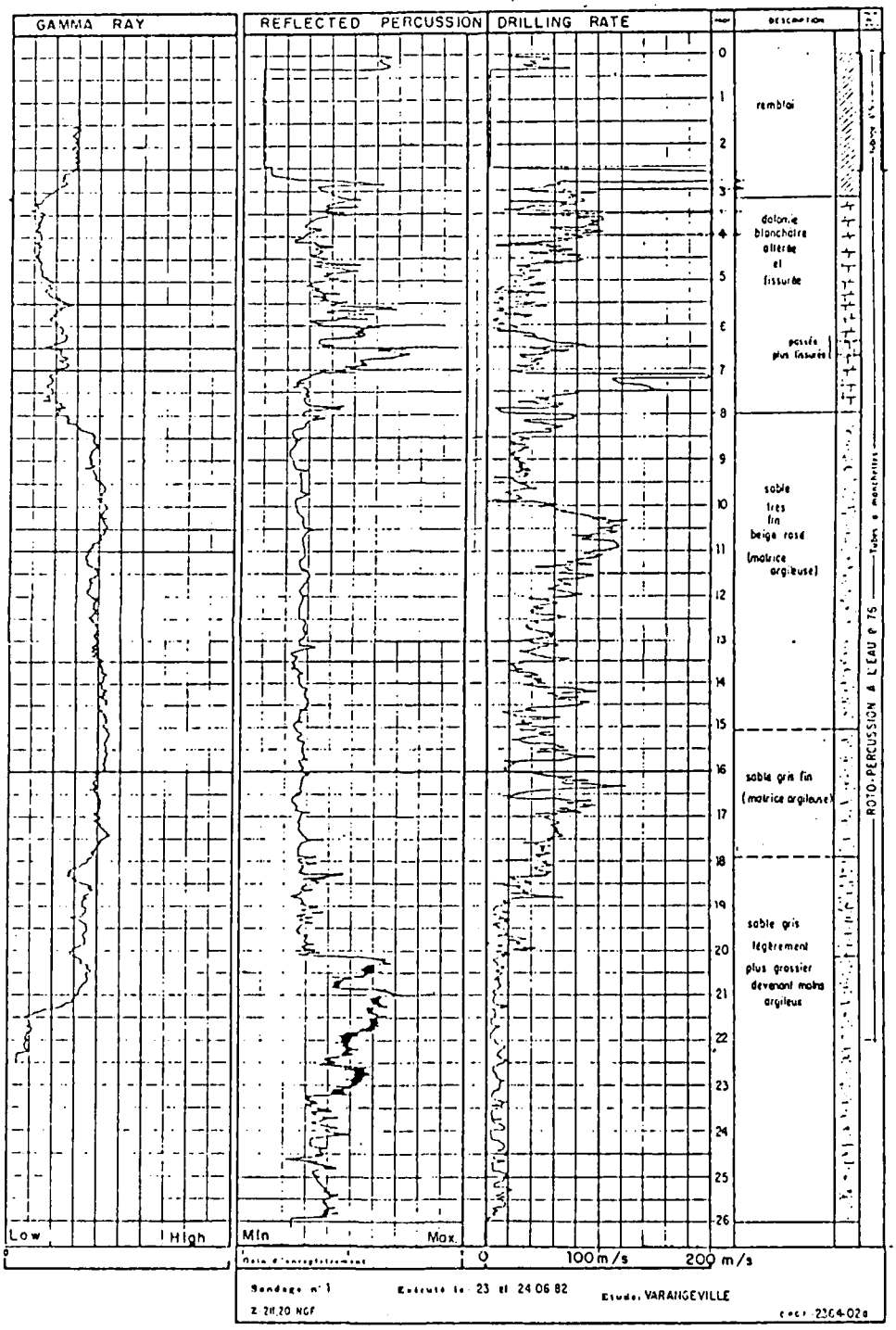

Figure 59(c): Varangéville railroad, drilling rate during drill hole F1

8.0 to 20.0 m : clayey sand or siltstone

After 20.0 (up to 26.0 m): hard siltstone or sandstone (without clay after 22 m)

The 4 drill holes found various loose zones, but not real voids. The probability of sink-holes can be appreciated by examining the cumulative ticknesses of zones where drilling rate exceeds 100 m/hour :

Table 19 : Varangéville railroad: 1982 drilling results

Drill hole		Total thickness	Gravity anomaly (microgals)
F4	7.4 m between 0 and 7.6 0.4 m " 22.3 and 22.7	7.8 m	-32
F3	4.5 m " 0 and 5 1.0 m " 6 and 10.5 2.3 m " 13.8 and 26.7	7.8 m	-6
F1	3.6 m " 0 and 4 0.4 m " 7.2 and 7.6 0.9 m " 10.3 and 17	4.9 m	-35
F2	3.5 m " 0 and 5.0	3.5 m	-44

161. The depths at which these loose zones were found confirm micro-gravity modelling, with loose zones mainly in the first 10 meters. However, no clear correlation is seen between the values of the gravity anomalies and the drilling results. We know from experience (see Civaux nuclear power plant in case history section) that in karstic zones, good correlation is obtained between microgravity and drilling results only when at least 15-20 drill holes are available. Following this drilling campaign, limited grouting (in the order of a hundred cu.m) was made at the end of 1982, using these holes.

162. Results, 1986 microgravity survey and comparison between the two surveys. This repeat survey confirms the general results of the first survey. On the lower part of figures 59(a) and (b), a residual map is plotted. The same regional was used as for the first survey. The three anomaly zones (a), (b) and (c) are clearly seen (zone (d) was not resurveyed). The comparison between the two microgravity surveys is shown

on figures 59(a) and 59(b) (specially prepared for this report). In the upper part of the figure, the Bouguer anomalies along both tracks for the 1981 survey are shown, overlaying the measurements made in 1986. The repeat profiles are very similar (even for certain small details, such as the small negative peak at 364.540 on the north track). The lower part of the figure shows the substratum between the two surveys (1986 minus 1981). Over the raw difference curves, we have plotted a smoothed difference curve.

163. Along the north track, several zones show out (note: "increase" means "values becoming more positive" ; "decrease" means "values becoming more negative").

1) 364.400 to 364.425: increase of about 10 microgals (this zone has been grouted through hole F4 at the end of 1982)
2) 364.435 to 364.475 } these two parts of anomaly zone (a) seem to have
3) 364.500 to 364.525 } decreased by 10 to 20 microgals, by reduction of previous positive zones
4) 364.535 to 364.640: variable increase, averaging 10 microgals (this zone has been grouted at the end of 1982, through holes F1, F2 and F3)
5) 364.650 to 364.675: decrease of nearly 10 microgals by extension towards the east of the main part of negative anomaly (b)
6) 364.685 to 364.720: increase of 10 microgals
7) 364.790 to 364.875: decrease of deep negative anomaly (c) by 10 to 30 microgals, suggesting that the cause of this anomaly is "moving up".

164. Along the south track, the repeat survey was shorter. However, the following features are confirmed:

+ 364.575 to 364.610: "positive" zone (4) seen along the north track is confirmed, with an increase of about 20 to 30 microgals (grout through F1)
+ 364.625 to 364.660: confirmation of decrease in zone (5) (-15 microgals)
+ 364.660 to 364.700: confirmation of increase in zone (6) (+10 to +15 microgals).

165. Detailed modelling of two incomplete lines is not easy. However, from the subtracted profiles, it is possible to infer approximate maximum depths at which changes have occurred. For above mentioned positive zone (1)

along the north tracks, depths would be less than 5-10 m (smoothed curves). Note that the grouting in hole F4 was made for the top 10 meters. For the negative zones (2), (3) and (5), depths of density reduction are also less than 5-10 m. For positive zone (4), as clearly seen on the south tracks, depth is less than 10 m. In fact, grouting was made at F1, for the top 10 m, as for drill holes F3 and F2 on the north tracks. The small positive zone (6) is difficult to explain, unless one supposes that the effect of grouting in 1982 extended to (6) through (5), and that after 1982, a sink-hole sector has developed in (5), separating positive zones (4) and (6). For the major negative increase (zone (7) along the north track), the difference profile suggests a cause about 20 m deep, while the 1986 profile suggests a depth of approximately 25 m for the total anomaly.

166. Results, 1987 drill hole survey. Two new drill holes have just been drilled up to 30-31 meters (F5 and F6, locations on lower part of map 3038-02). These two holes found soft zones (drilling rate over 100 m/h) at the following depths.

Table 20 : Varangéville railroad: 1987 drilling results

Drill hole		Total thickness	Gravity anomaly
F5	8.2 m between 0 to 8.2 m	8.2	
	1.7 m " 9.5 and 11.5		
	0.8 m " 13.2 and 14.5	12.2	-80 µgals (1981)
	1.5 m " 16.4 and 17.8	4.0	
	0.3 m " 18.9 and 19.4		
	0.2 m " 20.5 and 21.7		
F6	5.8 m " 0 to 5.8	5.8	
	0.7 m " 8.0 and 9.5	13.3	-60 µgals (1981)
	6.4 m " 12.4 and 18.7	7.5	-80 µgals (1986)
	0.4 m " 20.5 and 21.6		

The thicknesses of loose zones are much greater than for drill holes F1 to F4 , which is compatible with the gravity anomalies :

	Total loose thickness	Gravity anomaly
Average F1 to F4	6.0 m	-29 (1981)
Average F5-F6	12.75 m	-80 (1987)

The depth of occurrence of density anomalies (7.1) and (7.2) as modelled : 20-25 m, compares well with the deeper zones found in the drill holes (particularly at F6). These loose zones (7.1 and 7.2) are located in the "grès à roseaux" sandstone layer, between 8 and 21 m, while the underlying silstones seem compact.

167. Conclusions on the Varangéville surveys. The two microgravity surveys show that, despite several series of grouting campaigns, several zones (where sink-holes have already occurred) still show negative anomalies. These negative anomalies have "decreased" by 20 to 40 % during the past five years while limited grouting shows up by a positive "increase". Extra grouting in limited zones could be planned with the help of microgravity results. In the western part of the survey, the anomalies are located in the top 10 meters (fill and "Beaumont" dolomite). In zone C (anomalies 7.1 and 7.2), where a wide negative anomaly seems related to old salt mines, the negative amplitude has been accentuated by up to 30 microgals (probably over 30 % of 1981 value). Causes are mainly located between 8 and 20 m depths. However, no sink-holes have yet been observed in this east section.

It has been suggested to SNCF (French railways) that the section between 364.750 and 364.900 be carefully monitored, and that in addition, a third repeat survey be made in 1988.

168. These surveys show the possibility of using repeat microgravity surveys to monitor active changes in sink-hole areas, as well as the effect of grouting, and can be used to complete other monitoring techniques. such as surveying and stress measurements.

Other repeat surveys

169. Apart from the above described Varangéville case, which includes zones where repeat measurements controlled grouting and others where they show development of sink-holes in gypsum, CPGF has conducted several repeat microgravity surveys. They all aimed at observing changes in active karsts (particularly in gypsum). We should mention the Echaillon canal (in Savoy) where a first profile showed anomalies reaching -800 µgals (our record!). A year later, some of the anomalies had reached -850 µgals.

170. In another field, the work of Fajklewicz (1983) deserves a mention. He carried out repeat microgravity surveys in mines, in order to predict rock bursts.

171. The extensive repeat surveys carried out by J. Fett (unpublished) in California, in order to predict earth movements related to earthquake prediction, should also be mentioned.

PART 4: COMPARISON OF MICROGRAVITY WITH OTHER GEOPHYSICAL TECHNIQUES

Detection of cavities by other geophysical methods.

172. Detection of cavities by resistivity and electromagnetic methods. We will exclude radar, which has already been studied extensively for tunnel detection, for the U.S. orps of Engineers (Ballard, 1983). D.C. resistivity has often been tried, including at CPGF (Lakshmanan, 1963), because it is an easy-to-use method. However, its use in urban environments is generally impossible or very difficult, because of stray currents and of various conductors such as pipes or cables.

173. In addition, it has been shown (Habberjam, 1969) that the maximum depth at which a resistive sphere can be detected is very small ; the top of the sphere has to be buried at less than a radius under the surface. In the case of a Wenner array, with an electrode spacing of "a", above an infinitely resistive sphere of radius R, whose center is at a depth of z meters, the following ratios of $\frac{\rho app}{\rho_0}$ will be obtained.

Table 21: Effect of resistive sphere

z/R	Optimum a/R	$\frac{\rho app}{\rho_0}$
1.25	1.04	1.58
1.50	1.20	1.23
1.75	1.28	1.14
2.00	1.36	1.11
2.25	1.38	1.07

174. Considering that at least a 10 % change in apparent resistivity is necessary to obtain confident results, a sphere of 1,7 m radius should be at an axial depth of less than 3,4 m (corresponding gravity anomaly -24 µgals, for a density contrast of -2.0). For a sphere of radius 2.29 m (volume 50 cu.m), z < 4.6 m ; corresponding gravity anomaly -32 µgals).

175. Of course, if we need a 20 % change in resistivity, depth conditions become much more severe. Some tests have been made (Cabillard et al, 1977), using a combination of down-hole and surface electrodes, depth of penetration approaches the depth of the hole, but the radius investigated around the hole is not very large. Inductive (EM or AMT) methods have also been tried, but also have the same type of depth limitation (Gabillard and Dubus, 1977).

176. Detection of cavities by seismic methods. A test of seismic reflection over known, semi-horizontal, underground limestone quarries has been made (Frappa et al, 1977) ; the method is operative in certain cases. has occasionally used different seismic methods for locating large, open, semi-vertical cracks. Such cracks would give a sharp gravity anomaly, but unfortunately, very narrow and hardly exceeding the width of the crack or the fractured zone itself. Seismic refraction, with profiles perpendicular to the cracks, can be used. In order to ensure a regular 3-D coverage, a specific technique, the SISMOBLOC-CPGF, has been developed. The SISMOBLOC-CPGF (P. Lechat et al, 1971) includes :

- a regular grid of geophones
- two fixed shotpoints, as shown in the following sketch.

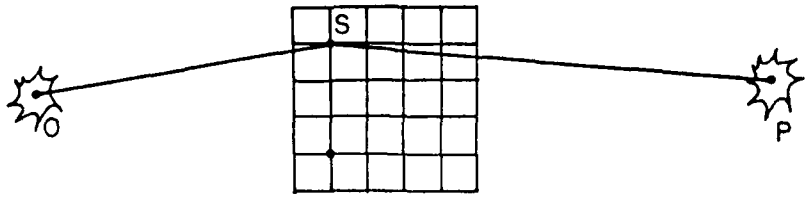

Figure 60. Schematic "SISMOBLOC CPGF"

177. The two fixed shotpoints can be located at the bottom of drill holes. Other small shotpoints can be distributed at different points of the grid. Processing of the OS and PS times first separates vertical and horizontal times, yielding:

- a delay map
- a "bedrock" velocity map

Introducing velocity laws computed from the other shotpoints, dalays can be transformed into depths to one or two refractors.

178. Case history - Corbeil les Tarterets. At Corbeil, near Paris, for a high-rise building project, a specific 3-D refraction technique, the "SISMOBLOC-CPGF" was used to locate large vertical cracks in tertiary limestone along the slopes of the Seine valley. These cracks are parallel to the valley, are about 0.5 to 1 m wide and are partly filled with clay. The corresponding gravity anomaly being small and particularly narrow, seismic refraction was successfully tested. In this case, the layout was selected so that raypaths had to cross the cracks.

179. Measurements were made with geophones along a 5 x 5 m grid, set out on the weathered bedrock, after overburden had been removed. The enclosed maps show:

- delay times (subvertical)
- bedrock velocity (subhorizontal)

The most significant correlation between seismic results and geotechnical properties (measured by drilling rate and by pressiometer tests in about 20 drill holes) is seen with the bedrock velocity where the rays have to cross the cracked zones. It appears, in the case of this tertiary limestone, that rock quality was sufficient for shallow foundations when the seismic velocity exceeded 1,600-1,700 m/s. Zones where velocities were less that this limit (particularly towers T2 and T3) had to be grouted. The east-west fractured zones show out well on the velocity map. The higher delay times have a certain relationship with the low bedrock velocity (except for tower T4). With an average overburden velocity close to 1,000 m/s, the delay times are similar to the depth in meters of the seismic "bedrock" (less factured limestone).

Grout control by other geophysical methods.

180. Resistivity methods. During a Ministry of Industry funded project in 1983, CPGF tested the use of resistivity methods before and after grouting (CPGF, 1983), making the measurements inside the grouting drill holes equipped with the usual "tubes à manchettes"(1). Various combinations of electrodes were used. The best (or at least the least bad!) was achieved with the following layout :

(1) The French expression is used all over Europe. It defines the rubber sleeved tubes used for grouting under pressure between packers.

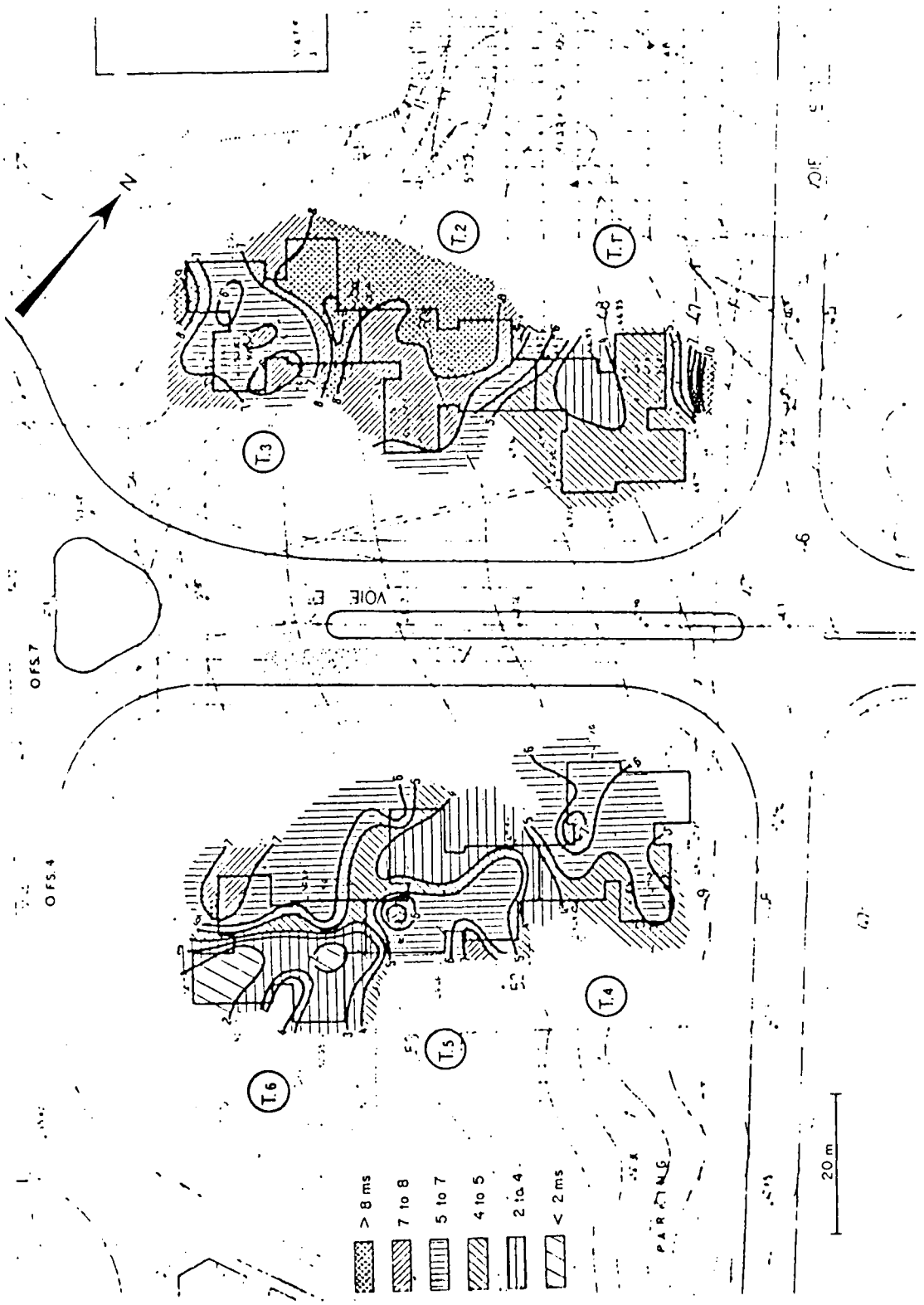

Figure 61. Corbeil-les-Tarterets - SISMOBLOC-CPGF - Delay times

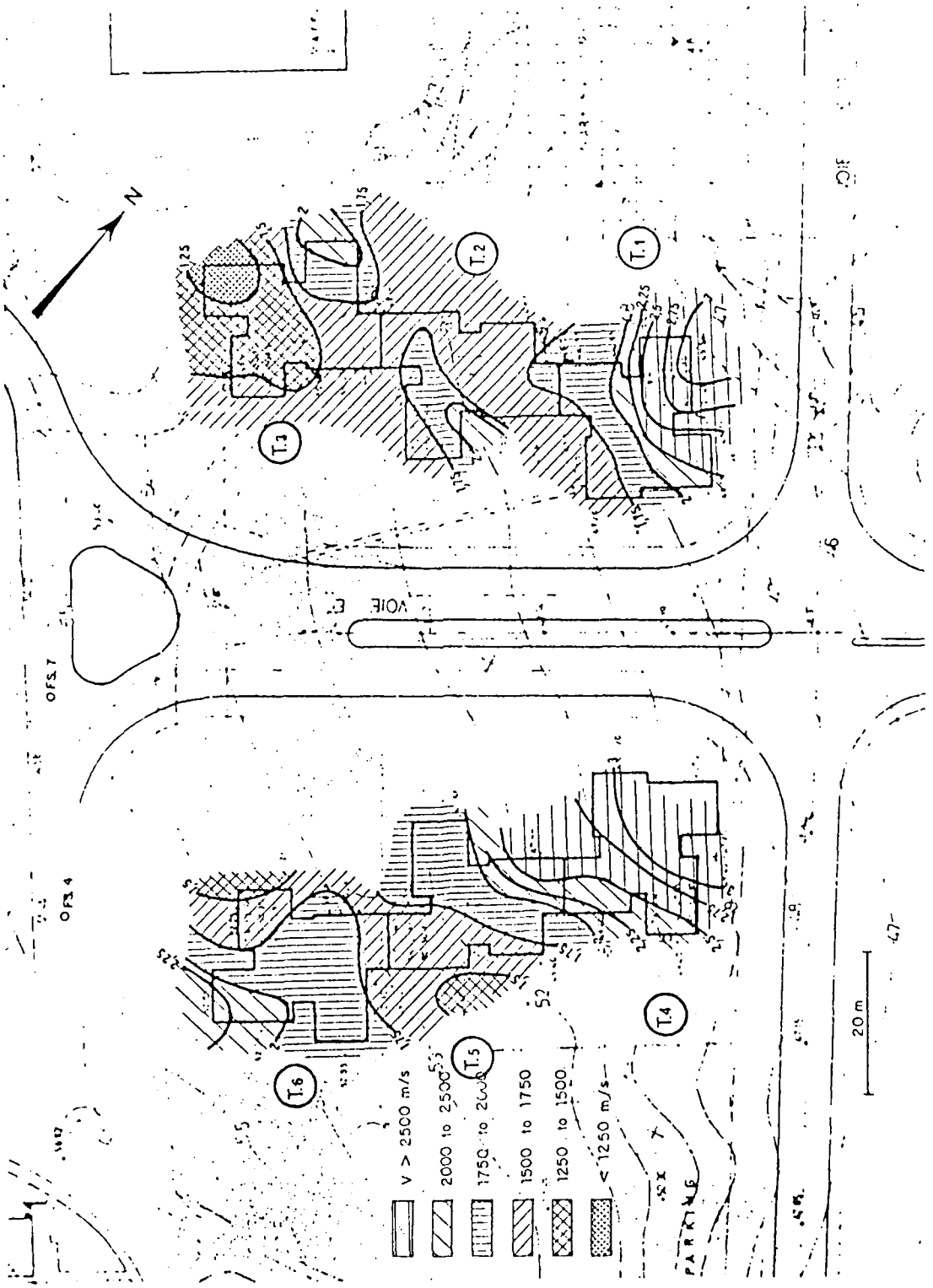

Figure 62. Corbeil-les-Tarterets - SISMOBLOC-CPGF - Refractor velocities

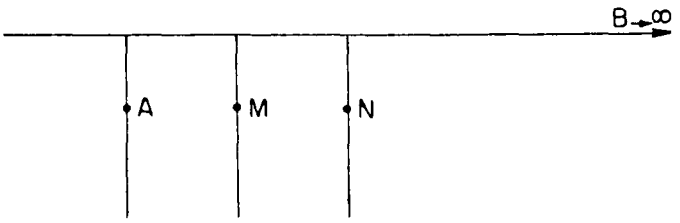

Figure 63. Resistivity between drill holes

A and B are the current electrodes (B is at a semi "infinite" distance, and is fixed),

M and N are the potential electrodes,

A, M, N, are simultaneously moved down three holes with 2-3 meter horizontal spacing. Significant changes of apparent resistivity were observed, with an increase with cement grout, and a decrease with silicate grout.

181. Seismic tomography. Very interesting results have been recently achieved by CPGF during repeat measurements made for the city of Bordeaux, along the future large Cauderan-Naujac waste water collector. The following is an abstract of a paper to be read shortly at a symposium in Bordeaux (Erling, Bertrand and Kutkan, 1987). In annexure 3, we supply a preprint of a general paper on seismic tomography to be read shortly at Denver (Bertrand, Herring, Lakshmanan and Sanchez, 1987) which summarizes the methods used at CPGF for acquisition and processing of curved ray seismic tomography, and gives a set of examples ranging from Busanga dam (Zaire, 1970) to Turkwel dam (Kenya, 1987) in various applications to foundation assessment.

182. Case history - Cauderan-Naujac tunnel. Along the Cauderan-Naujac waste water tunnel under construction at Bordeaux, a section crosses a zone of karstic limestone, where grouting prior to tunnelling is partly necessary. A set of seismic tomographies was made, some of which were repeated after grouting. The tomographies were made with a mini-Sheargun (42 mm) which could use the grouting holes directly, and with a mini-Sismopressiomètre. Comparison between the two tomographies of of figure 64 shows that between 8 and 9 m (which is the grouted section), velocities are generally increased from 1,900-2,100 m/s to 2,000-2,400 m/s. A limited zone near drill hole F38

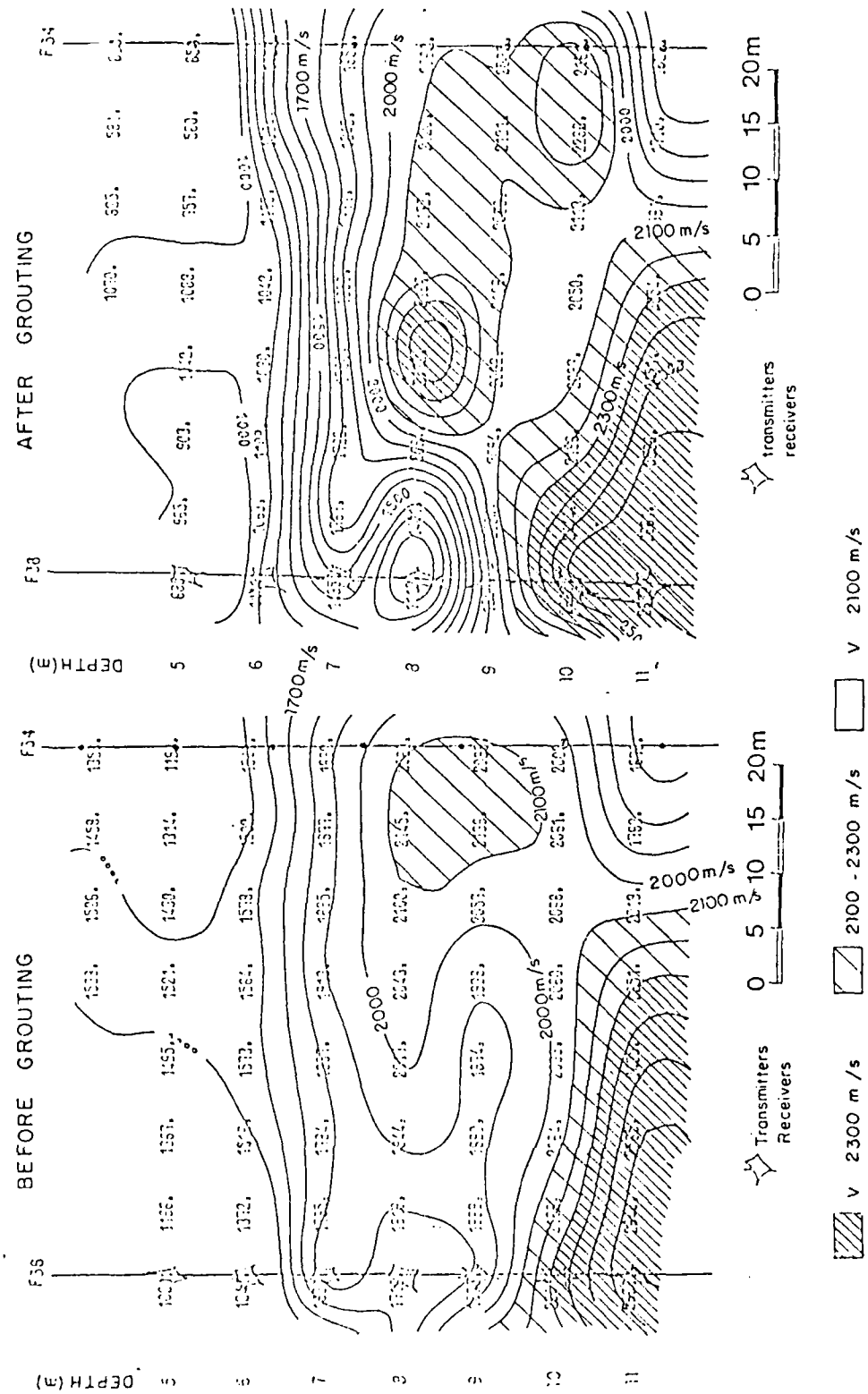

Figure 64. Cauderan-Naujac tunnel - Seismic tomography
Before and after grouting

(at 8 m) may however have been fractured and not completely grouted. Its velocity drops from 1,710 to 1,120 m/s.

183. Another seismic technique was also used at the same site. We compared the shape of the signals received before and after grouting (see left of figure 65). The high frequency content is increased as shown by the centre figures, which show the amplitude spectra. The 0-200 Hz energy (S-wave) does not change, but an appreciably strong energy in the 400-800 Hz appears (P-wave). We also divided the spectrum after grouting by the spectrum before grouting (see right figure), which shows ratios of about 2 for frequencies above 400 Hz (instead of 1 below 400 Hz). When similar processing was made at depths of 12 m outside the grouted zone, no frequency changes were observed. It should be noted that frequency comparison should preferably be made between 3 holes in line (one transmitter, 2 receivers), to eliminate the effect of changes close to the transmitter hole. This has already been done, particularly on the Paris express metro test site (CPGF, 1983).

Down-hole logging.

184. Logging while drilling. After detecting by geophysical methods anomalies due to caves or other mass deficits, it is necessary to control evaluation by drilling. Our experience, and that of several main French clients, is that coring is not a satisfactory method: it is expensive and mainly, when the anomalies are not due to open cavities , but to fractured zones, filled cavities or caved-in cavities, core recovery is very poor and correct interpretation is difficult. Static or dynamic penetrometer tests (or S.P.T.) can be used in certain cases, but are soon blocked by rock.

185. Twenty years ago, in the Paris district, underground quarry evaluation was often made by fast destructive drilling (with an up-hole hammer) and measuring drilling rate on each section of 25 cm, with a chronometer. This primitive technique has been superseded (for the last 10 years) by Logging While Drilling (L.W.D.) or Measurement While Drilling (M.W.D.). These petroleum techniques have been adapted to the public works and construction market by two main French manufacturers: Lutz S.A. (the Lutz recorders) and Soletanche (the Empasol system). Examples of applications by CPGF have been published by Erling, Lakshmanan, Rougé, 1981 and by Lakshmanan, 1983, while the manufacturer's points of view were given by Lutz (1978) and Richez (1981).

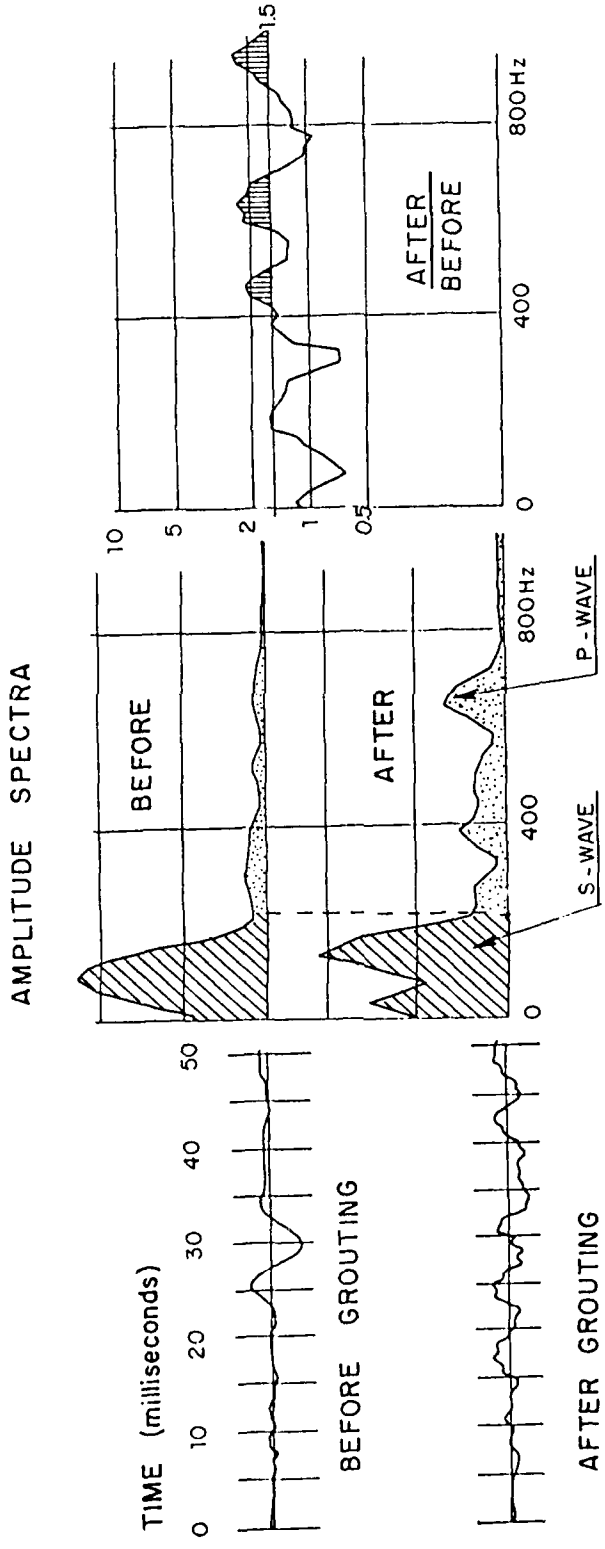

Figure 65. Cauderan-Naujac tunnel-Comparison of signals and amplitude spectra, before and after grouting

186. The main parameters measured are:

- drilling rate
- reflected percussion (a Lutz specialty)
- pressure on the tool (this should be kept as constant as possible by the driller
- water pressure (when the hole is water-flushed)
- torque (in rotary drilling).

187. These techniques are now really standard practice in France. Electricité de France, the French State Power Board, when investigating nuclear power plant foundations, generally drills 10 destructive holes, for one cored hole. The French railways's (SNCF) position is described by Erling and Roques (1983). The official recommendations for building design are mentioned further on chapter 195. Another opinion on the subject was expressed in a paper entitled "New Reconnaissance Techniques", written by a working group of the French National Committee on Large Dams, chaired by the author of this report (1982).

188. Examples of records are given in the case history section, as well as in the English summaries of papers written in French (references section). Interpretation of L.W.D. is based on the following criteria :

Table 22 : Logging while drilling interpretation

Percussion drilling	Drilling rate	Percussion rate
Voids	>500 to 1,000 m/h	very high
Very fractured zones, filled quarries,	200 to 500 m/h	high
Collapsed underground quarries Clay filled fractures or karsts	100 to 500 m/h	low
Fractured zones	50 to 200 m/h	medium
Hard rock	10 to 20 m/h	high

Rotary drilling

	Drilling rate	Water pressure
Voids	Very high	low to nil
Very fractured zones, filled quarries,	high	low
Collapsed underground quarries / Clay filled fractures or karsts	high	high
Fractured zones	medium	medium
Hard rock	low	medium to high

Interpretation is completed by observation of cuttings and, occasionally, by the use of gamma ray logging.

189. Correlation between gravity interpretation and L.W.D. results is shown on figure 66, which comes from the Civaux nuclear plant survey. Ordinates are the relative densities $\Delta\sigma$ computed by 3-D gravity inversion. Abscissas are the cumulated thicknesses of zones where drilling rate exceeds 100 m/h. General regression gives a density deficit of 0.036 gm/cc in these zones. However, regression on the points marked by crosses (except 2 of them) which corresponds to a particular zone, gives a density contrast of -0.21 gm/cc.

190. Conventional logging. When drilling through voids, fractured zones, etc ..., it is often difficult to keep the hole open, for subsequent logging. Therefore, these techniques have not become popular in France.

+ Resistivity and spontaneous potential: are seldom used, for the above mentioned reason; also, the holes are not often water filled.
+ Gamma-ray: is more often used as a geological mapper, as the usual 1" tools can be used in the smallest PVC casing. For example, in chapter 32, describing the important Varangéville case history, drill hole F1 log is supplied. The geological limits between delomite (lower activity) and clay (higher gamma activity, due to the isotope K-40) show out quite well.
+ Gamma-gamma: CPGF and other searchers such as the L.C.P.C. (Central Public Works Laboratory) had placed great hopes in the method, which evaluates down-hole densities, for controlling microgravity surveys. However, it is dangerous to put this tool down an uncased hole in fractured, unstable formations. Along the new "Paris-Atlantique" TGV fast railroad, CPGF recently had the L.C.P.C. carry out a test in PVC cased holes (cavity location in

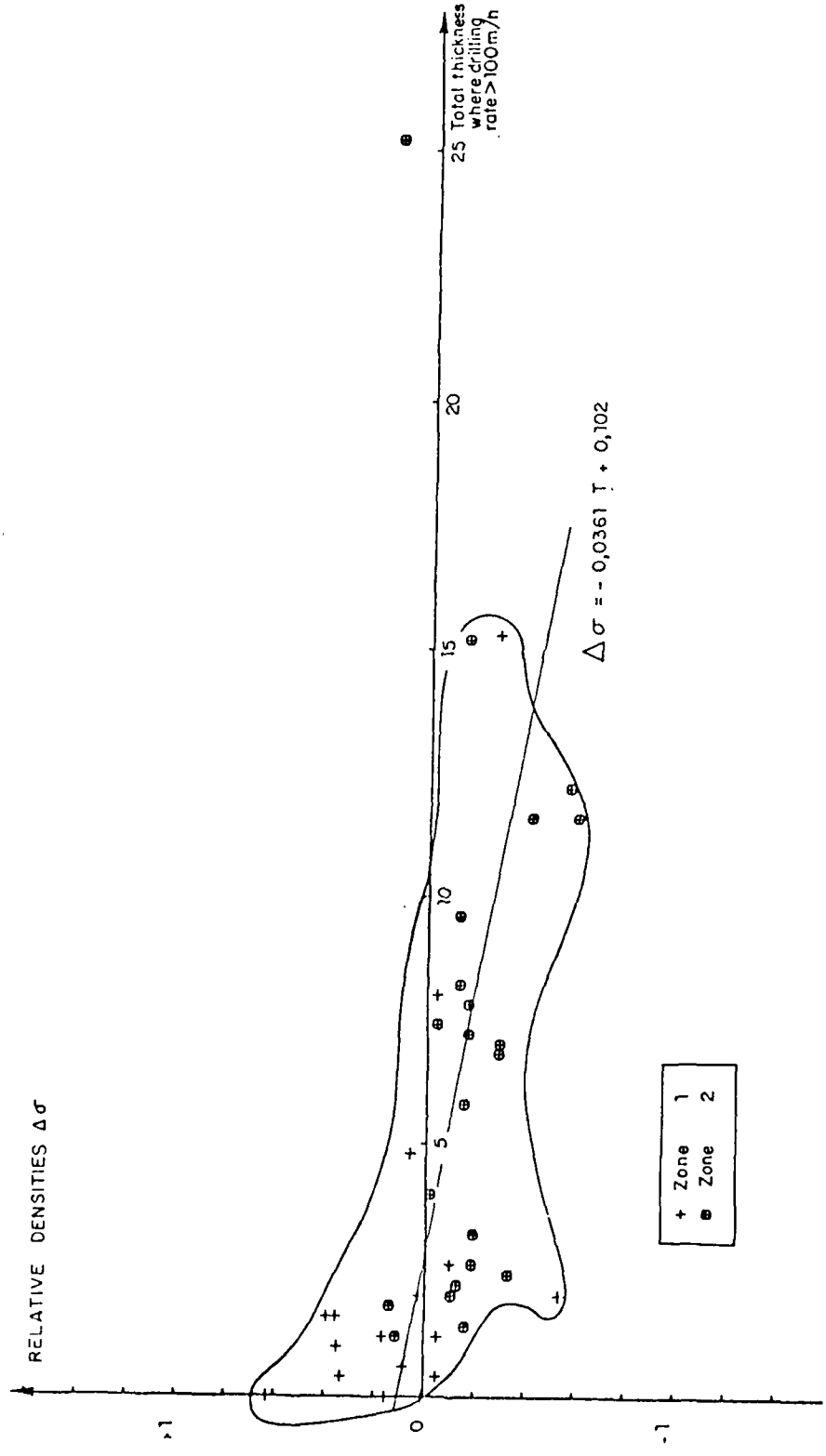

Figure 66. Civaux nuclear plant. Correlation between computed densities (10-20 m sheet) and drilling results

chalk). The sonde has 2 receivers and processing can eliminate the effect of variations of hole diameter, but only to a certain extent (Bru et al, 1983 and Vashkowski, 1983). During this test, it appeared that densities were only computed validly in the sound rock sections, while in the fractured zones, the "hole effect" could not be corrected, due to oversize hole diameter. The enclosed figure 67 shows:

- to the left: natural gamma log (clay deviates to the right)
- in the middle: $\gamma\gamma$ log, full line = far receiver, stippled line = close receiver ; the interpreted densities (γh) are the figures between the γ and the $\gamma\gamma$ ray logs (varying between 2.0 and 2.4 gm/cc).
- to the right: neutron-neutron log with 2 receivers ; between the $\gamma\gamma$ and the NN logs are the interpreted water content values (VV) which vary from 15 to 55 %.

+ Down-hole seismic logging: Point by point, down-hole seismic measurements are used in France for public works investigation, mainly for the evaluation of fracturing in major rock foundations (or stability of large cuts), but not really for cavity investigation. Continuous sonic logging is generally excluded, as it needs mud filled holes.

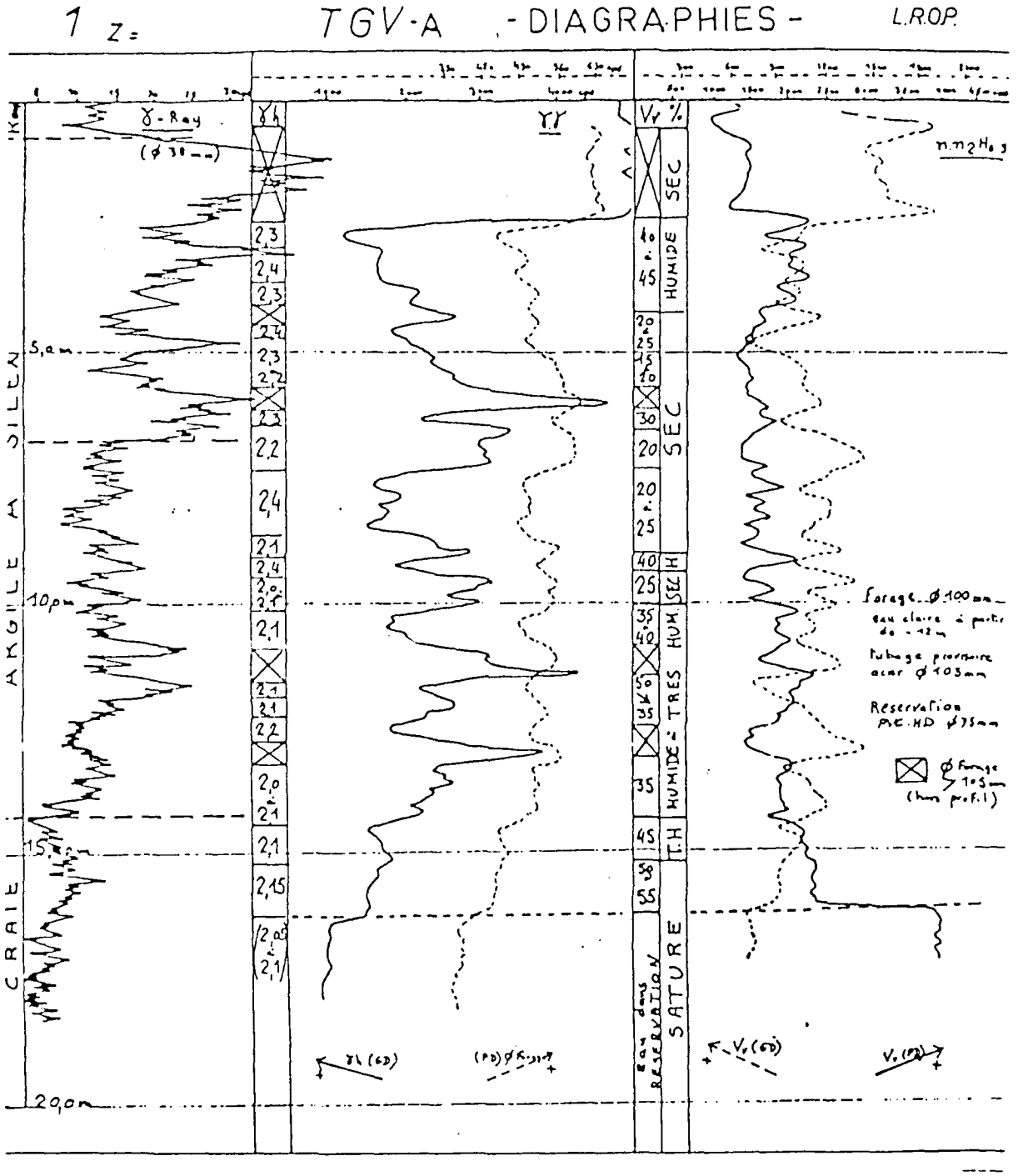

Annexe n° 2

Figure 67. TGV Atlantique fast railroad: gamma-gamma density logging

PART 5: COMPARISON OF FRENCH CURRENT PRACTICE WITH CAVITY DETECTION IN THE REST OF THE WORLD

Current French practice.

191. General. In part 1, para. 1 (historical background), we mentioned that "microgravity" had first been started in France, having been promoted by the author of this report at CPGF and by the late Robert Neumann at CCG.

192. A certain number of official documents confirm that microgravity has become common practice in many areas in France, and is officially recommended for locating cavities. Of course, it should be noted that France includes many limestone, chalk and gypsum areas, with extensive underground quarrying since the Middle Ages. Therefore, a large number of man-made voids are to be added here to karstic cavities, as they may exist in other parts of the world.

193. When an owner (whether private or public) wants to build a house or a building, he (or his architect) has to apply for a "construction permit" to the Ministry of Equipment and Housing. This Ministry can ask for proof that the site can offer sound foundation. Particularly, in certain areas subject to a risk of underground quarries, the applicant has to comply with the specifications set by the "Quarry Service" of the city or the "département" (France is geographically divided into 95 "départements"). A certain number of exposed cities (Paris, Caen) or "départements" (Nord, Yvelines, Maine et Loire, Gironde, etc ...) have such services. The specifications will include the need for a geotechnical survey and could state, for example:

- construction permit refused, project located over dangerous cavity,
- permit authorized, only if suitable soil improvement or special foundations be made,
- construction close to a dangerous zone, cavity limits not accurately known, proof of sound foundation to be made, by at least:
  - 2 drill holes for a small house
  - 2 to 4 drill holes + microgravity survey for a larger construction.

194. In addition to these formalities, the owner (except when he builds

for his own use) and the contractors have to contract an insurance policy. French insurance companies use the services of "Sociétés de contrôle" (certifying agencies) who give them technical assistance, and in particular for the control of foundations. Once the official demand for a geotechnical report concerning underground quarries has been made, the owner calls in a qualified soil mechanics or geophysical company. The geophysical company is quite often a subcontractor to a soil mechanics company. Quite often however, the architect, the contractor, the municipality and the "Société de contrôle" can be quite influential in making decisions as to the use of geophysical investigation, as opposed to drilling alone.

195. Official French recommendations (buildings). As seen above, geophysical investigation for buildings, and particularly for the location of voids, is never compulsory. Two official "recommendations" are however used as guidelines.

a) "Etude géotechnique et reconnaissance des sols", written by a group of eminent soil mechanics engineers, published by the "Presses de l'Ecole Nationale des Ponts et Chaussées", February 1983. The chapter concerning geophysical methods describes the uses and limitations of resistivity, gravity and seismic refraction surveys. Only gravity is recommended for "locating lateral changes in the structure of the sub-soil, when they are related to strong and localized changes in density (underground caves, trenches, tunnels, bomb craters filled with loose material".

b) "Recommandations sur le traitement des cavités souterraines et notamment des carrières" (quarries), Annales, I.T.B.T.P., n° 370, March 1979. This report, written by a group of soil mechanics engineers, geologists and geophysicists, describes the types of cavities found in France, the recommendable survey methods, and the methods of soil improvement.

Microgravity is reported as the most suitable method with, in certain cases, seismic reflection or refraction. When depth of cavities is less than 4 m, resistivity methods can be used. When the area to be surveyed is large, resistivity or seismic methods can be advised on the basis of reduced cost. When the area is inside city limits, gravity is generally the only valid method. The following grids are advised:

- general survey, large caves : 20 x 20 m
- localized survey, large caves : 7 x 7 or 15 x 15 m
- localized survey, small caves : 2 x 2 to 5 x 5 m

Some geophysical methods, using drill holes, are also mentioned (cross-hole seismics, hole-to-surface resistivity or seismic measurements).

196. Place of geophysics in France (buildings). Taking into account the above mentioned official "recommendations", we have noted that actual practice varies from one region to another. In the main carbonate and gypsum zones of the Paris basin and in the north of France, microgravity is quite regularly used, compared to all other geophysical methods which appear very rarely in the field of cavity detection. In the southern part of France, it is not yet so general. However, for small buildings or houses, owners often limit themselves to one or two drill holes (often destructive holes, drilled with an up-hole hammer drill, and more and more, with logging while drilling).

197. Case of public works. No rules or recommendations govern the need for geotechnical or geophysical investigation, except for road construction, where the Ministère de l'Equipement has published the following recommendations: "Recommandations pour la reconnaissance géologique et géotechnique des tracés d'autoroute", Ministère de l'Equipement, Laboratoire Central des Ponts et Chaussées, February 1967. The geophysical methods mentioned for road surveys are :

- resistivity
- seismic refraction
- microgravity, which is recommended for the detection of underground caves

198. Station spacing of 5 m is recommended. A rule-of-thumb limitation of the microgravity method: $h < 2d$, where h is the thickness of formations above the cave, and d the diameter of the cave, is mentioned in these recommendations.

199. The French railways (SNCF), who presently have an ambitious program of new, very fast railroads (TGV) construction, have unofficially expressed their policy in the field of void detection in the paper by Erling and Roques(1983). The part of this paper concerning geophysical investigation can be summarized as follows:

- resistivity cannot be used on existing railroads, due to stray currents,
- seismic methods are only applicable in certain cases ; seismic tomography can study detailed zones,
- well logging is only used in certain cases.

The main methods recommended by the authors are :

- microgravity, with grids ranging from 3 to 10 m, and special processing to compute density maps,
- destructive drilling, with "logging while drilling" (L.W.D.) ; the drill holes are often equipped with "tubes à manchettes" for subsequent grouting.

200. Another major promotor of public works, Electricité de France (EDF, the French state power board), has often ordered microgravity surveys, mainly for several nuclear power plants, such as Civaux (see references section of this report). In addition, this organization sponsorized the microgravity survey of the pyramid of Cheops (Montluçon and Lakshmanan, 1987).

201. Conclusions on void detection in France. As outlined above, geophysics and particularly microgravity, has become regular practice in many sections of French building construction and public works. However, despite general "recommendations", no geophysical investigation can be made compulsory. From one region to another, and from one client to another, the relative quantities of microgravity surveys, as opposed to drilling, can vary very considerably. On the whole, the number of microgravity stations measured annually in France is in the order of 10,000. At least four organizations (three geophysical contractors, one public) offer professional microgravity services.

Available information on the rest of the world

202. Rest of the world, excluding the United States. This chapter is not an exhaustive enquiry on the state of the art of microgravity in the rest of the world, but summarizes the impressions and experience of CPGF's engineers.

203. To our knowledge, South Africa is apparently the only country where microgravity is standard practice. It is used (and asked for by local authorities) for systematic mapping of dolomite karts around Johannesburg, prior to housing development projects. At least two professional companies offer microgravity services in R.S.A.

204. In Belgium, quite a lot of cavity problems have been studied by microgravity (by French companies or by the University of Liège):

- small tertiary sandstone quarries (along Brussels-Paris motorway for example)
- carboniferous limestone karsts
- karsts in chalk (example F.N. arms plant at Liège)
- mine shafts (near Tournai)

- underground chalk quarries (near Mons). We are not aware of any official position on microgravity in that country. It is rather when the constructor is in front of serious foundation problems that he thinks about geophysics in order to save part of the necessary drilling costs.

205. In West Germany, despite the existence of many sink-holes (see: Symposium of the International Society of Rock Mechanics, Hannover, 1971, on the theme of dissolution cavities), often related to salt, microgravity does not seem very popular.

206. In the United Kingdom, the geological conditions are very similar to France in the southern half of the country, but microgravity is not known to be popular.

207. CPGF has promoted microgravity and made surveys in the Middle East and the Far East, where a variety of cavities exist:

- caverns in gypsum and limestone (Saudi Arabia)
- low density zones in volcanics (Abu Dhabi)
- karstic pinnacles and caverns under sand and silt cover (Malaysia)
- old filled sand quarries (Singapore)

The local authorities were not aware of microgravity and used only drilling or, in Saudi Arabia, cross-hole seismics.

208. In some other countries, CPGF has carried out microgravity surveys but on the advice (or on behalf) of French clients. We were not in a position to evaluate the in-country regulations, if any, concerning cavity detection. Among these countries, we can mention:

Portugal: clay filled karst (for a cement plant)
Spain: open karsts (for a cement plant)
Argentina: gypsum karsts (for a dam under construction)
New Caledonia: coral limestone karsts (for an airport)

209. Status of cavity detection in the U.S. (as seen from France).
The comprehensive Corps of Engineers report (Engineering Manual, 1979) considers the main surface geophysical methods for engineering surveys to be resistivity methods and seismic methods. Microgravity is mentioned as a possible method for cavity detection, but with "relatively low sensitivity". Since this report, progress has been made in many fields.

210. It appears, seen from France, that a lot of work is done in the U.S. by ground penetrating radar (Ballard, 1983, Benson and Yuhr, 1987, Fisk

et al, 1987), but radar is excluded from the present report. In addition, it seems to have a very limited depth of investigation under temperate climates, where superficial soil is very conductive.

211. Quite a lot of work seems to have been done in the field of seismic reflection (Steeples and Miller, 1987) and in cross-hole seismics (Fisk et al, 1987). It is surprising to note that, while the only gravity meters in the microgal range are of U.S. construction (Lacoste and Romberg, model D), microgravity surveys seem to be far from standard practice. In the U.S., the use of microgravity for the survey of a nuclear power plant site has been reported by Arzi (1975), while Butler is a tireless pioneer (1980, 1984). Vertical gravity gradient measurements have been reported by Butler (1984) and by Smith and Smith (1987). The recent seminar on karst hydrogeology, held at Orlando, Florida, in February 1987, has shown that sink-holes - some of incredible extent - are very frequent in many states of the southern third of the United States.

- Roselend tunnel
- St Dalmas de Tende tunnel } gypsum
- Echaillon canal
- Oraison canal } low density lenses in quaternary alluvium
- Curbans canal

216. The French railways (SNCF), after a catastrophic failure at Vierzy in the sixties, has had CPGF survey several tunnels, to detect low density zones:

- Meudon tunnel (near Paris)
- Blaisy Bas tunnel along the main Paris-Lyons railroad
- Beaucaire tunnel (near Nimes, south of France)

Blaisy Bas survey is described in the case history section.

PART 6: EVALUATION OF THE APPLICATION OF MICROGRAVITY TO THE MONITORING OF THE FOUNDATIONS OF EXISTING STRUCTURES

212. A certain proportion of geophysical surveys carried out by CPGF concern the foundations of existing structures. The problem arises particularly in three cases:

- fissures and cracks in existing buildings due to differential settling of the foundation, particularly in the case of cavities and of evolutive sink-holes,
- movements and disorders in existing tunnels or embankments,
- modification of the superstructure, for example, the reconstruction or the heightening of an earth or rock fill dam.

213. There is no major difference in the design of a gravity survey of the foundation of existing structure and that of a future structure, except that one has to take into account:

- limitations of access
- severe corrections due to buildings, cellars, etc ...

214. CPGF has done several surveys in the northern part of Paris city, and in the northern suburbs, which can be considered as typical examples of this type of problem (see case history section, Porte Pouchet). Gypsum lenses are found at depths of 35 to 50 m, interbedded with Lutetian (tertiary marls). Pumping for industrial purposes of the sulfate saturated aquifer located in this stratum has activated the dissolution of gypsum and maybe 500,000 tons of gypsum have been dissolved for the past 50 years. A house disappeared in a sink-hole at Sevran in 1963 (Kutkan and Lakshmanan, 1969). Since then, other minor or major sink-holes (up to 10,000 cu.m just under the tracks of Gare du Nord railway station) have occurred, despite the reduction of pumping.

215. The problem of stability of tunnels can also be considered to be related to the same theme. Several hydroelectric tunnels cross dipping triassic gypsum layers in the Alps. Initally, small leakage creates fissures in the concrete lining, and the leakage then accelerates. Such surveys have been made, on behalf of Electricité de France (French state power board). We can mention :

PART 7: CASE HISTORY SECTION

The following 22 case histories have been selected among the several hundred surveys made by CPGF. (P. refers to paragraphs - C to case History numbers).

TARGET	LOCATION	CONSTRUCTION	CASE HISTORY N°.
Underground quarries	. Varangéville (Lorraine)	Existing SNCF Paris-Strasbourg railroad	P. 153 to 167
	. Joinville-le-Pont (near Paris)	Existing aqueduct (underground survey)	C. 3
	. Lille	6 storey residential building project	C. 15
Mine works	. St Etienne	Dowell-Schlumberger factory, location of cavities for disposal of excess grout	C. 10
	. Charleroi (Belgium)	Office building project over old coal mines	P. 38
Man made cavities	. Sailly-lez-Cambrai	Housing development project (location of World War 1 tunnel)	C. 12
	. Cheops pyramid (Egypt)	- Location of unknown chambers - Analysis of pyramids structure	P. 140 to 145
Karstic cavities (limestone)	. Corbeil-les-Tarterets (near Paris)	High rise building (SISMOBLOC-CPGF) for location of vertical cracks	P. 178 to 179
	. Liendo (near Laredo, Spain	Cement plant project	C. 13
	. Neuchatel-en-Bray (Normandy)	Access to channel tunnel roadway project	C. 7
	. Arrou (Touraine)	SNCF fast railroad bridge project (TGV Atlantique)	P. 190
	. Fosse Soucy (Normandy)	Existing highway	C. 1
	. St Germain-en-Laye (Paris)	Finance Ministry building	C. 17

TARGET	LOCATION	CONSTRUCTION	CASE HISTORY N°
Karstic cavities (limestone)	. Palais des Oliviers (Monte Carlo)	High rise building project	C. 6
	. Cauderan-Naujac (Bordeaux)	Waste water tunnel project	P. 181 to 183
Karstic cavities (gypsum and salt)	. Nanterre (near Paris)	C.E.B. existing water reservoirs	C. 8
	. Blaisy Bas (near Dijon)	SNCF railroad existing tunnel (underground survey)	C. 5
	. Varangéville (Lorraine)	(already mentioned survey above)	P. 153 to 167
	. Porte Pouchet area (Paris)	Constructed area + roads in a large part of N.W. Paris	C. 9
Low density zones	. Civaux (S.W. France)	Nuclear power plant (low density dolomite sand lenses)	C. 11
	. Jebel Dhanna (Abu Dhabi)	Existing petroleum tanks (scoria zones in volcanic bedrock)	C. 14
	. Dax	Projected hospital	C. 16
Before and after grouting surveys	. Varangéville (Lorraine)	Already mentioned above	P. 153 to 167
	. Cauderan-Naujac (Bordeaux)	Already mentioned above	P. 181 to 183
	. Nanterre (near Paris)	Already described above	C. 8
Embankment and structure control	. Arles viaduct	SNCF Lyon-Marseille railroad	C. 2
	. Beautiran-Langon (S.W. France)	SNCF railroad embankment	C. 4
	. Cheops pyramid	(already mentioned above). Structural analysis and density evaluation	P. 140 to 145

For each case history, we describe:

- the project (or the existing structure)
- the geological setting
- the purpose of the survey
- its contents
- results of the survey
- conclusions (results of drilling, effect on the project, etc ...)

and we attach a set of selected drawings.

The selection of case histories include:

Table 23 : Analysis of case histories

	Existing	Projects
- Foundations of buildings or houses	1	6
- " " industrial plants	2	2
- " " roads	1	1
- " " railroads	1	1
- Tunnels	2	1
- Structures: railroad embankments	2	-
- : *Cheops pyramid*	1	-
- Underground storage	-	1
	10	11

Among these 22 cases, 20 were studied by microgravity (including one with γ-γ density logging) and two by seismic methods.

Note: The selected drawings are copies of originals, the written part of the drawings is therefore in French. However, we have added at the end of each text, an English title and description of each figure. On certain figures, relevant English captions have been added, so that the figures should now be self-explanatory.

Case history 1 : Fosse-Soucy highway

Client : "Direction Départementale de l'Equipement" (Department of Public Works, Highways Division)

Survey references: March 1982, CPGF n° 2347

Site : Highroad crossing at la Fosse-Soucy in Normandy, France

Object : Sink-hole mapping after abnormal settlement on the road

Definition : Microgravity survey complemented with destructive drilling using L.W.D. (logging while drilling)

Geological setting

Outcropping mid-jurassic limestone locally subject to intensive fracturing. Surface run-off disappears at some fault traces. Road collapse took place at a similar location.

Why microgravity?

Map the underground density anomalies (voids, intensive fracturing, faulted zones) and variations of depth to the top of sound limestone.

Survey design

62 microgravity stations, with 3 to 6 m centers, in a 20 x 30 m cross-road
6 drill holes with MWD, 15 m deep.

Results

a) Microgravity survey

Bouguer anomalies of 50 to 75 microgals in two perpendicular directions. Causes seem to be very shallow.

b) Recording drilling parameters

Boreholes were drilled at critical locations. Drilling rate and reflected percussion information data obtained by microgravity were correlated to show that disturbances encountered are in relation with fracture systems

which gave rise to local intensive alterations, weakening the subsoil.

Conclusions

This survey is an example of the fact that microgravity can be used to map generally the underground, although the primary objective is often the detection of cavities.

In the present case, subsurface cavities are not the cause of the road collapse, but heavy weathering associated to a fault system; subsequent geological disturbances were mapped by the use of microgravity. The enclosed figure shows how accurately these anomalies can be mapped.

Enclosed documents: Figure 68 : residual gravity map (CPGF ref. 2347-04). Values in 10^{-2} milligals.

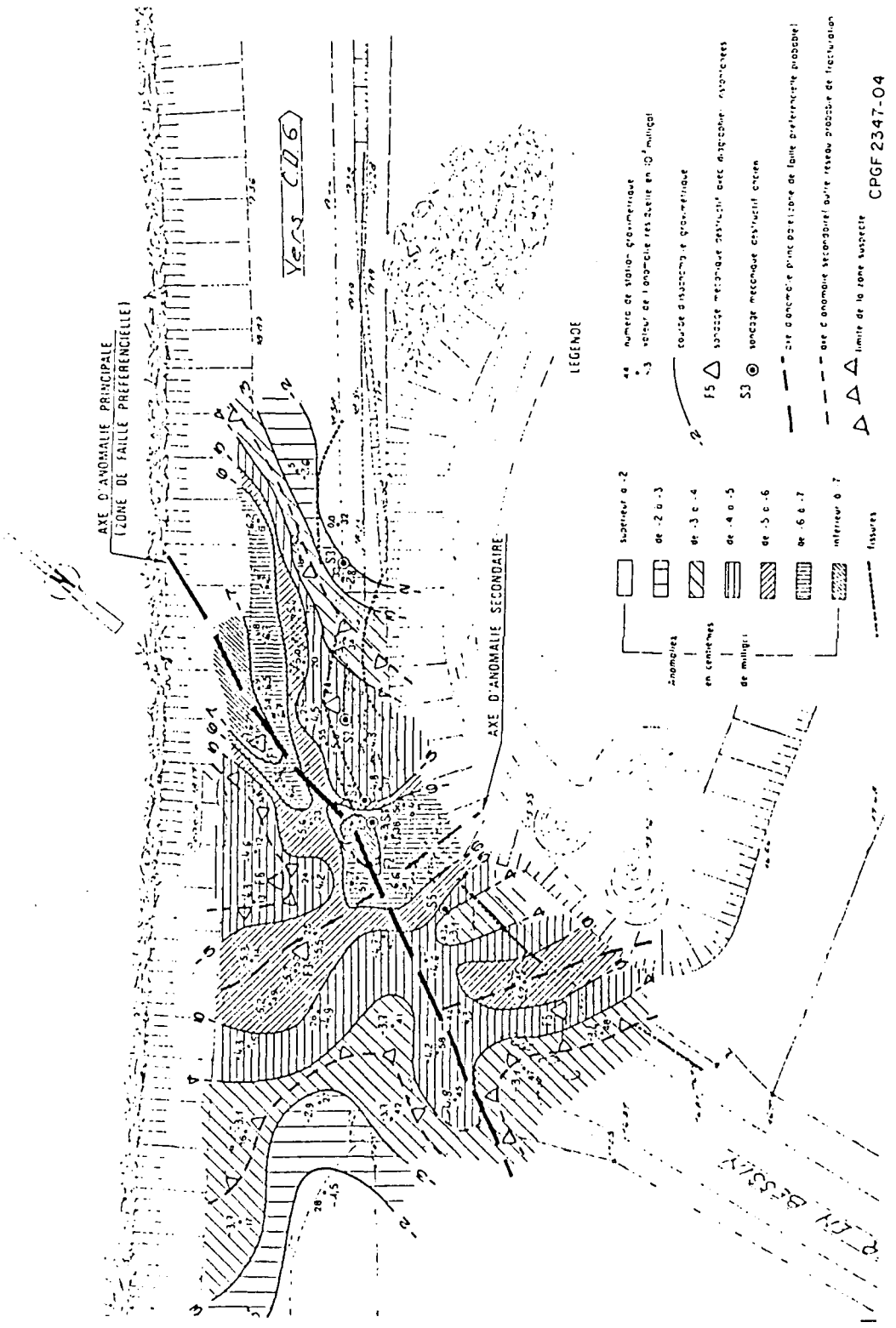

Figure 68. Fosse-Soucy case history, residual anomaly map

Case history 2 : Arles railway viaduct.

Client : S.N.C.F. (French Raiways Authority)
Survey references: January 1983, CPCF n° 2462
Site : Arles viaduct, near Marseille, south of France
Object : Railway viaduct/embankment under operation. Possible cavities within the embankment cause small collapse features on the platform
Definition : Microgravity profiles along and across the embankment to weigh it. Embankment embodies old partially destroyed viaduct (World War II)

Geological setting

Artificial geology : piles of the old viaduct contain voids ; heterogeneous material used in the embankment 9 m high.

Why microgravity?

Typical example of a high resolution survey including three components: regular profiles, sophisticated terrain corrections, variable density processing.

Survey design

A total of 191 gravity stations, spread along longitudinal and transverse profiles, with 6, 3 and 1,5 m spacing, were carried out. 112 EM measurements were also taken as a test and correlated with gravity.

Results

Gravity anomalies were quite difficult to isolate, for the piles of ancient viaduct yielded positive anomalies, while the arches gave negative anomalies. To complicate everything, maintenance chambers located in the upper part of the piles produced negative anomalies within the positive ones.

Heterogeneities within the bulk of the embankment, near its upper surface, created negative anomalies of 20 to 30 microgals. Local settlings possibly due to vibrations and materials evacuation are believed to be the cause of those anomalies.

The body of the embankment was found to include two types of densities after variable density processing of the gravity data. This is a mean to weigh a structure ; it also provides surface density maps. The core of the embankment constructed just after the war, has a density around 2.0 gm.cc, while the two flanks, more recently added to avoid toe-slipping, have a density of 2.2 gm/cc (see figure 2462-13).

Conclusions

Heavy superficial density along the embankment slopes is probably due to construction in 2 phases. Survey showed no major disturbances in the bulk of embankment. Subsequent drilling only detected minor disturbances right below the platform, as foreseen by microgravity survey.

Enclosed documents

Fig. 69 : example of longitudinal profile above an old pile (theoretical and experimental values) - CPGF ref. 2462-12

Fig. 70 : density map and cross-section (CPGF ref. 2462-13)

Fig. 71 : complete longitudinal section with:
- on top, deformation curves from 9/1981 to 10/1982
- at bottom: Bouguer anomaly in 10^{-2} milligals

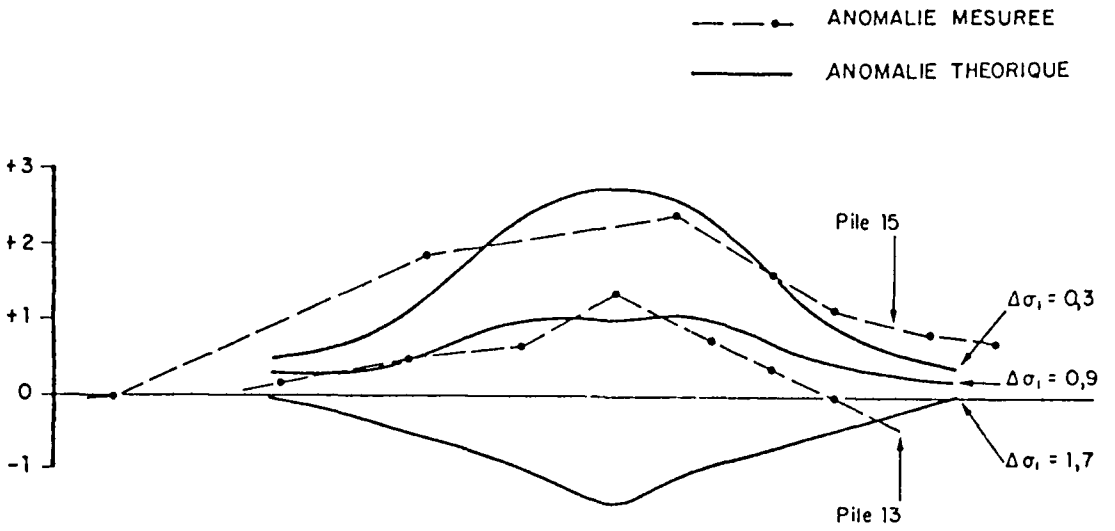

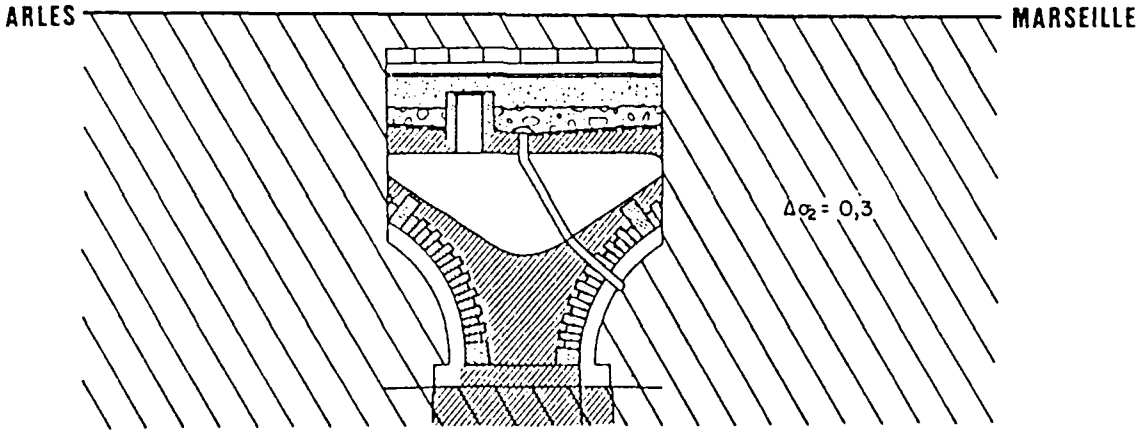

CPGF 2462-12

Figure 69. Arles railroad, example of longitudinal profile over an old pile

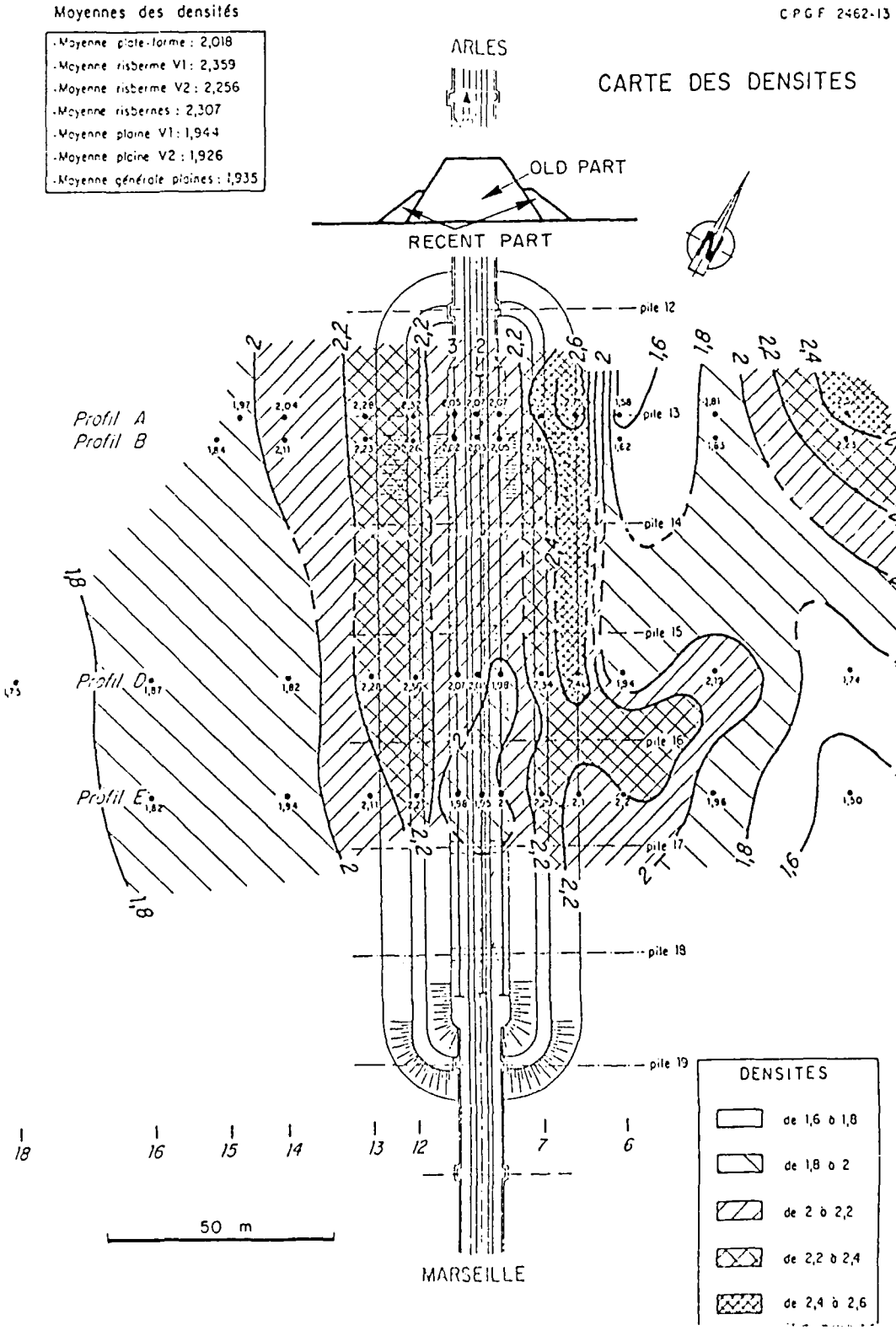

Figure 70. Arles railroad, density map and cross-section

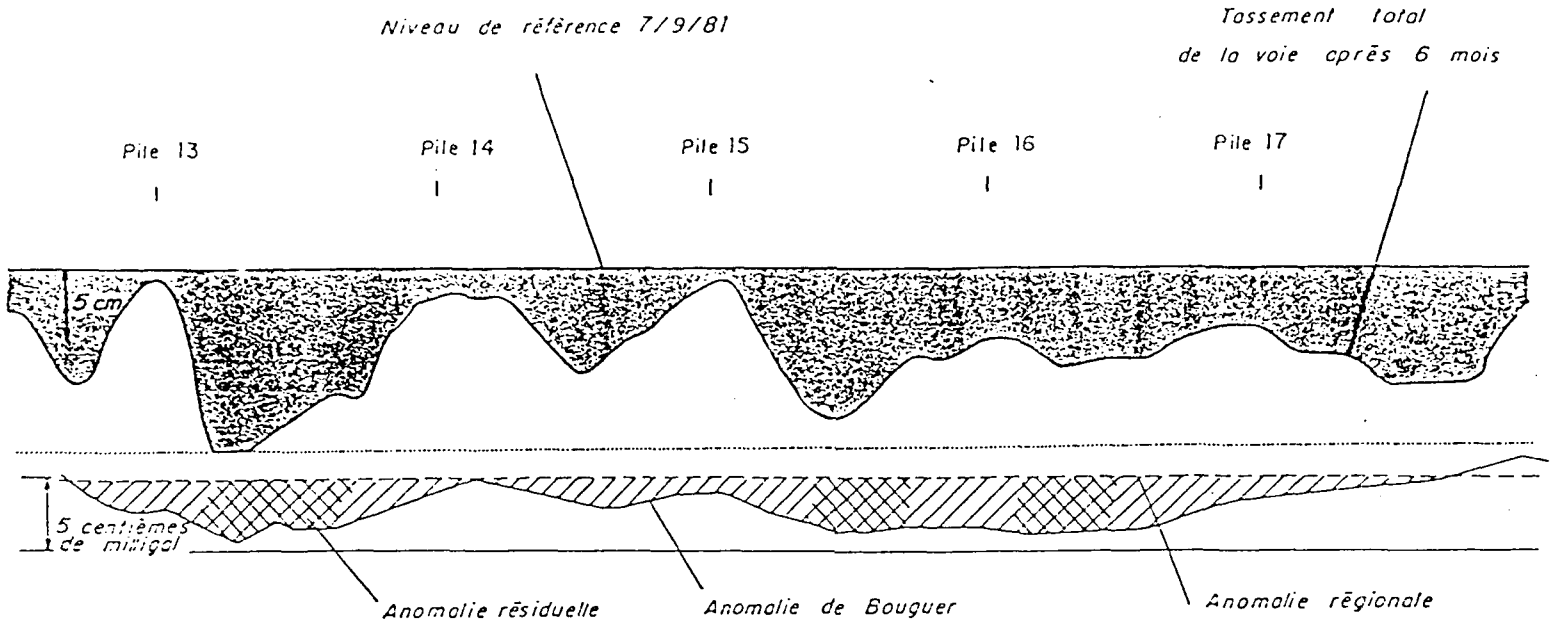

VIADUC D'ARLES

FIGURE Nº 1

Figure 71. Arles railroad: complete longitudinal section

Case history 3 : Joinville-le-Pont aqueduct.

Client : Paris city

Survey references: March 1984, CPGF n° 2610

Site : Joinville-le-Pont, near Paris, France

Object : Old underground aqueduct built over an ancient quarry. To be re-used as a future water main.

Definition : Microgravity in a tunnel to map an underground quarry

Geological setting

Quarries in tertiary limestone, overlain by marls with limestone beds.

Why microgravity?

Density anomalies to be discovered from the interior of a tunnel 4 m below the ground and with a diameter of 2 m. Specific terrain corrections and precise modelling required to perform this survey over 180 m of tunnel.

Survey design

106 gravity stations spread along two parallel profiles, 1.20 m apart, with 5 m and 2.5 m spacings.

Results

A very well marked negative Bouguer anomaly of 30 to 45 microgals is observed on both profiles, possibly related to quarry voids. Also, rather sharp and narrow positive anomalies show up and are associated with the pillars of the unlying quarry.

Conclusions

Subsequent core drilling proved the presence of pillars at positive gravity anomaly locations, whereas negative anomalies are believed to be produced by

very weak marly formations, rather than by voids.

Enclosed documents : Figure 72 : Gravity profiles (CPGF ref. 2610-01 - anomalies in 10^{-2} milligals).

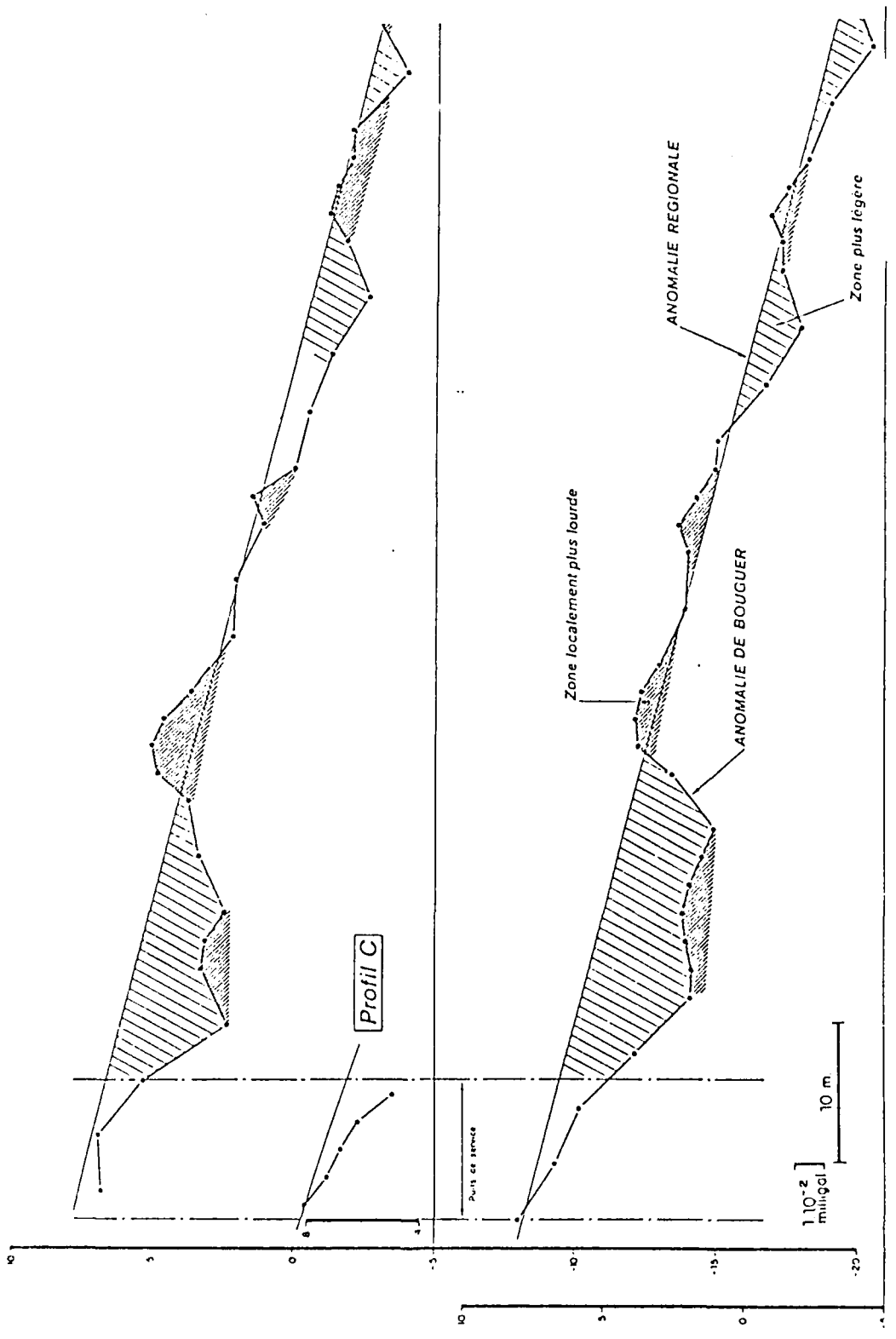

Figure 72. Joinville-le-Pont aqueduct: gravity profiles

Case history 4 : Beautiran-Langon railway embankment.

Client : S.N.C.F. (French Railways Authority)

Survey references: December 1984, CPGF n° 2734

Site : Beautiran-Langon railroad near Bordeaux, France

Object : Railroad under operation ; sink-holes appear along the tracks over 20 km.

Definition : Microgravity associated to EM and resistivity for a test survey along a railroad embankment, before and after grouting.

Geological setting

Karstified tertiary limestone overlain by sandy-clayey gravels.

Why microgravity?

Karst mapping may have to be performed at a big scale, so complementary methods are tested for the sake of cross-control and cost efficiency.

Survey design

Five critical sites were selected for multi-disciplinary investigations. A total of 36 gravity stations, 6 vertical electrical soundings (V.E.S.) and 390 m of EM profiles were carried out. One of the five sites was previously investigated by microgravity. Cavities were detected by drilling and grouted.

Results

The idea was to associate ground conductivity variations to gravity anomalies. Apparent shallow EM resistivities were obtained using an EM-31 equipment from Geonics. Resistivity soundings helped to calibrate EM resistivities. Very good correlations were obvious in areas where conductive superficial material fell in dissolution cavities within the mass of the limestone and in areas of sound bedrock.

Conclusions

Fast conductivity/resistivity traversing with inductive coupling systems like EM-31 provide in some cases a quick coverage of large areas in terms of general purpose subsurface mapping. Microgravity pinpointed the mapping, namely by yielding the vertical extent of local anomalies.

Resurveying of the already grouted area proved the expected efficiency of microgravity for grouting monitoring. As a matter of fact, negative anomalies of -58 microgals were strongly attenuated (-24 microgals) after grouting the limestone (see lower part of figure 2734-09).

Enclosed documents

Figure 73 : Electromagnetic and microgravity profiles (anomalies in 10^{-2} milligals), some before and after grouting - CPGF ref. 2734-09.

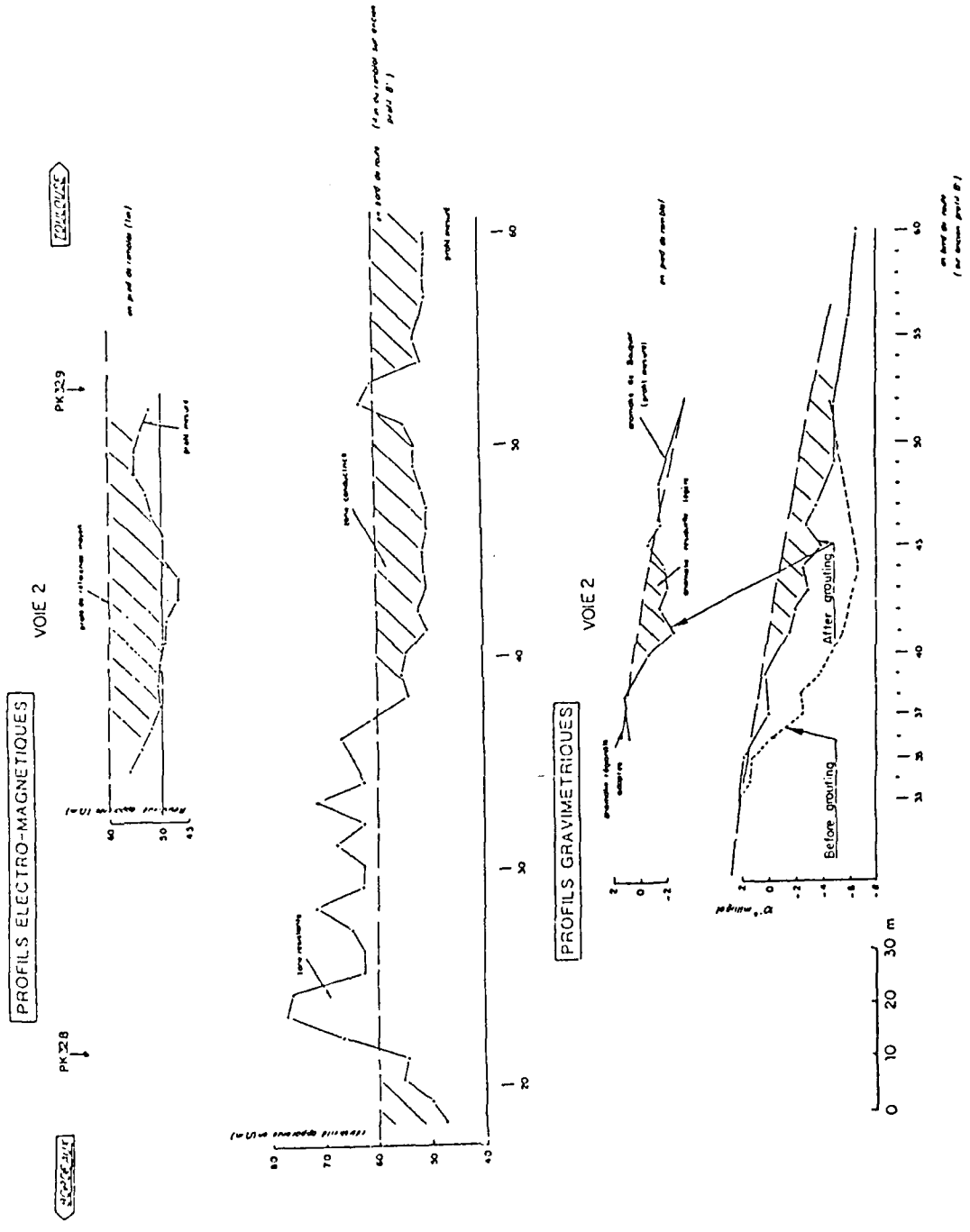

Figure 73. Beautiran-Langon railroad, electromagnetic and microgravity profiles, before and after grouting

Case history 5 : Blaisy-Bas railway tunnel.

Client : S.N.C.F. (French Railways Authority)
Survey references: May 1987, CPGF n° 3117
Site : Blaisy-Bas tunnel, Dijon area, Burgundy, France
Object : Railway tunnel through a hill, 4 km long ; dissolution cavities in gypsum caused minor collapse at platform level.
Definition : Microgravity and vertical gradient profiles along the two tracks of a railway tunnel.

Geological setting

Tunnel dug through lower jurassic and triasic dolomites, marls and gypsum. Lithological heterogeneities are associated to tectonics. Karstic cavities can be observed.

Why microgravity?

Method covers quickly and economically an investigation of two lines, 1.5 km long, to map underground disturbances and spot the most critical areas to be checked by drilling.

This is a major railroad (Paris-Marseille) and traffic ought not to be stopped by heavy tools operating in the tunnel. Special operational procedures were set by railway authorities to allow readings along the central axis of the tracks.

Survey design

300 gravity stations along 2 x 500 m of tracks, with 10 m centres, plus 40 stations at 5 m centres at anomalous zones. Besides, 20 gradient measurements 1.6 m above the platform level were taken on the flanks and at the maximum of residual gravity anomalies.

Results

A Digital Terrain Model was made out by digitizing topo maps. The terrain corrections for the hill (summit 195 m above tunnel level) were computed using special Tercor software. The tunnel itself was modelled using similar right prism technique, sliced to fit the real model and corrections computed. Terrain corrections in the order of 12 milligals were computed. Then residual anomalies of 30 to 75 microgals were contoured. Some of these are in relation with shallow dissolution in gypsum (see section of residual anomaly map 3117-09). Thanks to gradient measurements, some others were found behind the sidewalls or above the vault (see figure 3117-11).

Conclusions

Extensive modelling and precise terrain corrections had to be performed to compute tiny local gravity anomalies (terrain corrections 400 times bigger than smallest anomaly). Good correlation with lithology and tectonics.

Enclosed documents

Fig. 74 : Geological cross-section along the tunnel (CPGF ref. 3117-01)

Fig. 75 : Three-dimensional view of the DTM of the tunnel entrance, in view of terrain corrections (CPGF ref. 3117-03)

Fig. 76 (bottom) : Typical tunnel cross-section and its digitalization in view of modelling (CPGF ref. 3117-05b)

Fig. 76 (top) : Part of the residual anomaly map (CPGF ref. 3117-09)

Fig. 77 : Vertical gradient measurement (when $g < 0$ and $\frac{dg}{dz} > 0$: <u>light</u> causes, under the tunnel, when $g < 0$ and $\frac{dg}{dz} < 0$: <u>heavy</u> causes, above the tunnel (CPGF ref. 3117-11).

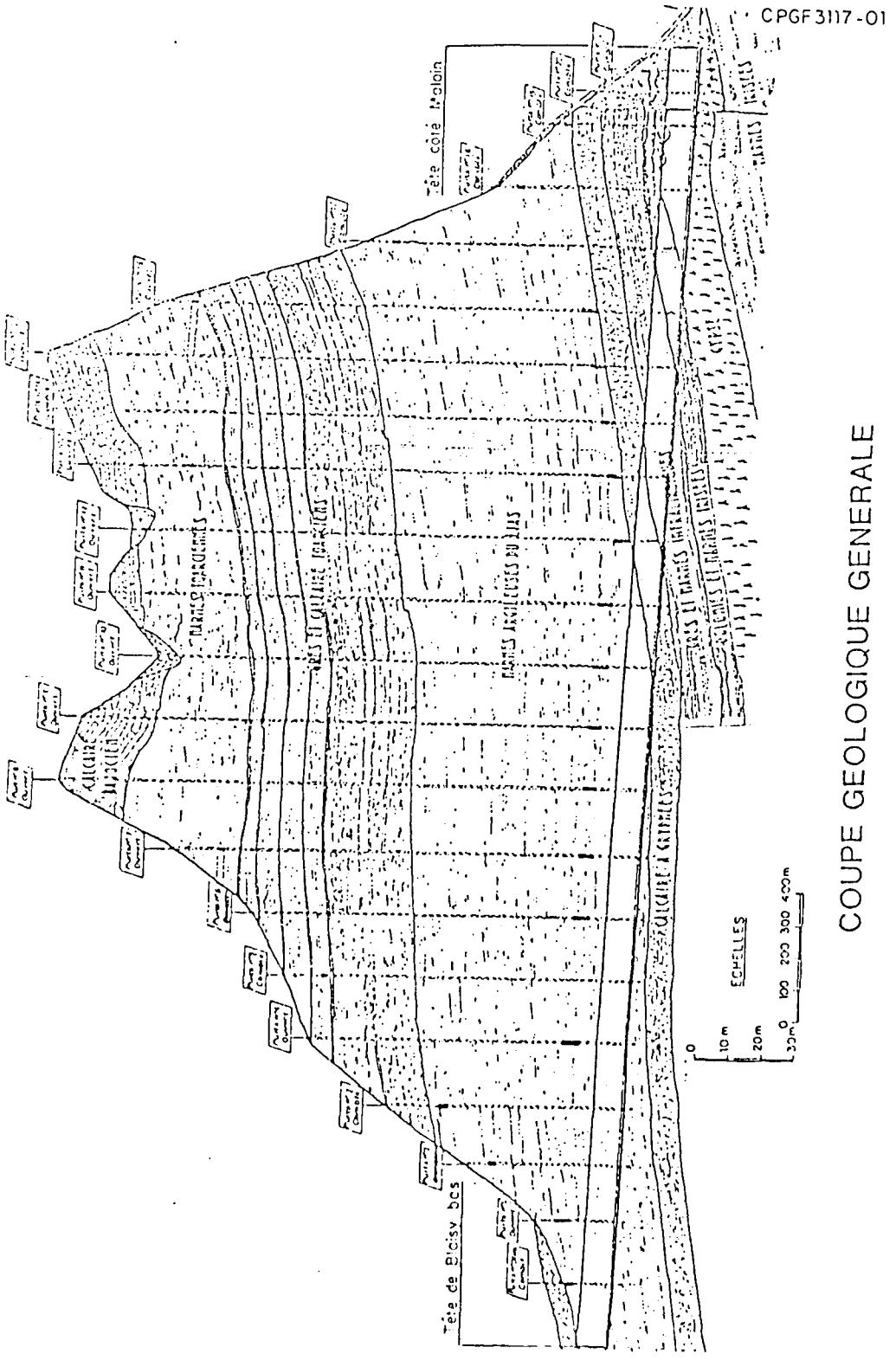

Figure 74. Blaisy-Bas tunnel: geological cross-section

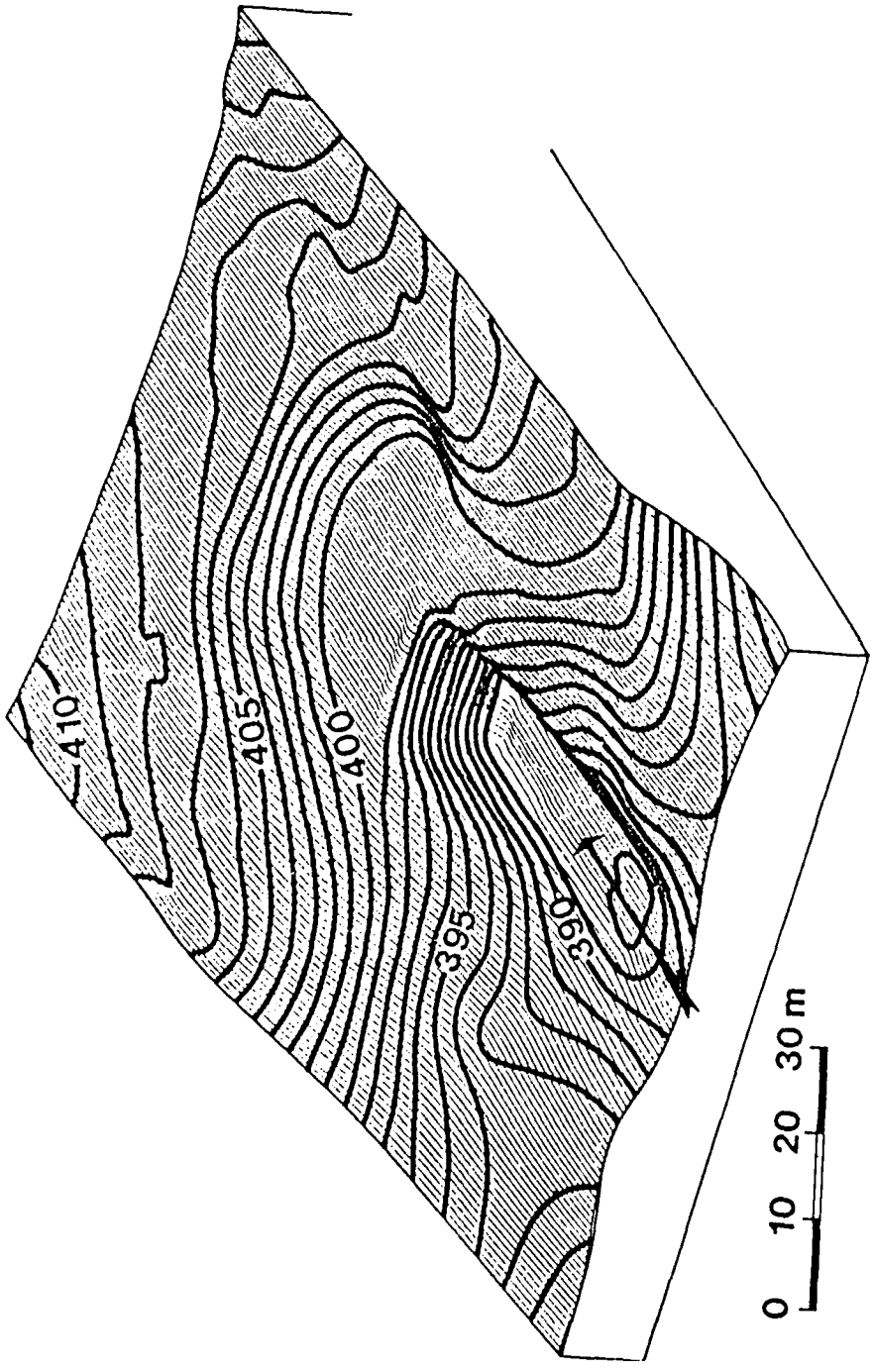

Figure 75. Blaisy-Bas tunnel: 3-dimensional view of DTM model at tunnel entrance

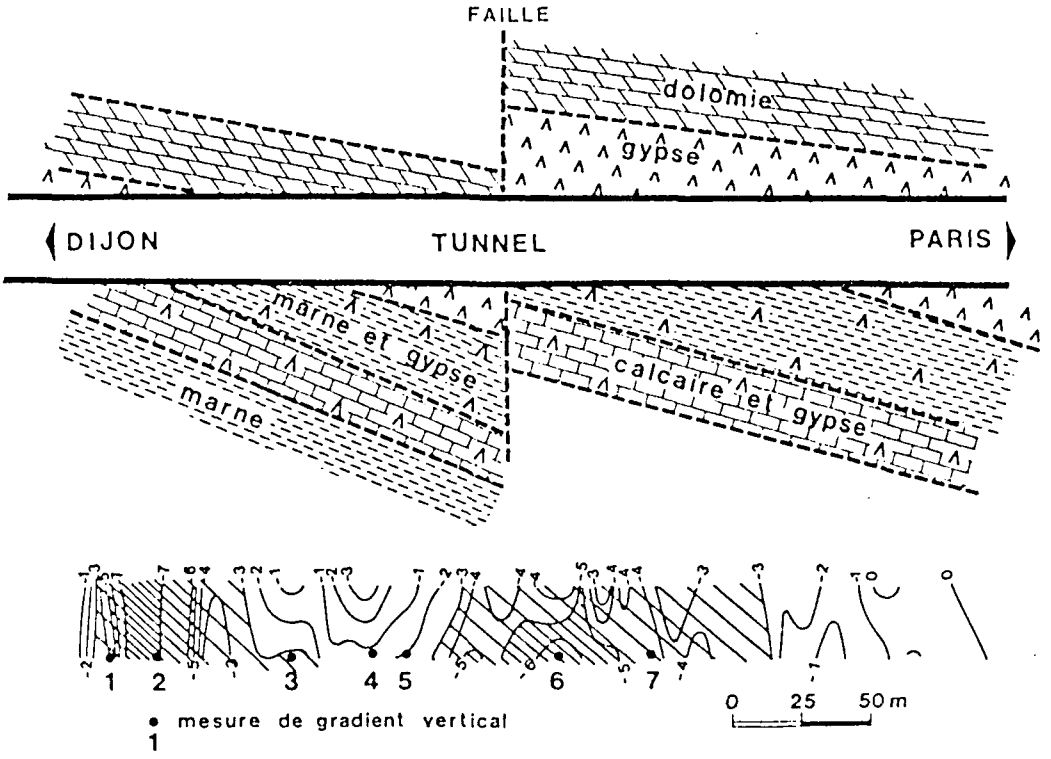

CPGF 3117-05 b

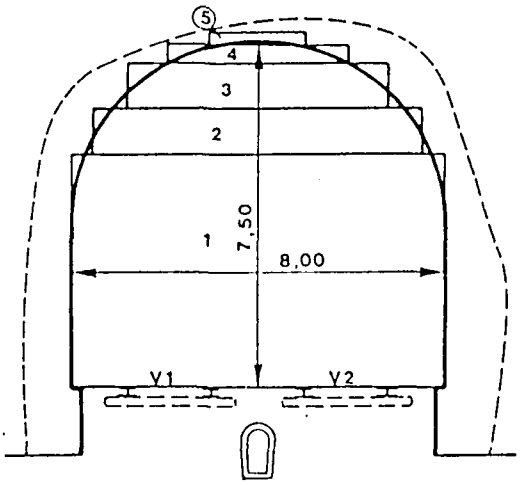

Figure 76. Blaisy-Bas tunnel: part of residual anomaly map and typical tunnel cross-section

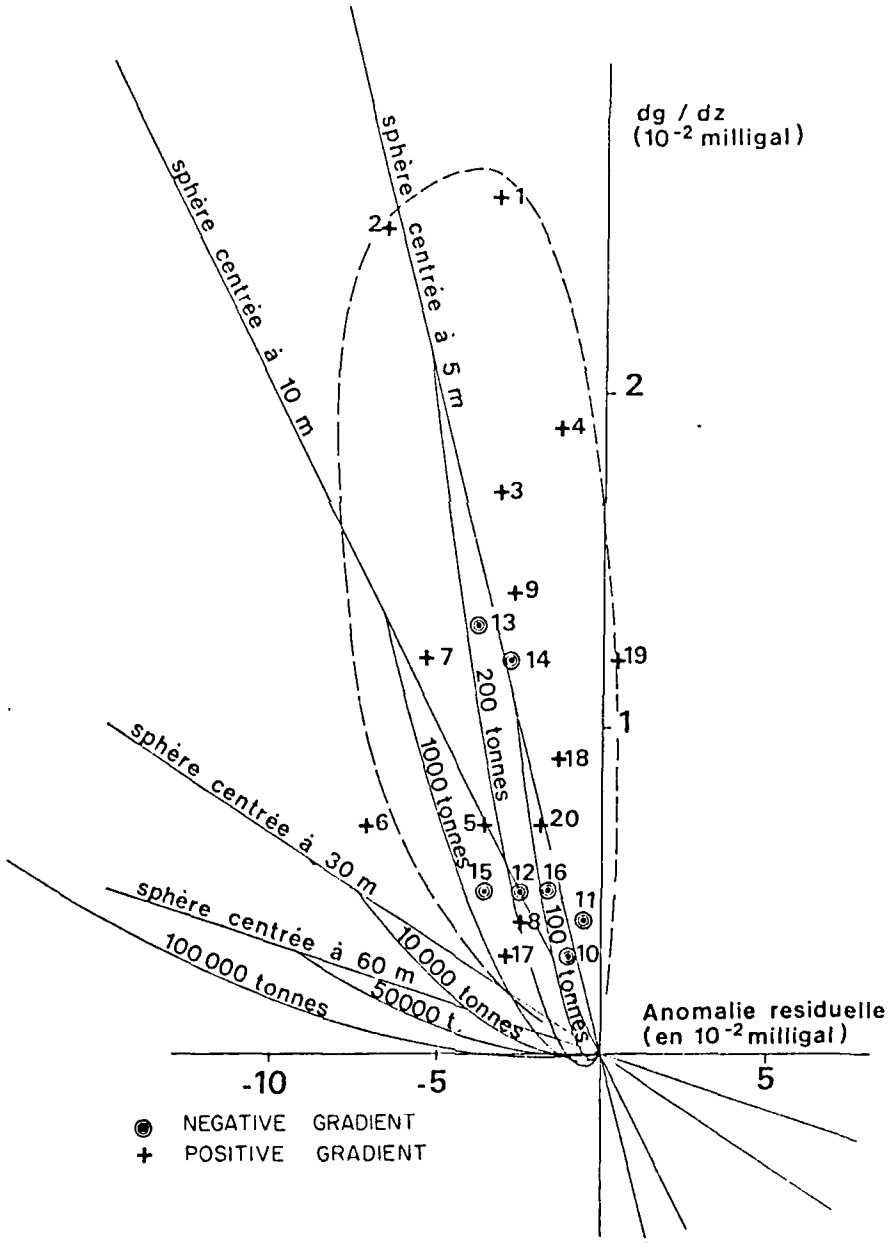

Figure 77. Blaisy-Bas tunnel: vertical gradient measurements

Case history 6 : Palais des Oliviers high rise building, Monte Carlo.

Client : Private developer
Survey references: December 1982, CPGF n° 2448
Site : Palais des Oliviers, Monte Carlo
Object : Karstic cavity detection
Definition : Microgravity survey complemented with destructive drilling using L.W.D. for a high rise building.

Geological setting

Cretaceous limestone, fractured over the first 10 m.

Why microgravity?

Works have started on this high rise building project. During excavation for foundations, small cavities were encountered. We have been asked to look for more possible undetected cavities below excavated level.

Survey design

- 3 x 3 m rectangular grid, a total of 98 gravity stations
- 9 boreholes, 9 m to 17 m deep, with L.W.D. (parameters recorded: drilling rate and reflected percussion).

Results

- Microgravity : a main negative anomaly of 60 to 90 microgals covers most of the known cavity locations and shows possible extension. Very irregular surface topography (natural and man-made) has been taken care of, using very sophisticated CPGF Tercor terrain correction programme. Part of the area covered by measurements was declared sound.
- Drilling : most of the boreholes were drilled within the major gravity anomaly area. No cavities, but differential fracturing and

and small voids were met.
As usual in hard rock environment, drilling parameters showed sharp signatures related to fissured, fractured and sound limestone and small voids.

Conclusions

This is a trap-type survey where gravity anomalies could have been artificially distorted, suppressed or enhanced by terrain effects, should these have not been properly corrected. It is also another example of subsurface geological mapping by microgravity, showing the power of such high resolution surveys to go beyond the simple detection of cavities.

Enclosed documents

Fig. 78 : microgravity residual map, values in 10^{-2} milligals (CPGF 2448-02)

Fig. 79 : drill record of drill hole 2 (center of gravity anomaly) with fractured zone from 9.5 to 11 m (CPGF ref. 2448-03b)

Fig. 80 : drill record of drill hole 6 on the edge of an anomaly - sound rock (CPGF ref. 2448-03f)

Fig. 81 : drill record of drill hole 6B close to 6, but near axis of gravity anomaly, fractured zones between 8 and 13 m (CPGF ref. 2448-03g)

Note : drill records show : reflected percussion to the left,
drilling rate to the right.

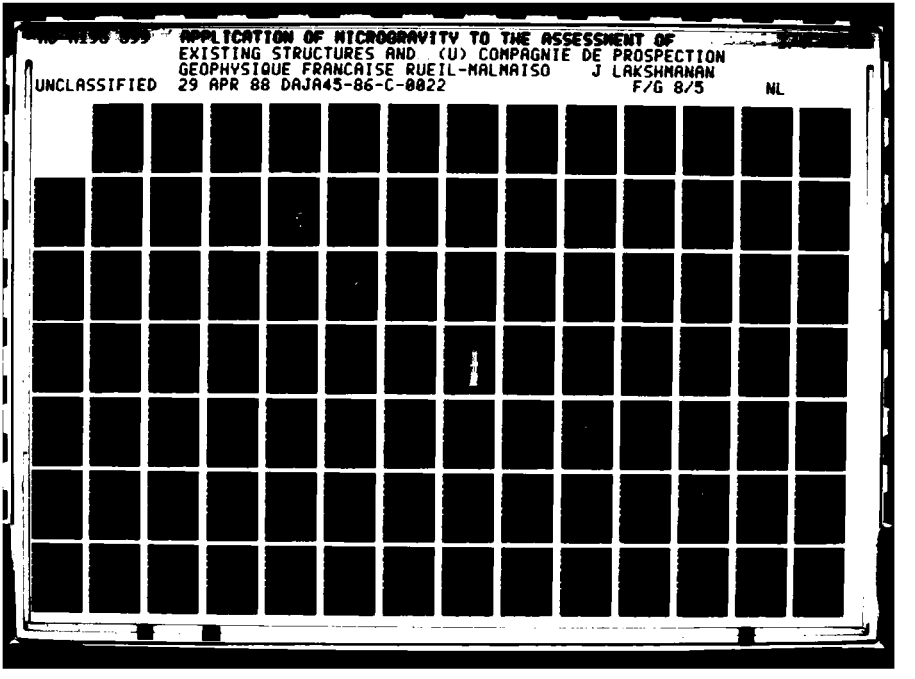
APPLICATION OF MICROGRAVITY TO THE ASSESSMENT OF
EXISTING STRUCTURES AND (U) COMPAGNIE DE PROSPECTION
GEOPHYSIQUE FRANCAISE RUEIL-MALMAISO J LAKSHMANAN
UNCLASSIFIED 29 APR 88 DAJA45-86-C-0022 F/G 8/5 NL

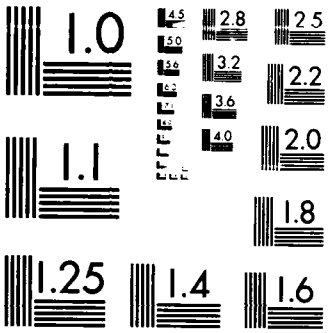
1.0
1.1
1.25
1.4
1.6
1.8
2.0
2.2
2.5
2.8
3.2
3.6
4.0
4.5
5.0
5.6

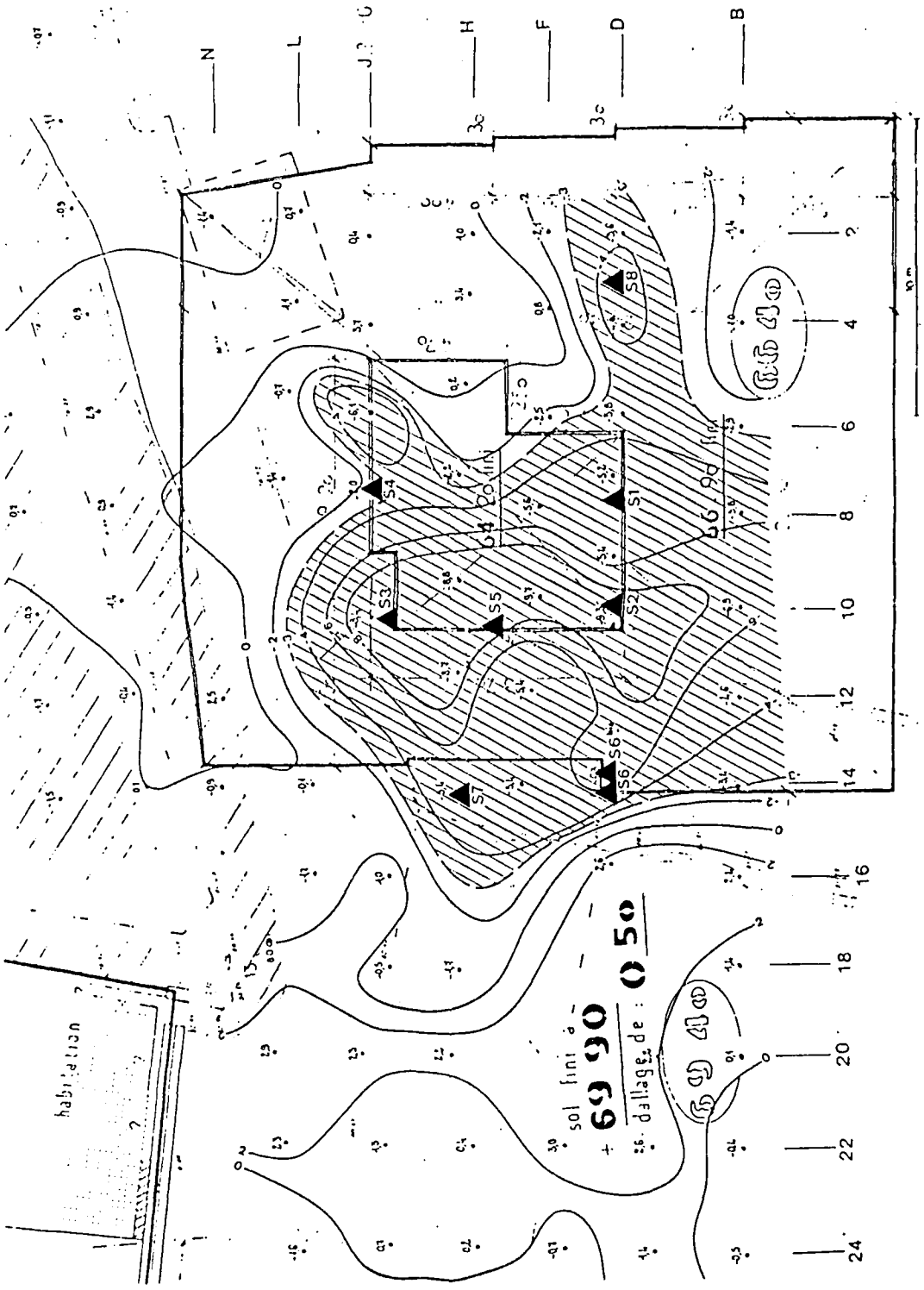

Figure 78. Palais des Oliviers, Monte Carlo, microgravity residual map

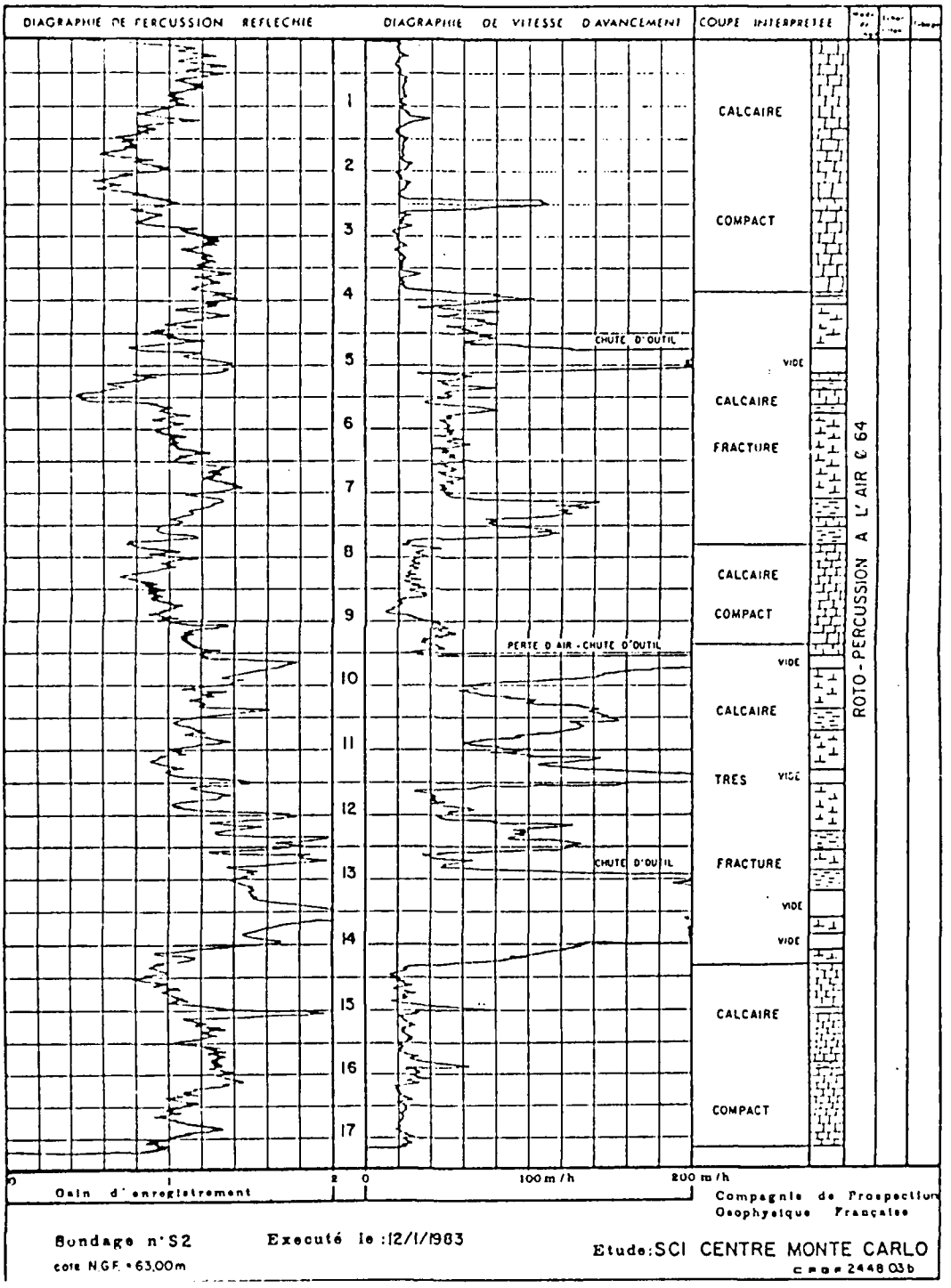

Figure 79. Palais des Oliviers, Monte Carlo, drill record of drill hole 2

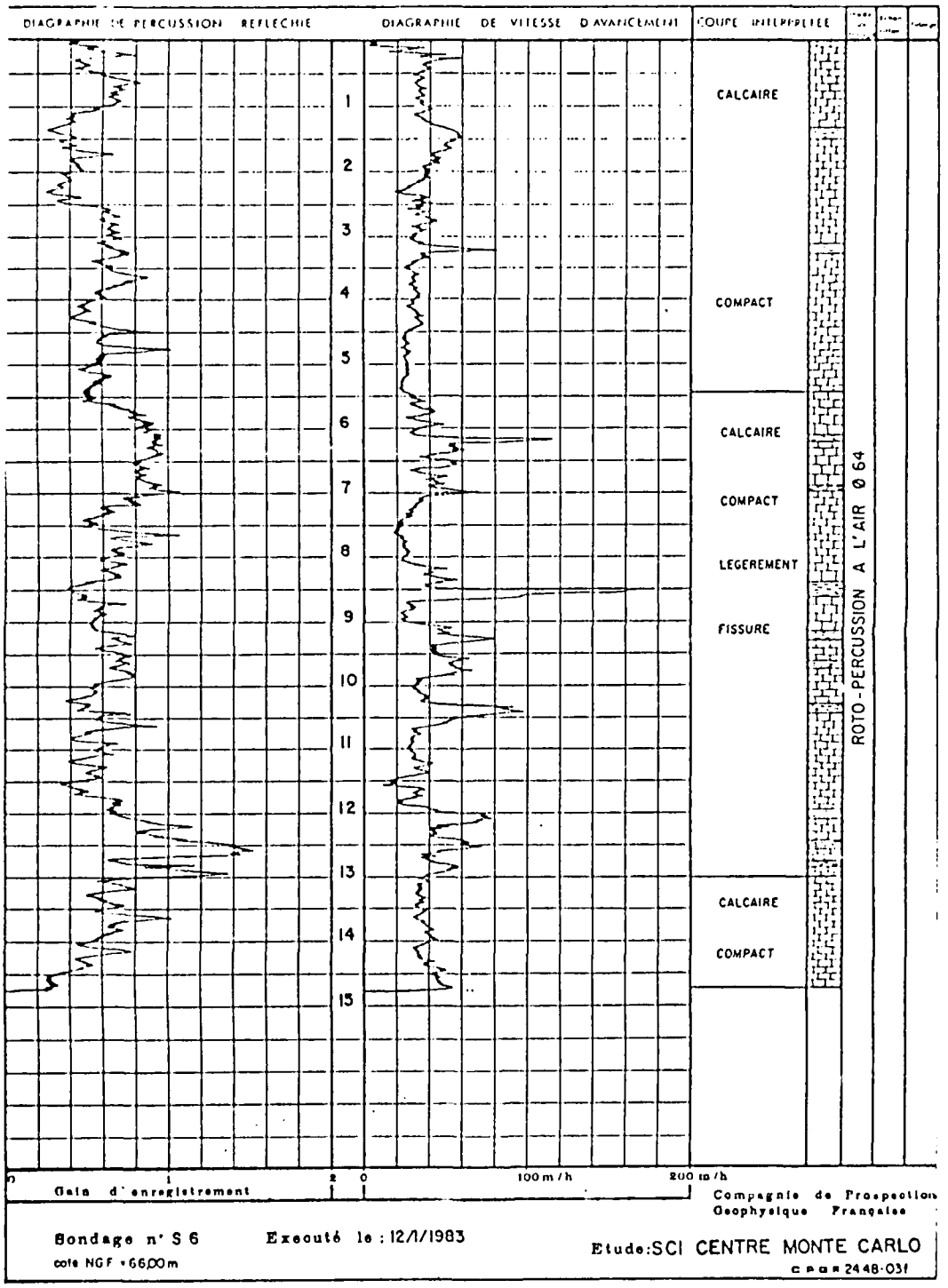

Figure 80. Palais des Oliviers, Monte Carlo, drill record of drill hole 6

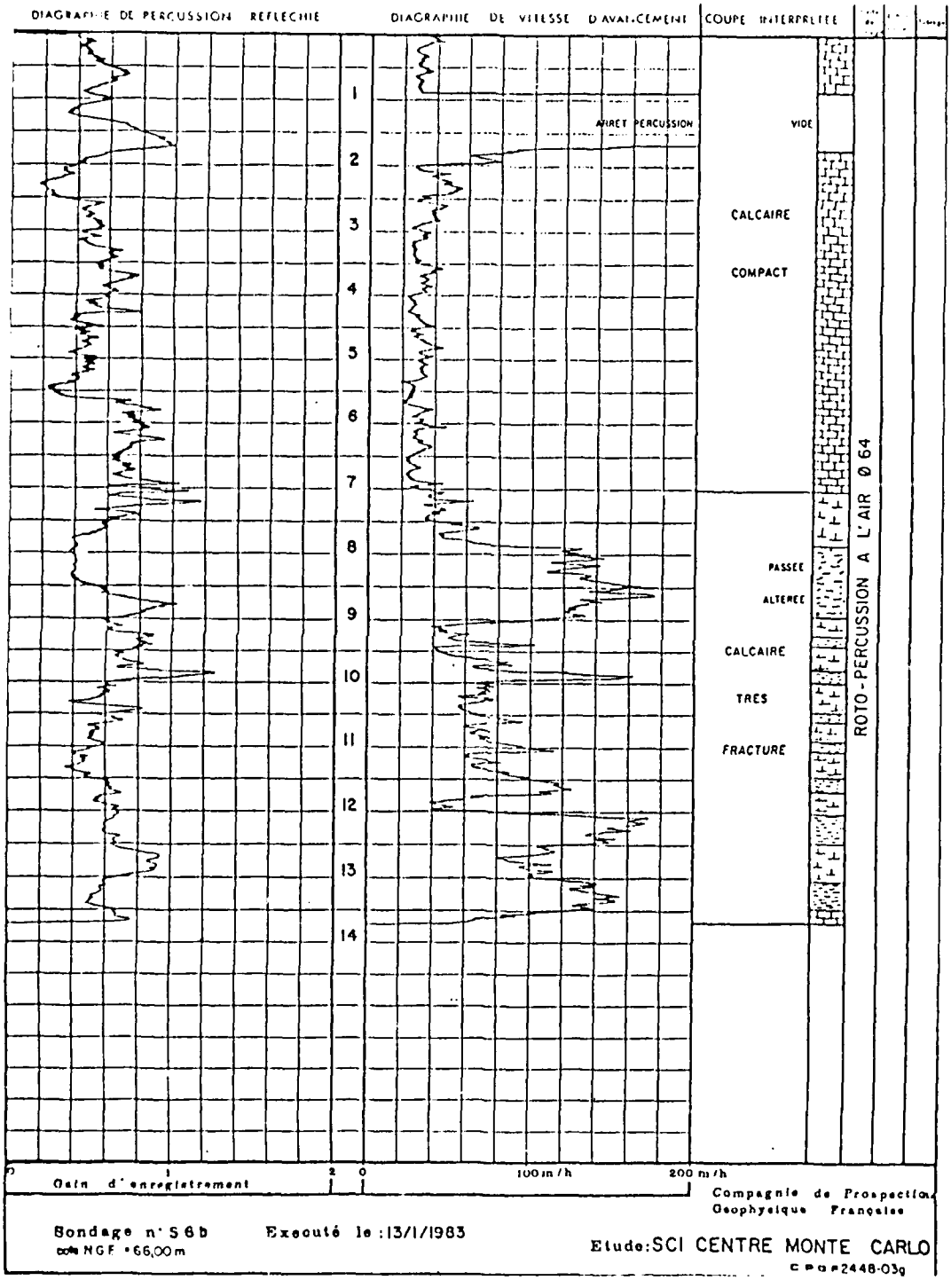

Figure 81. Palais des Oliviers, Monte Carlo, drill record of drill hole 6B

Case history 7 : "Chunnel" highway, Normandy (access to channel tunnel).

Client : Public Works Department, Département of Seine-Maritime - Roads and Highways Rouen Technical Center (CETE)

Survey references: June 1987, CPGF n° 3120

Site : "Chunnel" highway, Normandy section (8 km)

Object : Possible underground quarries along the main axis of the highway. Several occurrences of sink-holes, collapse features and shafts visible along the project.

Definition : microgravity profiling

Geological setting

Upper cretaceous chalk overlain by clay.

Why microgravity?

Fastest and more reliable method to investigate long sections of a linear project in terms of density anomaly mapping.

Survey design

Longitudinal and transverse profiles, 5 m and 10 m centres.

Results

Several well-marked 10 to 40 microgals negative anomalies were detected. These are usual signatures of quite well known exploitation patterns. Modelling was done for a best fit between gravity expressions and possible quarry design.

Other portions of surveyed profiles were declared not subject to underground density anomalies.

Conclusions

Typical example of a regular preliminary geophysical survey before geotechnical investigations along a road centerline. Here is a most effective approach to detect underground quarries, microgravity being in this setting the only possible geophysical tool to use.

Enclosed documents

Fig. 82 : zone 1, example of gravity modelling (CPGF ref. 3120-04a)
Fig. 83 : zone 2, example of gravity modelling (CPGF ref. 3120-04b)

C.P.G.F 3120-04a

ANOMALIE TYPE INTERPRÉTÉE

ZONE 1

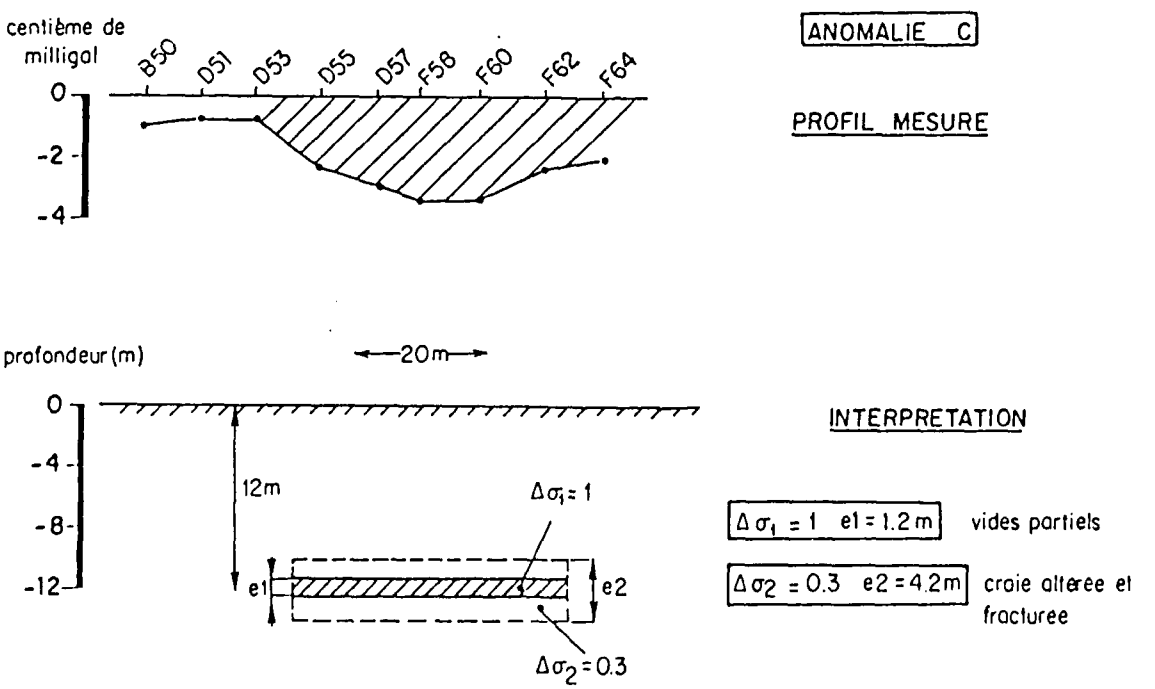

Figure 82. "Chunnel" highway, zone 1, example of gravity modelling

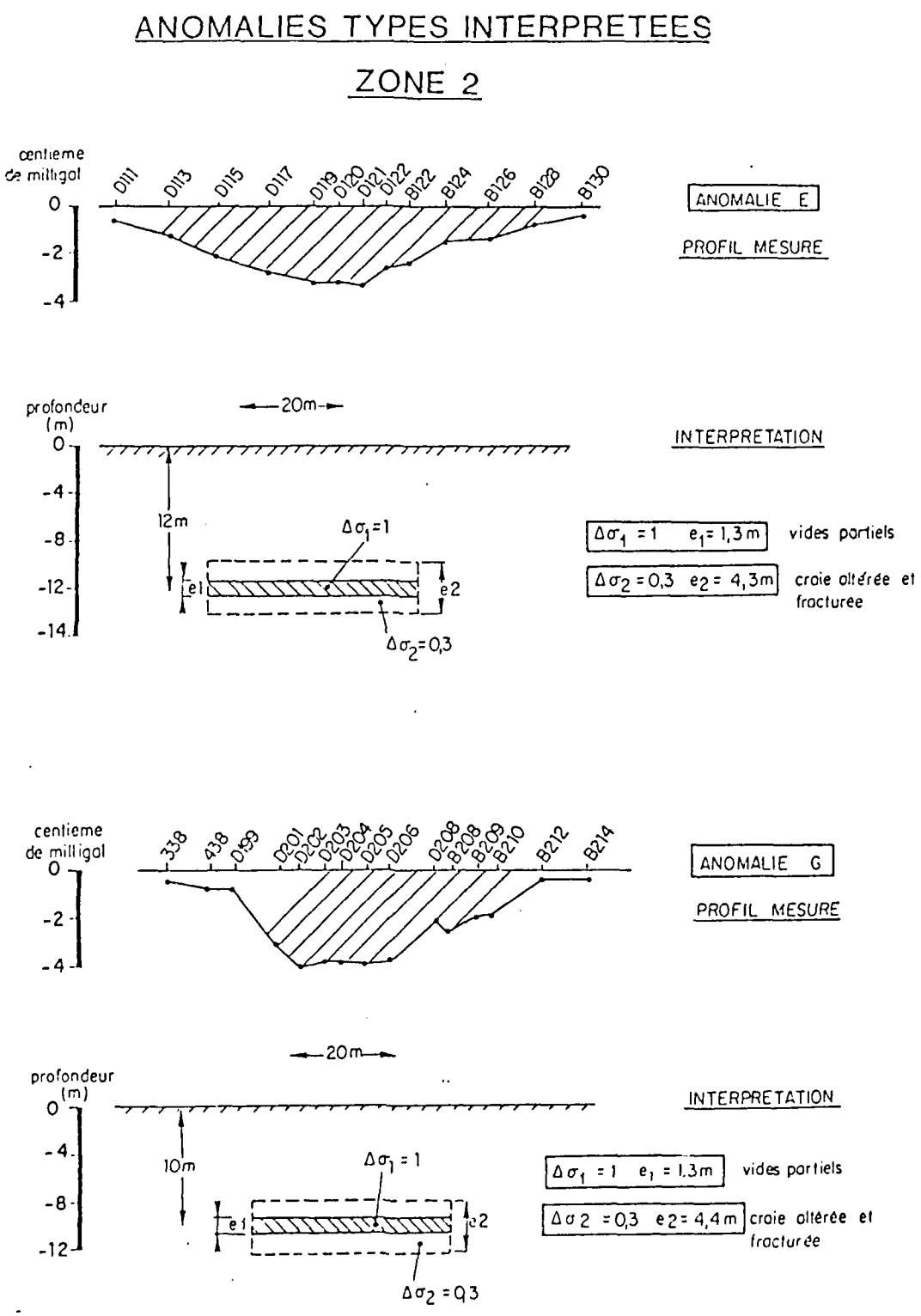

Figure 83. "Chunnel" highway, zone 2, example of gravity modelling

Case history 8 : Nanterre water reservoirs.

Client : Société Lyonnaise des Eaux (Water supply Company)
Survey references: June 1987, CPGF n° 3131
Site : Nanterre, western Paris suburb, France
Object : Water reservoirs and filters suffer foundation unstability caused by underground cavities due to gypsum dissolution.
Definition : Microgravity gridding to map the weak underground and repeat survey for grouting monitoring.

Geological setting

Reservoirs are sitting on tertiary gypsiferous marls underlain by limestone.

Why microgravity?

This water supply facility installation comprises many civil works, ponds, reservoirs, filters, buildings, etc ... Three-dimensional underground mapping and checking of grouting efficiency could only have been accomplished by high resolution microgravity.

Survey design

349 gravity stations were put on grids and profiles with 4 m to 8 m spacing.

Results

A very particular artificial mass distribution above and below the survey surface had to be taken care of to suppress the undesired effects. Empty or full, or half-full reservoirs and filters, a whole network of water mains and several buildings had to be modelled. The remaining measured anomalies were found to be the expressions of dissolution cavities ready to produce surface collapse.

Grouting took place below a few filters, where a previous microgravity survey had detected cavities. Some stations were re-run this time to show that in

all cases, residual anomalies completely disappeared after grouting.

Conclusions

20 to 30 microgals residual anomalies isolated in a difficult operational environment delineated very precisely the contours of underground dissolution features.

A remedial action was proposed and subsequent grouting was planned according to the microgravity map indications.

Enclosed documents

Fig. 84 : location map and geological cross-section (CPGF ref. 3131-01)

Fig. 85 : reservoir 1 zone, residual anomaly before and after grouting (CPGF ref. 3131-05)

Fig. 86 : filter n° 4 zone, residual anomaly before and after 2 phases of grouting (CPGF ref. 3131-07).

C.P.G.F 3131-01

PLAN DE SITUATION

ECHELLE 1/10000e

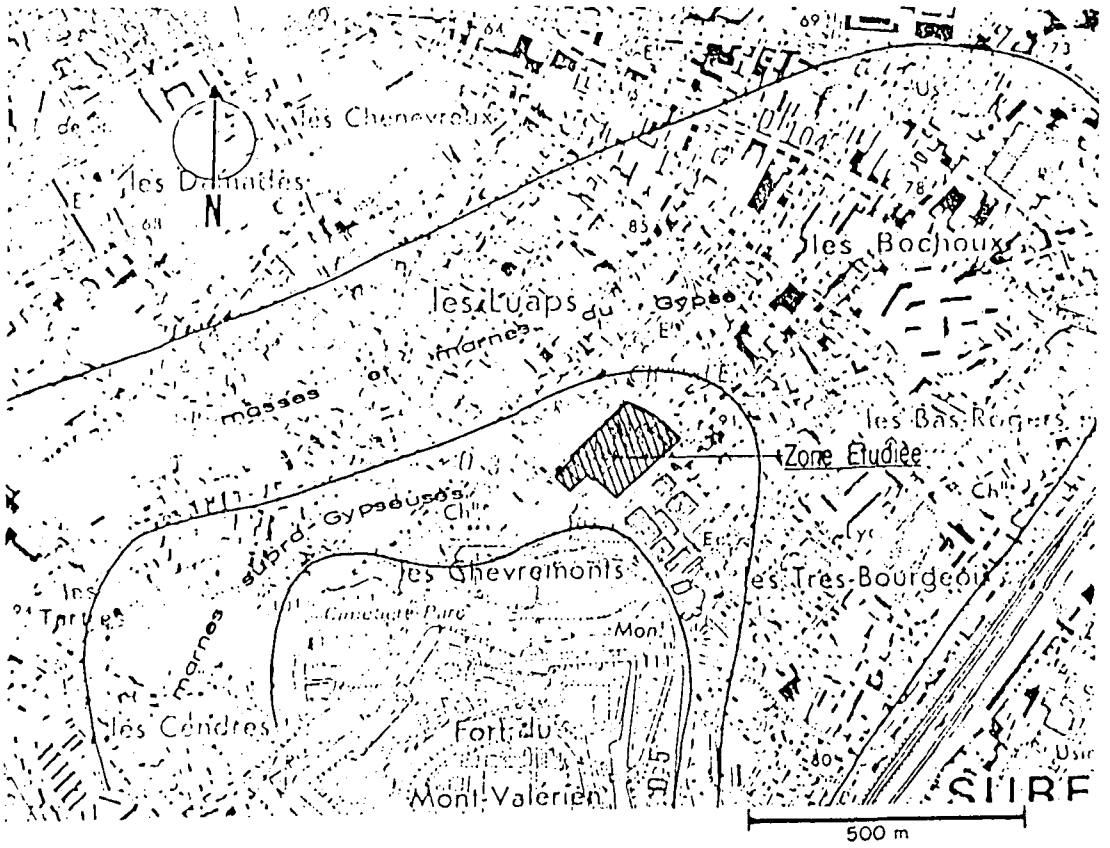

COUPE GEOLOGIQUE

sud — nord

ECHELLE 1/50.000e

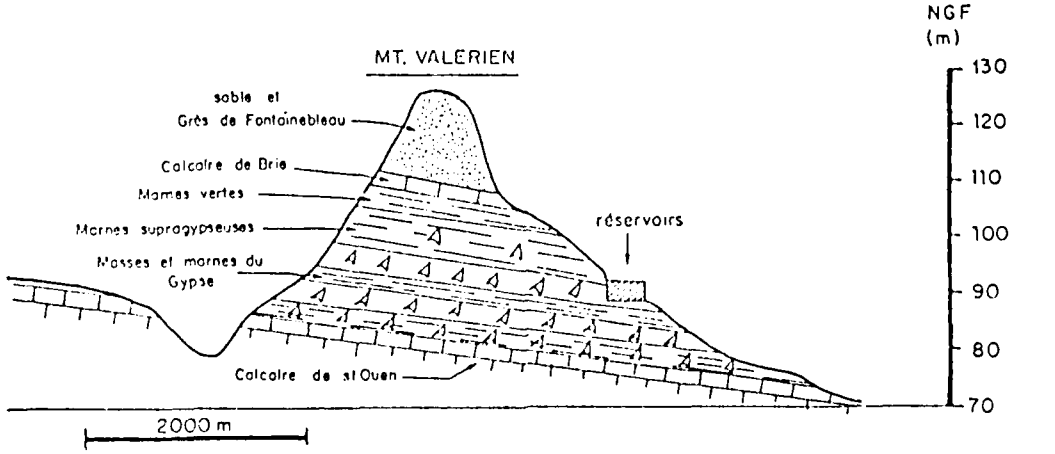

Figure 84. Nanterre water reservoirs: location map geological cross-section

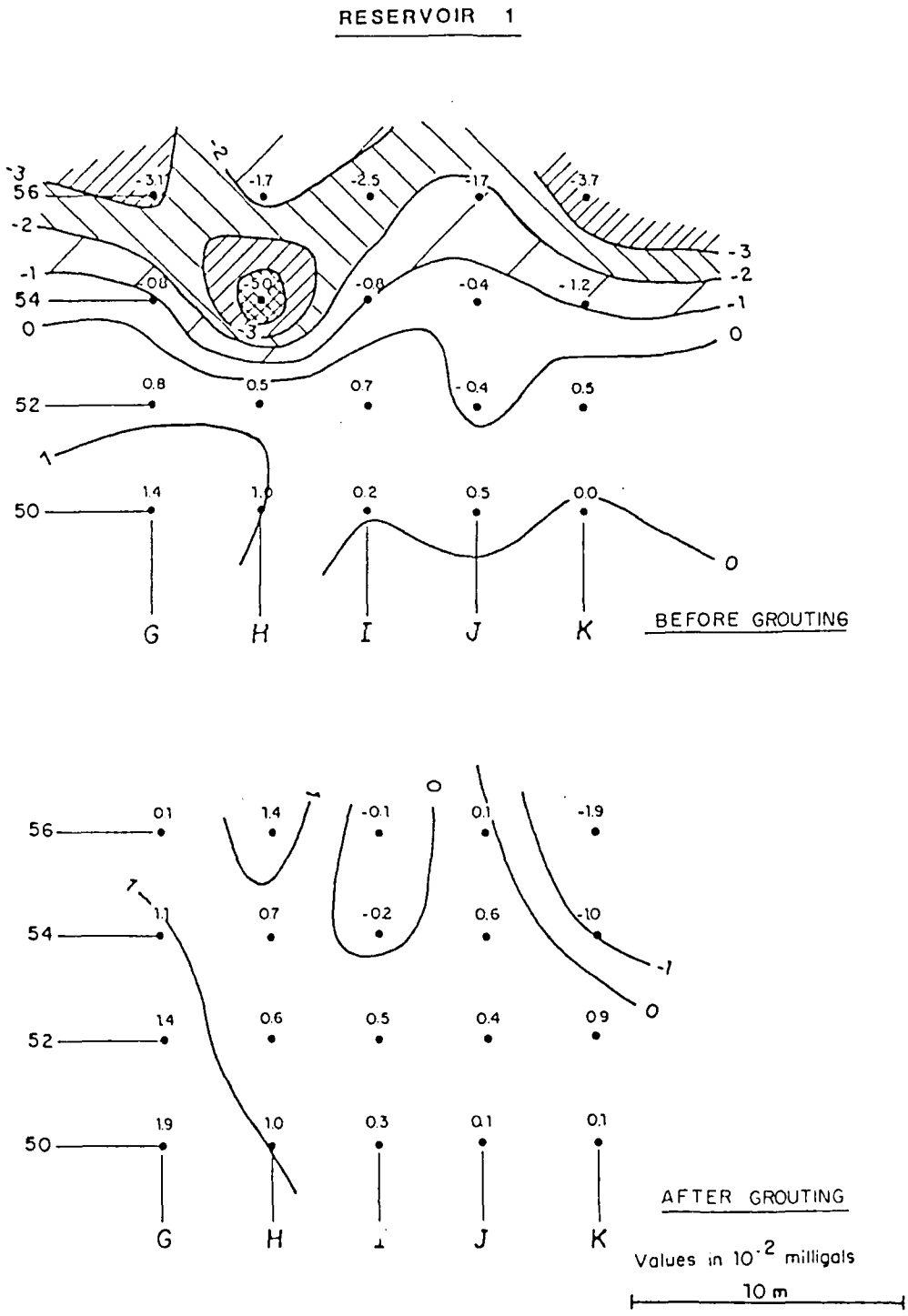

Figure 85. Nanterre water reservoirs: reservoir 1 zone, residual anomaly before and after grouting

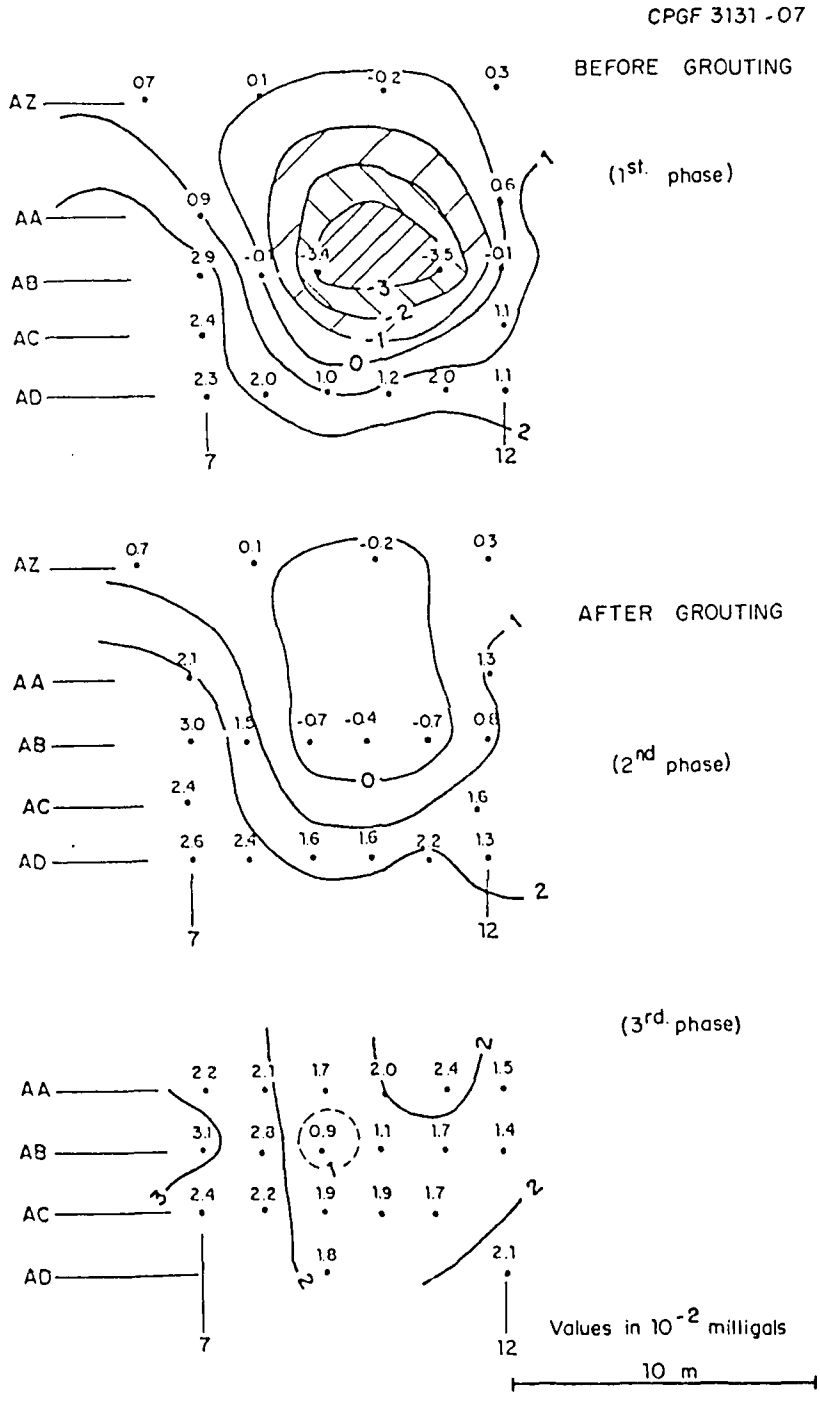

Figure 86. Nanterre water reservoirs: filter 4 zone residual anomaly map before and after 2 phases of grouting

Case history 9 : Porte Pouchet constructed area, Paris.

Client : City of Paris/Underground Quarries Authority, France
Survey references: September 1986, CPGF n° 2973
Site : Porte Pouchet site, northern border of Paris, France
Object : Large dissolution cavities in gypsum, 30 to 40 m deep, create sink-holes at the surface and jeopardize buildings, infrastructure.
Definition : microgravity gridding and profiling of an urban area of 800 x 400 m.

Geological setting

Damages to buildings, road pavements, mains and the like have been identified in this part of town. Cavities occur by dissolution of gypsum contained in tertiary marl formation at a depth of about 30 to 40 m. Cavities "progress" upwards when overlying sandy and fractured marly formations fall into the cavities. Weakening shallower materials became cohesionless, sink-holes appear.

Why microgravity?

When applied with maximum efficiency, this is the only method which may have yielded satisfactory results in such a complicated urban site to detect underground cavities.

Survey design

A total of 929 gravity stations were spread along boulevards, streets and cross-roads with 20 m spacing. Several hundred other stations from previous surveys in the area were integrated into the present network to better assess the regional extent of the cavitation phenomenon. Part of the survey was carried out at night to avoid heavy traffic.

Results

Prior to field gravity operations, an extensive investigation has been run in the area to classify all construction features above and below the street level: buildings, pavements, civil works, caves, underground openings, mains, etc ... All these data were digitized and specific terrain correction software was applied to correct raw Bouguer values from known artificial effects.

A terrain correction map was produced at the main office to be used by field crews for daily processing needs.

Negative residual gravity anomalies of 20 to 70 microgals were isolated. Modelling was performed to identify main causative bodies as dissolution cavities at a depth of 10 to 40 m, with weakened overlying formations.

Conclusions

Isolating a local density anomaly has seldom been so dependent of environmental constraints. CPGF's special skills in data collection and terrain correction procedures made such surveys possible. Subsequent drilling confirmed density anomalies identified by microgravity.

During a previous nearby survey, a weak zone shown by gravity was consequently grouted. We re-run this portion of the adjacent survey and found that the gravity anomaly had completely disappeared, confirming hence the efficiency of the grouting.

Fig.

Enclosed documents

Fig. 87 : portion of terrain correction map (CPGF ref. 2973-02)

Fig. 88 : portion of raw Bouguer map (CPGF ref. 2973-03)

Fig. 89 : portion of corrected Bouguer map (CPGF ref. 2973-04).

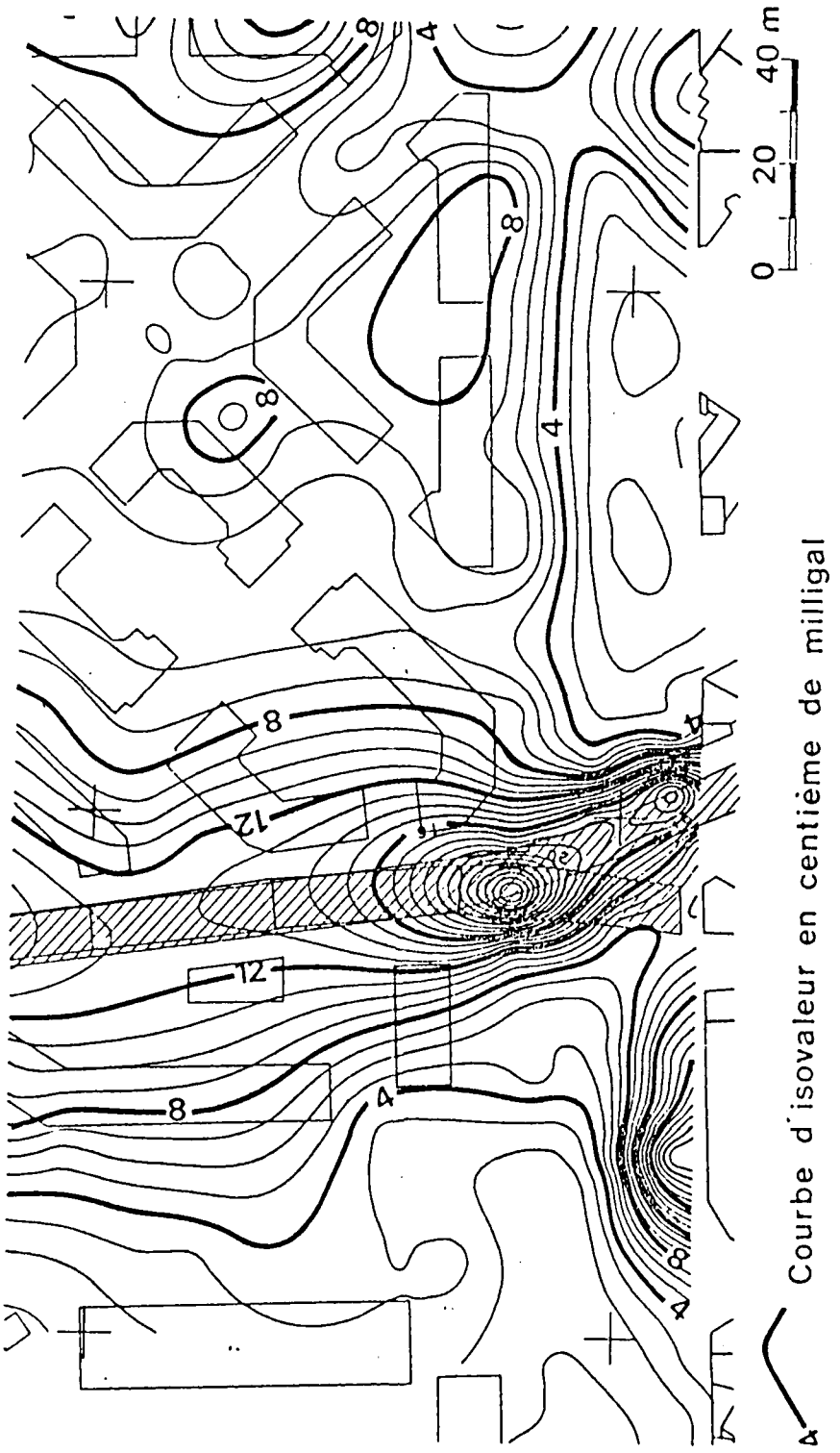

Figure 87. Porte Pouchet area, Paris, portion of terrain correction map values in 10^{-2} milligals)

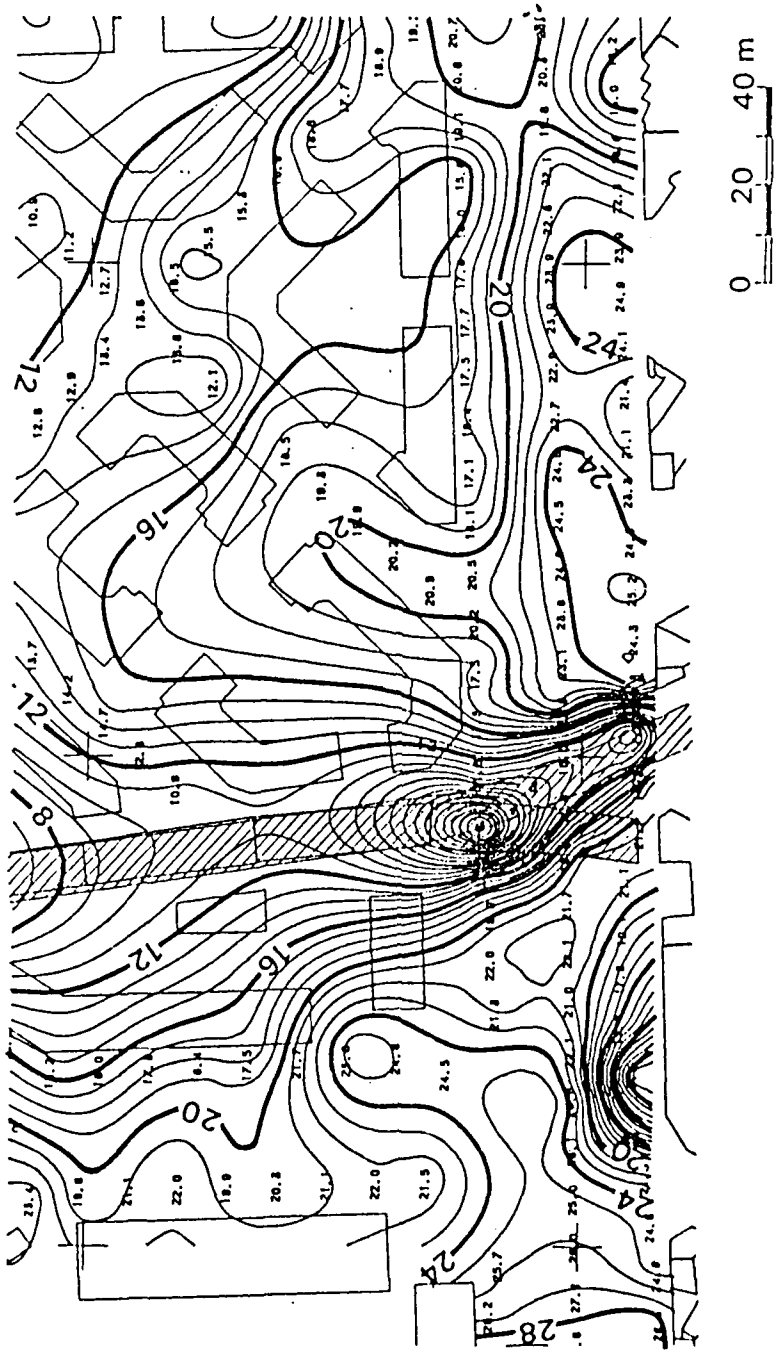

Figure 88. Porte Pouchet area, Paris portion of raw Bouguer map

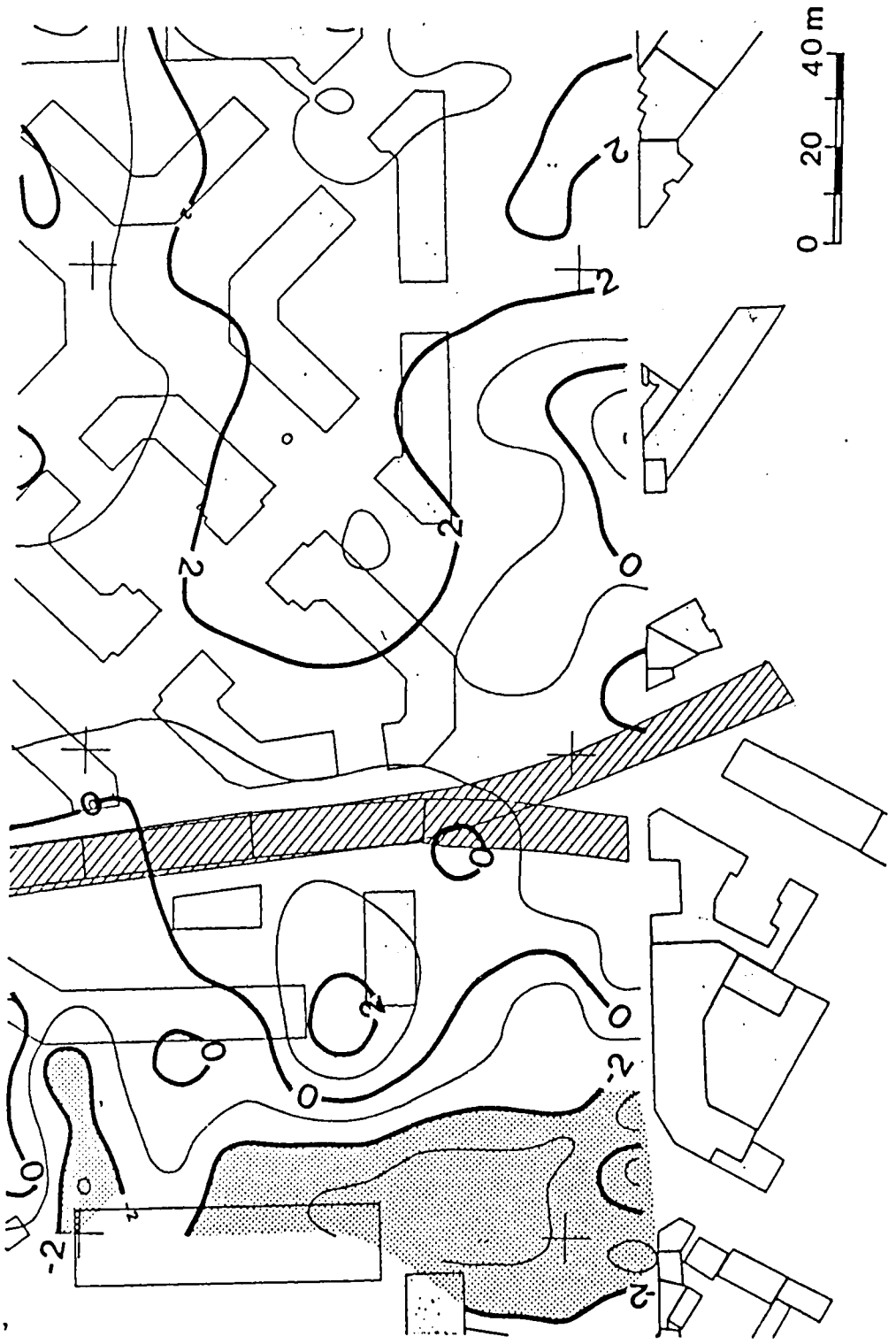

Figure 89. Porte Pouchet area, Paris, portion of corrected Bouguer map

Case history 10 : Dowell-Schlumberger factory, St Etienne.

Client : Dowell-Schlumberger
Survey references: June 1987, CPGF n° 3144
Site : Z.I. Molina la Chazotte at St Etienne (S.E. France)
Object : Elimination of excess cement grout from laboratory testing by underground storage
Definition : Microgravity survey for evaluation of residual densities of caved-in coal mines

Geological setting

Carboniferous strata under 0-20 m quaternary with slightly dipping coal measures.

Why microgravity?

Old unchecked maps of mine works are available, but mines have caved in, and the actual volume of voids available for grouting the excess cement is not known.

Survey design

157 microgravity stations with 10 x 20 m grid, including some additional stations located after initial processing.

Results

3 main anomalies attain -60 to -100 microgals, corresponding to three known mined zones. 2-D models confirm depth of 10 m for anomaly 3, 30-40 m for anomalies 1 and 2. Special processing was made on residual gravity, by modelling three known zones, 10 meters thick, and computing their densities by regression (other inversion techniques could not be used due to small survey area). Density deficits computed were:
Zone 1 (depth 30 to 40 m): -0.102 gm/cc
Zone 2 (depth 25 to 35 m): -0.093 gm/cc

Zone 3 (depth 5 to 15 m) : -0.269 gm/cc

Second residual map (difference between initial residual and computed gravity), shows possible extension of mined zones, particularly between zones 1 and 2 and confirms available volume V (for average density contrast 0.1 in areas 1 and 2). V = surface x 10 m x 0.1.

V (cu.m) $\simeq$ S(sq.m).

Conclusions

The position of two drill holes has been selected following gravity survey, and the project has been deemed feasible (sufficient volume available).

Enclosed documents

Fig. 90 : modelled profile

Fig. 91 : initial residual map (CPGF ref. 3144-04)

Fig. 92 : final residual map (CPGF ref. 3144-05)

Values of residuals are in 10^{-2} cmgals.

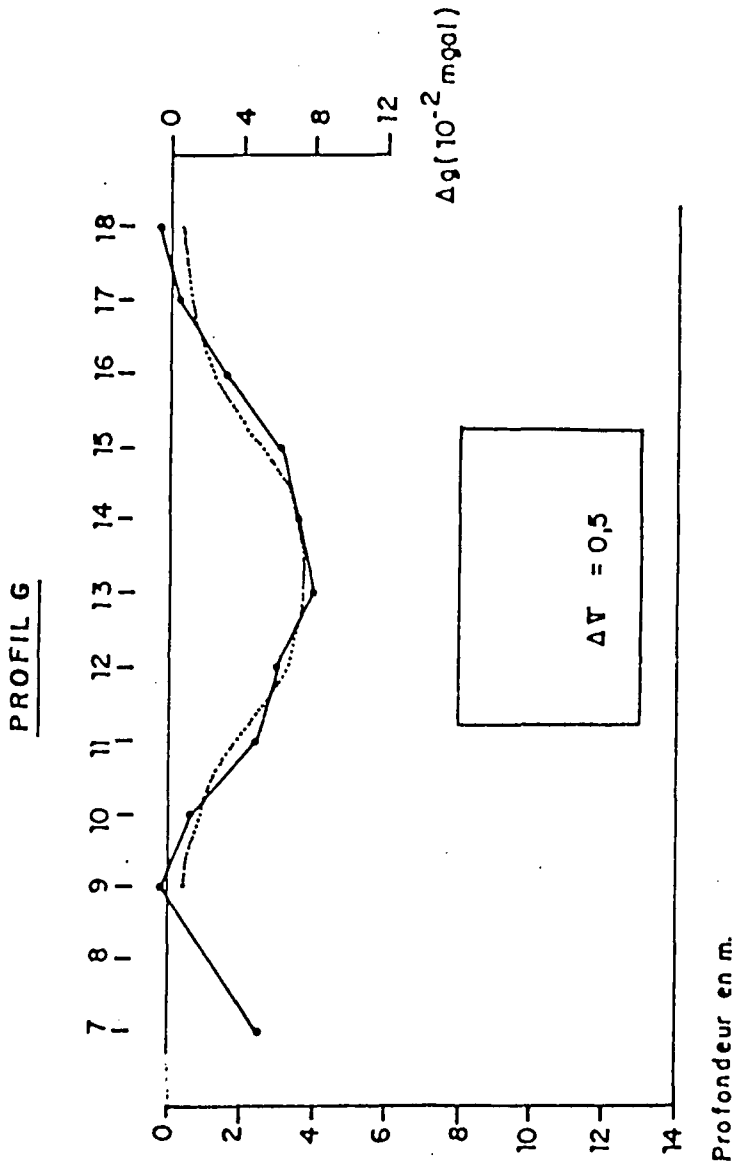

Figure 90. Dowell-Schlumberger factory, St Etienne, modelled profile

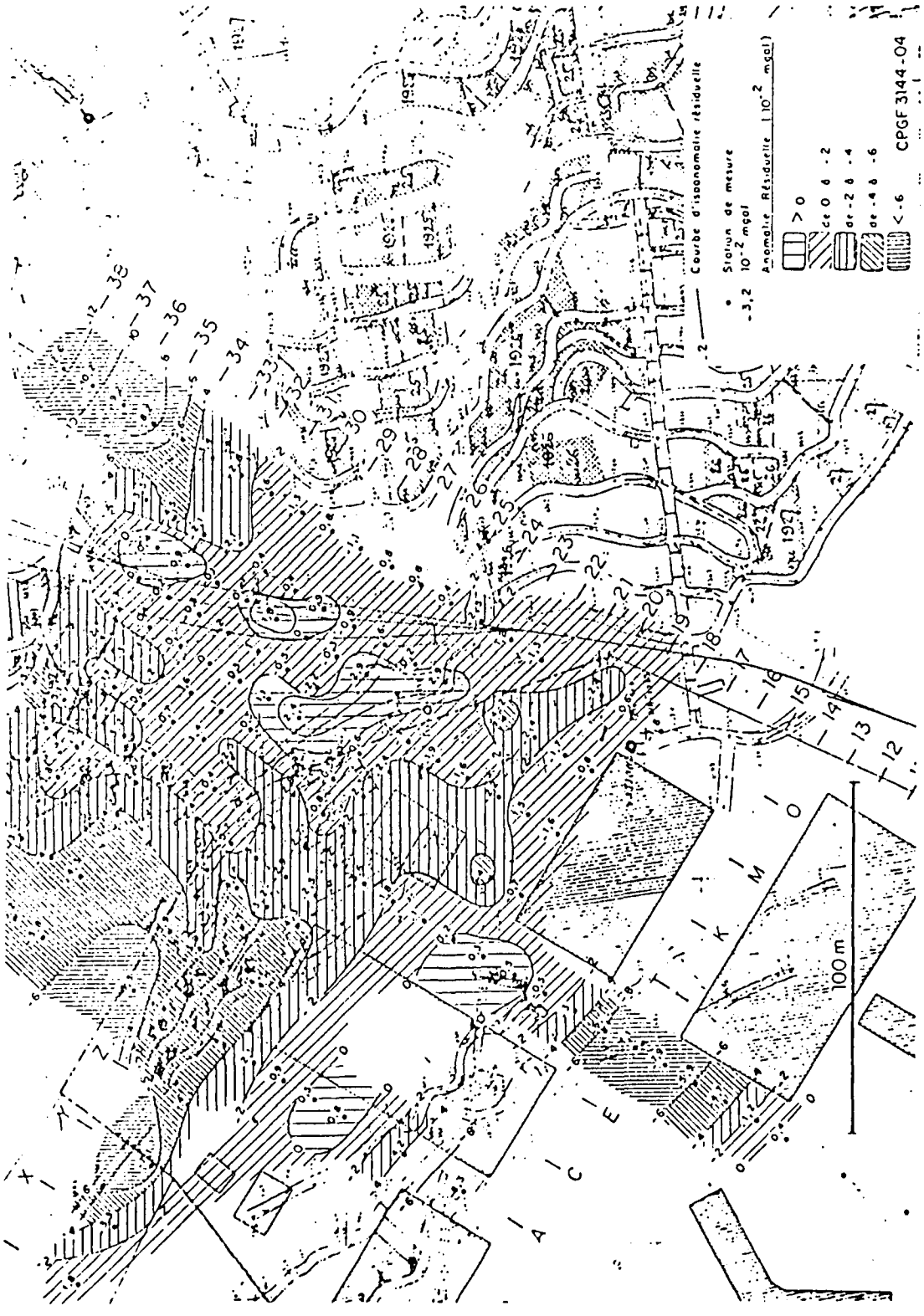

Figure 91. Dowell-Schlumberger factory, St Etienne, initial residual map

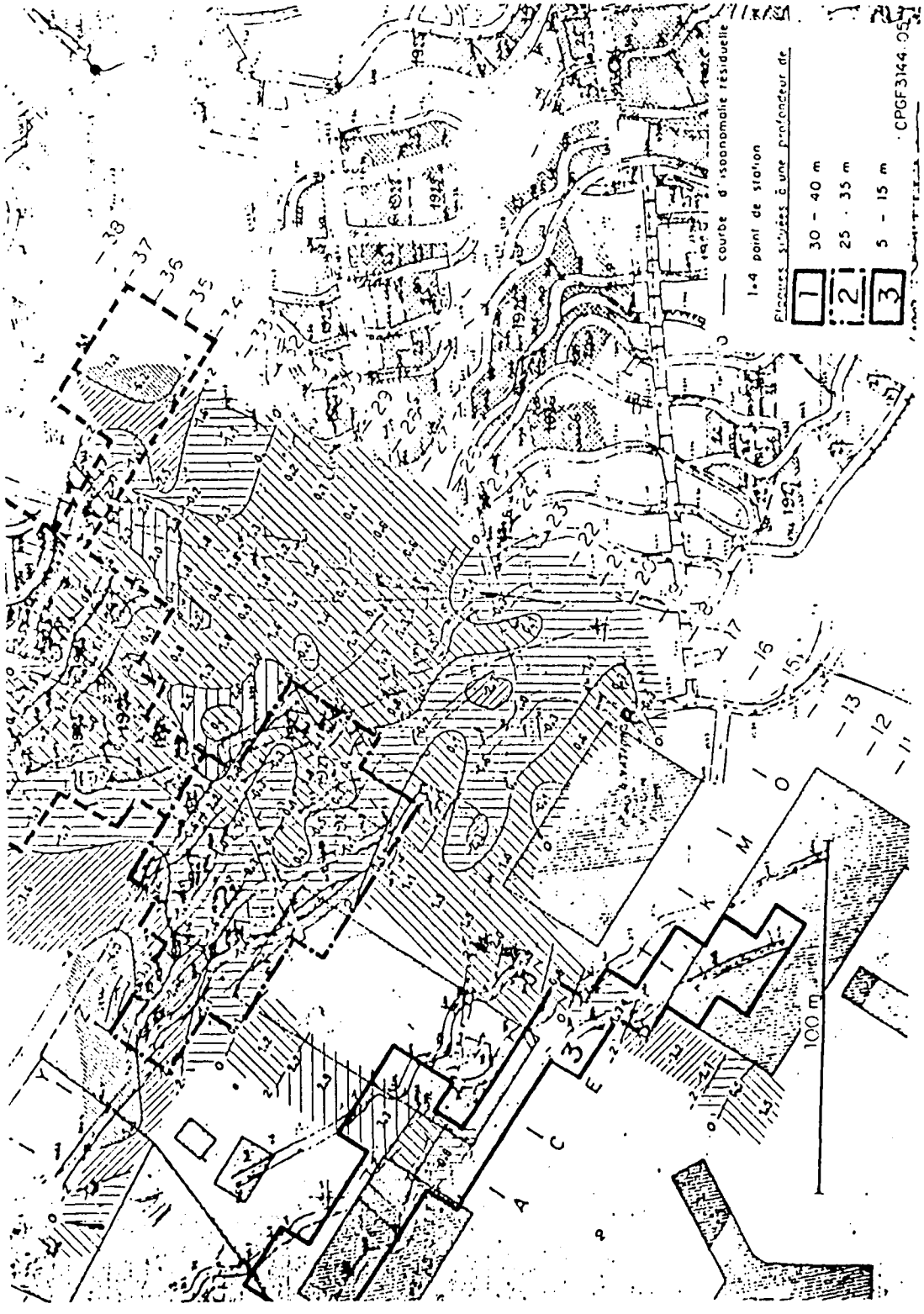

Figure 92. Dowell-Schlumberger factory, St Etienne, second residual map

Case history 11 : Civaux nuclear power plant.

Client : Electricité de France (French state power board)
Survey references: - September 1980, CPGF n° 1980
- November 1984 to February 1985, CPGF n° 2747
Site : Civaux, Poitou region, France
Object : Future nuclear power plant - foundation study
Definition : Microgravity and seismic refraction to map loose dolomite sand.

Geological setting

Vienne river valley: 5 to 12 m sand and gravel overlay Bajocian and Bathonian weathered and fractured limestone. A deep, loose zone has been found locally between depths of 30 and 50 m, corresponding to dolomite and dolomitic sand, overlain by fractured limestone, and overlaying compact limestone.

Why microgravity?

- Help map base of sand and gravel
- Delimitate loose dolomitic sand lenses and map density of foundation rock.

Survey design

First survey (1980): 277 stations (10 x 10 m grid)
Second survey (1984): 1,571 stations (10 x 10 m grid)
In addition, 15 vertical gradient measurements were made, with a tripod 1.60 m high. The survey was completed by 64 seismic refraction spreads, 120 m long each. Extensive drilling, mainly with L.W.D. recording was subsequently made.

Results

Vertical gradient measurements are developed in section 172 of this report. They show that main anomalies are located at depths around 30 m.
Special gravity processing included:

- 2 1/2-D modelling (CPGF's Modcong program) along geological profiles, using drilling results : interpretation shows that residual gravity anomalies are mainly due to sources located in the dolomitic sands, between depths of 30 to 50 m, and that density anomalies range from -0.2 to -0.6 gm/cc. Locally, densities are also reduced in the fractured limestone overlaying the dolomite.
- 3-D density inversion (CPGF's TESTFIL inversion technique): most appropriate slab is located between 30 and 50 m depths. Several positive anomalies show up with density contrasts of 0 to +0.2 gm/cc. One large negative zone and two negative axes correspond to density contrasts of -0.1 to -0.3 gm/cc.
- Variable thickness inversion: first model selected had horizontal top (10 m depth, below alluvium) and variable base. Map supplied is similar to the density contrast map, but with greater contrasts. In a second model, variable top, corresponding to base of sand and gravel found in drill holes, was selected.

Seismic refraction interpretation shows following velocity sequence:

1. Dry sand and gravel:	: 600-800 m/s
2. Weathered limestone (below water table)	: 1700-2500 m/s
3. Fractured limestone	: 3000-3800 m/s
4. Dolomitic zone	: 2500-3300 m/s
5. Compact limestone	: 3800-4400 m/s

Deep refractor corresponding to layer 5 occasionally disappears and deep velocities around 3000 m/s are found along gravity low axes, corresponding to dolomitic sand lenses.

Conclusions

Position of nuclear power plant was adjusted to fit with sound zones found by geophysical investigation:

- positive densities in the 30-50 m section
- deep refractor with velocities exceeding 3500 m/s.

Numerous drill holes with L.W.D. confirmed geophysical results. No clear cavities were found, all anomalies seem to correspond to loose dolomitic sand.

Enclosed documents

Fig. 93 : residual gravity map, anomalies in 10^{-2} milligals, with negative values of -230 µgals towards N.W., -130 µgals towards E, -8 to -12 µgals along two axes. These two negative axes delimitate main positive zone (R2) with values of 0 to +10 µgals (CPGF ref. 2747A-05)

Fig. 94 : density inversion (slab between 10 and 50 m depth) (CPGF ref. 2747A-08)

Fig. 95 : depth to deep seismic refractor (generally V > 3 500 m/s ; along deep axes, velocity can drop below 3 000 m/s) (CPGF ref. 2747B-02)

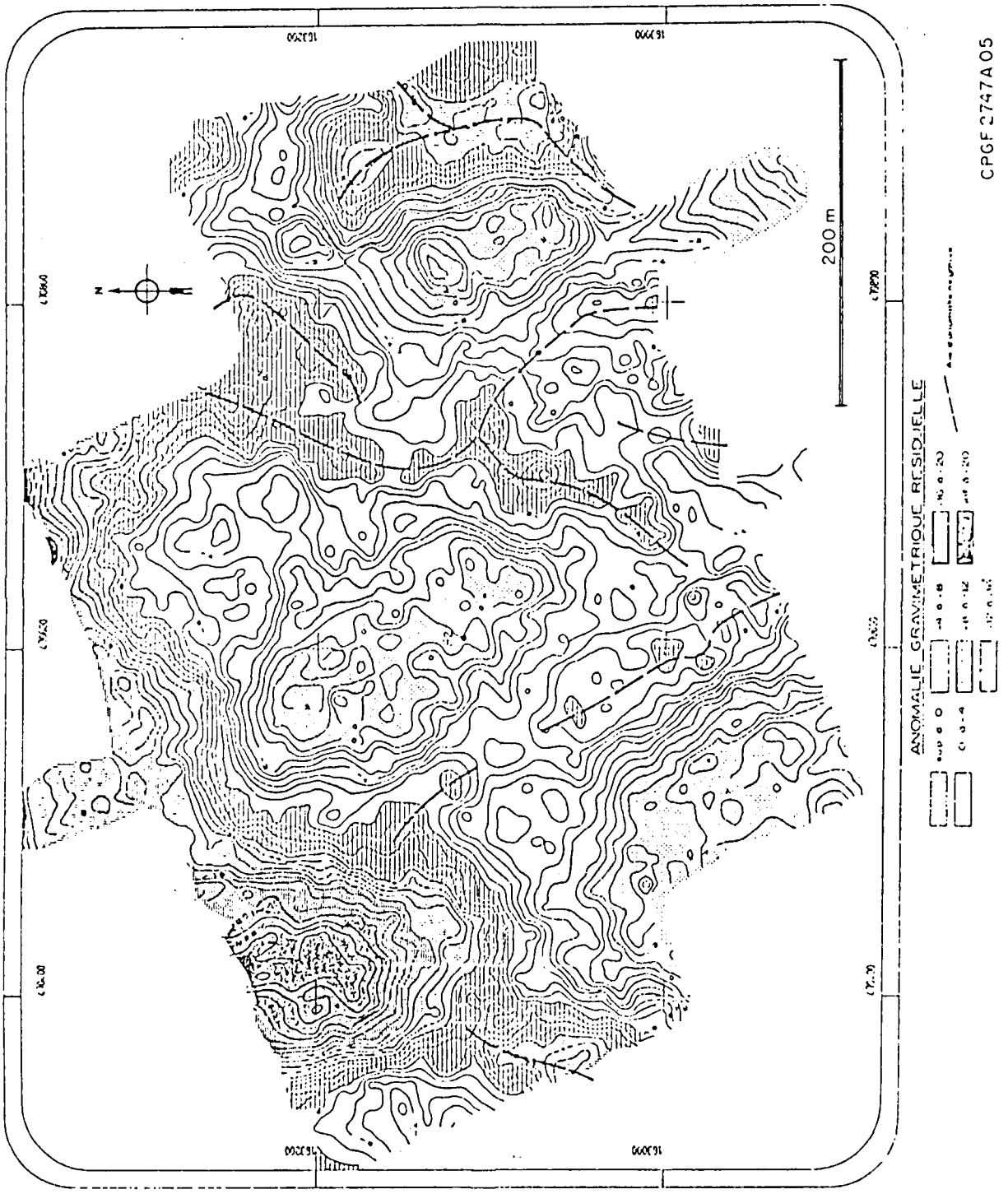

Figure 93. Civaux nuclear power plant, residual gravity map

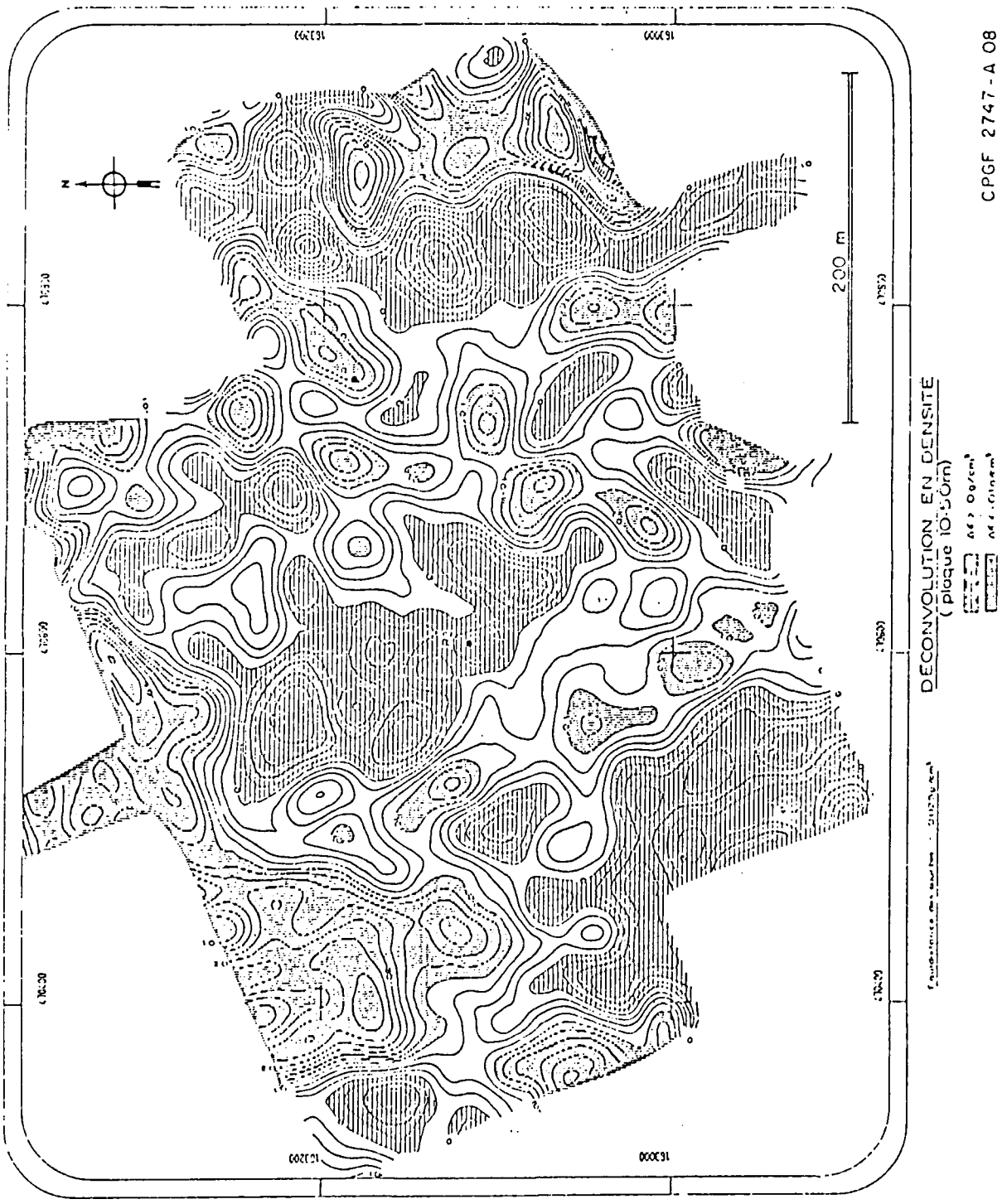

Figure 94. Civaux nuvlear plant, density inversion

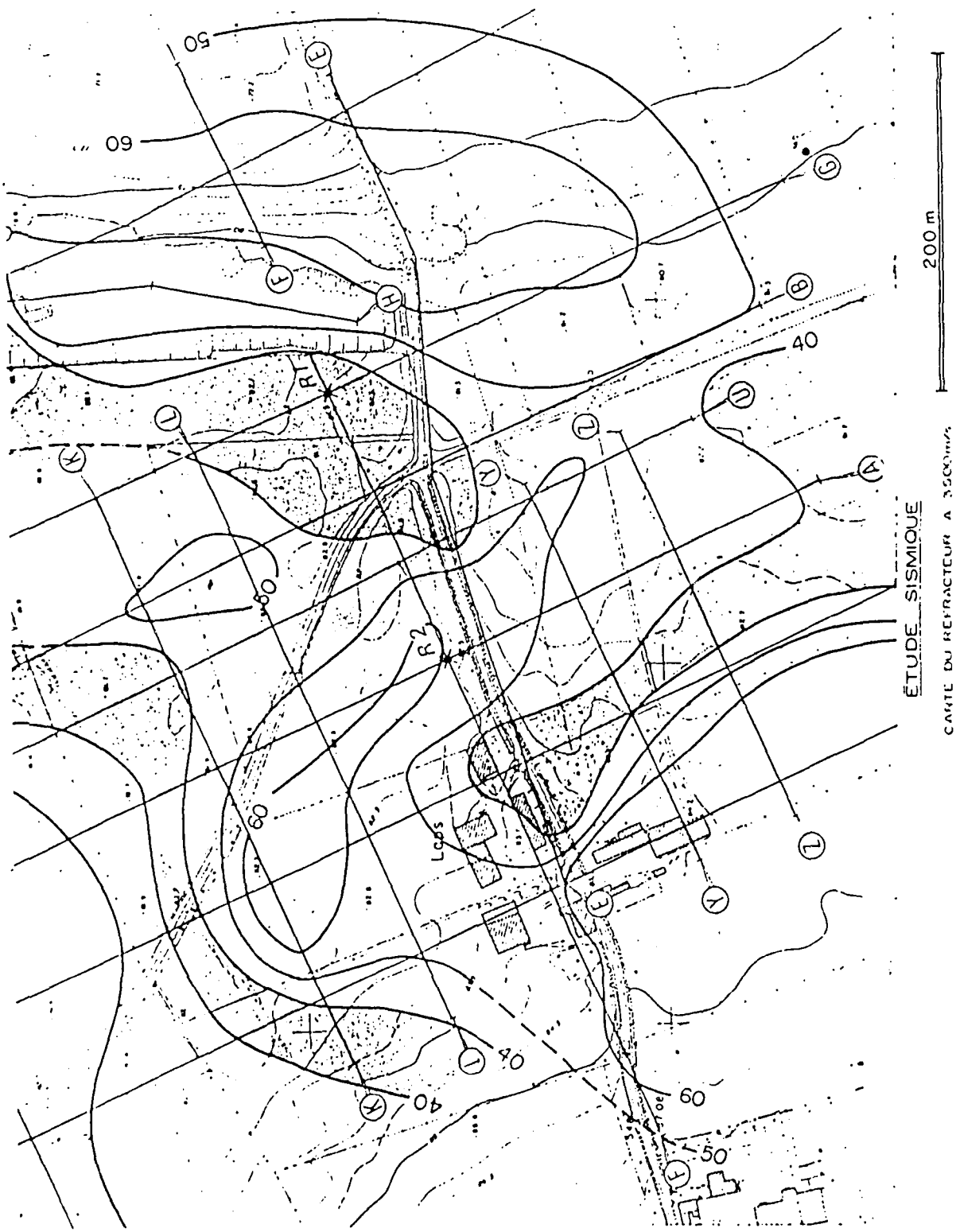

Figure 95. Civaux nuclear power plant, depth to deep seismic refractor

Case history 12 : Sailly-les-Cambrai housing project.

Client : Département du Nord, Inspection des Carrières Souterraines (Underground Quarries Inspection Authority)

Survey references: November 1985, CPGF n° 2854

Site : Sailly-lez-Cambrai, near Douai, northern France

Object : Housing development project ; underground quarrying with chambers and galleries built during World War I, suspected.

Definition : Gravity survey to map the cavities.

Geological setting

Sub-outcropping cretaceous chalk, partly covered by tertiary silt, clay and sand.

Why microgravity?

This is a typical setting where only very detailed gravity survey and interpretation could map the possible cavities.

Survey design

10 x 10 m gridding over the entire zone (4000 sq. m) ; grid tightened to 5 m in most suspected sector, for a total of 266 stations.

Results

At the southwest corner of the survey, there is a known old opencast quarry now backfilled. It has an obvious lateral effect on gravity readings. This has been taken care of by modelling (15 m of fill, lack of density of 0.2 gm/cc).

Corrected residual anomaly map shows very clean contours of closed negative anomalies of about 70 microgals. Quarries are suspected to be situated at a depth of 10 to 15 m. Modelling was done using known dimensions ; results show

that residual anomalies cannot be totally explained by possible unknown quarries. Then 3-D density inversion was successfully tempted using a slab situated between depths of 7 and 12 m. Very sharp density contrasts are met along different axes, possibly in relation with galleries. Quarried thickness bigger than the model used for inversion yielded a better result, because of possible decompressed upper sections. Unexplained residual is almost nil, so the 0-7 m slab shows no significant density variations.

Conclusions

A sophisticated inversion technique was used to help interpret this gravity survey where simple modelling was unsatisfactory. Exploration and mapping of partly filled chambers and tunnels has started. Mapped part has been drawn on residual map. Very clear correlation are visible.

Enclosed documents

Fig. 96 : Residual anomaly map not corrected for opencast quarry influence at the southwest corner of the survey (CPGF ref. 2854-03)

Fig. 97 : same as 2854-03, but corrected for known quarry effect (2854-04)

Fig. 98 : typical gravity anomaly and interpretational models (2854-05)

Fig. 99 : density deconvolution, 7-12 m slab (CPGF ref. 2854-06).

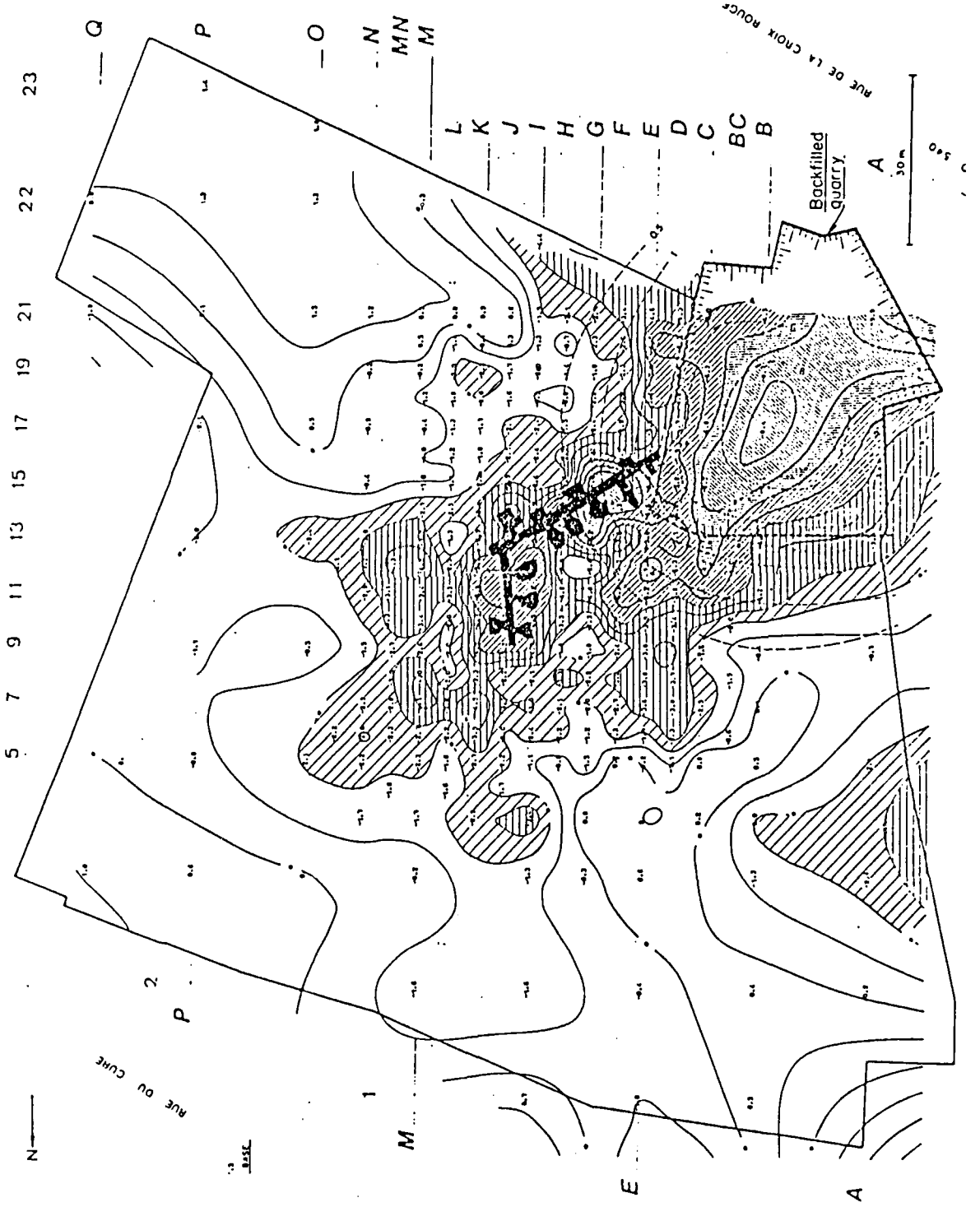

Figure 96. Sailly-lez-Cambrai housing project residual anomaly map (values in 10^{-2} milligals)

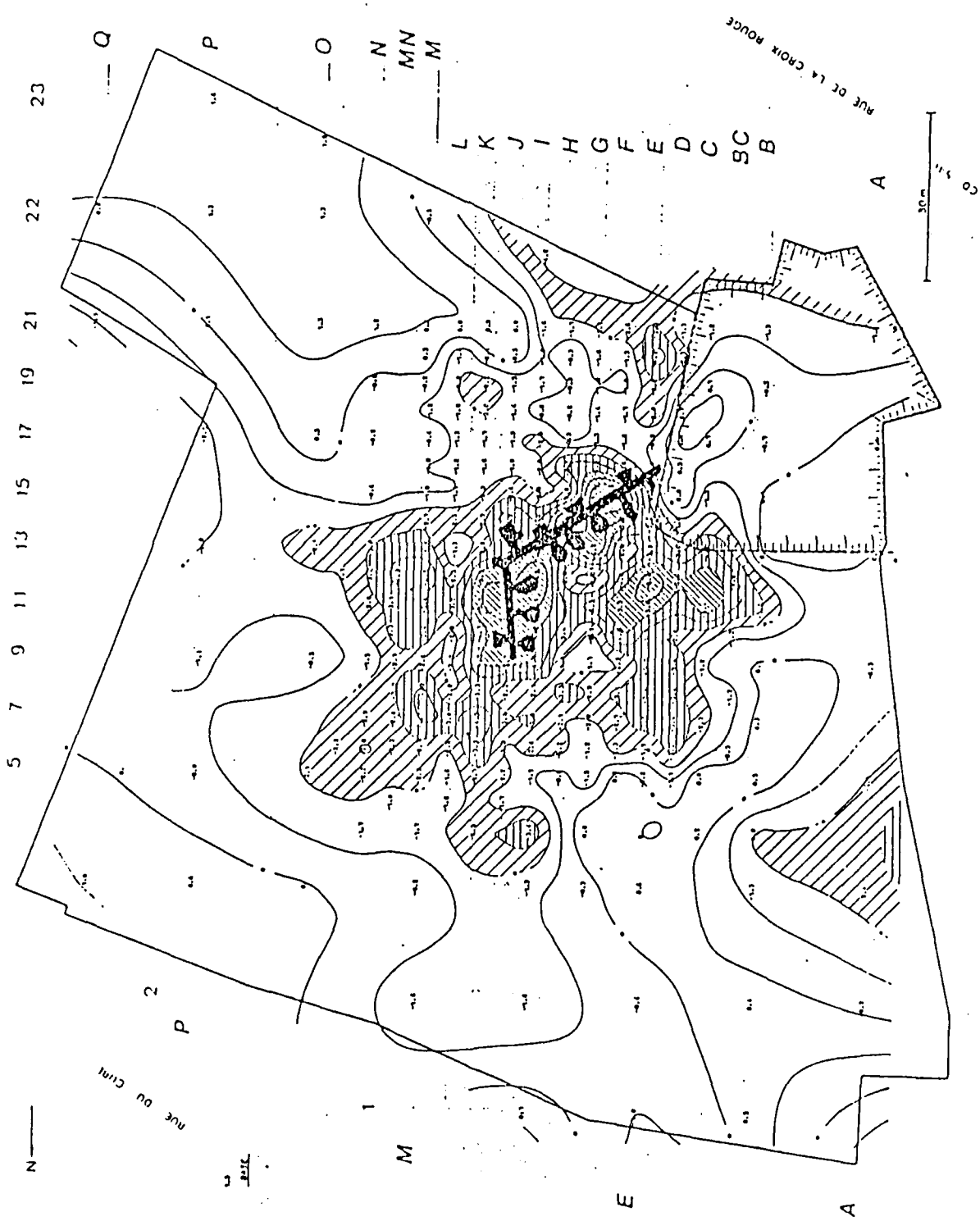

Figure 97. Sailly-lez-Cambrai housing project, residual anomaly map corrected for effect of opencast quarry (values in 10^{-2} milligals)

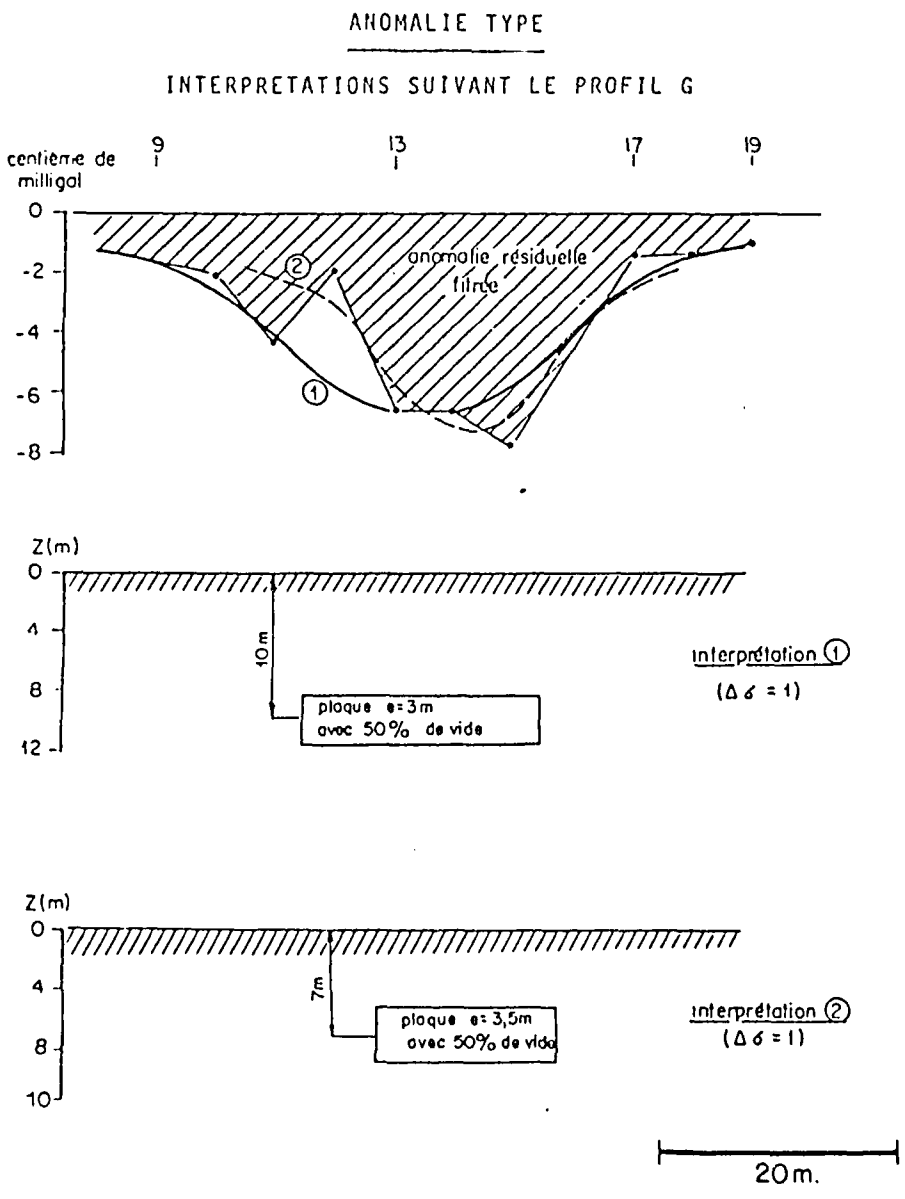

Figure 98. Sailly-lez-Cambrai housing project. Typical gravity anomaly and interpretational models

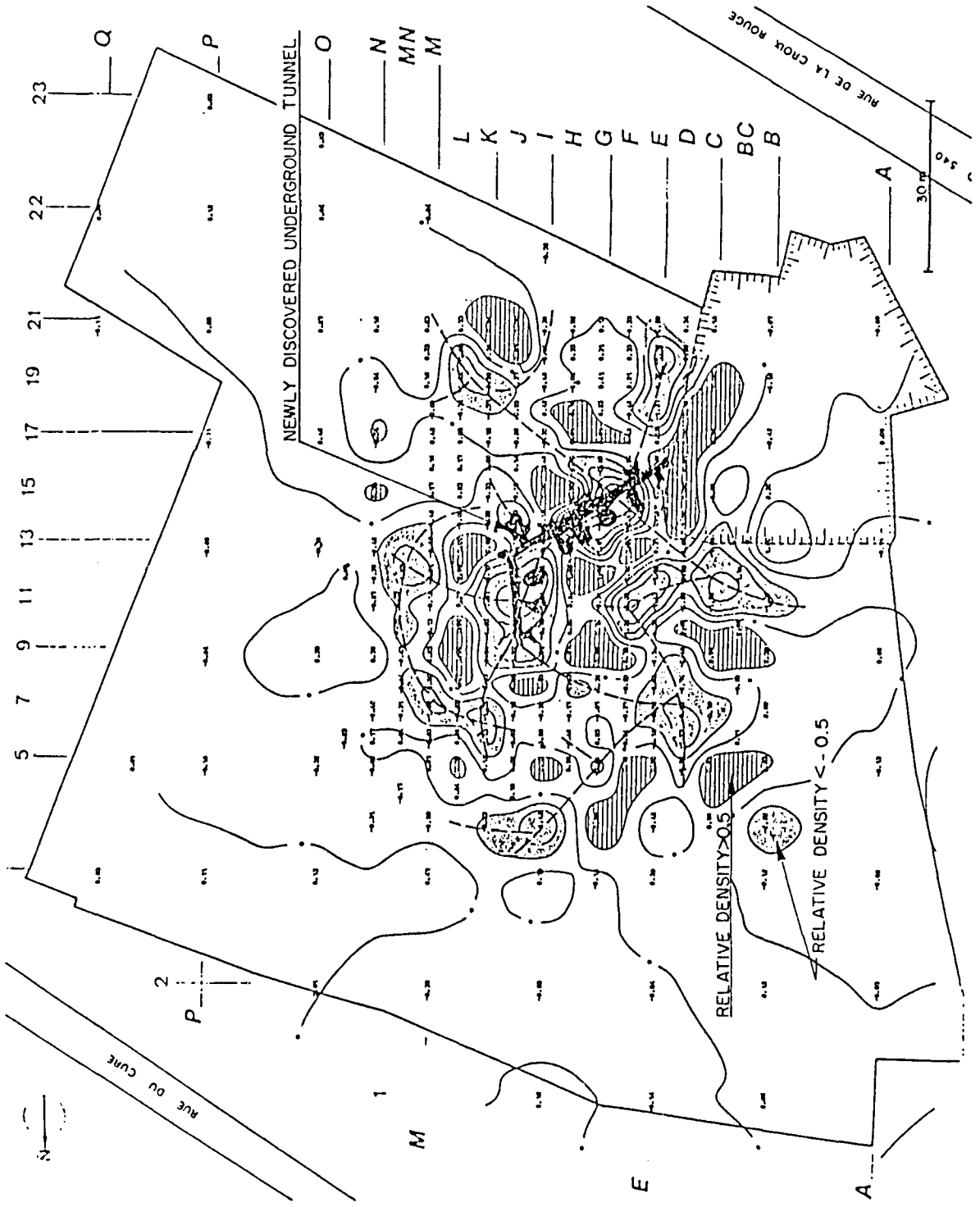

Figure 99. Sailly-lez-Cambrai housing project: density deconvolution (7-12 m slab)

Case history 13 : Liendo cement plant project (Spain).

Client : Ciments Lambert
Survey references: January-May 1966, CPGF n° 348
Site : San Julian, Liendo (near Laredo), Spain
Object : Future cementation plant. Site surveys
Definition : Microgravity to map karstic cavities network.

Geological setting

Upper cretaceous limestone, highly tectonised and karstified. Seashore site, cliff about 30 m high.

Why microgravity?

Complete the geological investigations by mapping the underground voids network in the most economical manner at a site of difficult access and rough surrounding topography.

Survey design

803 gravity stations carried out along profiles and on a grid with 10 m spacing. Check boreholes drilled.

Results

Very large negative residual anomalies (50 to 300 microgals) are mapped. The drilling proved, as expected from the gravity survey, that superficial dissolution features were connected to huge underground cavities sometimes partly infilled with debris. Geomorphology suggested a certain downward extension of surface dissolution sink-holes, but microgravity mapped the invisible part of the karsts.

Conclusions

Survey took place in two steps. First, profiles and calibration boreholes, very satisfactory results. Then, gridding and more boreholes. Large terrain corrections had to be handled carefully to filter out lateral effects.

Enclosed documents

Figure 100 : gravity profiles P5-P2 (CPGF ref. 348-02c)

- Note in the corner of the figure, a Nettleton profile to determine surface densities. Best adjustment for density of 2.35 gm/cc
- Values in 10^{-2} milligals.

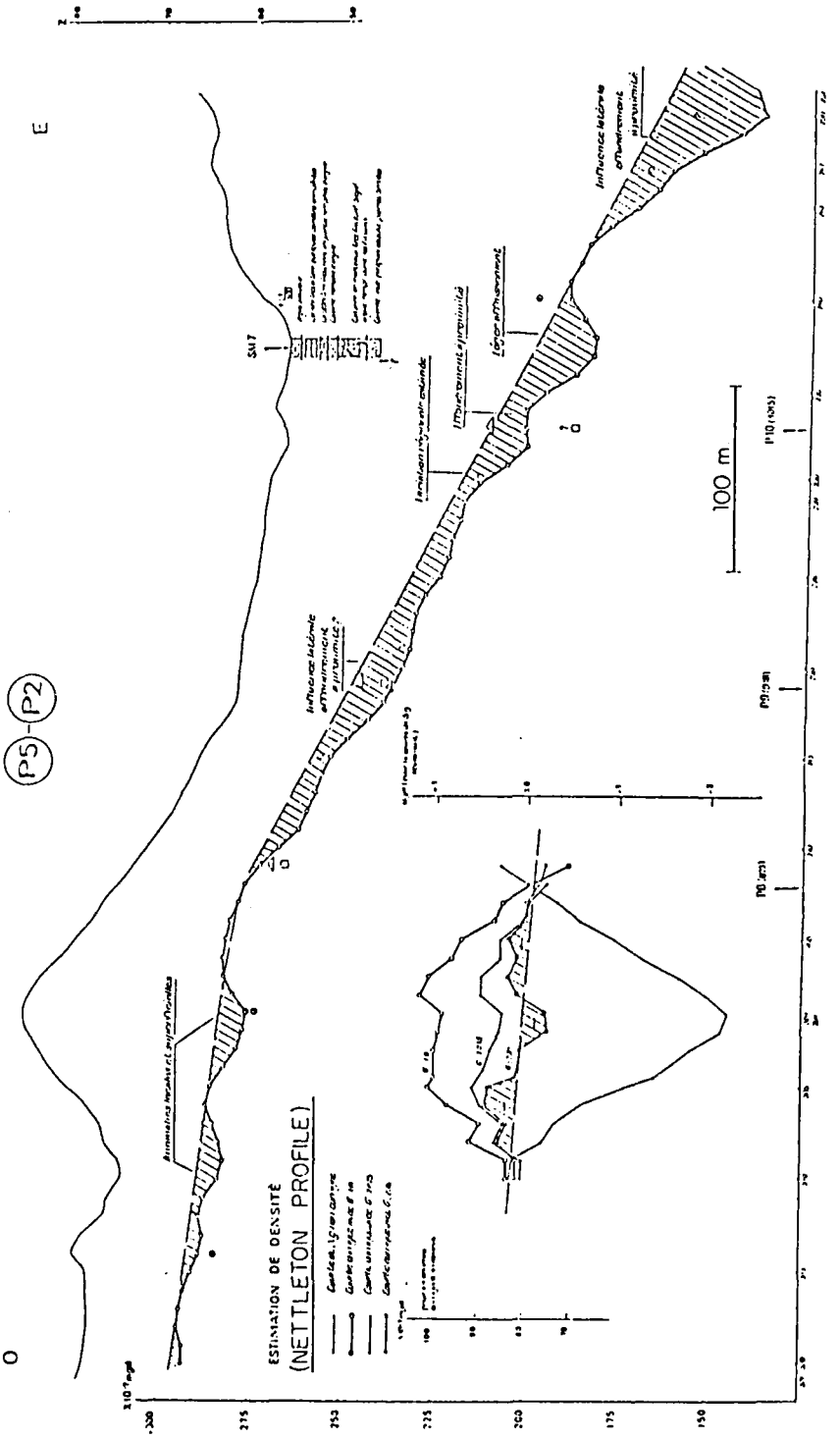

Figure 100. Liendo cement plant project (Spain)
Gravity profiles and Nettleton profile

Case history 14 : Jebel Dhanna existing petroleum tank farm (Abu Dhabi).

Client : ADCO, Abu Dhabi (owner), PARTEX, Lisbon (consultant)
Survey references: August-September 1983, CPGF n° 2550
Site : Jebel Dhanna tank farm, Abu Dhabi, U.A.E.
Object : Tank farm under operation. Foundations stability jeopardized by weak underground due to dissolution features.

Definition : Complete soil investigation scheme by geophysics and drilling to anticipate a soil improvement programme.

Geological setting

Miocene sandstone and limestone filling a closed basin, basement made up of rhyolites. The whole site is an uplift feature related to salt plug phenomenon well known in the Gulf area. Basin is highly tectonized ; gypsum outcrops and is weathered.

Why microgravity?

Major underground anomalies are suspected to be voids due to dissolution of gypsum and limestone, and a vast area had to be covered by investigations within the tank farm under operation. Only microgravity could be able to map density anomalies under present conditions.

Survey design

Typical layout for geological mapping : 707 gravity stations spread over a grid with 15 to 25 m centers ; a few vertical electrical soundings for depth calibration ; aerial photos examined for a better approach of the local geology.

27 boreholes drilled (by Fugro). Supervised and results interpreted by CPGF ; logging while drilling carried out on each borehole (rate of drilling and fluid pressure) ; piezometers installed on each borehole and water table monitored ; water samples taken and chemical analyses performed mainly to obtain the sulphate content.

Results

The residual Bouguer map obtained was fully interpreted in terms of underground structural geology helped by drilling, water table monitoring and surface geology. Beyond the detection of small voids, we were able to map the differential weathering and possibly identify lithology. Weak terrain was very clearly identified for further investigations, while sound basement showed up as gravity "highs" (positive residual anomalies).

3-D gravity inversion was carried out to output underground densities map at selected slab thicknesses. Hence, the client was provided with the variations of a usual parameter easy to interpret and showing possible problem areas between the surface and a depth of about 40 m.

Conclusions

This survey shows how microgravity can be a very powerful, yet a cost-effective investigation tool when complemented with drilling and other surveying techniques. Geophysics were able here to design the expected grouting works by suggesting the grouting technique and layout to be used.

Enclosed documents

Fig. 101 : residual anomaly map (CPGF ref. 2550-02)
Fig. 102 : density variation map (CPGF ref. 2550-03)
Fig. 103 : synthesis map (CPGF ref. 2550-08)

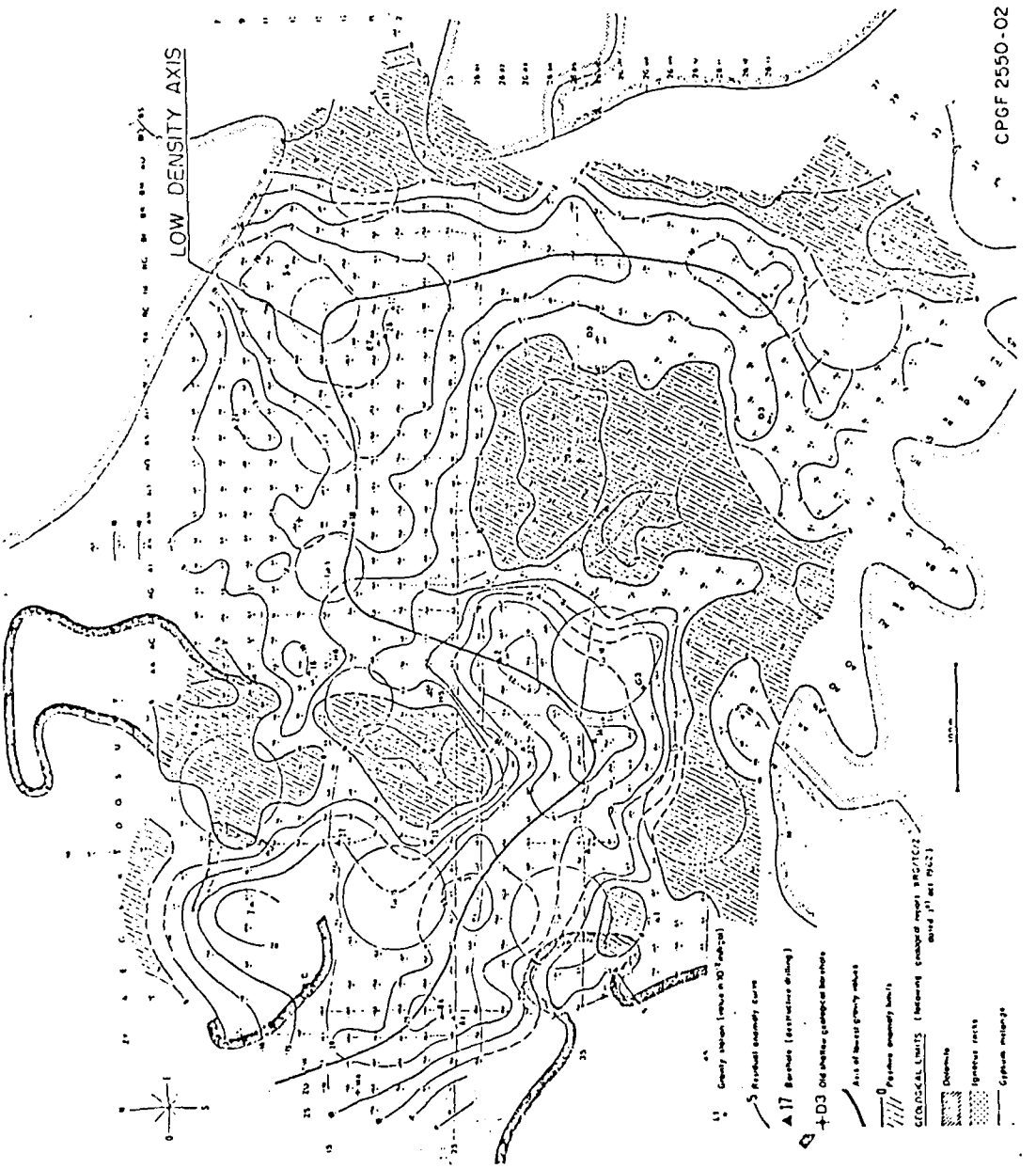

Figure 101. Jebel Dhanna tank farm - Residual anomaly map
Values in 10^{-2} milligals
Hatched zone: positive residual

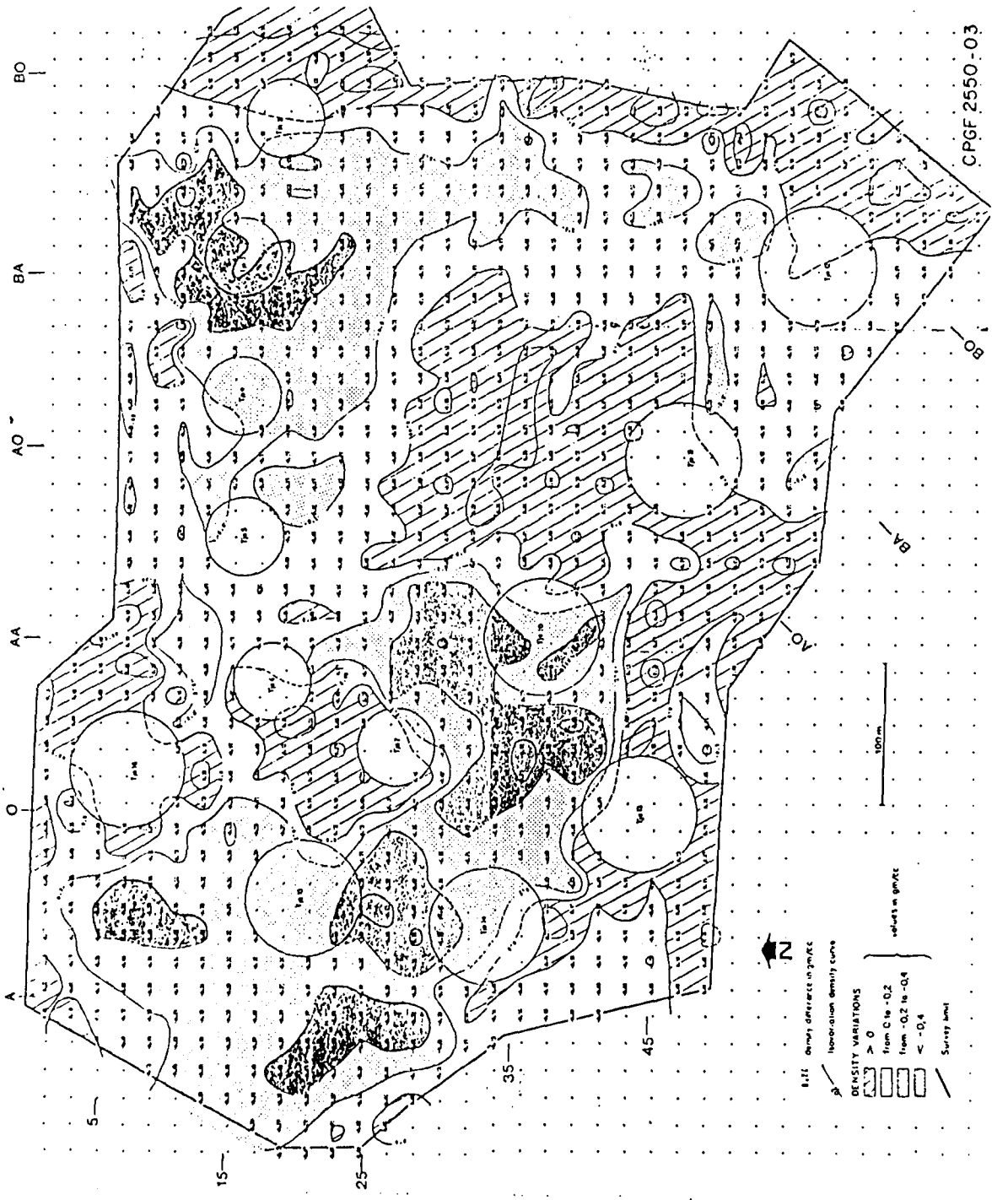

Figure 102. Jebel Dhanna tank farm: density variation map

Darkest zones: < -0.4 gm/cc

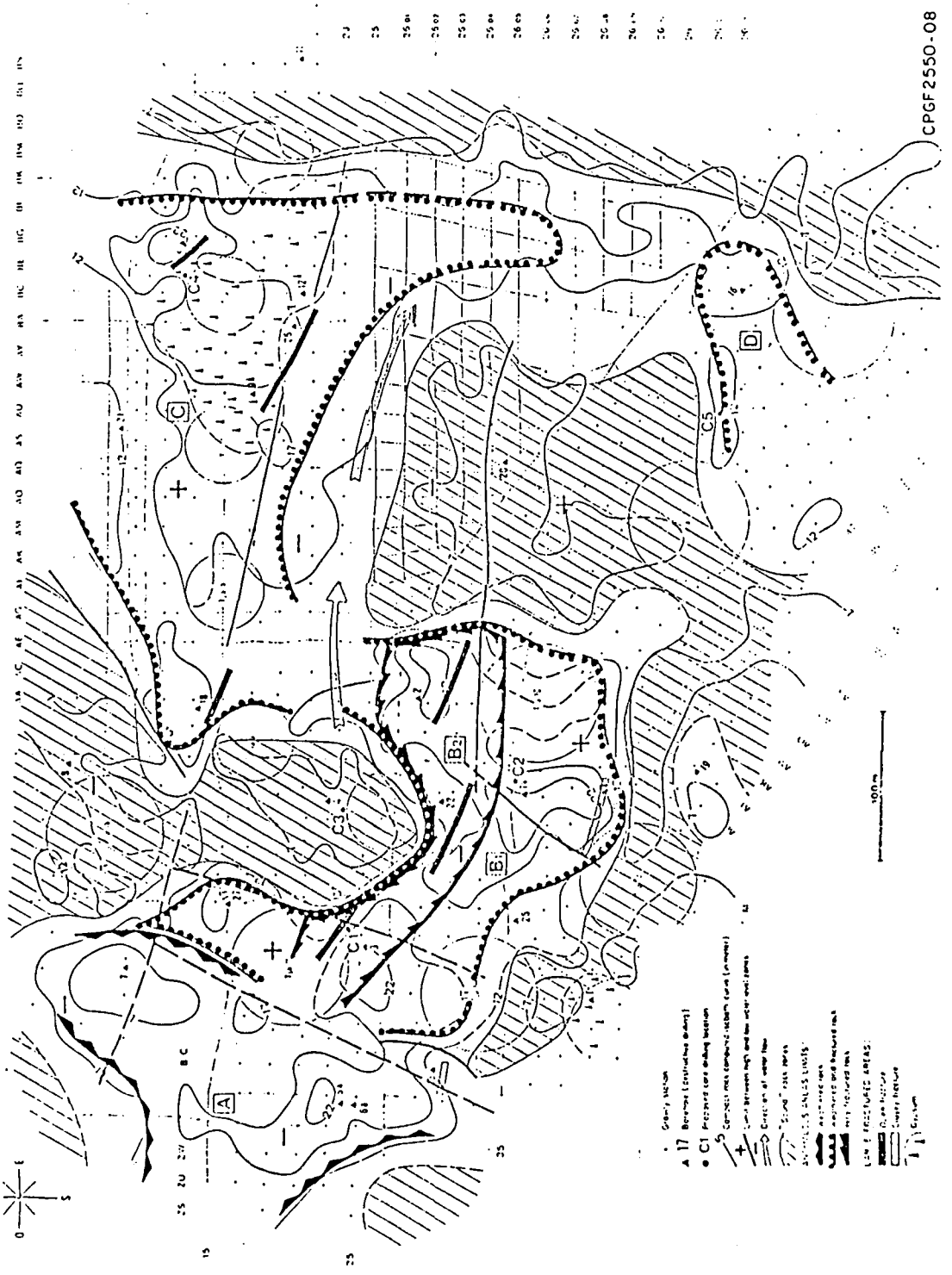

Figure 103. Jebel Dhanna tank farm: synthesis map

Case history 15 : OPHLM Lille building project.

Client : Epale (New Town Authority)
Survey references: July 1981, CPGF n° 21988
Site : New town of Villeneuve d'Ascq, near Lille, northern France.
Object : Look for possible extensions of a known underground quarry.
Definition : Very large underground chalk quarries exist over the southern belt of the town of Lille. Land developers are required to make sure that no cavities exist in the underground of the construction zone.

Geological setting

Cretaceous chalk is outcropping in the entire area.

Why microgravity?

The question here was to investigate the site of a large building in order to detect the possible extensions of a known quarry, previously surveyed by CPGF. Microgravity is the most reliable method to certify whether quarry voids are present or not.

Survey design

85 gravity stations were carried out over a square grid of 10 x 10 m. Nine boreholes were sunk for calibration purposes. Drilling rate and reflected percussion parameters were recorded while drilling.

Quarry voids were detected in several boreholes ; in one of them, a panoramic view was taken by a stand-still camera.

Results

Residual Bouguer map shows negative anomalies of about 20 to 50 microgals as an extension of known quarries. Drilling confirmed the presence of partly filled quarry chambers within the contours outlined by microgravity. Logging

while drilling helped distinguish between silt, backfill and weathered chalk on one hand and quarry voids on the other hand, as possible causes of computed density anomalies. As a matter of fact, similar gravity expressions occur caused by radically different features.

Conclusions

A very reliable microgravity survey, backed up by borehole data, drilling parameters and detected caves" panoramic views helped resolve a foundation problem quickly and in a most economical way. Once the void was located by drill hole S4, a well was dug and voids mapped by surveying. Very complicated limits explain irregular drilling results.

Enclosed documents

Fig. 104: Location map and known quarry limits (CPGF ref. 2281-01)

Fig. 105: Residual anomaly map. Borehole locations. Residual values in 10^{-2} cmgals (CPGF ref. 2281-03). Drill holes results:
S4: void (quarry)
S5, S10: filled quarries
S2, S3, S7: weathered and fractured chalk
S1, S6, S8, S11: sound chalk

Fig. 106: Panoramic view of a quarry detected by microgravity located by drill hole S4 and taken by drill hole camera (CPGF ref. 2198B-04).

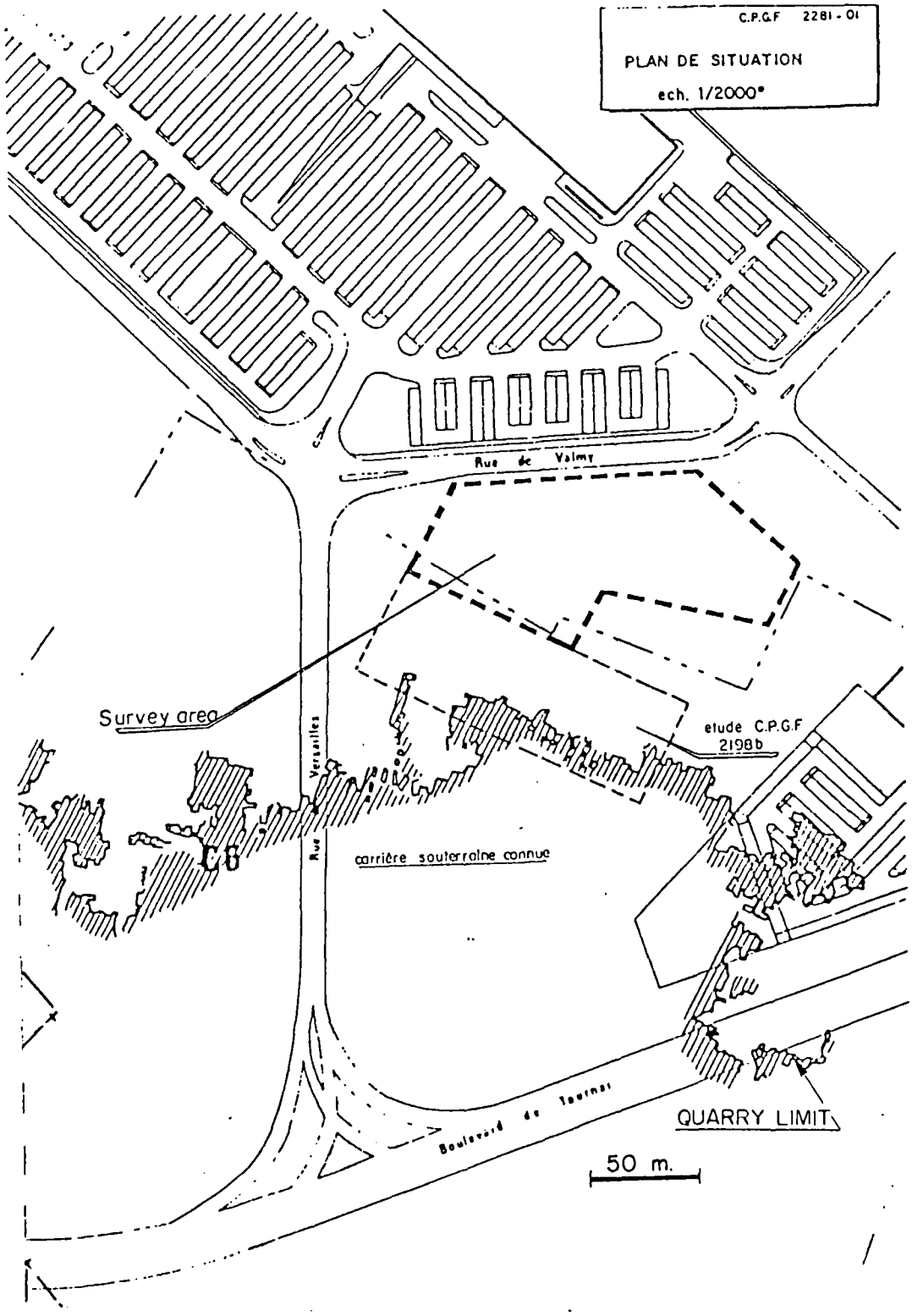

Figure 104. OPHLM Lille building project - Location map and known quarry limits

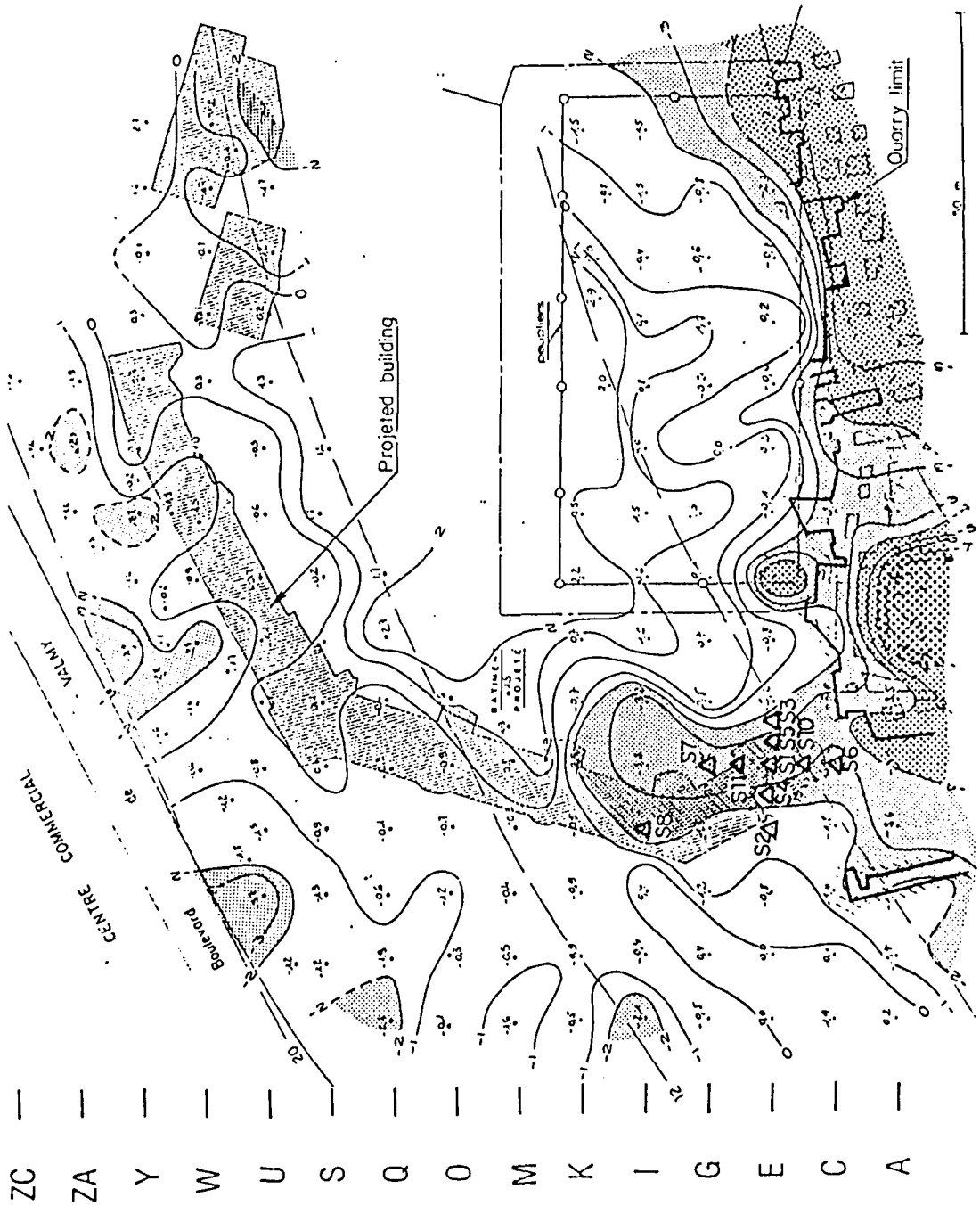

Figure 105. OPHLM Lille building project. esidual anomaly

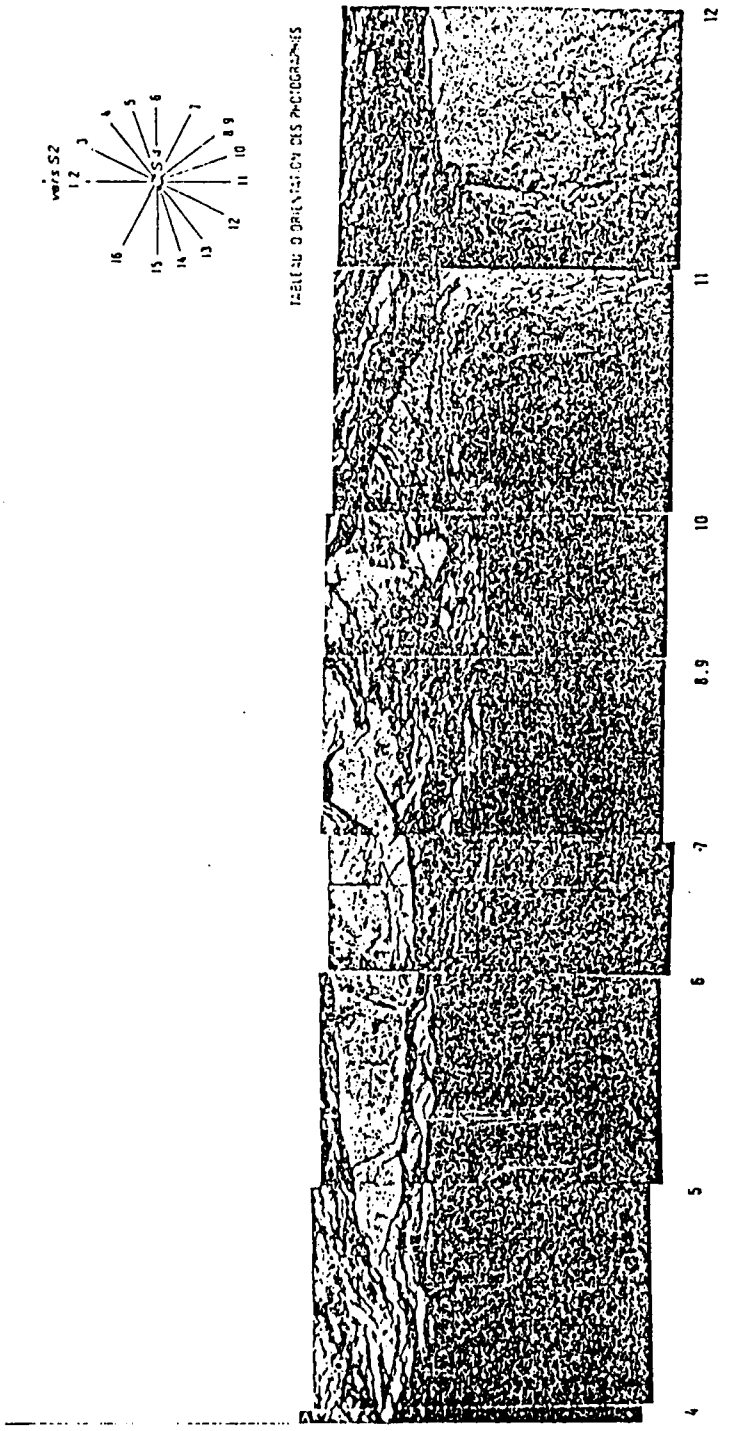

Figure 106. OPHLM Lille building project: panoramic view of a quarry taken by a drill hole camera

Case history 16 : Dax hospital project.

Client : Dax hospital (owner), SEDIM (consultant)
Survey references: June 1981, CPGF n° 2172
Site : Dax hospital, extension, south west of France
Object : Basement mapping. Irregular marly limestone steeply dipping westward
Definition : The positioning of the future buildings in optimum foundation conditions.

Geological setting

Marly limestone overlain by recent deposits.

Why microgravity?

Appreciable density contrast was expected between the overburden and the substratum. Hence, the gravity method was welcome to provide with structural map with density information following a 3-D inversion.

Survey design

A regular grid of 20 x 20 m centres was carried out with individual antennas stretching out of the grid area for a better regional control. A total of 165 gravity stations were taken.

Results

A very deep regional gradient is observed on the Bouguer map which shows on the other hand a very well defined residual anomaly extending almost at right angle to the dip. Inversion in terms of structure gives the contours of the deepening of the basement which involves a large portion of projected buildings.

Conclusions

Microgravity is used once again outside of its usual application of underground void detection. Inversion techniques inspired from oil exploration are used here to resolve a foundation engineering problem.

Enclosed documents

Fig. 107 : residual anomaly map (CPGF ref. 2172-03)

Fig. 108 : computed structural maps (CPGF ref. 2172-04)
Values in 10^{-2} gals for maps (a), (b) and (c)
(a) residual anomaly (regridded for processing)
(b) Computed anomaly
(c) difference (b) - (a)
(d) depth to bedrock (in meters).

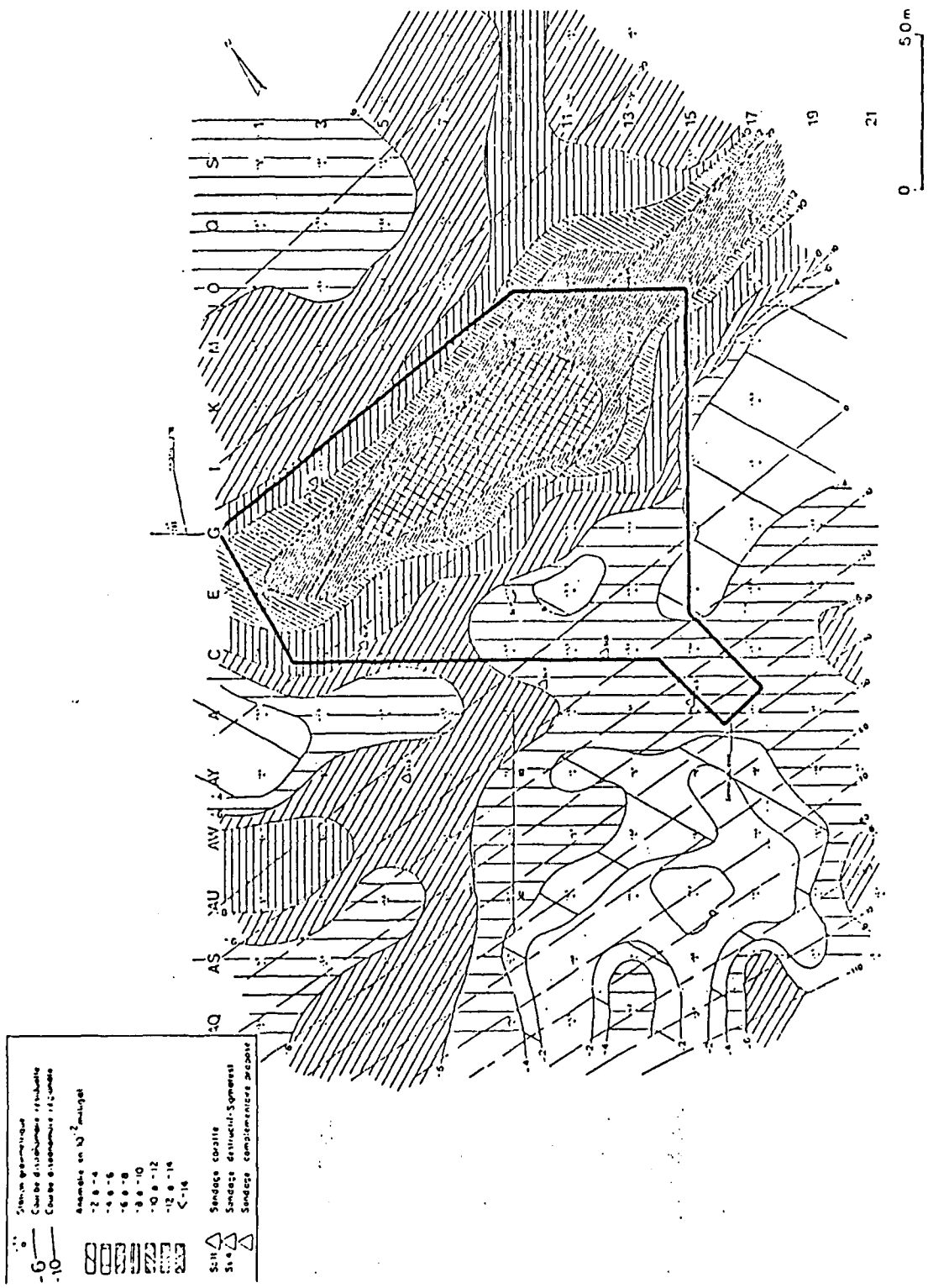

Figure 107. Dax hospital project: residual anomaly map

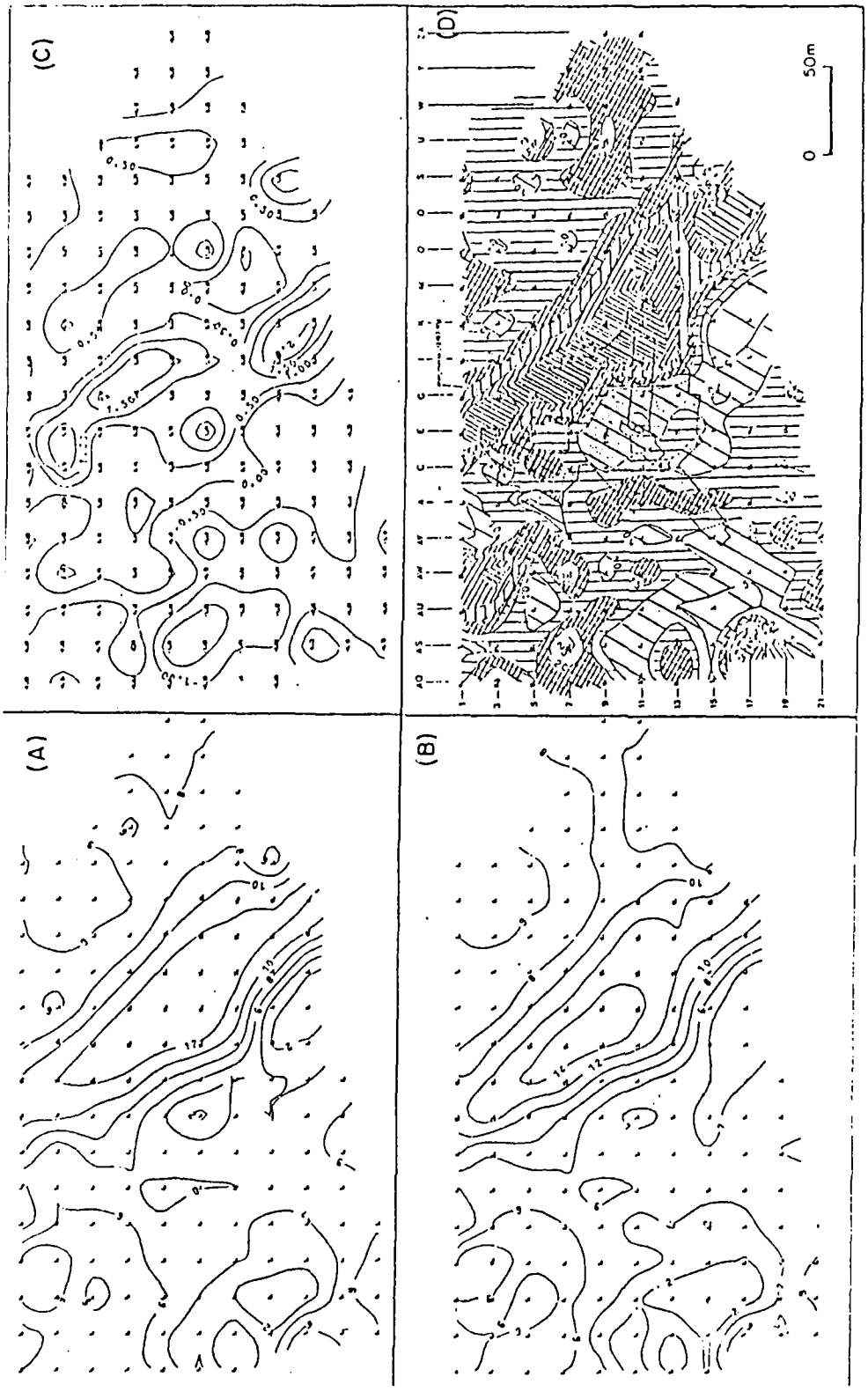

Figure 108. Dax hospital project: computed structural maps

Case history 17 : St Germain-en-Laye Finance Ministry Building.

Client : Ministry of Finances, Paris
Survey references: August 1976, CPGF n° 1564
Site : St Germain-en-Laye, 20 km West of Paris
Object : Construction of a new building, location of karstic cavities
Definition : Microgravity survey to map karstic zones.

Geological setting

The building was to be constructed on piles, 10 m long, crossing 6 m of soft top soil and tertiary marls. The piles following a 7.2 by 7.2 m grid, and located under a series of ground-floor pillars, were to be anchored in tertiary limestone below the marls. A conventional (core drills and laboratory testing) survey had specified the foundation conditions. Some of these piles were to support quite heavy loads, exceeding 200 T.

Why microgravity?

After the conventional survey, a sink-hole appeared 50 m North of the projected building. It was suspected to be related either to medieval water drainage tunnels (excavated from the side of a valley located North of the zone), or to karstic phenomena in the limestone.

Survey design

The microgravity survey was designed to follow exactly the pattern of the pillars. So, 92 gravity stations were made along a 7.2 x 7.2 m grid.

Results

Anomalies slightly in excess of -30 microgals were found, mainly in the eastern part of the building. Analysis of these anomalies showed that they were due to causes located between 5 and 20 m.

Other methods

Control was made by 3 destructive drill holes with L.W.D. They correspond to the following values of residual anomalies:

Drill hole S1: -13 microgals
S2: -20 "
S3: -28 "

Drilling rate log of drill hole S1 showed soft ground up to 6 m, then sound limestone. S2 showed, with an average gravity anomaly, soft ground up to 6 m, then sound limestone, with a karstic zone from 14 to 19 m. S3, with a high gravity anomaly, showed karstic limestone from 8 to 20 m.

Conclusions

Taking into account the good correlation between L.W.D. and microgravity, the residual anomaly map was used to plan the foundation project. It was decided not to deepen the pil s (the soil located below the limestone at over 20 m depth is not very sound), nor to grout the karstic zone (not economical in this case), but to connect the bottom of the pillars located in the eastern part of the building by reinforced concrete beams (calculated to "bridge" the cavities up to 3 m in diameter) and to replace the 10 m piles by cheap 6 m concrete filled wells.

Enclosed documents

Fig. 109 : residual anomaly

Fig. 110 : drilling rate recorded during drill holes S1, S2, S3. Vertically: depths. Horizontally: drilling rate in meters/hour.

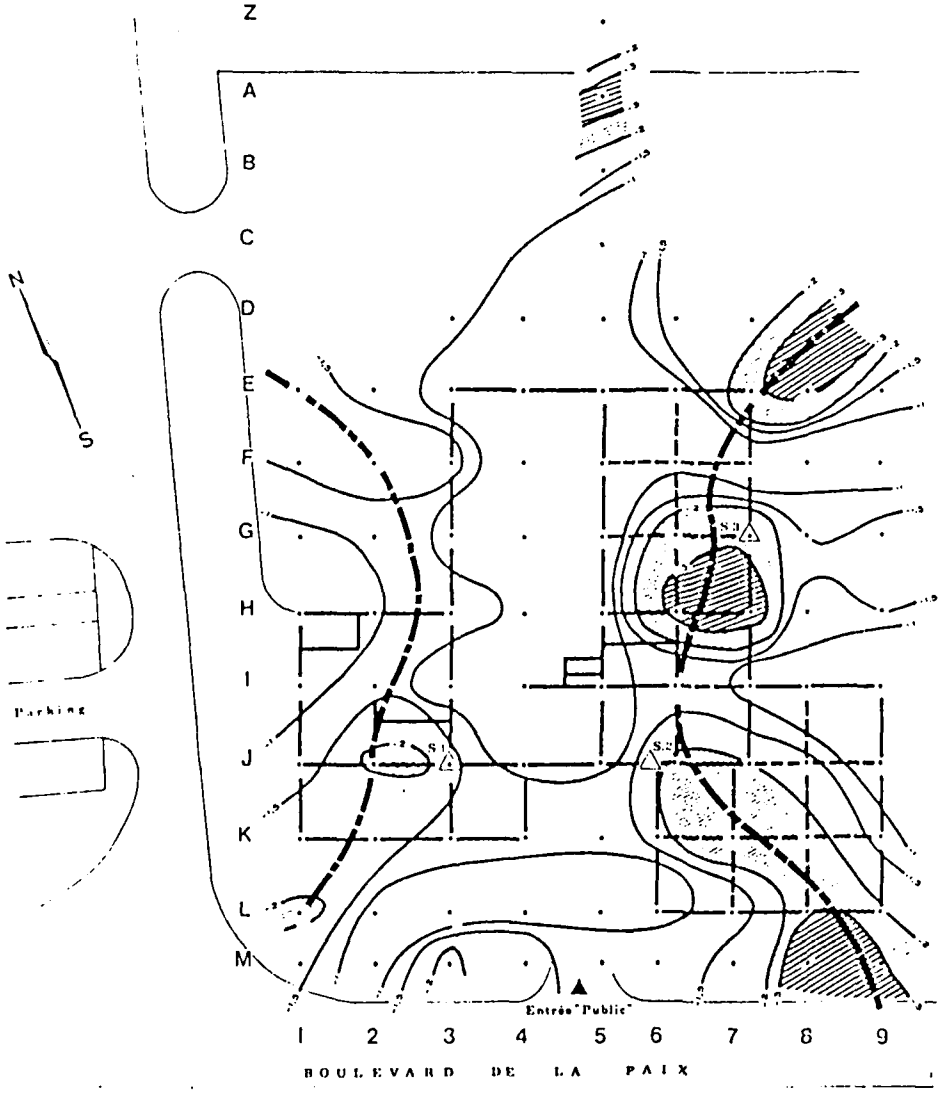

Figure 109. St Germain-en-Laye finance ministry building
Residual anomaly

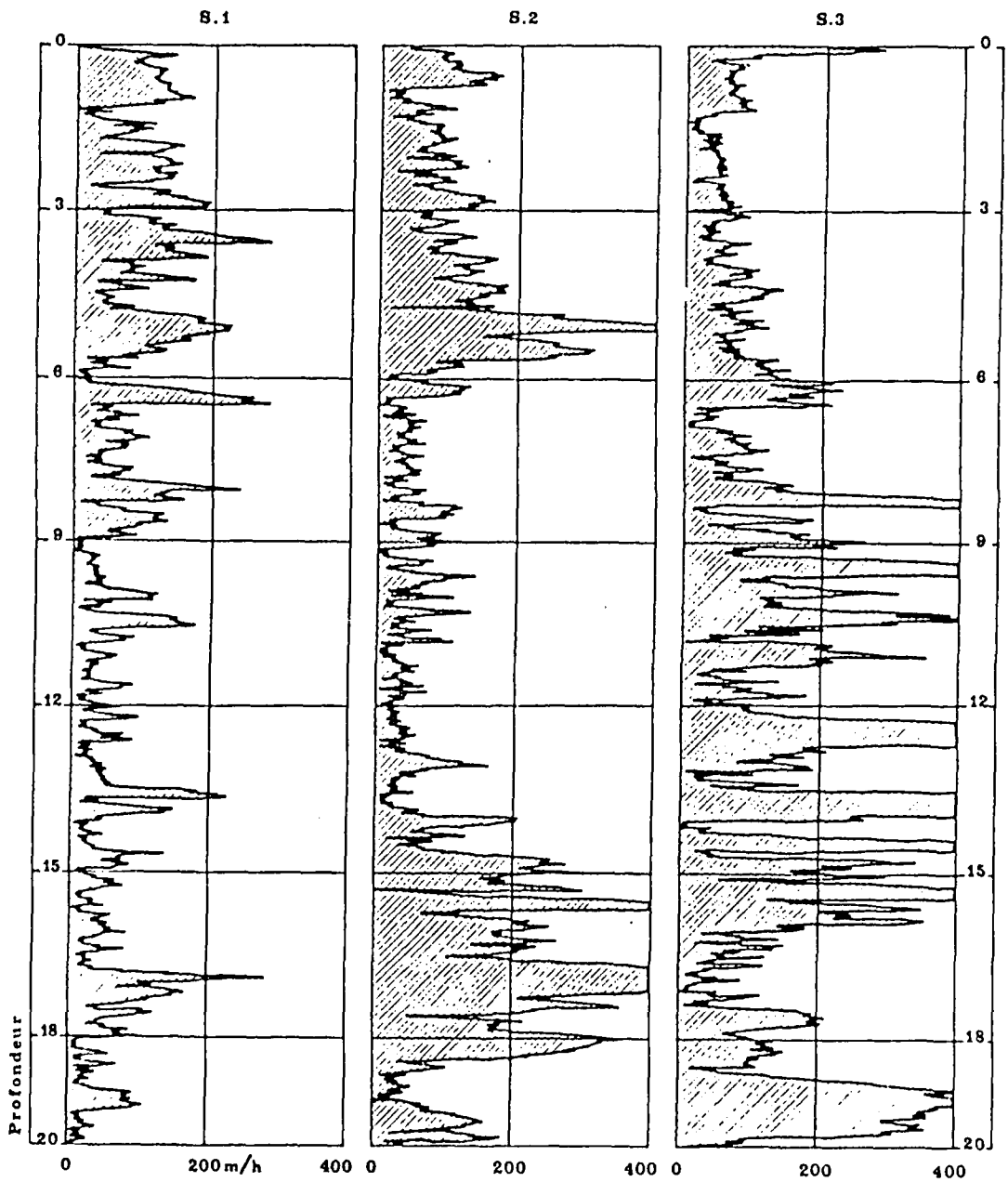

Figure 110. St Germain-en-Laye finance ministry building
Drilling rates during drill holes S1, S2 and S3

PART 8: REFERENCE SECTION

References Mentioned in the Report

Note: an * mentions papers written with the participation of CPGF personnel including:

- Yves Bertrand
- Marc Bichara (1)
- Edmond Bolelli (1)
- Jean-Claude Erling
- Erkan Kutkan
- Jacques Lakshmanan
- François Lantier
- Yves Lemoine
- Jacques Rougé (1)
- Manuel Sanchez
- Erik Siwertz

(1) at time of publication of corresponding paper

REFERENCES

*Alessandrello, E., Bichara, M. and Lakshmanan, J. 1983. "Automatic Three-layer, Three-Dimensional Deconvolution of the Pays de Bray Anticline". Geophysical Prospecting, vol. 31, pp 608-626.

Arzi, A.A. 1975. "Microgravity for Engineering Applications". Geophysical Prospecting, vol 23, n° 3, pp 408-425.

Ballard, R.F. 1983. "Cavity Detection and Delineation Research, Report 5, Electromagnetic (radar) Techniques Applied to Cavity Detection". Tech. Rept. GL-83-1, US Corps of Engineers, Waterways Experiment Station, CE, Vicksburg, Miss.

Benson, R.C., Yuhr, L.B. 1987 . "Assessment and Long Term Monitoring of Localized Subsidence using Ground Penetrating Radar". Karst Hydrogeology, A.A. Balkema, Ed. Boston, pp 161-170.

*Bertrand, Y., Herring, A.T., Lakshmanan, J. and Sanchez, M. 1987. "Curved Ray Seismic Tomography, 17 Years Experience from Zaire (1970) to Kenya (1987)" 2nd Int. Symp. on Borehole Geophysics for Minerals, Geot. and Ground Water Appl., Golden, Colorado.

*Bichara, M. and Lakshmanan, J. 1979. "Automatic Deconvolution of gravity anomalies". Geophysical Prospecting, vol 27, pp 798-807.

*Bichara, M., Laurin, P.J., Black, A., LaFehr, Tr. 1981. "Borehole Gravity Meter : an example of Application to Civil Engineering", SAID/SPWLA Logging Symposium, Paris

*Bichara, M., Erling, J.C. and Lakshmanan, J. 1981. "Technique de Mesure et d'Interprétation Minimisant les Erreurs de Mesure en Microgravimétrie", Geophysical Prospecting, vol 29, pp 782-789.

*Bichara, M. and Lakshmanan, J. 1983. "Détermination Directe des Densités du Sol et des Remblais à partir des Mesures Gravimétriques", Int. Assoc. of Eng. Geologists, Int. Symp. on In-Situ Testing, Paris.

Blizkovsky, M. 1979. "Processing and Applications in Microgravity Surveys", Geophysical Prospecting, vol 27, n° 4, pp 848-861.

*Bolelli, E. and Lakshmanan, J. 1965. "Aperçu sur les limites d'Application de la Géophysique à la Reconnaissance des Karsts". Chronique Hydrogéologie, 7, pp 111-114.

Bott, M.H.P., Smith, R.A. 1958. "The Estimation of the Limiting Depth of Gravitating Bodies". Geophysical Prospecting, vol 6, n° 1, pp 1-10.

Bru, J., Ledoux, J.L., Ménard, J., Waschkowski, E. 1983. "Les diagraphies et les Essais de Mécanique des Sols en Place". Int. Assoc. of Eng. Geologists, Int. Symp. on in-situ Testing, Paris.

Butler, D.K. 1977. Proceedings of the symposium on Detection of Subsurface cavities, U.S. Army Engineer Waterways Experiment Station, Vicksburg Miss.

Butler, D.K. 1980. "Microgravimetric Techniques for Geotechnical Applications". US Corps of Engineers, Waterways Experiment Station, Misc. Pap. GL-80-13.

Butler, D.K. 1984. "Microgravimetric and Gravity Gradient Techniques for Detection of Subsurface Cavities". Geophysics, vol 49, n° 7, pp 1084-1096.

Cagniard, L. 1960. "Introduction à la Physique du Globe". Editions Technip, Paris.

*CPGF (unpublished report). 1983. "Grouting Control Test at Fontenay s/Bois metro tunnel", CPGF ref. 2505 (resistivity) and ref. 2552 (seismic frequency analysis).

Elkins, T.A. 1951. "The Second Derivative Method of Gravity Interpretation", Geophysics, vol 16-1, pp 29-50.

Engineer manual 1110-1-1802. Geophysical Explorations, Department of the Army, US Corps of Engineers, USA, May 31, 1979.

Eötvös, R.V. 1896. "Untersuchungen über Gravitation und Erdmagnetismus", Annalen der Physik, vol 59, pp 354-400.

*Erling, J.C., Lakshmanan, J. and Rougé, J. 1981. "Apport des Diagraphies pour la Réalisation d'Injections de Carrières Effondrées". Journées Nationales Géotechniques, Nantes, France.

*Erling, J.C. and Roques, G. 1983. "Reconnaissance et Traitement de Cavités Naturelles ou Artificielles dans le Domaine Ferroviaire". Int. Assoc. of Eng. Geologists, Int. Symp. on In-Situ Testing, Paris.

*Erling, J.C., Bertrand, Y., and Kutkan, E. 1987. "Prospection Détaillée du Sous-sol Urbain, en vue de Travaux Souterrains". Int. meeting, AFTES, Bordeaux.

Fajklewicz, Z.J. 1976. "Gravity Vertical Gradient Measurements for the Detection of Small Geologic and Anthropomorphic Forms", Geophysics, vol 41-05, pp 1016-1030.

Fajklewicz, Z.J. 1983. "Rock-burst Forecasting and Genetic Research in Coal Mines by Microgravity Method", Geophysical Prospecting, vol 31, n° 5, pp 748-765.

Fisk, P., Gover, C., Holt, R. and Jones, G. 1987. "Strength of Material in and around Sink-holes by in-situ Geophysical Testing". Karst Hydrogeology, A.A. Balkema, Ed., Boston, pp 153-156.

Frappa, P., Horn, R., Muraour, P. and Peragallo, J. 1977. "Contribution à la Détection par Sismique Réflexion des Cavités Souterraines de Faible Profondeur". Bull. Liaison Labo. P et Ch., 92, pp 59-65.

Gabillard, R. and Dubus, J.P. 1977. "Procédé Electromagnétique par Focalisation des Courants". Bull. Liaison Labo. P. et Ch., Paris, 92, pp 80-86.

Habberjam, G.M. 1969. "The Location of Spherical Cavities using a Tripotential Resistivity Technique". Geophysics, vol 34-5, pp 780-784.

Hadj-Aissa, M.L. 1987. "Applications de la Méthode Micro-gravimétrique dans les Etudes de Fondations de Barrages et dans le Contrôle de la Réalisation de Remblais". Thesis, Univ. Liège, Faculté des Sciences Appliquées.

Hammer, S. 1939. "Terrain Corrections for Gravimeter Stations. Geophysics, vol 4, pp 184-194.

Henderson, R.G. and Zeitz, L. 1949. "The Computation of Second Vertical Derivatives of Geomagnetic Fields". Geophysics, vol 16-4, pp 508-516.

*Kutkan, E. and Lakshmanan, J. 1966. "Le Fontis de Sevran, Prospection Gravimétrique, Bull. Assoc. des Géologues du Bassin de Paris.

LaFehr, T.R. 1980. "History of Geophysical Exploration, Gravity Method". Geophysics, vol 45, pp 1634-1639.

LaFehr, T.R. 1983. "Rock Density Borehole Gravity Surveys. Geophysics, vol 48, pp 341-356.

*Lakshmanan, J. 1963. "Reconnaissance de Cavités dans le Sous-sol par Procédés Electriques et Gravimétriques". Sol-Soils, Paris,

*Lakshmanan, J. 1973. "Cartographie Microgravimétrique et Radioactive des Zones de Dissolution du Gypse du Lutétien au Nord-Est de Paris". Int. Symp. on Dissolution Cavities, Int. Assoc. of Eng. Geologists, Hannover.

*Lakshmanan, J., Bichara, M. and Erling, J.C. 1977. "Etudes de Fondation en Terrain Caverneux : Place de la Gravimétrie". Bull. de Liaison du Labo. des P. et Ch., Paris, 92, pp 74-79.

*Lakshmanan, J. 1982. "Variable Density Bouguer Maps Obtained by Generalized Nettleton Procedure". 44th E.A.E.G. meeting, Cannes.

*Lakshmanan, J. 1983. "Diagraphies et Paramètres de Forage". General Report, Revue Française de Géotechnique, n° 23, Paris.

*Lakshmanan, J. and Kutkan, E. 1985. "Utilisation du Gravimètre de Forage pour la Détermination in-situ des Densités". Nat. Coll. Belg. Com. Eng. Geol., Liège.

*Lakshmanan, J. 1985. "Corrections Généralisées de Nettleton". Potential Fields in Rugged Topography, Lausanne, IGL Bulletin, n° 7, paper 2.5.

*Lakshmanan, J. and Montluçon, J. 1987. "Pyramid of Cheops : Microgravity weighs the Structure and Detects Cavities". The Leading Edge, january 1987.

*Lechat, P., Monjoie, A. and Lemoine, Y. 1971. "Apports des Etudes Sismiques et Pressiométriques à l'Etude de la Fracturation du Rocher dans le Cas d'un Site de Barrage". Symp. Int. Soc. Rock Mech., Nancy.

Legatt, P.B. 1984. "Selecting a Density that Minimizes Elevation and Bouguer Gravity Corrections". Manuscript, Johannesburg, March 9, 1984.

Lutz, J. 1978. "Les diagraphies Instantanées de Forage". Chantiers Magazine n° 91, Paris.

McConnell, R.K., Hearty, D.B. and Winter, P.J. 1975. "An Evaluation of the Lacoste and Romberg Model D Microgravimeter". Bureau Gravimétrique International, Bull. n° 36.

*Michel, J.P., and Erling, J.C. 1975. "Détection de Cavités Souterraines de Petites Dimensions par Microgravimétrie Réalisée en Cours de Travaux". Coll. Belg. Com. on Eng. Geol.

Moudressov, E.A., Varlamov, A.C., Filatov, V.G. and Kamarov, G.M. 1979. "Interpretation of High Accuracy Gravity Measurements for Non Structural Deposits of Oil and Gas". Ed. Nedra, Moscow (in Russian).

Nagy, D. 1966. "The Gravitional Attraction of a Right Rectangular Prism". Geophysics, vol 5, pp 176-183.

Nettleton, L.L. 1939. "Determination of Density for Reduction of Gravimetric Observations". Geophysics, vol 5, pp 176-183.

Nettleton, L.L. 1940. "Geophysical Prospecting for Oil". McGraw-Hill Book Company, Inc., New York.

Neumann, R. 1967. "La Gravimétrie de Haute Précision, Application aux Recherches de Cavités". Geophysical Prospecting, vol 15, pp 116-134.

Olivier, R.J. and Simard, R.G. 1981. "Improvement of the Conic Prism Model for Terrain Correction in Rugged Topography". Geophysics, vol 46, pp 1054-1056.

Parasnis, D.S. 1952. "A Study of Rock Density in the English Midlands. Mon. Not. R. Astr. Soc. Geoph. Suppl. 6, pp 252-271.

Parasnis, D.S. 1961. "Exact Expressions for the Gravitional Attraction of a Circular Lamina at all Points of Space and of a Right Circular Vertical Cylinder at Points External to it". Geophysical Prospecting, vol 9, pp 382-398.

Richez, P. 1981. "L'Enregistrement des Paramètres de Forage". Travaux magazine, n° 522.

*Rimbert, F., Erling, J.C. and Lakshmanan, J. 1987. "Variable Density Bouguer Processing of Gravity Data from Herault, France". The First Break, vol 5, n° 1, pp 9-13.

Rosenbach, O. 1953. "A Contribution to the Computation of the Second Derivative from Gravity Data". Geophysics, vol 18-4, pp 894-912.

Schoeffler, J. 1975. "Gravimétrie Appliquée aux Recherches Structurales et à la Prospection Pétrolière et Minière". Ed. Technip, Paris.

Sharma, P. Vallabh. 1976. "Graphical Evaluation of Magnetic and Gravity Attraction of the Three-dimensional Bodies". Geophysical Prospecting, vol 15, PP 67-173.

Singh, S.K. 1977. "Gravitional Attraction of a Vertical Right Circular Cylinder". Geophys. J.R. Astr. Soc. 50, pp 243-246.

Smith, D.L., Smith G.L. 1987. "Use of Vertical Gradient Analyses to Detect Near-surface Dissolution Voids in Karst Terranes". Karst Hydrogeology, A.A. Balkema, Ed., Boston, pp 205-210.

Steeples, D.W. and Miller, R.D. 1987. "Direct Detection of Shallow Subsurface Voids Using High-resolution Seismic Reflection Techniques". Karst Hydrogeology, A.A. Balkema, Ed., Boston, pp 153-156.

Talwani, M. and Ewing, M. 1960. "Rapid Computation of Gravitional Attraction of Three-dimensional Bodies of Arbitrary Shape". Geophysics, vol 25, n° 1, pp 203-225.

Talwani, M. and Heirtzler, J.R. 1962. "The Mathematical Expression for the Magnetic Anomaly over a Two-dimensional Body of Polygonal Cross-section". Tech. Rep. n° 6, Lamont-Doherty Geolog. Observ., Columbia University.

Waschkowski, E. 1983. "Les Diagraphies et les Essais de Mécanique des Sols en Place. Int. Assoc. of Eng. Geologists, Int. Symp. on in-situ Testing, Paris.

Working Group presided by Habib, P. 1979. (included Lakshmanan, J. and Erling, J-C.). "Recommandations sur le Traitement des Cavités Souterraines et notamment des Carrières (C.S. 78)". Annales de l'I.T.B.T.P., Paris, n° 370.

Working Group of the French National Committee on Large Dams, chaired by Lakshmanan, J. 1982. "Nouvelles Techniques de Reconnaissance". 14th Int. Congress, Int. Com. on Large Dams, Rio de Janeiro.

Working group. 1983. "Etude Géotechnique et Reconnaissance des Sols", Presses de l'Ecole Nationale des Ponts et Chaussées, Paris.

Working Group. 1967. "Recommandations pour la Reconnaissance Géologique et Géotechnique des Tracés d'Autoroute, Ministère de l'Equipement, Laboratoire Central des Ponts et Chaussées, Paris.

Summaries of relevant papers

A certain number of papers, originally written in French, have been summarized in English. They are supplied with their main figures, with captations translated into English as follows :

PAPER 1 : Foundation engineering using the gravimeter in cavernous terrain.

PAPER 2 : Measuring and interpretation techniques minimizing acquisition errors in microgravimetry.

PAPER 3 : Surveying ang grouting natural or artificial cavities in railway civil engineering works.

PAPER 4 : Detailed urban subsurface investigations in conjunctions with underground works.

PAPER 5 : Gravity and gamma-gamma mapping of sink-hole in Lutetian gypsum, north-east of Paris.

PAPER 6 : Use of "logging while drilling" for grouting design in collapsed underground quarries.

PAPER 7 : Microgravity adapted to the investigation of underground quarries.

PAPER 1

ETUDES DE FONDATION EN TERRAIN CAVERNEUX: PLACE DE LA GRAVIMETRIE

(FOUNDATION ENGINEERING USING THE GRAVIMETER IN CAVERNOUS TERRAIN)

by J. Lakshmanan, M. Bichara and J.C. Erling

Bulletin de Liaison des Laboratoires des Ponts et Chaussées (Highway Deaprtment, monthly bulletin), n° 92, November-December 1977, pp 74-79.

Abstract

The position of geophysical investigation in foundation engineering over caverns is first examined, separating cases of extensive caverns or underground quarries from those of small holes. Microgravimetry is shown to be the only method directly measuring the prospected anomaly: mass deficit in tons. Control by drill holes is not always easy to interpret and monitoring of drilling velocity and reflected percussion is recommended. Various prospection plans are described, as well as foundation solutions, following different types of constructions and of geological problems. Lastly, several field examples are given.

Note: the last example is already in section 717.

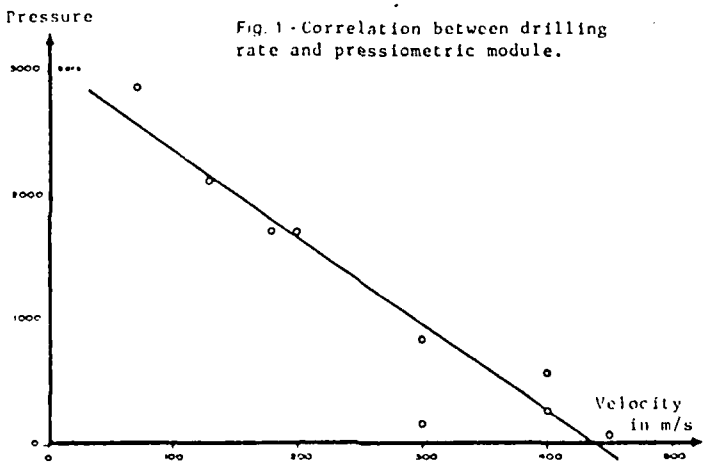

Fig. 1 - Correlation between drilling rate and pressiometric module.

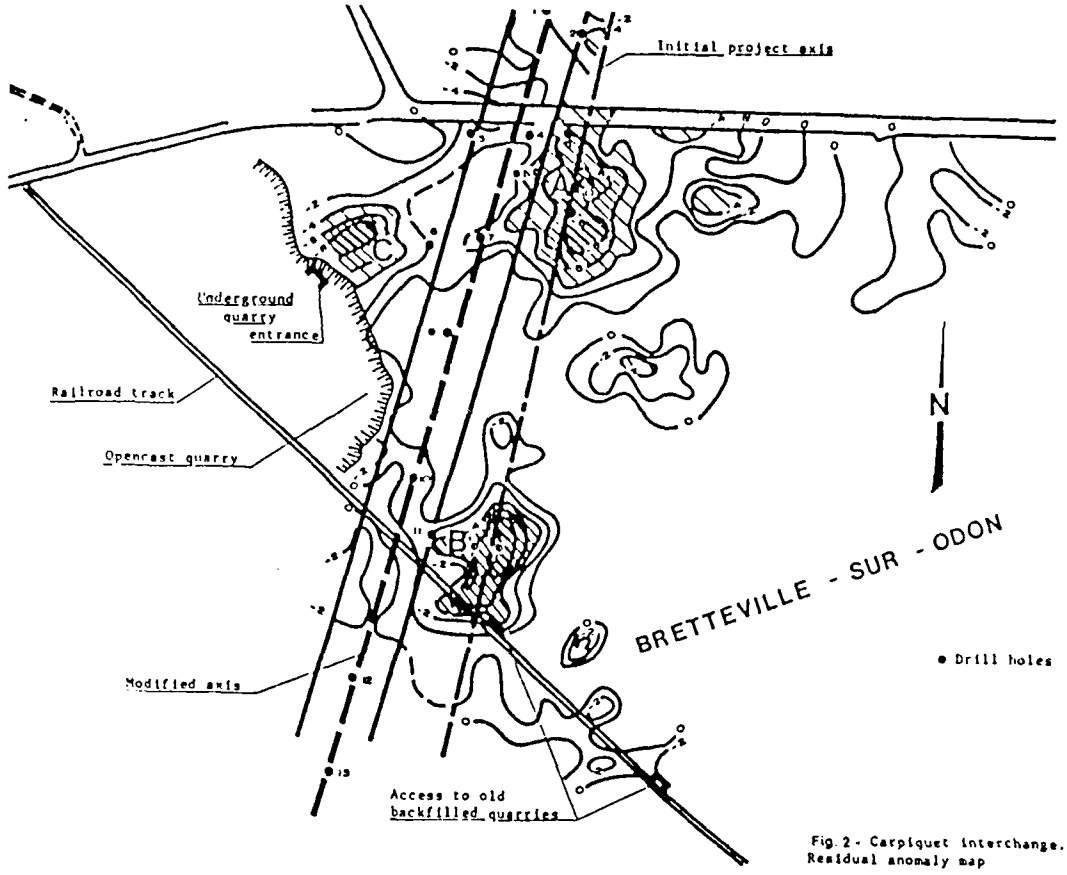

Fig. 2 - Carpiquet interchange. Residual anomaly map

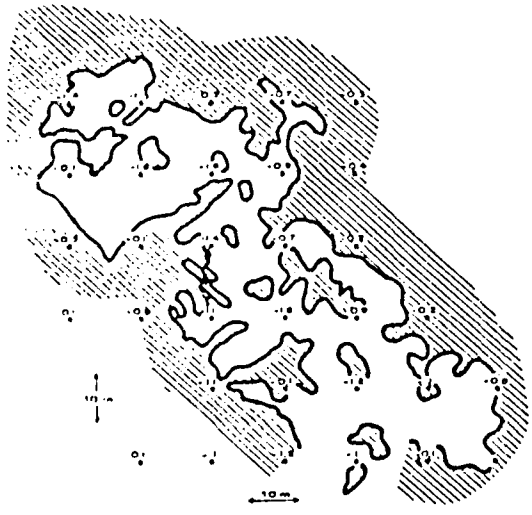

Fig 3 - Comparison between a quarry outline and densities restored by Filt software

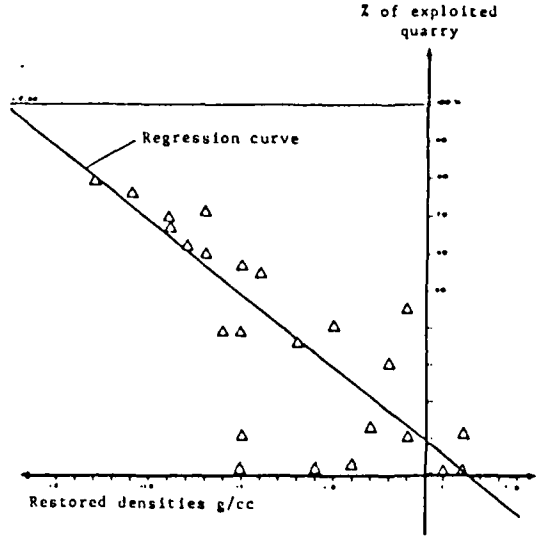

Fig. 4 - Correlation between restored densities and void percentage

PAPER 2

TECHNIQUE DE MESURE ET D'INTERPRETATION MINIMISANT LES ERREURS DE MESURES EN MICROGRAVIMETRIE

(MEASURING AND INTERPRETATION TECHNIQUES MINIMIZING ACQUISITION ERRORS IN MICROGRAVIMETRY)

by M. Bichara, J.C. Erling and J. Lakshmanan

Geophysical Prospecting, 9181, vol 29, pp 782-789.

Abstract

Different sources of error influence gravity surveys, particularly shallow "microgravity surveys. Experiments show that the most frequent source of error in gravimetric prospecting is bad estimation of drift. Better control of drift exists with the field procedure and interpretation technique developed by the authors, as can be shown theoretically as well as experimentally. The method implies a random or semi-random spatial sequence of measurement points. A real case of field prospecting is described.

Fig. 1. Processing flow chart

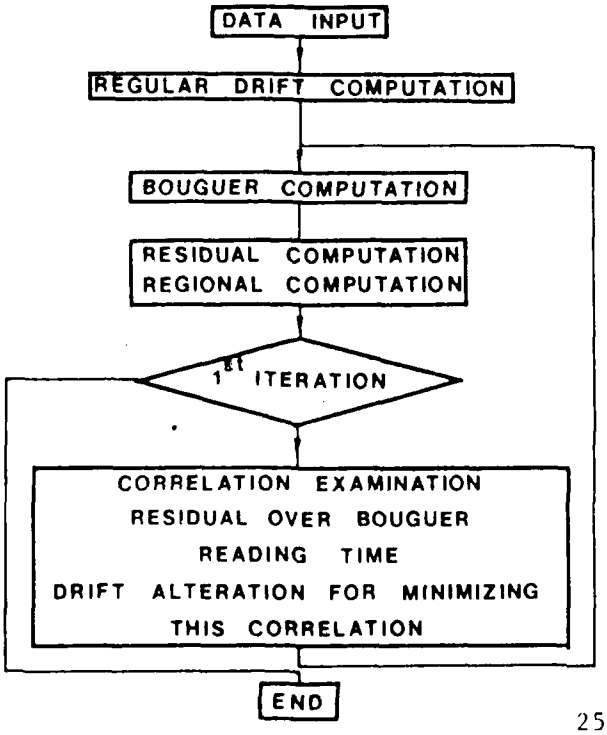

Fig. 2. Drift correction exemple

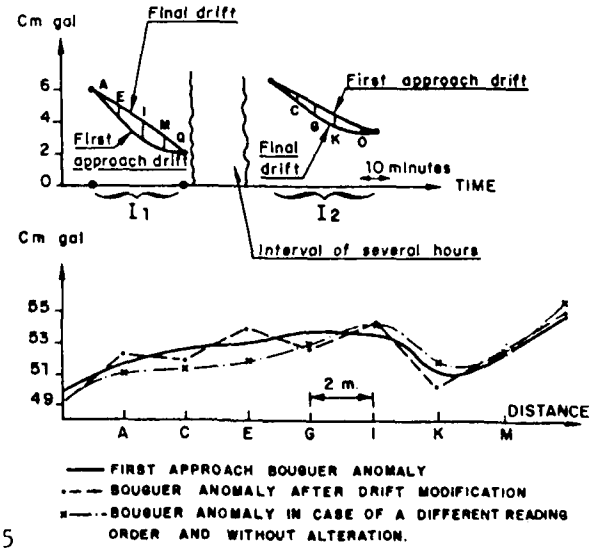

PAPER 3

RECONNAISSANCE ET TRAITEMENT DE CAVITES NATURELLES OU ARTIFICELLES DANS LE DOMAINE FERROVIAIRE

(SURVEYING AND GROUTING NATURAL OR ARTIFICIAL CAVITIES IN RAILWAY CIVIL ENGINEERING WORKS)

by G. Roques, J.C. Erling

Bull. Int. Assoc. Eng. Geology, n° 26-27, pp 299-308

Abstract

The presence of underground quarries and networks of karstic voids may generate stability problems concerning the existing or projected SNCF platforms. Following a preliminary inquiry, a line of survey and handling is set up securing against the risk of collapse at the surface of natural ground. A microgravity survey is run, completed with a campaign of tricone drilling, enhanced through the recording of drilling parameters. This is the logical approach to optimize the grouting program. The method is illustrated by a few examples of survey done at Massily on the new TGV track between Paris and Lyon, and also on three sites on already existing SNCF tracks.

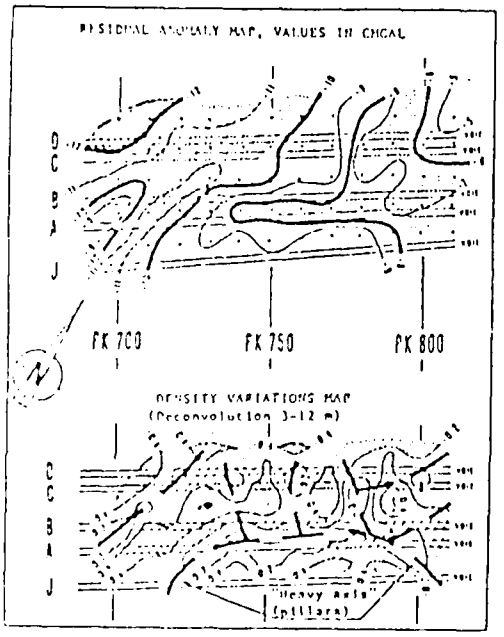

Fig. 7. Express roadway along the TGV East railroad, microgravity + logging while drilling.

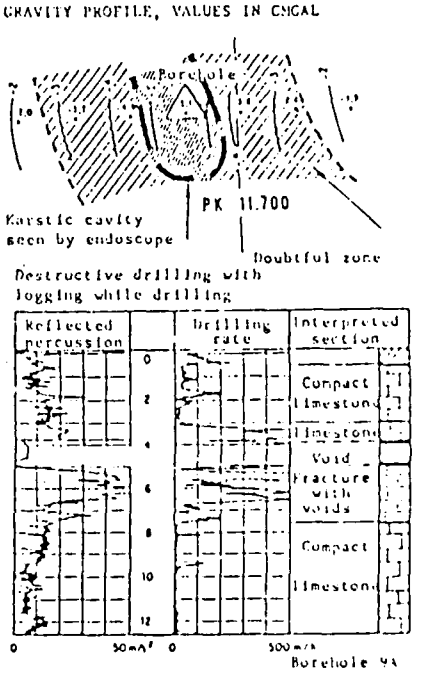

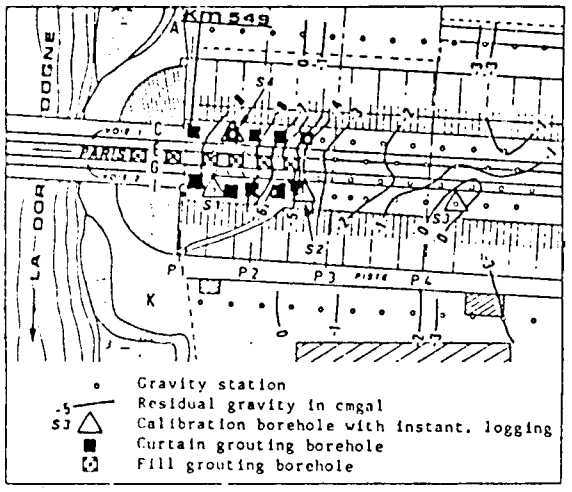

Fig. 10 : SNCF railway bridge at Libourne. Location of voids in an embankment, grouting by microgravity and L.W.D.

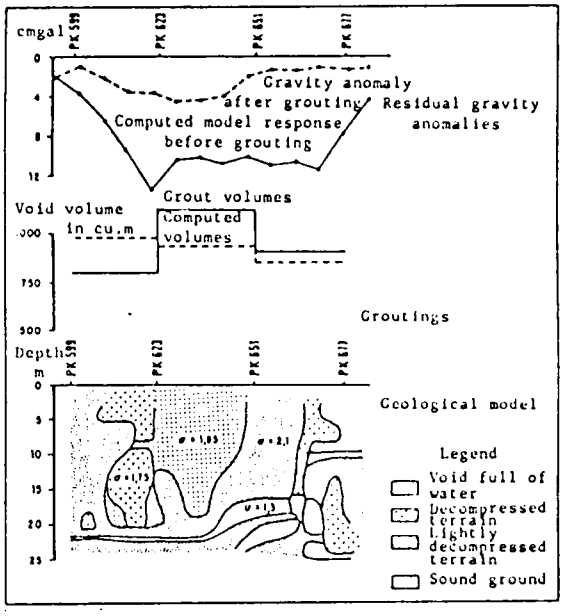

Fig. 18 : SNCF railroad from Paris to Strasbourg at Varangéville. Computer modelling of a micro-gravity anomaly

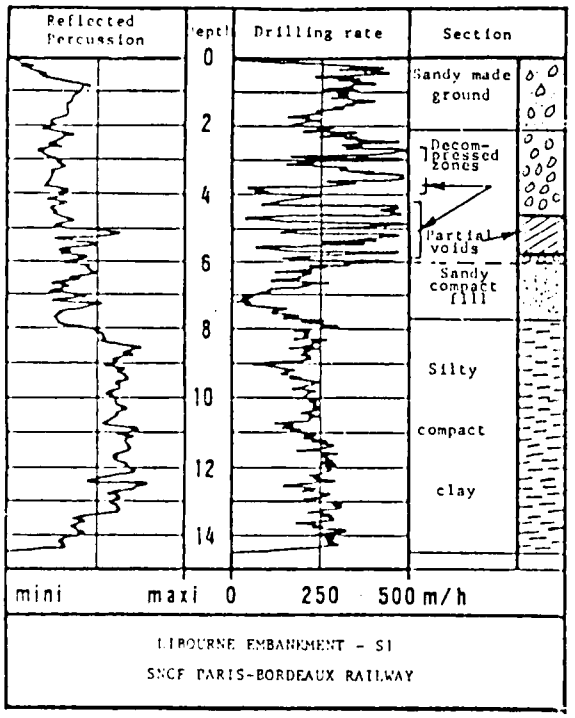

Fig. 11 : SNCF embankment at Libourne. L.W.D. on a gravity anomaly

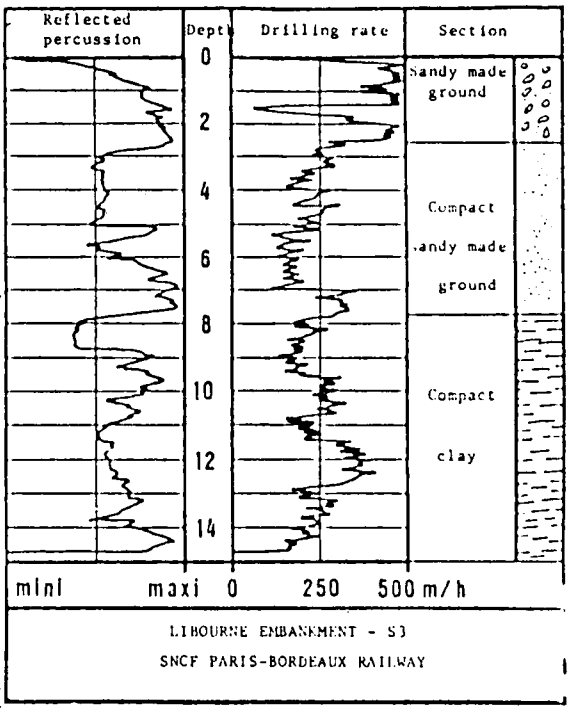

Fig. 12 : SNCF embankment of Libourne. L.W.D. outside gravity anomalies

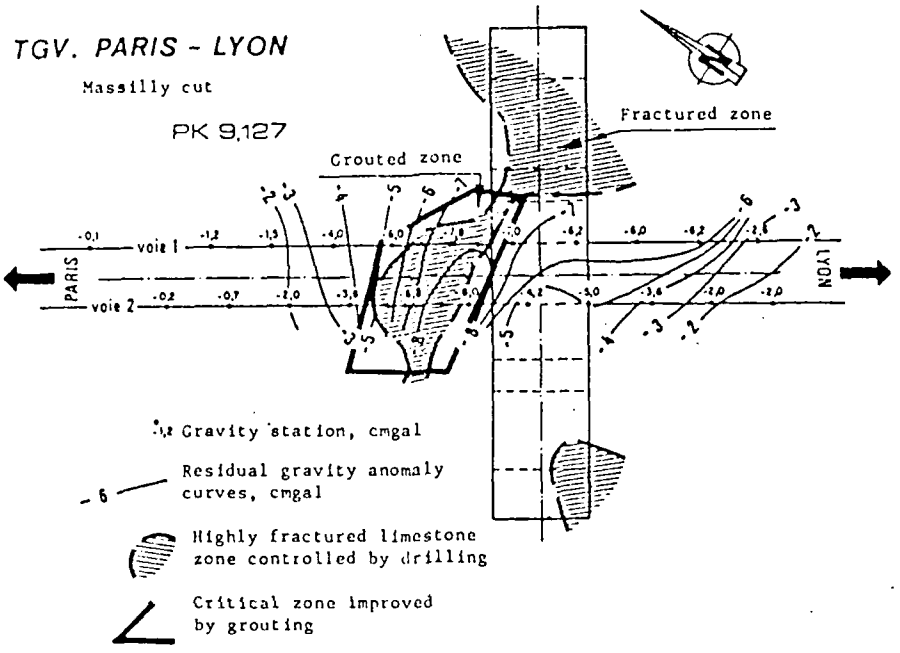

Fig. 15 : Fast TGV railroad from Paris to Lyons, Massily sector. Survey of a karst near a bridge, by microgravity, and soil improvement by grouting

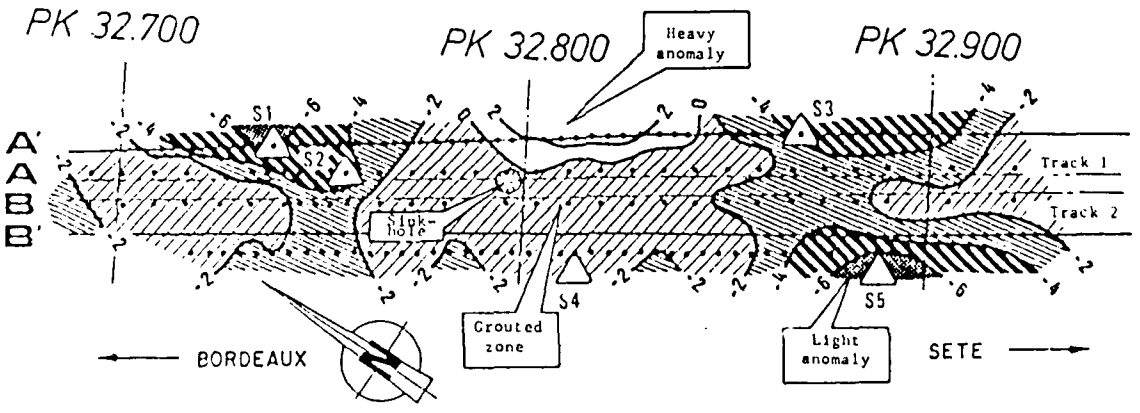

Fig. 16 : SNCF railway from Bordeaux to Sète at Barsac. Location and grouting of karst below the embankment

PAPER 4

PROSPECTION DETAILLEE DU SOUS-SOL URBAIN EN VUE DE TRAVAUX SOUTERRAINS

(DETAILED URBAN SUBSURFACE INVESTIGATIONS IN CONJUNCTION WITH UNDERGROUND WORKS)

by J.C. Erling, Y. Bertrand and E. Kutkan
Assoc. Fr. Travaux Souterrains, AFTES (Fr. Assoc. on underground works),
International Technical Meeting, Bordeaux, October 1987.

Abstract

Subsurface investigations in urban environment are delicate operations, owing to buildings, pavement, pipes, cellars, cables, etc ... Underground geological disturbances have to be mapped to enable a better design of subsurface works. Two very particular geophysical techniques are described in the paper: very high resolution microgravimetrics help to map density anomalies, while seismic tomography yields a cross-sectional image of the underground in terms of velocity distribution, attenuation and dynamic moduli.

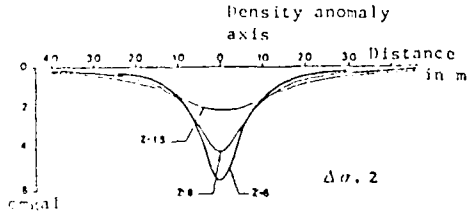

Figure 1. Gravity anomaly of a cylindrical body of 2 m radius, at depth "Z".

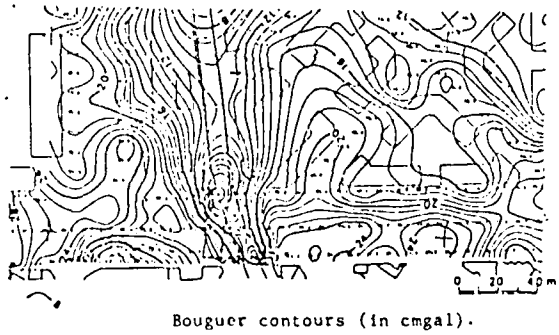

Bouguer contours (in cmgal).

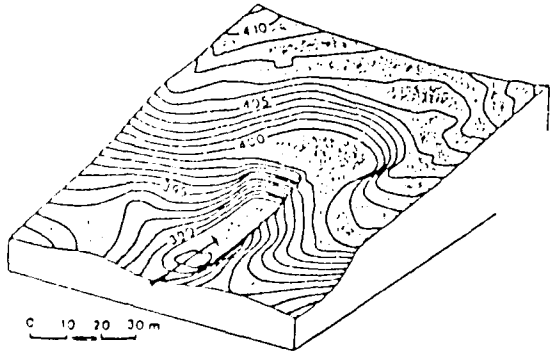

Figure 3. Blaisy railway tunnel. 3-D view of the south entrance.

TERRAIN CORRECTIONS MAP

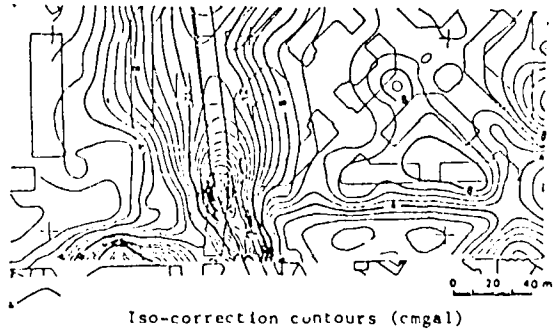

Iso-correction contours (cmgal)

Figure 2. Paris, Porte Pouchet. Microgravimetric survey.

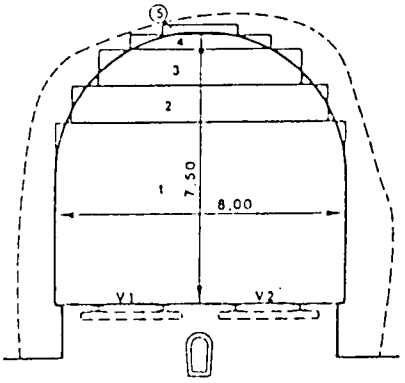

Figure 4. Dijon area, typical tunnel section
Adopted geometrical model.

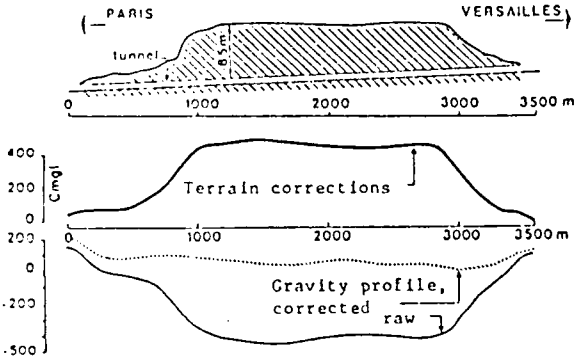

Figure 6. SNCF Meudon tunnel. Microgravity survey.
Terrain corrections.

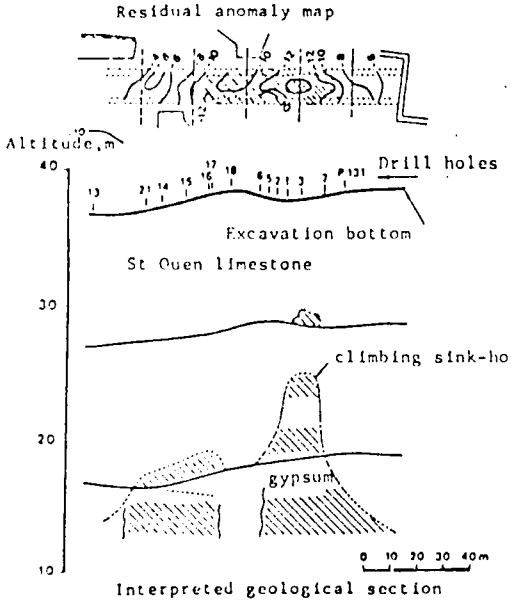

Figure 7. Paris, Porte Poucher. SNCF Montmorency-Invalides line. Microgravity survey.

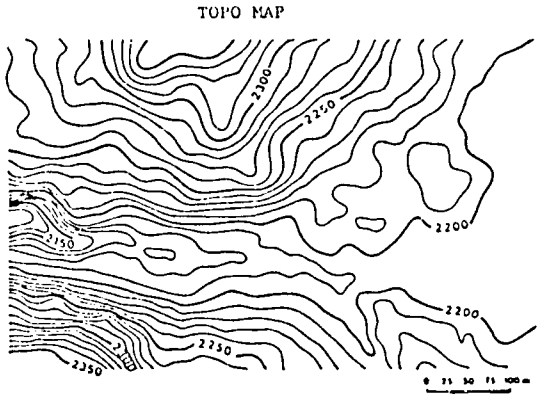

Terrain corrections map

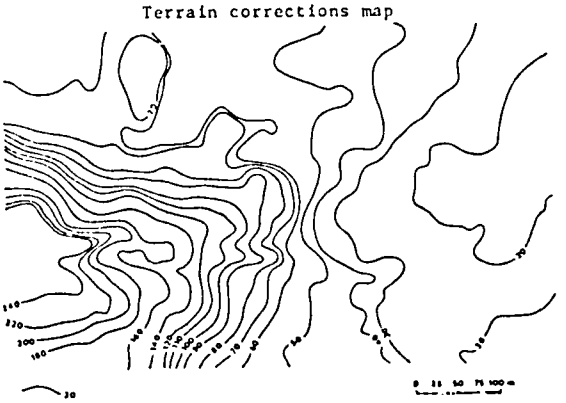

Figure 5. EDF RIF-TORT site. Microgravity survey. Terrain corrections.

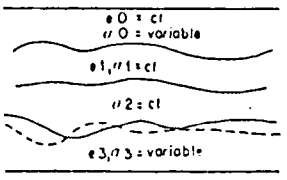

Unexplained residual transfer

Successive automatic adjustment of density and depth

MODCONG PROCESSING
Exemple of model application.

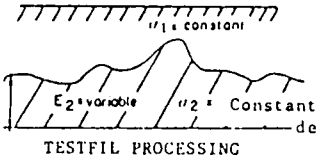

TESTFIL PROCESSING
Exemple of application.

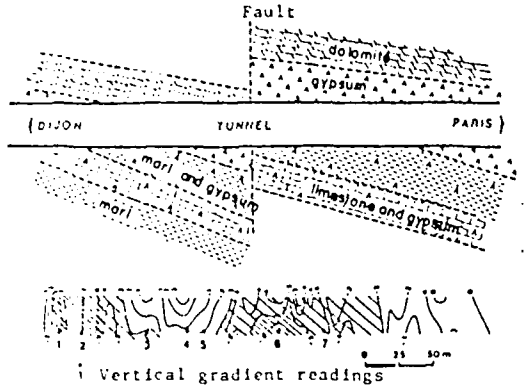

Fig. 8. Dijon area. SNCF Blaisy tunnel. Micro-gravity survey.

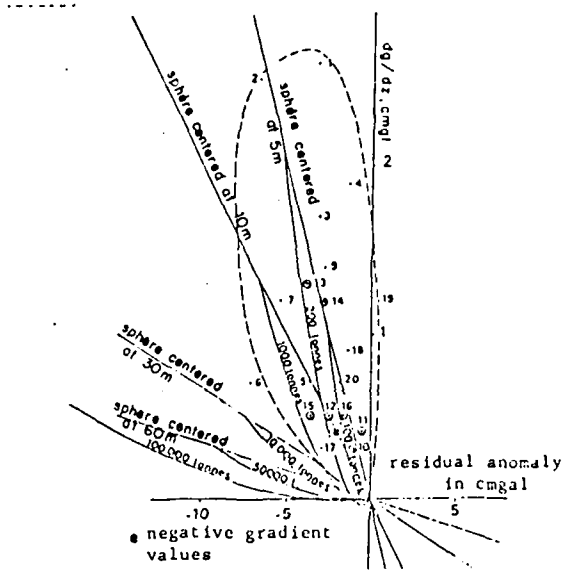

Figure 9. Dijon district. Blaisy railroad tunnel. Vertical gradient measurements.

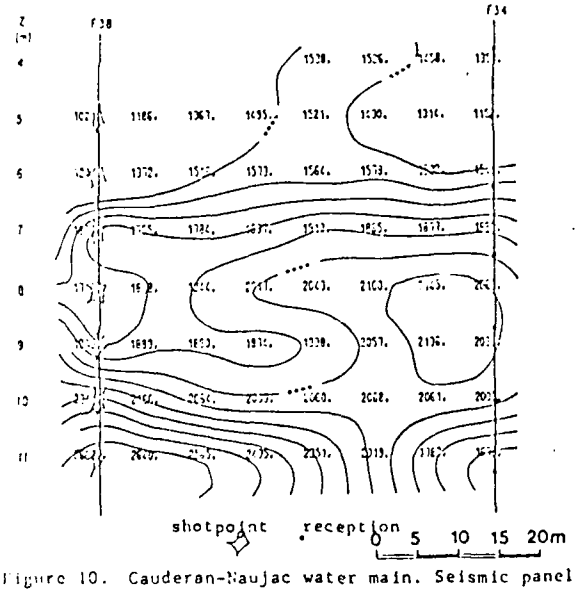

Figure 10. Cauderan-Naujac water main. Seismic panel before grouting.

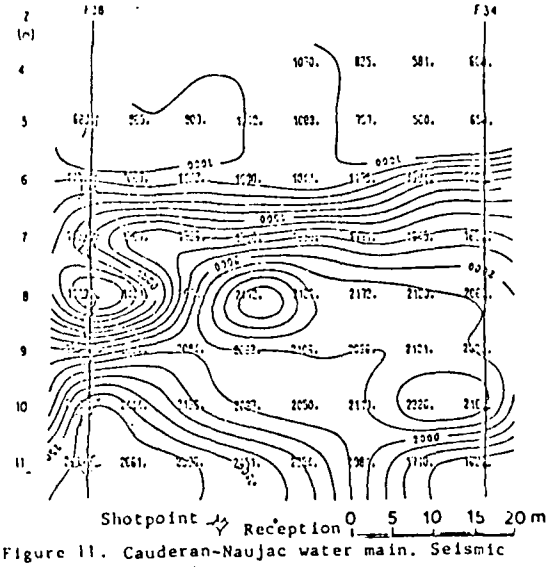

Figure 11. Cauderan-Naujac water main. Seismic panel after grouting.

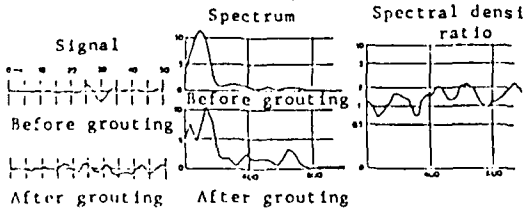

PAPER 5

CARTOGRAPHIE MICROGRAVIMETRIQUE ET RADIOACTIVE DES ZONES DE DISSOLUTION DU GYPSE DU LUTETIEN AU NORD-EST DE PARIS

(GRAVITY AND GAMMA GAMMA MAPPING OF SINK-HOLE AREAS IN LUTETIAN GYPSUM NORTH-EAST OF PARIS)

by J. Lakshmanan

Int. Assoc. on Rock Mechanics, International Symposium, Hannover, 1973.

Abstract

Following some spectacular sink-holes, Lutetian gypsum lenses have been detected in the north-east of Paris region. Gravity methods are now regularly used for the location of sink-hole areas. New computation techniques give directly average heights of underground voids. Drill holes are completed by in-situ density measurements (gamma-gamma).

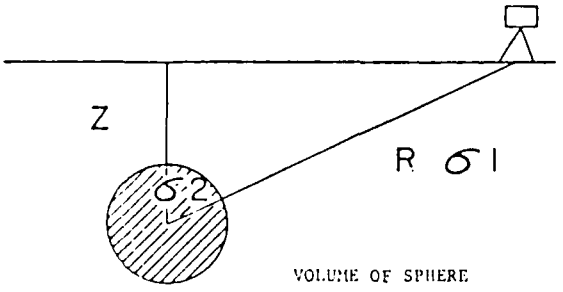

VOLUME OF SPHERE

$$V = \frac{4}{3}\pi r^3$$

Figure 1

$$\Delta\sigma = \sigma_1 - \sigma_2$$

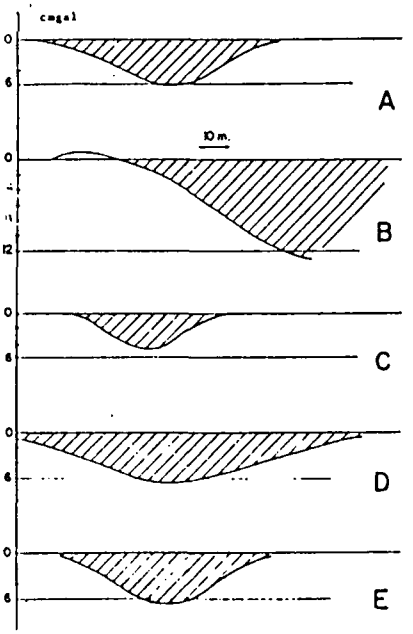

Fig 2. Typical gravity anomalies.

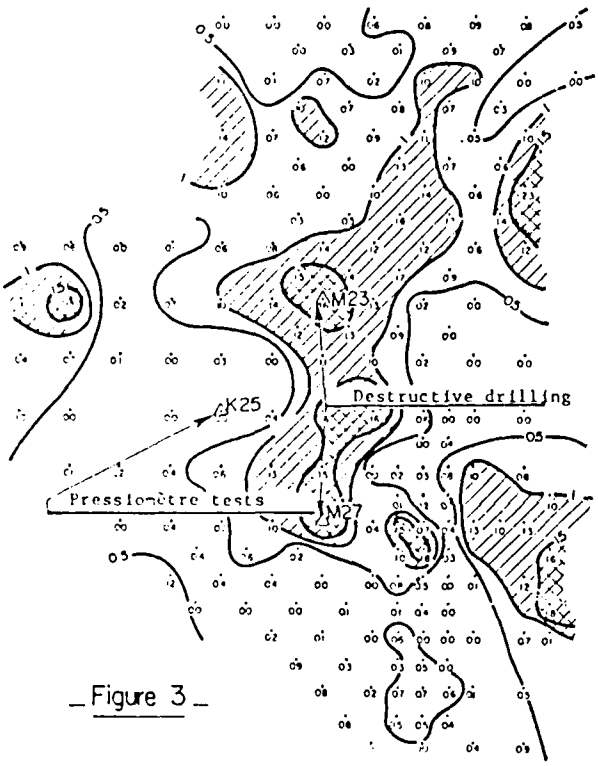

Figure 3

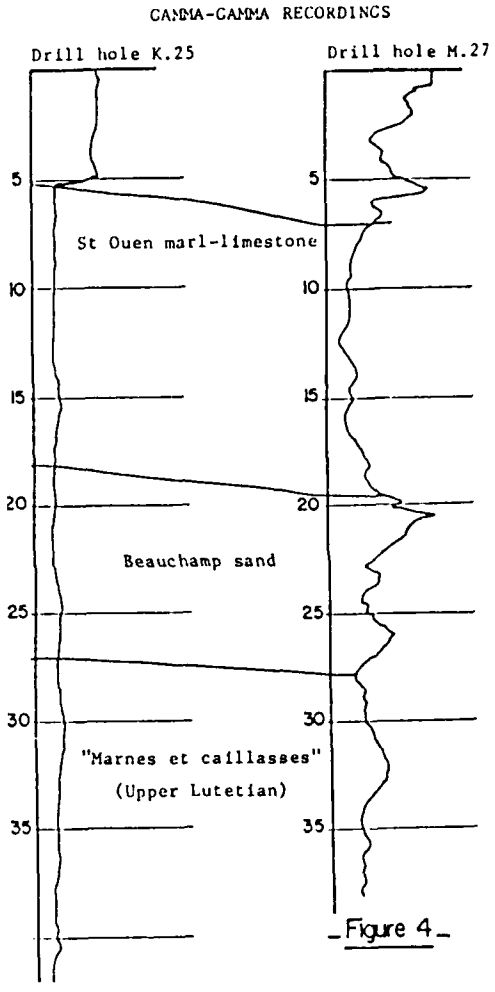

Figure 4

PAPER 6

APPORT DES DIAGRAPHIES POUR LA REALISATION D'INJECTIONS DE CARRIERES EFFONDREES

(USE OF "LOGGING WHILE DRILLING" TECHNIQUE FOR GROUTING DESIGN IN COLLAPSED UNDERGROUND QUARRIES)

by J.C. Erling, J. Lakshmanan and J. Rougé

Journées Nationales Géotechniques (National Geotechnical Symposium), Nantes, March 1981.

Abstract

The improvement of collapsed underground quarries, because they are inaccessible, is a technical and economical problem ; the latter aspect is vital, as the volumes to be grouted are much lesser than the known layout of the quarry (or of karstic cavities). The permanent use of the "logging while drilling" technique, and particularly drilling rate and reflected percussion parameters help to fill the gap between detailed investigation and grouting works. Interpretation of recordings allows the geophysicist to provide the contractor with such information as the exact location of zones to be grouted and the type of grout to be used.
On the other hand, post-grouting drilling with instantaneous logging provides a final calibration and control of the grouting.

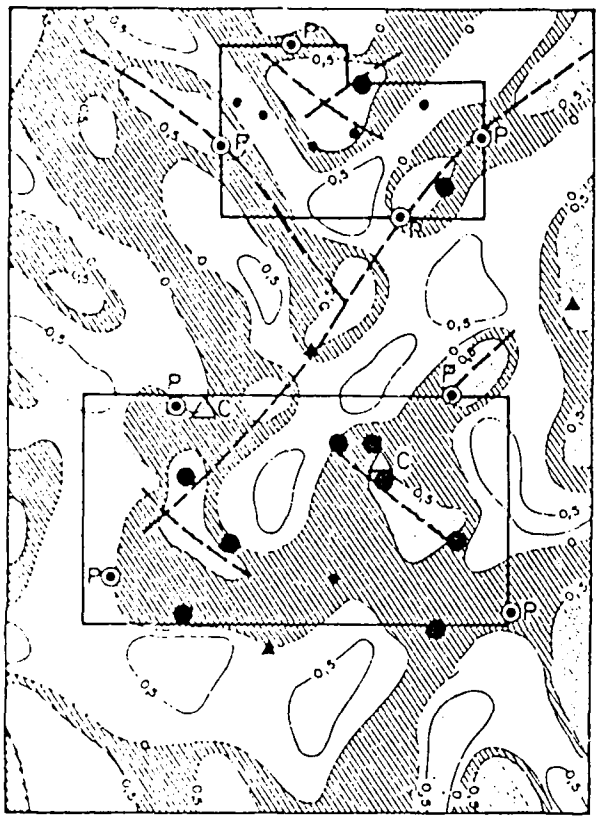

LE LUDE. Map of computed densities and grout volumes
FIG 1

- Densities > 1.8
- 1,3 < densities < 1.8
- 0.9 < densities < 1.3
- Densities < 0.8
- Possible axis of galleries
- P Peripheral drill holes
- Fill-in drill holes 10 cu.m
- Fill-in drill holes 1 to 10 cu.m
- Drill hole not grouted
- C Calibration drill hole

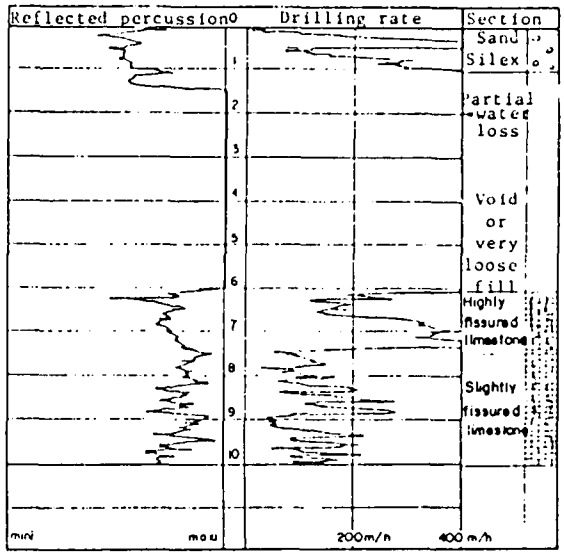

A.C.L. CONSTRUCTION CARRIERES sur SEINE FIG 2
Limestone quarry

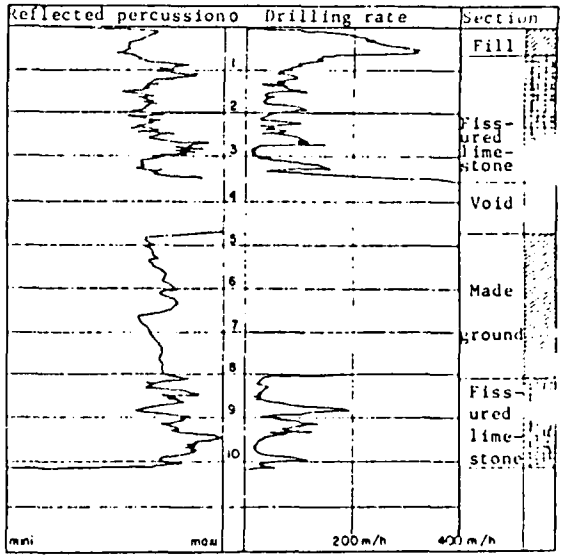

A.C.L. CONSTRUCTION — CARRIERES sur SEINE FIG 3
Limestone quarry

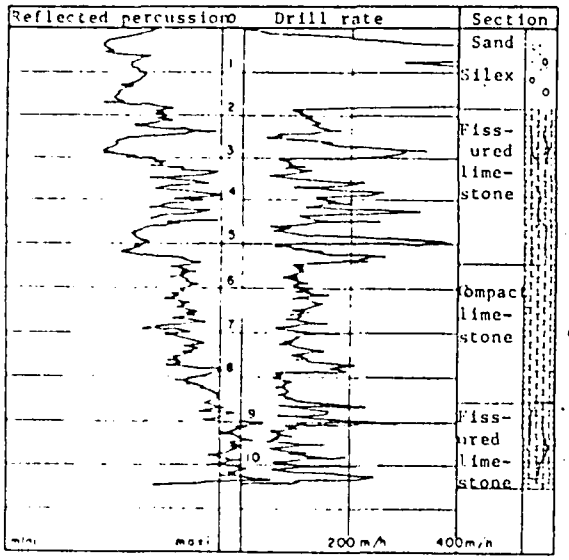

A.G.L. CONSTRUCTION — CARRIERES sur SEINE FIG 4

Limestone quarry

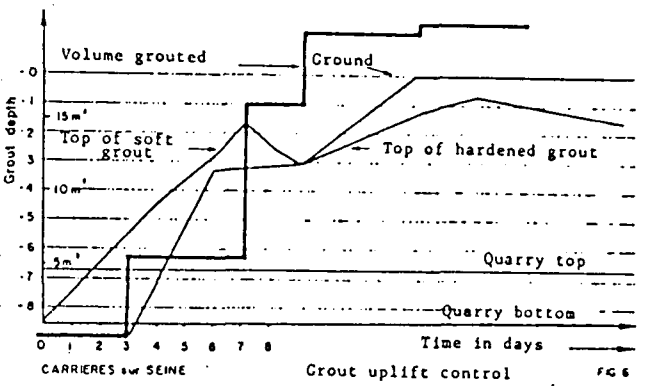

CARRIERES sur SEINE Grout uplift control FG 6

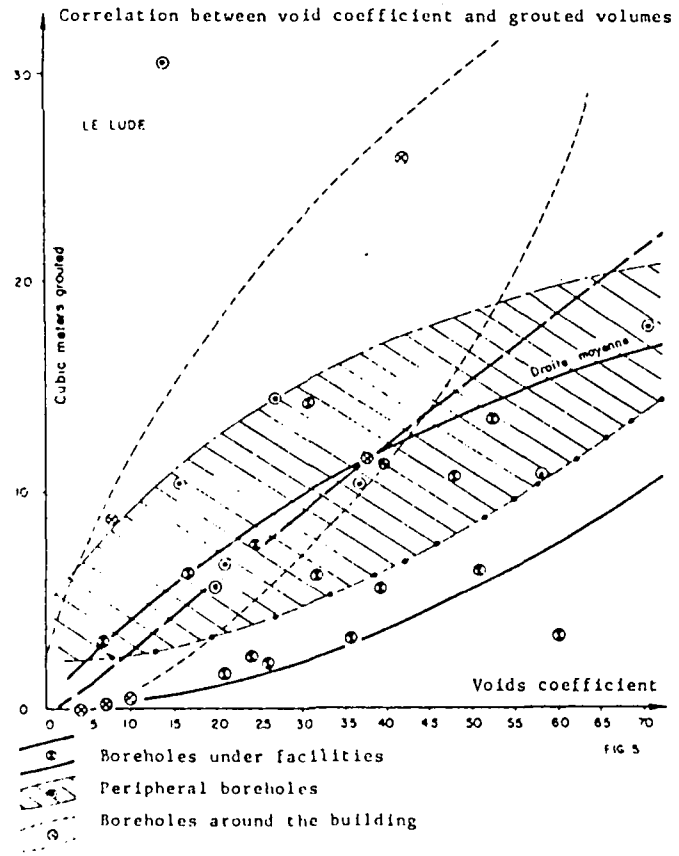

FIG 5

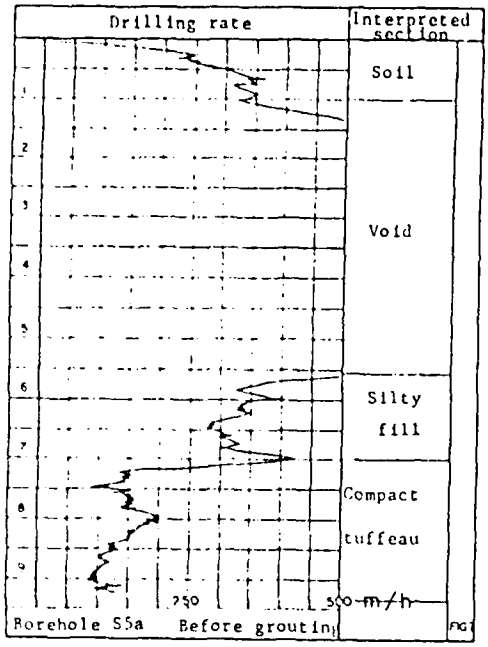
Drilling rate
Interpreted section
Soil
Void
Silty fill
Compact tuffeau
250
500 m/h
Borehole S5a Before grouting

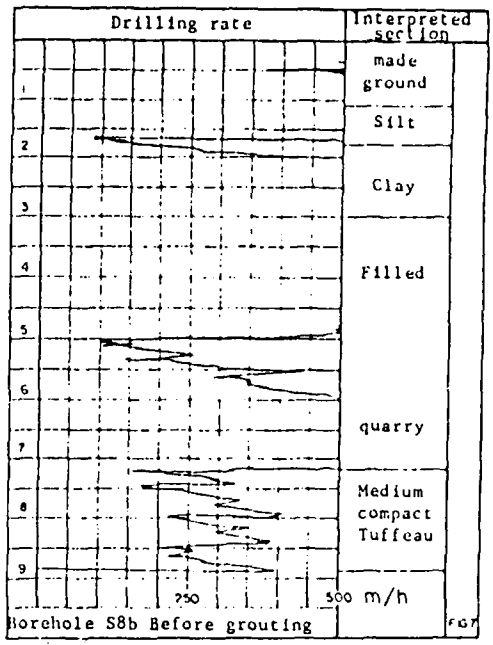
Drilling rate
Interpreted section
made ground
Silt
Clay
Filled quarry
Medium compact Tuffeau
250
500 m/h
Borehole S8b Before grouting

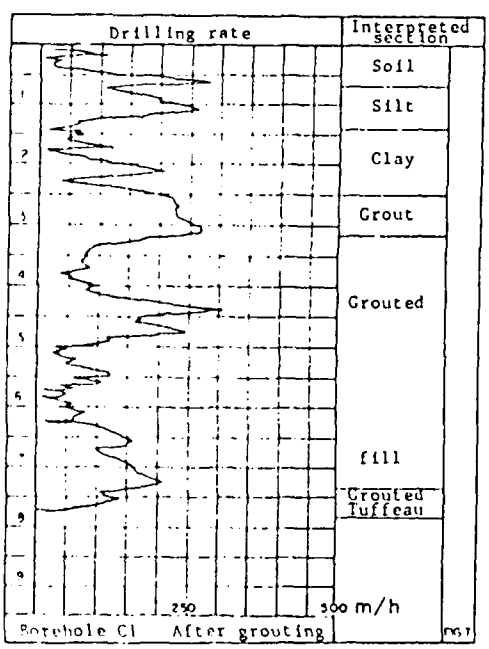
Drilling rate
Interpreted section
Soil
Silt
Clay
Grout
Grouted fill
Grouted Tuffeau
250
500 m/h
Borehole C1 After grouting

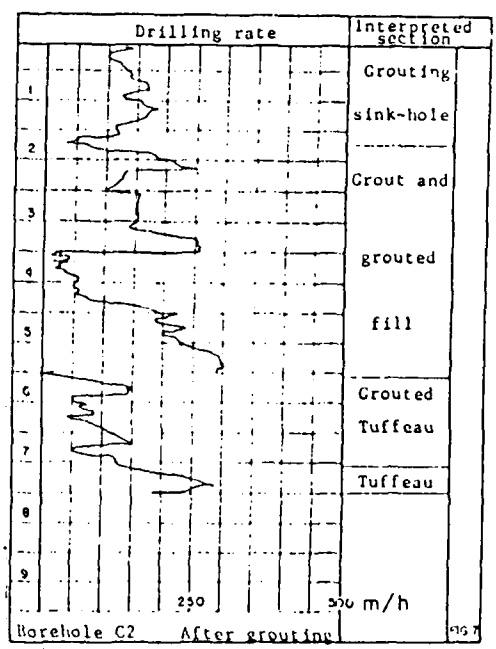
Drilling rate
Interpreted section
Grouting sink-hole
Grout and grouted fill
Grouted Tuffeau
Tuffeau
250
500 m/h
Borehole C2 After grouting

PAPER 7

LA PROSPECTION MICROGRAVIMETRIQUE ADAPTEE A LA RECONNAISSANCE DE CARRIERES SOUTERRAINES

(MICROGRAVITY ADAPTED TO THE INVESTIGATION OF UNDERGROUND QUARRIES)

by J.C. Erling and J. Lakshmanan

Quarry Inspection Authorities, Versailles. Technical meeting on old underground quarries, October 1985.

Abstract

The authors first describe the use of various geophysical techniques for the location of underground cavities, insisting on the interest of microgravity. After describing the position of microgravity in the planning of a complete survey, special aspects of microgravity interpretation are described:

- Vertical gradient measurement
- Gravity surveys inside tunnels
- 2-D processing with the Modcong program
- 2-D inversion with the Testfil program

The authors then give a series of practical examples:

+ underground limestone quarries in the city of Arras
+ " " " at Caen
+ TGV Atlantique fast railroad: location of gypsum quarries at Fontenay-aux-Roses
+ Housing project at Chanteloup-les-Vignes (west of Paris) above collapsed gypsum quarries
+ Adaptation of the construction of a building at St Germain-en-Laye (west of Paris) following results of a microgravity survey above a karstic zone
+ Density evaluation of embankments
- Grouting control at Varangeville (eastern France).

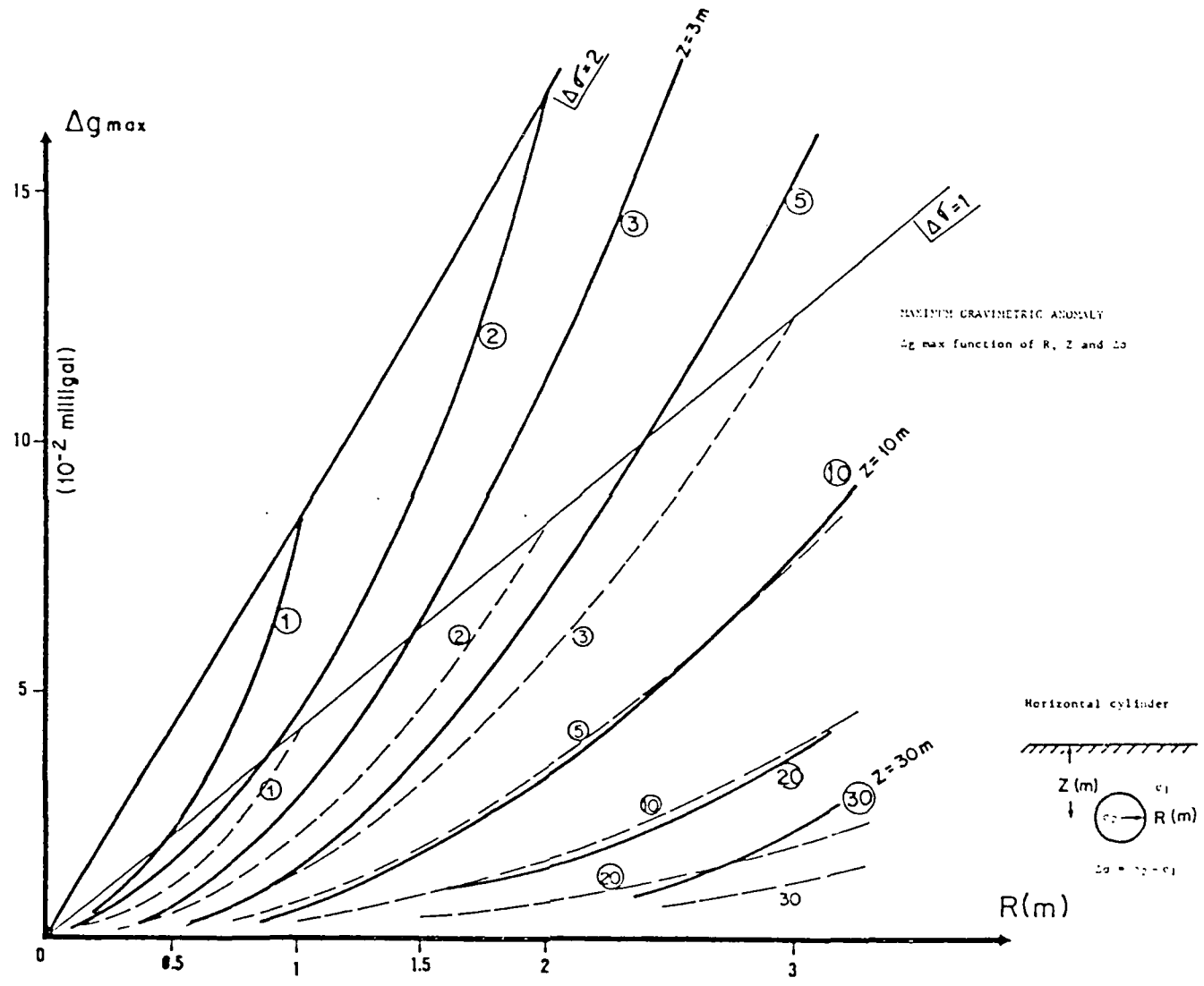
Δg max
15
10
5
(10⁻² milligal)
Δσ=2
Z=3m
Δσ=1
Z=10m
Z=30m
0
0.5
1
1.5
2
3
R(m)
Horizontal cylinder
Z (m)
R (m)

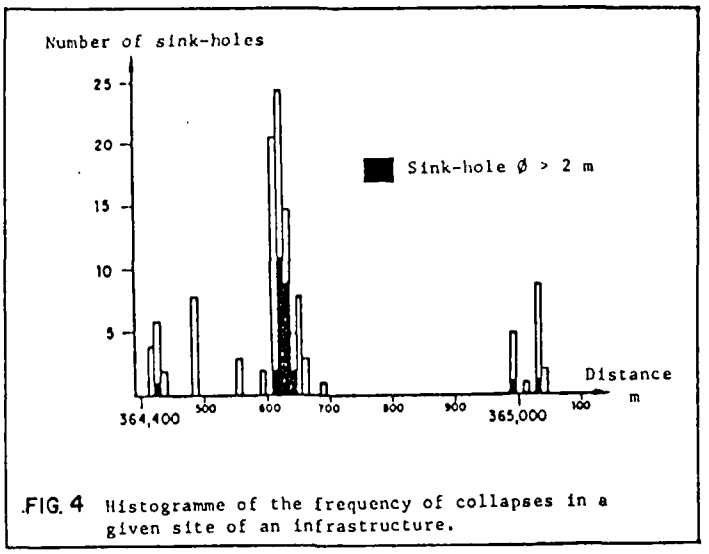

FIG. 4 Histogramme of the frequency of collapses in a given site of an infrastructure.

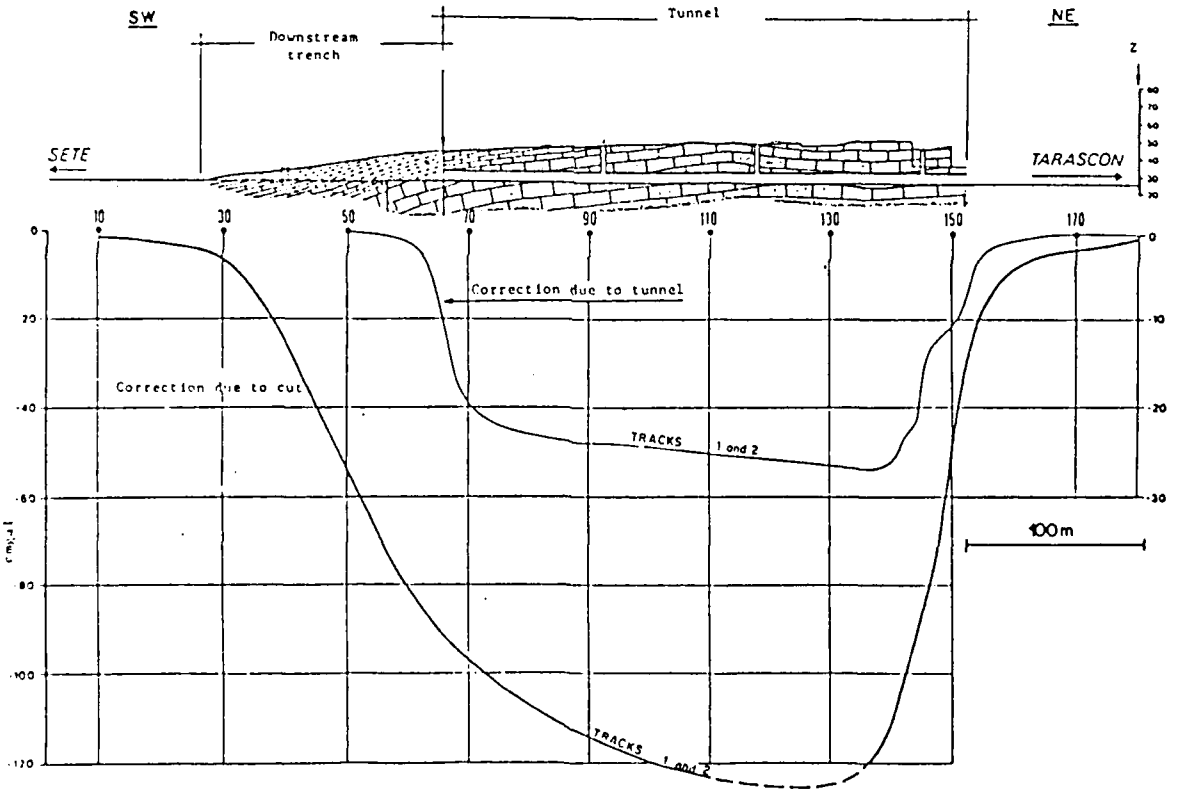

FIG 6

BEAUCAIRE TUNNEL SITE
GRAVIMETRIC SURVEY
TERRAIN CORRECTIONS

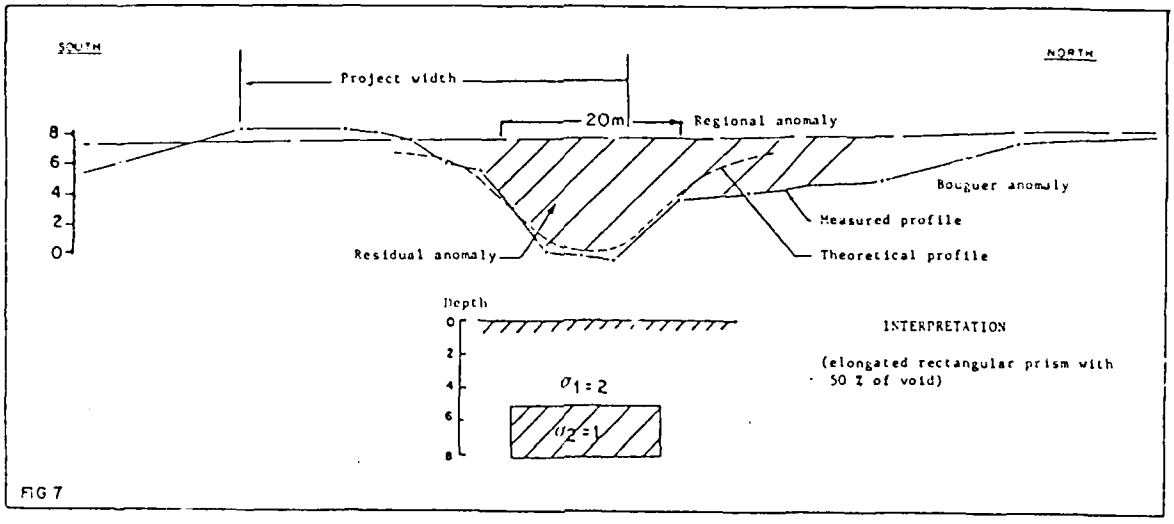

FIG 7

"MODCONG" PROCESSING

EXAMPLE OF APPLICATION

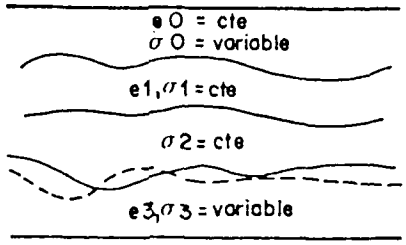

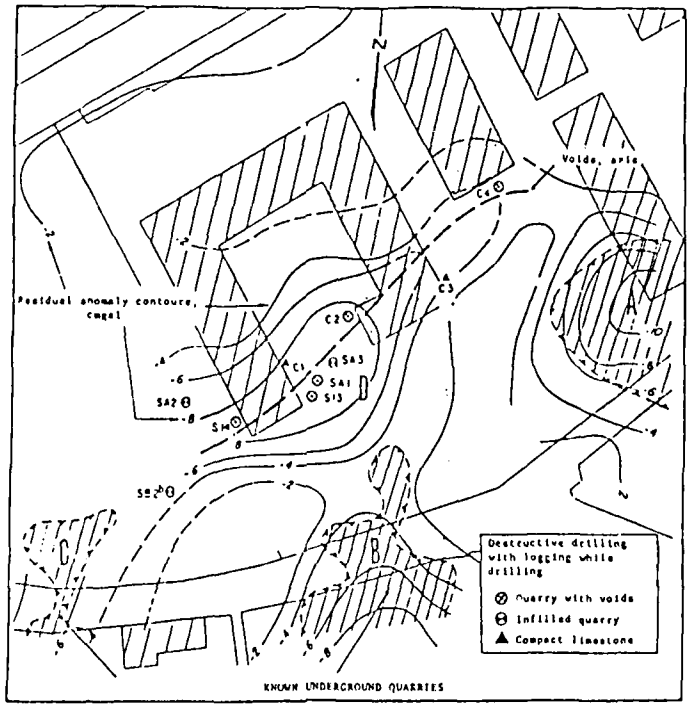

FIG. 11 Eastern suburb od CAEN. Microgravity survey.

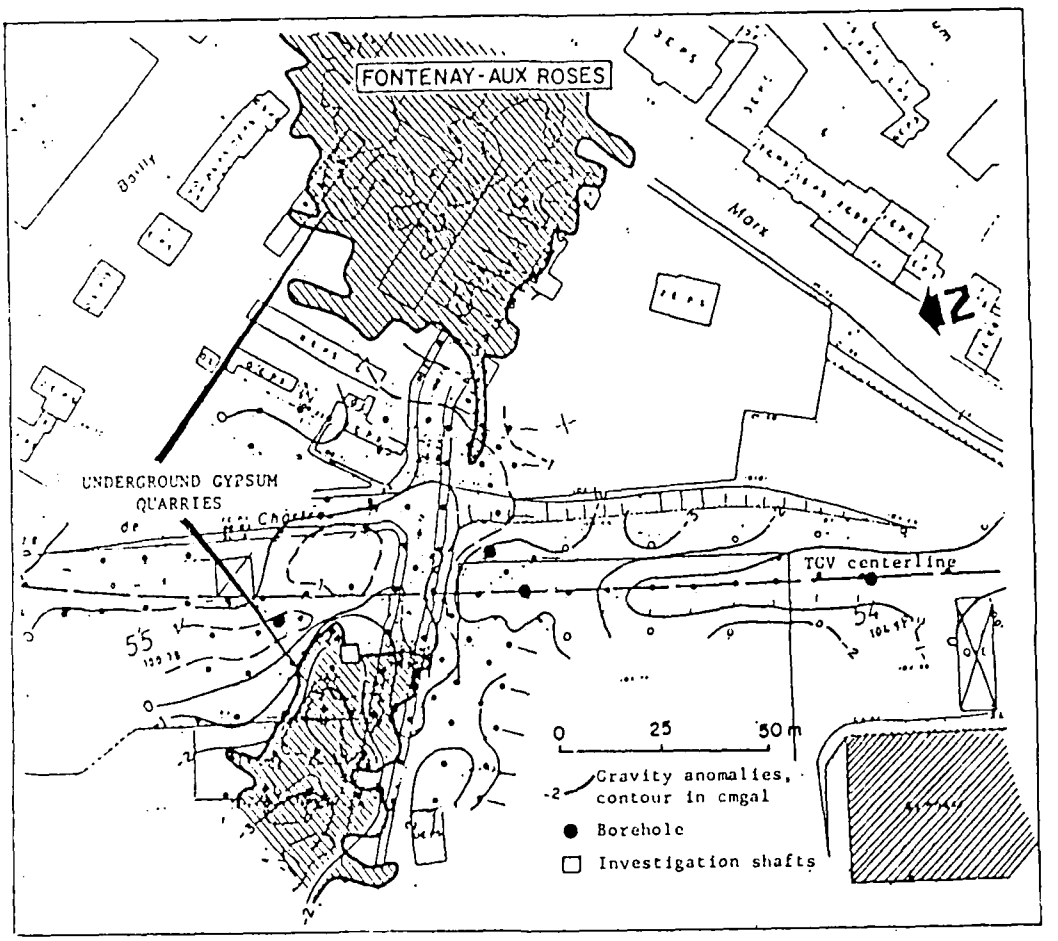

FIG 12 ATLANTIC LINE TGV (fast train) - FONTENAY-AUX-ROSES TUNNEL
GRAVITY SURVEY BEFORE WORKS

Figure 3. Blaisy railway tunnel. 3-D view of the south entrance.

Figure 2. Paris, Porte Pouchet. Microgravimetric survey.

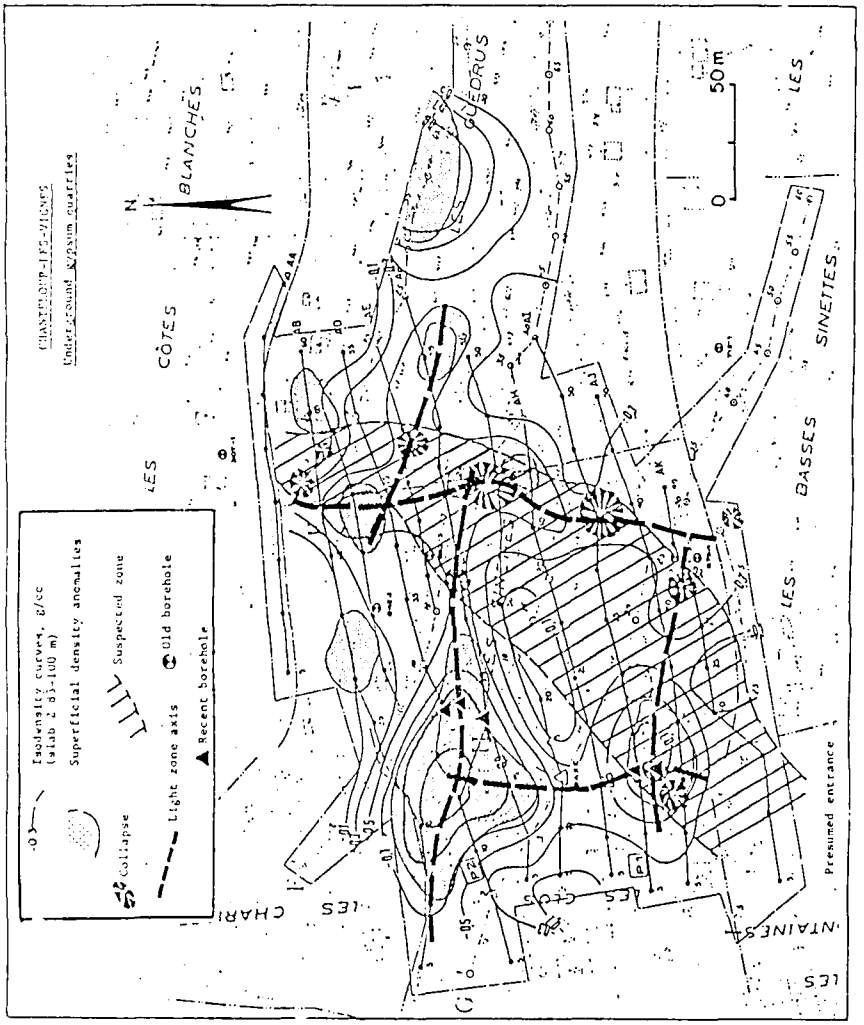

FIG. 13 CHANTELOUP-LES-VIGNES - DETAILED MICROGRAVITY SURVEY

FIG. 14

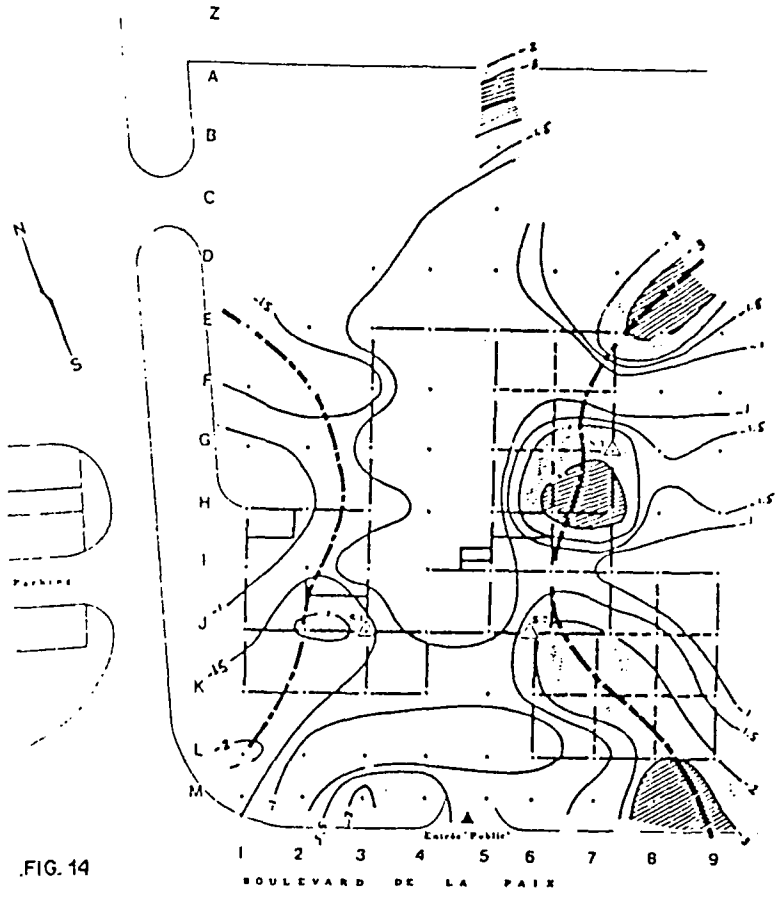

ST GERMAIN-EN-LAYE

Residual gravimetric anomaly

FIG. 14

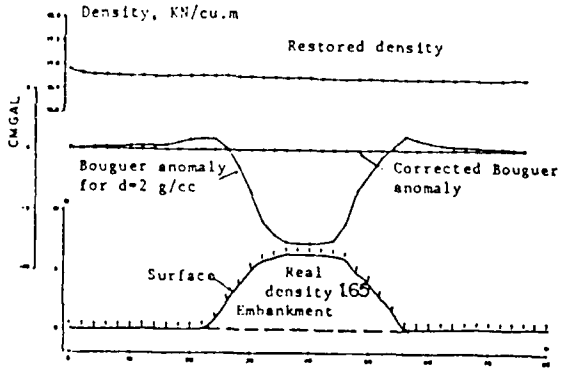

FIG. 15 Theoretical model. Nettleton processing.

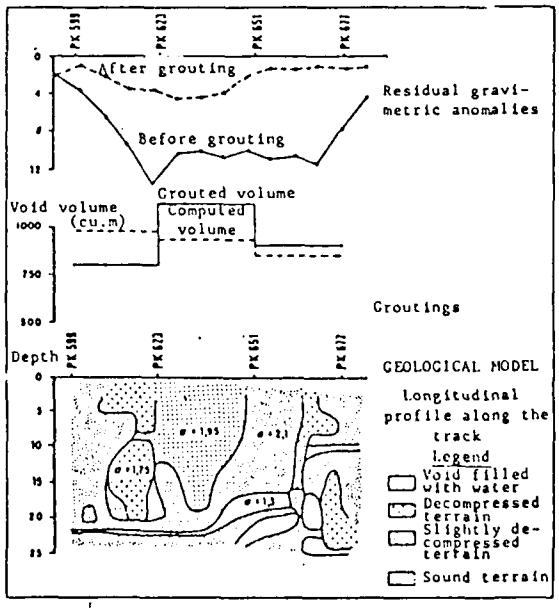

Fig. 16. Varangéville - SNCF Paris-Strasbourg line
Grouting control using microgravimetry

APPENDIX A : REPRINTS OF MAIN PAPERS IN ENGLISH

(A1) : Automatic three-layer, three dimensional deconvolution of the Pays de Bray anticline

(A2) : Microgravity probes the great pyramid

(A3) : Curved ray seismic tomography, 17 years experience from Zaire (1970) to Kenya (1987)

(A4) : Automatic deconvolution of gravimetric anomalies

(A5) : Variable density Bouguer processing of gravity data from Herault, France

APPENDIX A - PAPER A1

Geophysical Prospecting 31, 608-626, 1983.

AUTOMATIC THREE-LAYER, THREE-DIMENSIONAL DECONVOLUTION OF THE PAYS DE BRAY ANTICLINE*

E. ALESSANDRELLO, M. BICHARA and J. LAKSHMANAN**

ABSTRACT

ALESSANDRELLO, E., BICHARA, M. and LAKSHMANAN, J. 1983, Automatic Three-Layer, Three-Dimensional Deconvolution of the Pays de Bray Anticline, Geophysical Prospecting 31, 608-626.

Gravity data have been transformed into a three-layer, three-dimensional model by using an automatic procedure based on linear filtering. The Bouguer anomaly is first transformed by linear filtering into density variations located between two planes 1100 and 2500 m deep. These densities are then transformed into thicknesses with a constant density contrast of 0.4 g.cm^3 with two geological constraints for the second and third interface:

—minimum at 2500 m depth;
—maximum below a variable limit given by geology.

This gives the contact between the second and third layer. Differences between measured and computed gravity are then applied by a similar procedure to a layer located between depths of 0 and 500 m, giving the contact between the first and second layer. Interesting secondary anticlines and transverse faults are shown by various structural maps.

RESUME

ALESSANDRELLO, E., BICHARA, M. et LAKSHMANAN, J. 1983, Déconvolution Gravimétrique Tridimensionnelle et à Trois Couches de l'Anticlinal du Pays de Bray, Geophysical Prospecting 31, 608-626.

Utilisant un procédé automatique de déconvolution basé sur un filtrage linéaire, les auteurs ont transformé des données gravimétriques existantes en un modèle tridimensionnel à trois couches. L'anomalie de Bouguer est d'abord transformée par filtrage linéaire, en variations de densité d'une plaque horizontale, située entre 1100 et 2500 m de profondeur. Ces

* Paper read at the 43rd meeting of the European Association of Exploration Geophysicists, Venice, May 1981, revised version accepted December 1982.

** Compagnie de Prospection Géophysique Française, 77-79 avenue Victor Hugo, 92500 Rueil-Malmaison, France.

0016-8025/83/0800 0608 $02.00

densités sont ensuite transformées en épaisseurs en utilisant un contraste constant de densité de 0.4 g.cm^{-3}, avec deux contraintes géologiques pour la limite entre la deuxième et la troisième couche:

- minimum fixe à 2500 m de profondeur;
- maximum situé sous une limite variable en chaque point, fixée d'après la géologie.

Ayant obtenu ainsi le contact entre la deuxième et la troisième couche, la différence entre le champ mesuré et le champ dû à cette première structure est appliquée à une deuxième plaque située entre 0 at 500 m de profondeur, pour en déduire le contact entre la première et la deuxième couche. Les diverses cartes structurales obtenues mettent en évidence plusieurs anticlinaux secondaires, ainsi que de nombreuses failles transverses.

1. Introduction

The hydrogeology department of CPGF has been charged by the French Ministry of Agriculture (DDA of Seine Maritime) to evaluate ground water resources in the Pays de Bray area, northwest of Paris. In order to supply detailed structural information from the area, it was decided to carry out a quantitative analysis of existing gravity data, published by the BRGM, at a scale of 1 : 200 000.

The computer program developed by Lakshmanan (1973) and Bichara and Lakshmanan (1979) supplies, after introducing various geological constraints, a three-layer, three-dimensional model. The procedure, using linear filtering, is much faster than an iterative system described by La Porte (1963), involving a two layer method.

The procedure works as follows:

- —in the first step, construction of density maps of thick horizontal plates by linear filtering;
- —the use of geological buffers in the construction of the model.

2. Existing Data

We used the BRGM gravity maps of France, i.e., sheets of Abbeville, Rouen, Amiens, and Paris, corresponding to the southeast half of the famous Pays de Bray anticline (between Neufchatel-en-Bray and Beauvais), and starting with the Bouguer anomaly with a 2.3 g/cm^3 density. Unfortunately, the station spacing is quite high: 5–10 km^2 per station, equivalent to a 2.5–3 km square grid, and the measurements are rather old (BRGM North American gravity meter). The maps were digitized on a 2 × 2 km square grid. The interpretation was made on 20 × 20 = 400 central points, using a maximum of 28 × 28 = 784 points. Location of the area is shown in fig. 1.

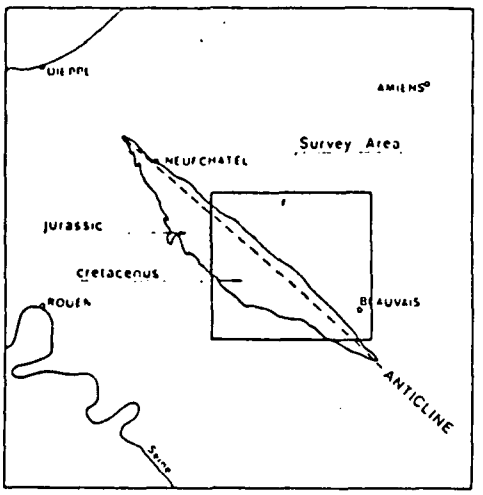

Fig. 1. Location of the survey. [Situation de l'étude.]

The Bouguer anomaly corresponding to the 400 central points is shown in fig. 2. The values increase from −30 mGal in the southwest towards the anticline, along which −15 mGal is observed towards the southeast and −4 towards the northwest. Northeast of the main anticline, the Bouguer anomaly stays high (−4 to −10), decreases along a syncline (−16 to −20), and finally increases to −13 in the northeast corner.

The maximum Bouguer variation is thus 26 mGal, the average anomaly compared to the minimum is 17 mGal, and the median anomaly is 22.7 mGal.

3. Systematic Deconvolution by Variable Density Horizontal Sheets

For each sheet, the entire Bouguer anomaly is used, giving four different density maps. The following depths were selected, starting from a datum plane located at 100 m above sea level:

0–500 m
500–1500 m
1500–2500 m
2500–3500 m

For each density map, the corresponding gravity field is computed as well as a map of differences between measured and computed fields and a map of the correlation coefficient r_0. This coefficient corresponds to the correlation between the computed field and measured Bouguer anomaly, inside a $7h \times 7h$ moving window, where h is the central depth of the plate:

$$r_0 = \frac{\sum_{S1 \cdot S2} (Th_i - Th_0)(\mathrm{Exp}_i - \mathrm{Exp}_0)}{\sqrt{[\sum_{S1 \cdot S2} (Th_i - Th_0)^2 (\mathrm{Exp}_i - \mathrm{Exp}_0)^2]}},$$

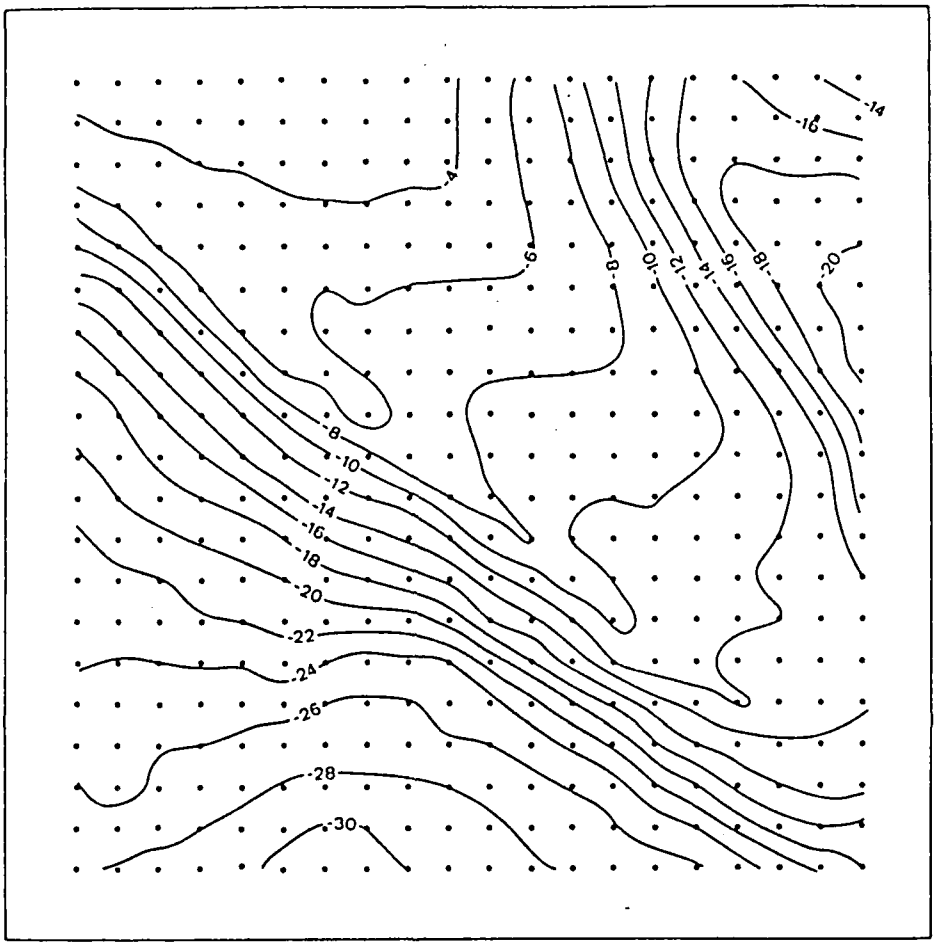

Fig. 2. Bouguer anomaly (in mGal). [Anomalie de Bouguer (mGal).]

where Th_i is the computed value at the running point i, Th_0 is the computed value at the considered point 0, Exp_i is the experimental Bouguer value at the running point i, Exp_0 is the experimental Bouguer value at the considered point 0, and $\Delta 1$, $\Delta 2$ are the intervals defining the moving window.

It should be noted that the use of a correlation coefficient, or rather of a similarity coefficient for depth determination, has been suggested by Naudy (1971). However, the following two points are different:

—Naudy's method supposes several standard shapes for the anomaly, while we determine the shape itself by deconvolution.

—Naudy supposes a two-dimensional anomaly and only examines profiles, while we study three-dimensional anomalies.

Figures 3 to 6 show the four computed density maps. The general statistics are as follows:

Bouguer anomaly

maximum	−2.3 mGal;
median	−8.2 mGal;
minimum	−30.9 mGal;
variation of amplitude	28.6 mGal;
median variation	M = 22.7 mGal.

In order to give a homogeneous set of densities corresponding to a 1000-m-thick slab, the 0- to 500-m map was transformed into a 0- to 1000-m map.

In fig. 7, variations of mean square difference of the whole area are shown as functions of the average depth of each slab. It can be seen that the mean square difference increases with depth without a minimum. However, this parameter increases quite suddenly after an average depth of about 2000 m (*see* table 1).

The correlation coefficient is very close to 1. The obtained values decrease for depths greater than 2000 m for the entire area, 1700 m for the main anticline (i.e., 1200 m for its top), and 2200 m for a syncline located 8 km SW of the center of the

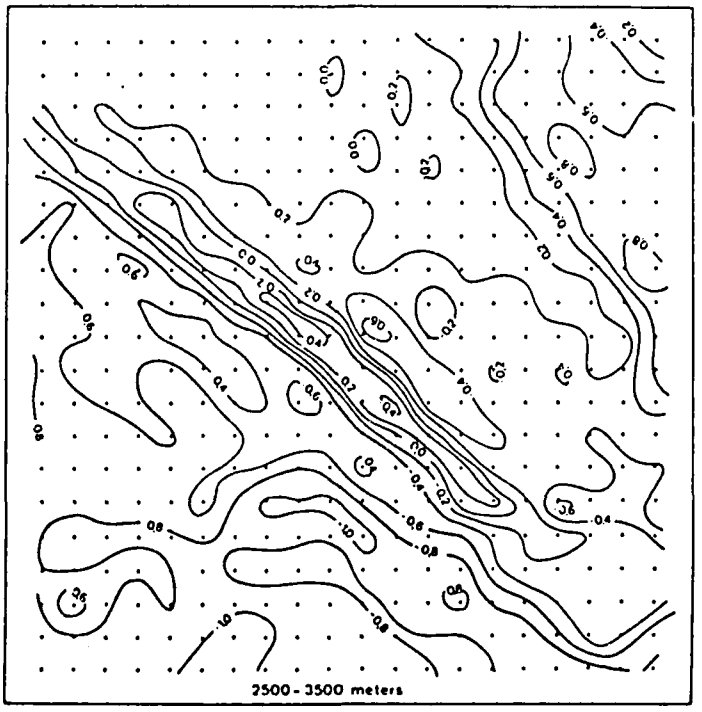

Fig. 3. Inverted density between 2500 and 3500 m (g/cm^3). [Densité obtenue par inversion, entre 2500 et 3500 m (g cm^{-3}).]

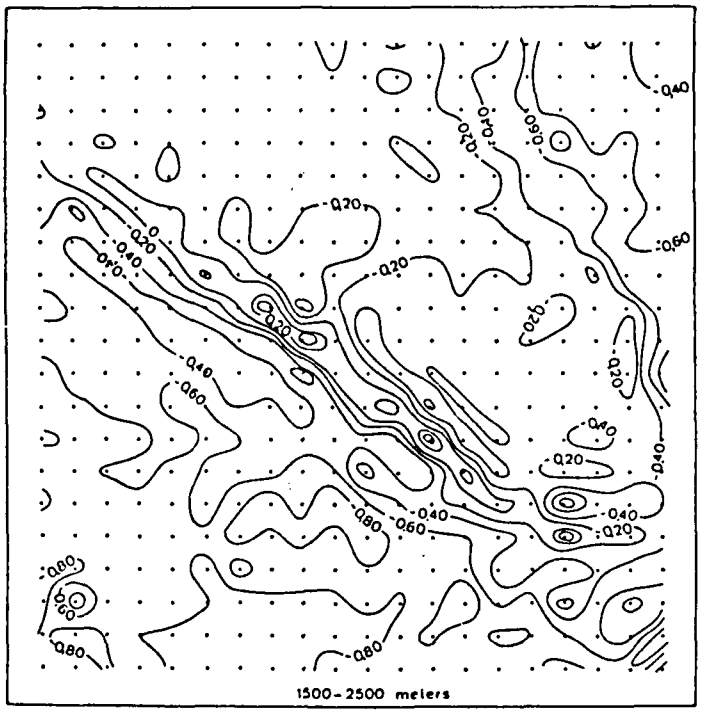

Fig. 4. Inverted density between 1500 and 2500 m (g/cm^3). [Densité obtenue par inversion entre 1500 et 2500 m (g/cm^3).]

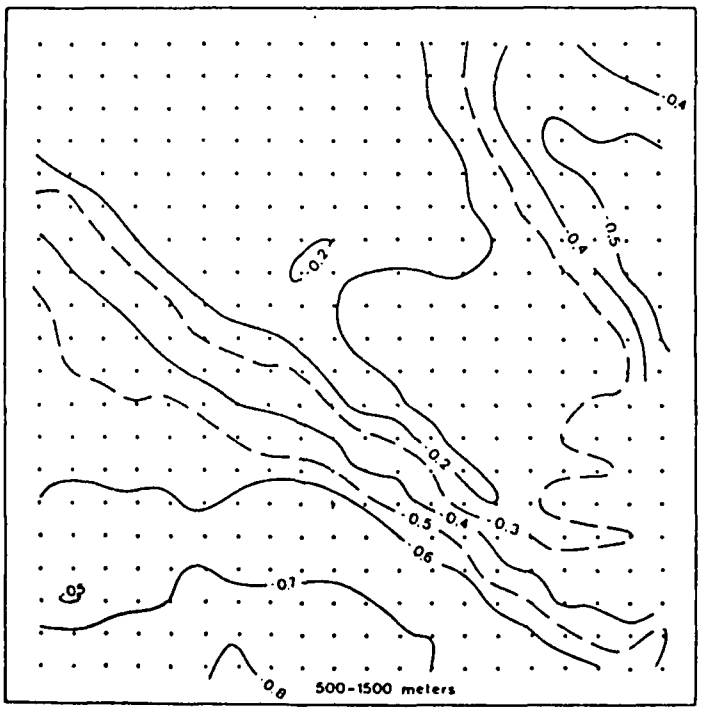

Fig. 5. Inverted density between 500 and 1500 m (g/cm^3). [Densité obtenue par inversion entre 500 et 1500 m (g/cm^3).]

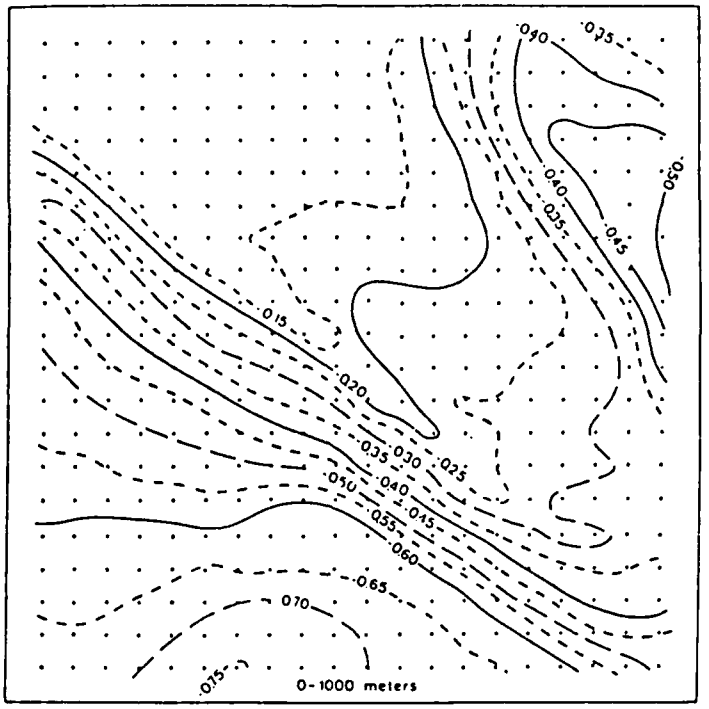

Fig. 6. Inverted density between 0 and 1000 m (g cm^3). [Densité obtenue par inversion entre 0 et 1000 m (g cm^3).]

main anticline. It should be pointed out that the actual depths to the top of the anticline found in five wells were 1110, 1207, 1078, 959 and 979 m (datum plane 100 m above sea level).

It should be noted that, if both mean square difference and correlation coefficient show a semi-horizontal section for the plate center located between 1000 and 2000 m, another improvement in these criteria can be seen when the plate outcrops.

Table 1. *Correlation statistics and average densities.*

Depth (m)	Mean square difference		Correlation coefficient		Relative densities (g/cm^3)		
	mGal	Percent of M	Whole area	Main anticline	Maximum	Minimum	Amplitude of variation
0-500	0.05	0.2	0.99999	0.99999	−0.11	−1.51	1.40
(0-1000)	—	—	—	—	(−0.06)	(−0.76)	(0.70)
500-1500	0.15	0.7	0.99988	0.99993	−0.016	−0.814	0.80
1500-2500	0.21	0.9	0.99964	0.99983	+0.53	−0.94	1.47
2500-3500	0.46	2.0	0.99772	0.99859	+0.57	−1.12	1.69

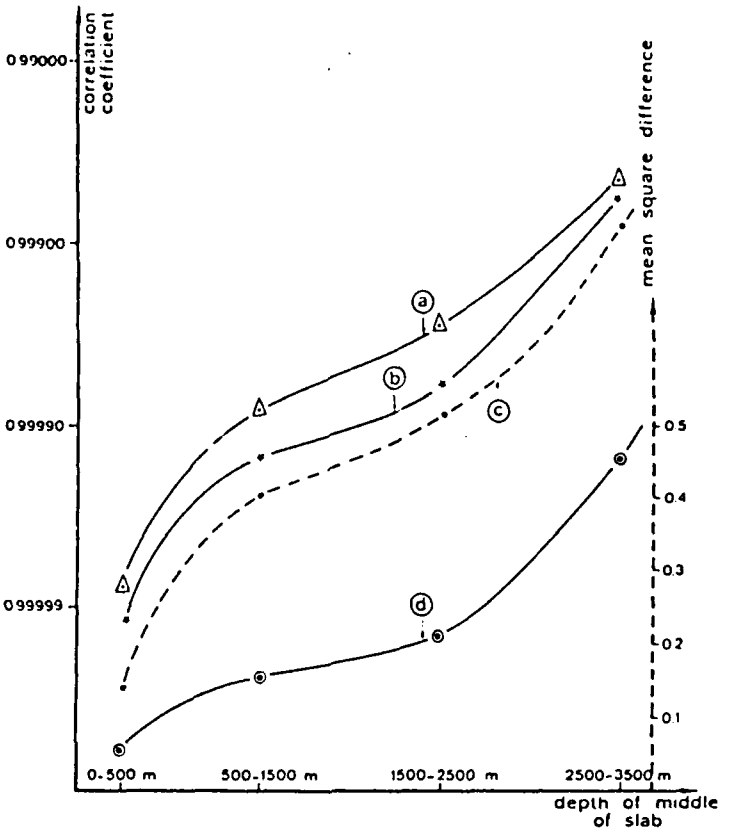

Fig. 7. Variation of mean square differences and correlation coefficients with depth. (a) Correlation coefficient, entire area; (b) correlation coefficient, main anticline; (c) correlation coefficient, southwest syncline; (d) average mean square difference. The arrow indicates average depth computed in next step.

[Variation des écarts types et des coefficients de corrélation avec la profondeur. (a) Coefficient de corrélation, ensemble de la prospection; (b) coefficient de corrélation, anticlinal principal; (c) coefficient de corrélation, synclinal du Sud-Ouest; (d) écart type moyen. La flèche indique la profondeur calculée à l'étape suivante.]

The general shape of those curves suggests that, in addition to the main causes situated at 1000–2000 m, there exists some gravimetric noise, due to superficial causes, or due to imperfections in the system itself.

These two parameters can thus be used to determine the maximum depth of gravity anomalies, similar to the rules given by Bott and Smith (1958) for simple bodies.

A third criterion is the absolute value of density variations shown in fig. 8 for the entire area, the main anticline and the southwest syncline. The values are close to the theoretical density limit (σ_0) for the outcropping slab (0–500 m), which is

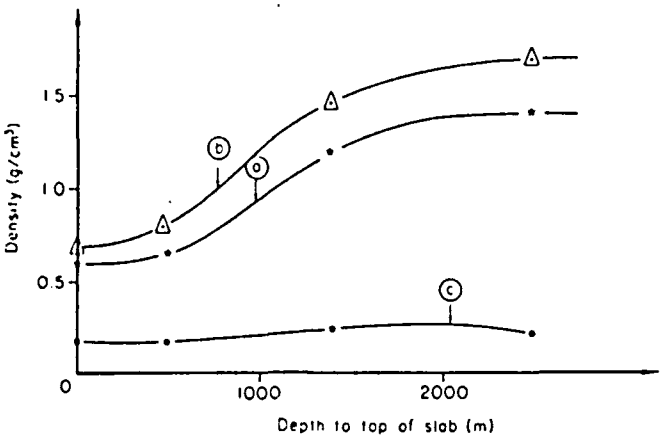

Fig. 8. Variation of densities with depth. (a) Entire area; (b) main anticline; (c) southwest syncline. The arrow indicates depth to top of slab computed in next step.

[Variation des densités avec la profondeur. (a) Ensemble de la prospection; (b) anticlinal principal; (c) synclinal Sud-Ouest. La flèche indique la profondeur jusqu'au toit de la plaque, calculée à l'étape suivante.]

$$\sigma_0 = \frac{23.87\ \Delta g_{max}}{e}.$$

For $\Delta g_{max} = 28.6$ mGal and $e = 500$ m, one has $\sigma_0 = 1.365$ g/cm^3 instead of the computed value of 1.4 g/cm^3. Maximum density contrast increases for depths greater than 500–700 m, considering either the whole area or the main anticline, reaching 1.4 or 1.6 g cm^3 for depths to the top of basements of about 2000 m. These values are geologically impossible; to reduce them, it would be necessary to assume a thicker plate, bringing back the top of the plate to depths of around 1000 m (thickening the plate downwards would not substantially reduce the density contrast). The maximum density contrast thus provides another constraint on the depth to the top of the anomalous layer.

4. Structural Interpretation with Geological Constraints

In order to use a three-layer model, it was necessary to simplify the complex geology. The general stratigraphy of the area is, very schematically, as shown in table 2 (with depths relative to a datum plane 100 m above sea level).

The interpretation starts by supposing that the anomaly is due to density variations of a horizontal slab. We selected 1100 m as depth to roof and 2500 m as depth to base, following the results of the systematic interpretation by slabs and the geological data.

Table 2. *General stratigraphy of the area.*

	Presumed density	SW of the anticline	Anticline	NE of the anticline
	(g/cm³)			
Tertiary (sand, clay, limestone)	2.0	100 m	0	150 m
Cretaceous (chalk, marl)	2.0	100 + 150 = 250 m	0	150 + 150 = 300 m
Jurassic (marl, limestone)	2.4	250 + 1250 = 1500 m	100 m	300 + 1200 = 1500 m
Permo-Triassic (clay, sandstone)	2.4	1500 + 1000 = 2500 m	Absent	Absent
Primary (limestone, slate, sandstone)	2.4	1500 + 1000 = 2500 m	Absent	Absent
Crystalline basement (gneiss + local basalt intrusions)	2.8			

The map obtained (fig. 9) shows variations of density between −0.60 and +0.20 g/cm³, that is a maximum contrast of 0.80. This excessive contrast (compared to the theoretical 2.8–2.4 = 0.4) could mean that:

—the plate is thicker than 1400 m;
—and/or more superficial anomalies are superimposed.

A first test with the same top and a higher base (in that case, Primary and Permo-Triassic sediments were included in the basement) gave even more unrealistic density contrasts. We therefore concluded that a more correct model consisted in grouping the Primary and the Permo-Triassic with the Jurassic.

Structural analysis of this density map shows many interesting features. Several secondary anticlines and synclines parallel to the main anticline can be seen. In addition, several transverse faults (NE–SW or ENE–WSW) can be seen, and should be compared to geological features described by, e.g., Weber (1973), Pomerol (1980) and Debeglia (1977).

The second step, which follows automatically, transforms these density variations into thickness changes, assuming:

—a flat base at a depth of 2500 m;
—a variable top, situated between two "buffers": the lower "buffer" at a depth of 2500 m, the upper "buffer" determined from the general geological structure, translated 100 m upwards, to allow some freedom;

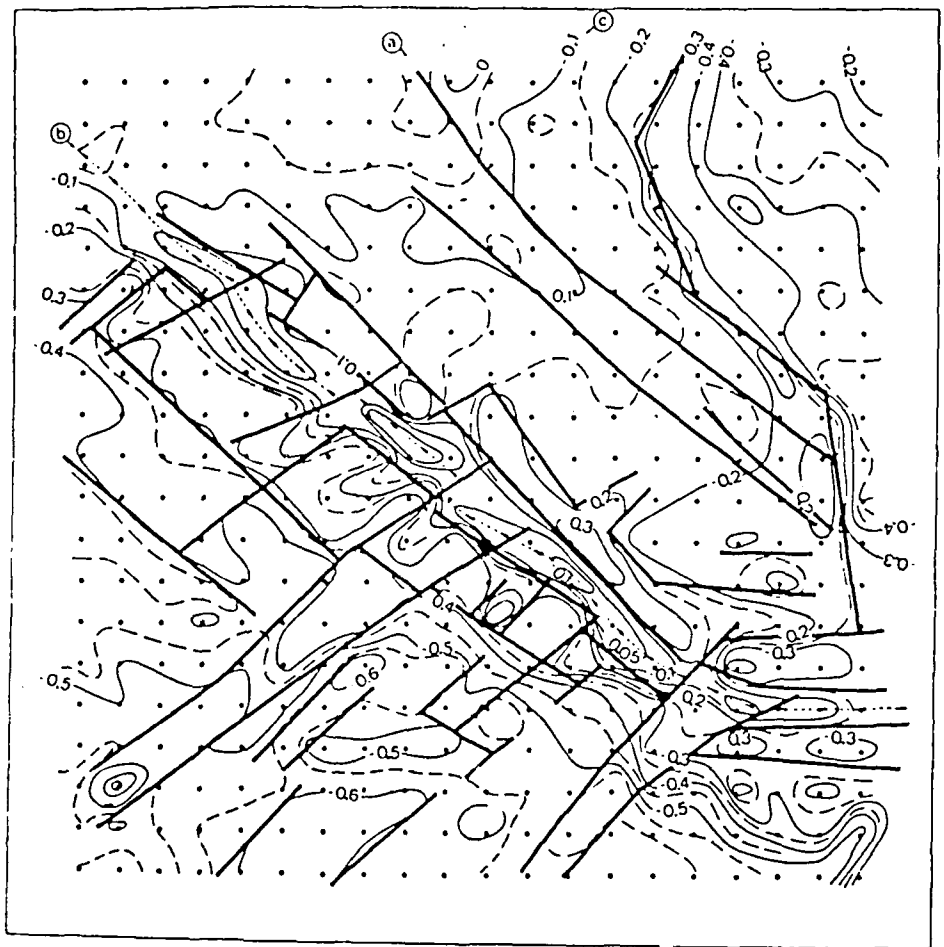

Fig. 9. Structural map, densities between 1100 and 2500 m. (a) Fault; (b) major anticline; (c) density (g/cm³).

[Carte structurale, densités entre 1100 et 2500 m. (a) Faille; (b) anticlinal principal; (c) densité (g/cm³).]

a constant density contrast of 0.4 g/cm³ (basement 2.8 g/cm³, sedimentary strata 2.4 g/cm³).

The upper buffer is shown on fig. 10. The transformation in each 2 × 2 km prism of densities into thicknesses is done in two steps:

– first, a linear transformation of density contrasts $\Delta\sigma$ into

$$h \approx \frac{(2500 - 1100) \times \Delta\sigma}{(2.8 - 2.4)}.$$

AD-A195 399 APPLICATION OF MICROGRAVITY TO THE ASSESSMENT OF EXISTING STRUCTURES AND (U) COMPAGNIE DE PROSPECTION GEOPHYSIQUE FRANCAISE RUEIL-MALMAISO J LAKSHMANAN

4/4

UNCLASSIFIED 29 APR 88 DAJA45-86-C-0022 F/G 8/5 NL

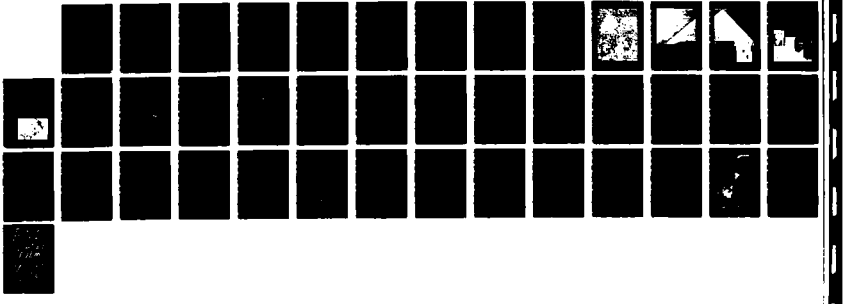

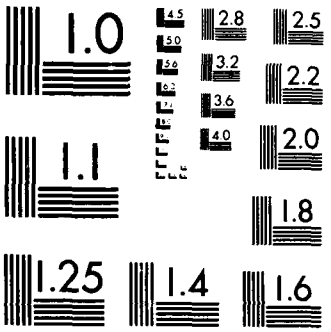
1.0
1.1
1.25
1.4
1.6
1.8
2.0
2.2
2.5
2.8
3.2
3.6
4.0
4.5
5.0
5.6

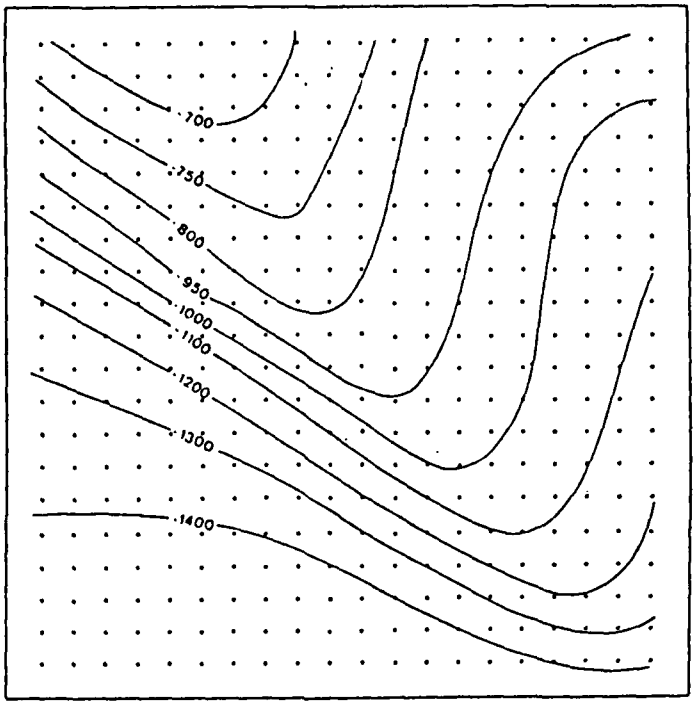

Fig. 10. Geological "buffer": minimum depths below sea level of interface between second and third layer. ["*Butoir*" *géologique: profondeurs minimales* sous le niveau de la mer, du contact entre seconde et troisième couches.]

The exact correction takes into account displacement of the prism's center of gravity and is not described here;

—a second iteration slightly modifies the top of the prism by treating differences between measured field and the field due to the approximate structure. Improvements by further iterations are very small.

After computing the final basement map, the corresponding field is computed and compared to the measured field.

The residual is mainly due to the fact that along the main anticline as well as in the northeast of the area, the buffer has often been reached. This residual is then supposed to be due to variations of a first layer located between depths of 5 and 500 m, corresponding approximately to the Tertiary and the Cretaceous (in other surveys, the residual could also have been attributed to basement density changes).

Structural analysis of this first layer is then carried out in a similar manner:

—density map between 5 and 500 m;

—transformation into changes of thickness, supposing a density contrast of 0.4 g/cm^3 (first layer 2.0 g/cm^3, second layer 2.4 g/cm^3).

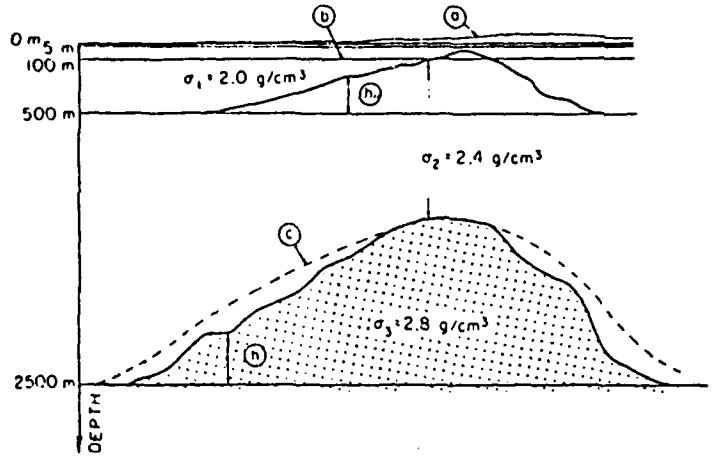

Fig. 11. Geological constraints of the model. (a) Ground level (average elevation 100 m above sea level); (b) sea level; (c) geological "buffer" for top of third layer; (h) height of interface between second and third layer limit above base (2500 m below datum); (ho) height of interface between first and second layer limit above base (500 m below datum).

[Contraintes géologiques du modèle. (a) Altitude moyenne du terrain + 100 NGF; (b) niveau de la mer; (c) "butoir" géologique pour le toit de la troisième couche; (h) hauteur de la limite 2ème–3ème couches, au-dessous d'une base située à 2500 m de profondeur; (ho) hauteur de la limite 1ère–2ème couche avec base située à 500 m de profondeur.]

A three-layer model is thus obtained. The various parameters and buffers are shown on fig. 11.

The computer program supplies the following maps:

—Bouguer anomaly;
—top of the deep structure;
—field due to the deep structure;
—difference between Bouguer and computed field;
—top of the superficial structure;
—field due to the superficial structure;
—last residual;
—for each step, difference maps and correlation maps.

The first two maps are shown in figs. 11 and 12. A general SW–NE cross-section (fig. 13) illustrates the complete interpretation.

5. Comments and Interpretation

5.1. Basement Map (fig. 12)

This map shows a series of NW–SE anticlines and synclines, parallel to the main Pays de Bray anticline. Several short transverse faults can be seen; several of them

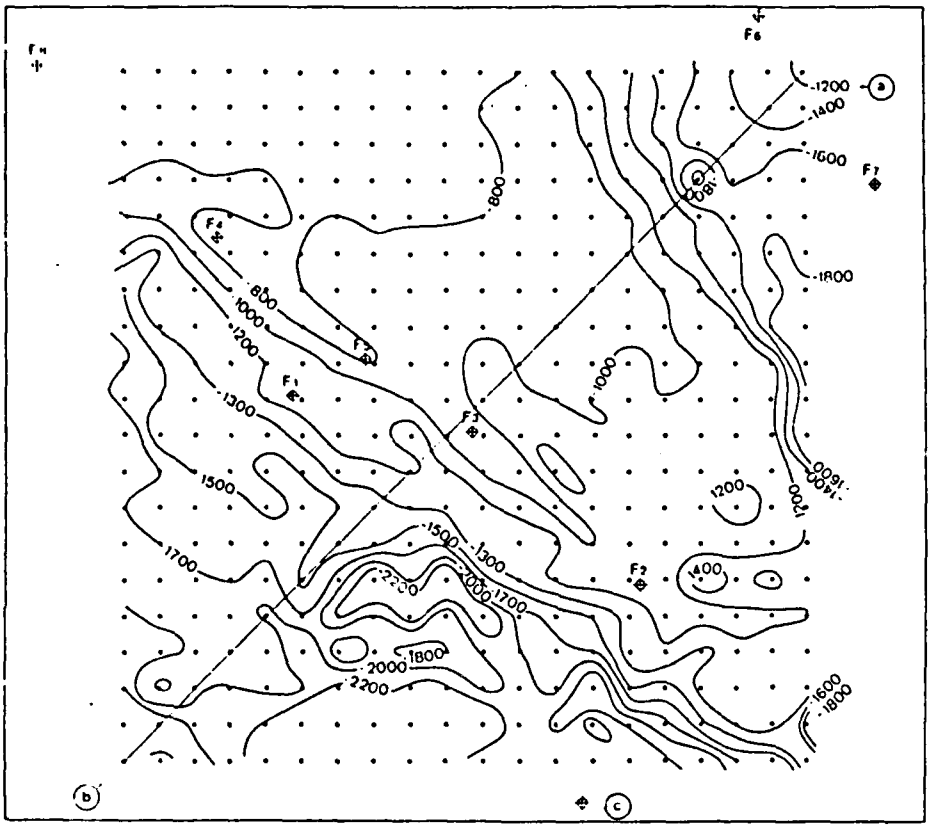

Fig. 12. Basement map. (a) Depth below sea level; (b) cross-section; (c) wells.
[Carte en courbes de niveau du socle. (a) Profondeurs sous le niveau de la mer; (b) coupe d'interprétation; (c) forages.]

seem to be connected. The main transverse fault is NE–SW and connects the center of the survey to the SW corner.

Five wells where the igneous basement was reached were compared to the final interpretation as shown in table 3.

These very small differences are surprising, particularly since well 1 is located on a secondary anticline on the southwest flank of the main anticline. This secondary anticline is practically invisible on the Bouguer map. Three other wells lie outside the survey area, two near the NE corner, and another one near the NW corner. The differences are more important:

F6 (Bellcuse), real depth 871 m instead of about 1300 m;
F7 (Mardivilliers), real depth 144 m instead of about 1650 m;
F8 (Compainville, PB 201), real depth 861 m instead of about 700 m.

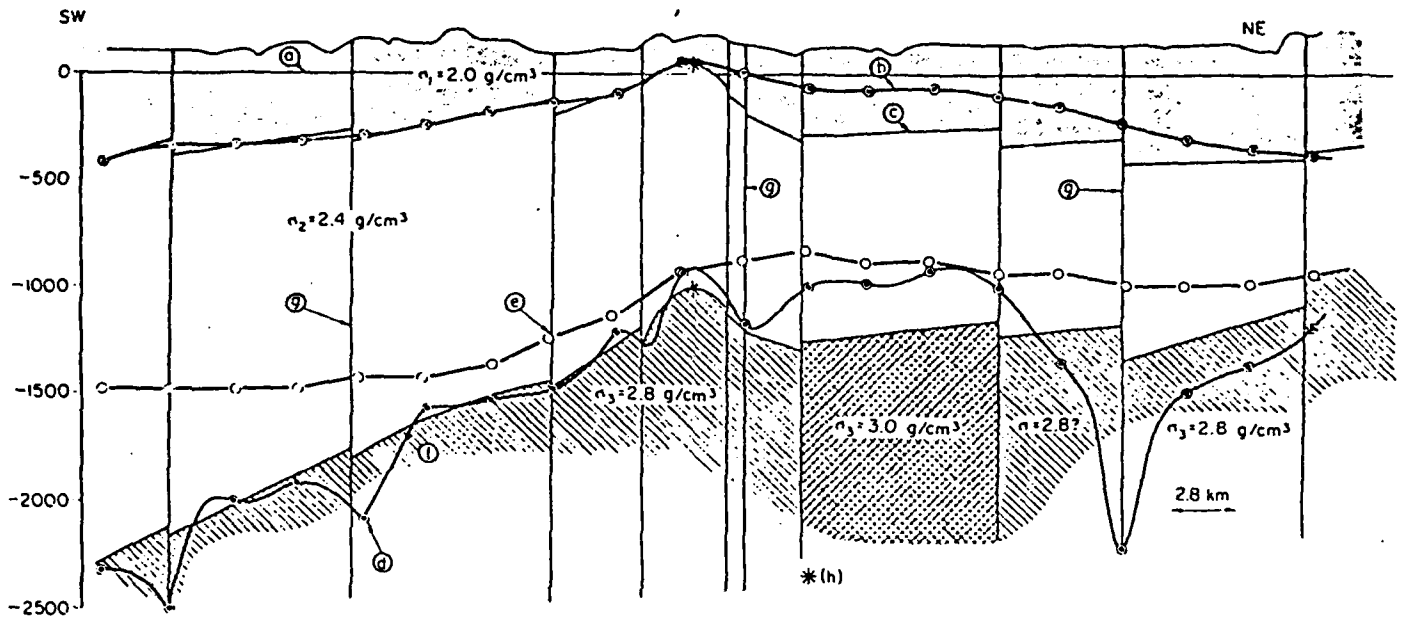

Fig. 13. Interpreted cross-section. (a) Sea level; (b) first and second layer gravity limit; (c) interpreted base of Kimmeridgien; (d) second and third layer gravity limit; (e) geological upper "buffer" for limit (d); (f) interpreted basement; (g) low density faulted zones; (h) geological boundaries, after drill holes.

[Coupe d'interprétation. (a) Niveau de la mer; (b) limite 1ère–2ème couches d'après déconvolution; (c) base interprétée du Kimmeridgien; (d) limite 2ème–3ème couches, d'après déconvolution; (e) "butoir" supérieur géologique pour la limite (d); (f) toit interprété du socle; (g) zones faillées, à plus faible densité; (h) limites géologiques, d'après forages.]

Table 3. *Comparison of depths at five wells.*

	Actual depth (m)	Computed depth (m)
Well F1 (Ferrières-en-Bray)	−1010	−1100
Well F2 (aux Marais)	−1107	−1060
Well F3 (Hodenc-en-Bray PB402)	−978	−900
Well F4 (Villers Vermont)	−859	−800
Well 5 (Hanaches PB101)	−879	−900

These differences can be explained by:

—unreliability of the extrapolation of our results out of the survey area;
—lower quality of deconvolution due to edge effects, particularly in the corners;
—for wells F6 and F7, influence of the low-density NW–SE axis crossing the NE corner of the survey;
—influence of a regional anomaly.

This last reason seems to be the most important: all the wells along the main anticline (except F1) have real depths greater than computed depths, while wells F6 and F7, near the NE corner, have real depths smaller than computed depths.

5.2. First computed field and first residual

The computed fields look very much like the Bouguer anomaly, and the residual map is more important. The mean square residual is 1.86 mGal (8.2% of the median Bouguer anomaly). The main differences are due to points where the structure reaches the buffer, principally along the main anticline. The residual map is therefore a "ghost" of the Bouguer anomaly.

5.3. Superficial structural map

The main anticline shows up clearly, as well as another parallel anticline 11 km to the NE. Three transverse features appear, one of which corresponds to the major transverse fault visible on the basement map. The northern feature was not visible on the other maps.

5.4. Second computed field and last residual

The second computed field is very similar to the first residual field. The mean square difference is 0.17 mGal, 3.8% of the average amplitude of the first residual

(4.5 mGal) or only 0.8% of the average amplitude of the original Bouguer anomaly (22.7 mGal). The figure of 0.8% is to be compared with the mean square difference of 8.2% on the basement map.

It should be noted that the remaining differences are due to:

—four points reaching the second buffer, along the main anticline, with differences of 0.63, 0.96, 0.31, and 0.37 mGal, respectively;
—edge effects.

If these four points and one line close to the margin were removed, the mean square difference would be only of 0.13 mGal (0.6%).

Taking into account these remarks, it can be seen that the last residual map still has an organized look. First, an extensive "anticline" of small amplitude, with the same axis as the main anticline, can be seen; it may be related to regional variations in the basement. This "regional" anomaly has the following values:

Northeast	−0.4 mGal;
Anticlinal axis	+0.2 to +0.3 mGal;
Southwest	−0.2 mGal.

The corresponding gradients are very small: 0.02 mGal/km.

Apart from this regional effect, two other slight "anticlines" can be seen parallel to the main anticline. However, after comparison with the basement map, it seems that the deep deconvolution was slightly too powerful and that the two synclines separated by the main anticline on the basement map are somewhat shallower than indicated. Of course, other geological interpretations are also possible.

5.5. *Edge effects*

The above-mentioned edge effects are mainly due to the calculation of the resultant field and not to the deconvolution itself. When this job was carried out, the resultant field was computed without extrapolation of the structure out of the survey area. Since then, the program has been adjusted to suppress this minor defect.

5.6. *Final geological interpretation*

The general geological interpretation is shown in fig. 13, which is a SW–NE diagonal cross-section. We have drawn:

—the interface between the second and the third layer according to deep deconvolution;
– the geological buffer;
—top of the basement (third layer);
—the interface between first and second layer according to residual deconvolution.

The comparison between the top of the second layer and our geological interpretation based on surface data shows a remarkable coincidence between this

interface and the base of the Kimmeridgian, except in an area located between 2 and 13 km NE of the main anticline. In order to have regular variation of thicknesses, it was necessary to lower both gravimetric limits. Part of the gravity high can then only be explained by an increase in basement density, which would be around 3.0 g/cm^3. This axis would correspond to the important (but rather flat) gravity high to be seen on the Bouguer map, with an axis located at 9 km NE of the main anticline. This part of the interpretation was carried out by semi-manual calculation, using the two-dimensional prism formula.

Lastly, there remain local negative differences between geological and gravity interpretation. These negative residuals are probably due to narrow vertical faulted zones, where the second layer density could be reduced to 2.3 g/cm^3 and/or the basement density reduced to 2.6 g/cm^3.

6. Comparison Between Classical Downward Continuation and Density Maps

Though this paper does not deal with the theoretical aspects of the described method, it seems useful to place what we call "deconvolution" within the context of classical map filtering by Fourier transforms or grid operators.

First, it should be noted that "gravity deconvolution" (Bichara and Lakshmanan 1979) is no more than a particular map filtering. Nevertheless, two differences between "deconvolution" and classical map filtering should be stressed:

a. Map filtering aims at obtaining either an enhancement of certain anomalies (e.g., second derivative at various grid spacing, regional or residual filtering) or a map representation of fields at different altitudes (upward or downward continuation). "Deconvolution" aims at obtaining a density distribution for a plate of chosen thickness and depth.
b. Map filtering can, at least theoretically, be done perfectly. This is due to the fact that frequency domain representations of upward, downward, and second derivative operators have analytical expressions (Fuller 1967). We do not know of any frequency domain analytical expression for density operators.

Nevertheless, one could argue that classical downward continuation is a density operator which also has the advantage of being well defined in the frequency domain, and thus would be more advantageous to use as an operator. In fact, downward continuation can only give a surface density distribution which has less physical significance and is more difficult to use for structural mapping. Another disadvantage of downward continuation is that, in our experience, it is a much more noise-generating filter than "deconvolution". In any case, downward continuation can be (and has been) used for structural mapping (La Porte 1963); in this respect, "deconvolution" could be described as a generalization of downward continuation: downward continuation is a "deconvolution" with a layer of thickness 0 and at a depth which is a multiple of the grid dimension.

7. Conclusions

The three-dimensional, three-layer deconvolution of existing gravity data along the Pays de Bray anticline has supplied a powerful structural tool to the geologists, helping to locate various features, such as secondary anticlines and transverse faults, particularly for a secondary anticline on the flank of the main one, practically invisible on the Bouguer map.

Three-layer modeling was possible here by the use of geological constraints, available in this well-known area.

The basement map compared to five wells shows a mean square difference of 72 m (6.4%). This accuracy is in part due to the absence of lateral density variations and also to an abrupt variation between sedimentary and basement densities.

In regions where no geological information is available, the described procedure results in several parameters (mean square difference, correlation coefficient, and limiting densities) that can be employed to automatically construct a maximum-depth basement map. It should be stated that the interpretation tool described in the present paper has been used regularly by us for several years; various improvements update the technique each year. Of course, this new methodology of the interpretation of gravity anomalies does not render obsolete classical interpretation methods, such as downward continuation. There will always be the necessity of separating regional trends from residual; classical methods for depth determination are always useful and we do use them frequently. Nevertheless, density maps allow a quantitative look at Bouguer anomalies which have proved useful in many instances. Furthermore, provided a given density contrast, these maps are easily transformed into basement maps, which in many cases were confirmed by drilling. We are presently studying the application of these techniques to air, land, or sea magnetic surveys.

References

Bichara, M. and Lakshmanan, J. 1979. Automatic deconvolution of gravimetric anomalies. Geophysical Prospecting 27, 798–807.

Bott, M.H.P. and Smith, R.A. 1958. The estimation of limiting depth of gravitating bodies. Geophysical Prospecting 6, 1–10.

Debeglia, N. 1977. Apports de synthèses géophysiques à la connaissance du socle du Bassin de Paris, 1977, BRGM Orléans, 77 SGN 535 GPH.

Fuller, B. 1967. Mining Geophysics, Vol. 2, published by SEG, Tulsa, October 1967.

Lakshmanan, J. 1973. Gravity and gamma-gamma mapping of sink-hole areas in Lutetian Gypsum, North East of Paris. IAEG Symposium on Engineering Geology, Hannover, September 1973.

La Porte, M. 1963. Calcul de la forme d'une structure homogène à partir de son champ gravimétrique. Geophysical Prospecting 11, 276–291.

Naudy, H. 1971. *Automatic determination of depth on aeromagnetic profiles*. Geophysics 36, 717–722.

Pomerol, B. 1980. Style tectonique des Pays au Nord-Ouest de l'Oise—Rôle des différentes directions structurales. Bulletin d'Information des Géologues du Bassin de Paris 17, 21–25.

Weber, D. 1973. Le socle antetriasique sous la partie Sud du Bassin de Paris d'après les données géophysiques. Bulletin BRGM Orléans, Sect. II 1973, 219–343.

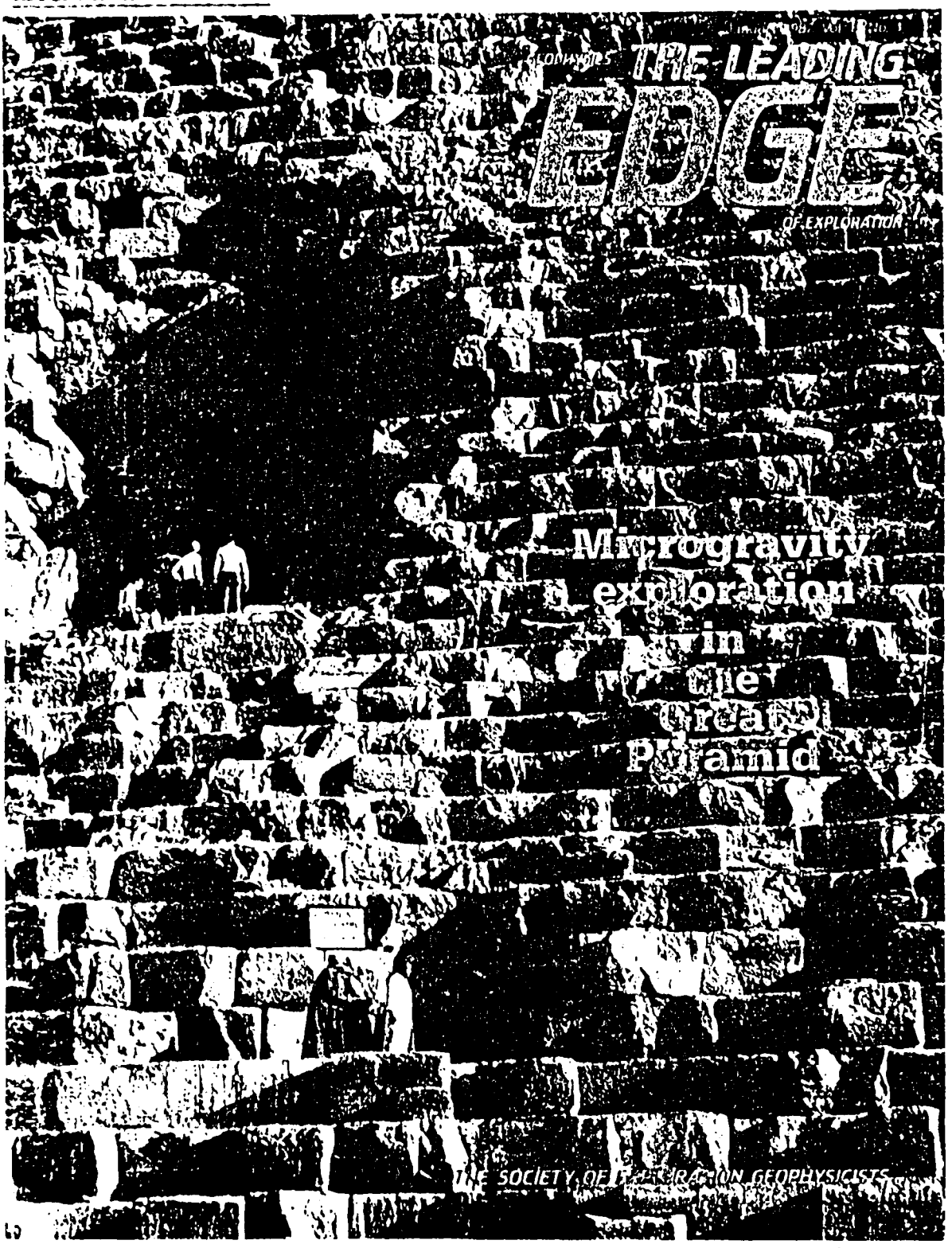
THE LEADING
EDGE
OF EXPLORATION
Microgravity exploration in the Great Pyramid
THE SOCIETY OF EXPLORATION GEOPHYSICISTS

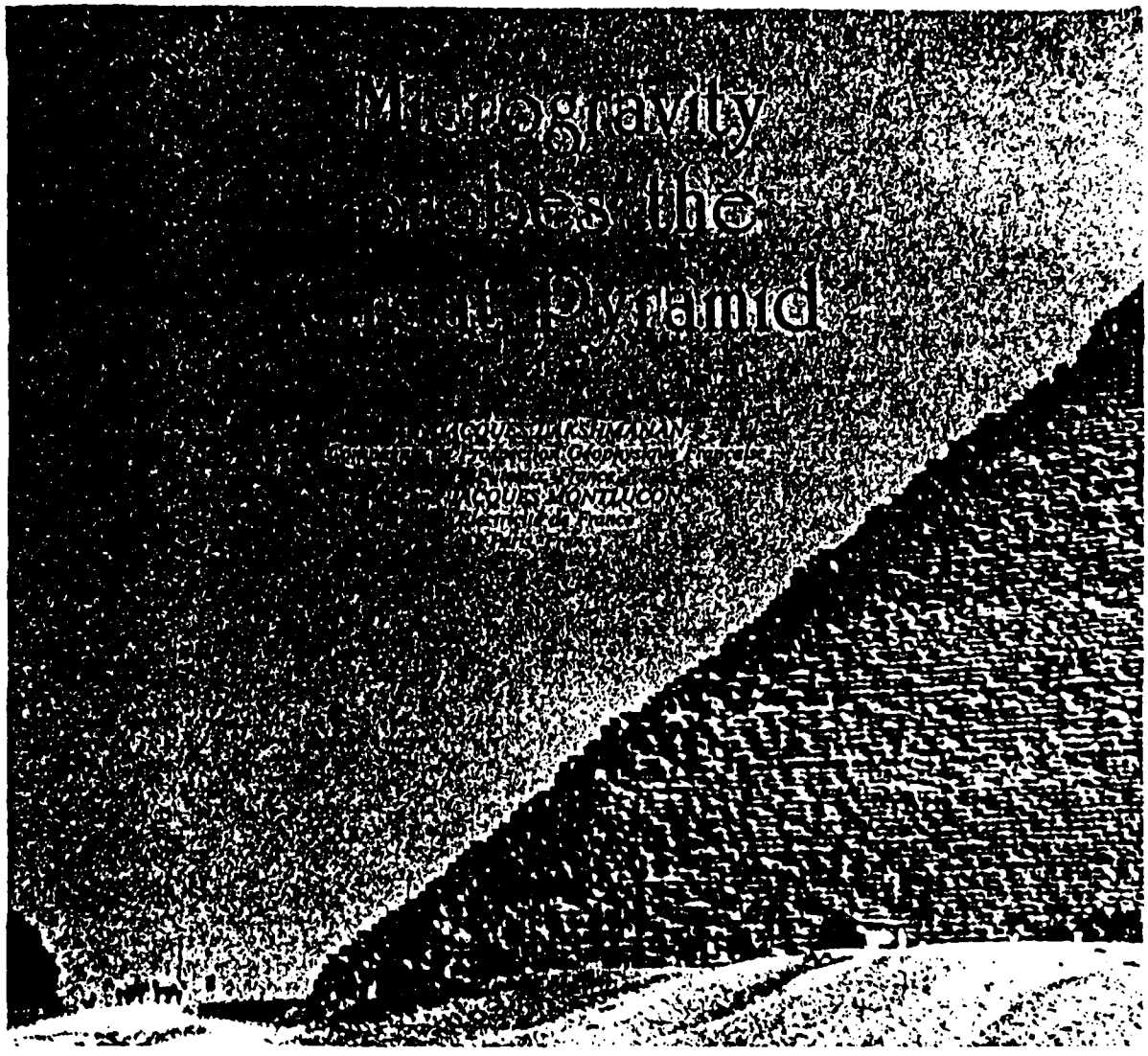

Microgravity Probes the Great Pyramid

JACQUES VONTILLON
Compagnie de Prospection Géophysique Française

Treasure hunters and some archeologists have been convinced, since at least the 12th century, that mysterious chambers exist in the Great Pyramid which conceal the real tomb and treasures of Cheops. A year ago two French architects, Gilles Dormion and Jean-Patrice Goidin, examined the construction features of the tunnels and chambers inside the Great Pyramid — one of the largest buildings, ancient or modern, ever constructed — from an architectural point of view. They observed several anomalies, particularly:

- The huge vault, much too high, above the entrance of the pyramid.
- The offset of the King's chamber — all other chambers in this and other Giza pyramids are exactly in the pyramid's vertical axis (see Figure 1, inset).
- The abnormal position of the slabs in the Queen's chamber tunnel.
- The abnormally large superstructure (decompression chambers) above the King's chamber.

Dormion and Goidin accepted these anomalies as proofs that the so-called King's chamber is just a decoy which hides the real King's chamber, and that "stores" should exist close to the Queen's chamber.

Early in 1986, the two French architects convinced the Egyptian Antiquities Department, the French Foreign Ministry and Electricité de France (the French State Power Board) that their theories were sound enough to be tested in the field. Electricité de France, following its policy of technological sponsorship, decided to head the funding of an expedition and start with a geophysical survey. Compagnie de Prospection Géophysique Française was hired as a consultant. Resistivity, electromagnetics and seismic methods were soon rejected. Radar was carefully examined but, in the end, Electricité de France and CPGF selected microgravity as the most efficient technique for cavity detection in the very special conditions existing in the pyramid.

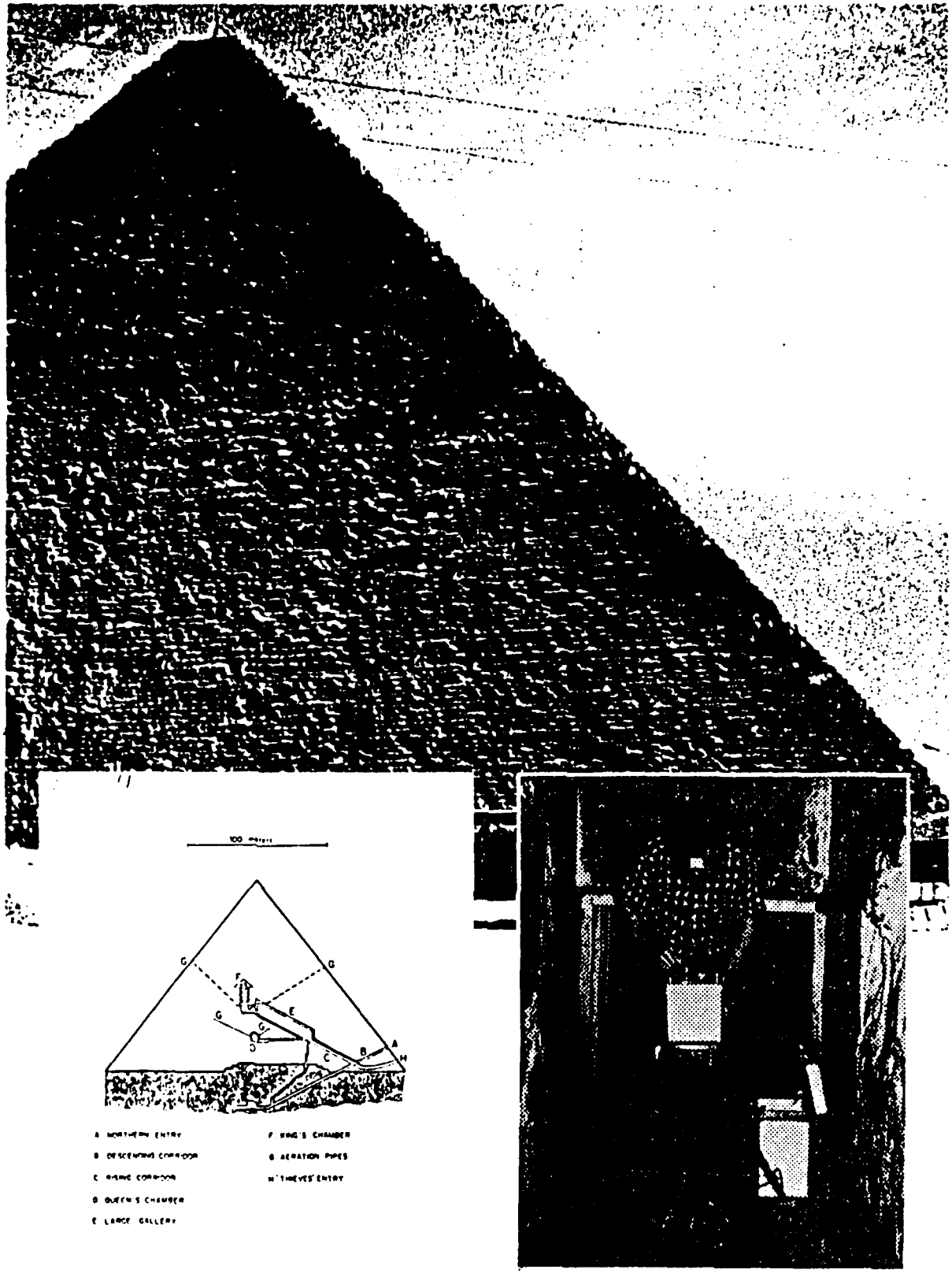

Vertical gravity gradient measurement (1 m off the ground!)

Figure 1.

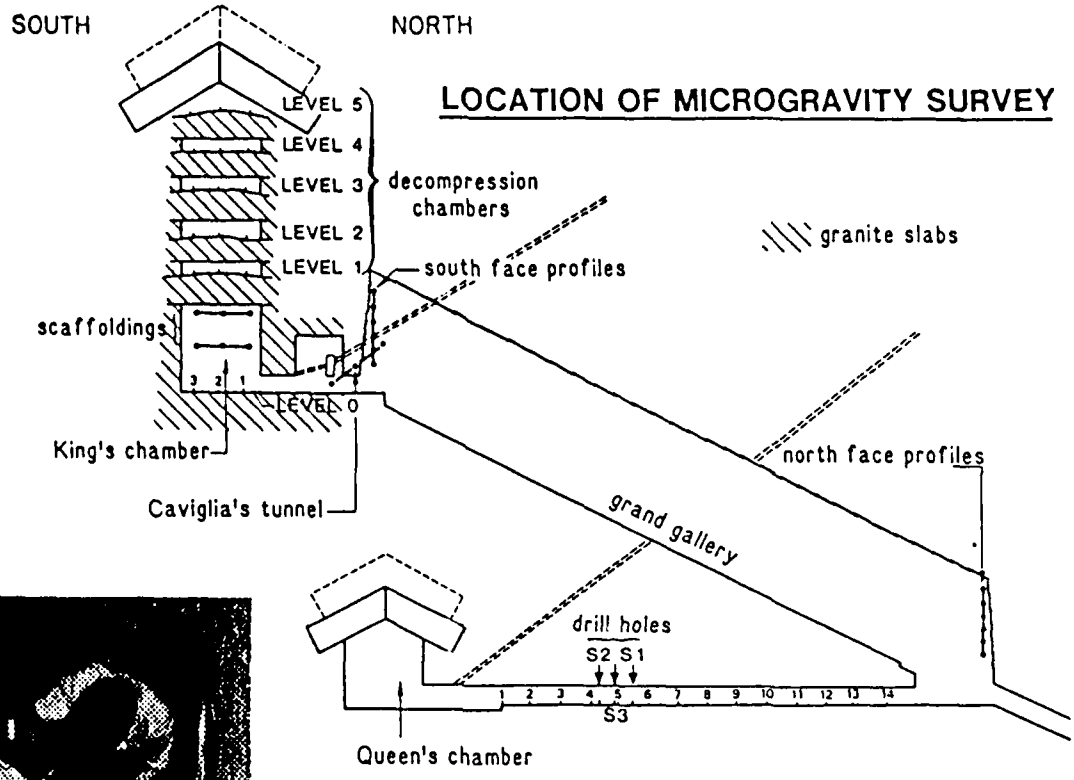

Figure 2.

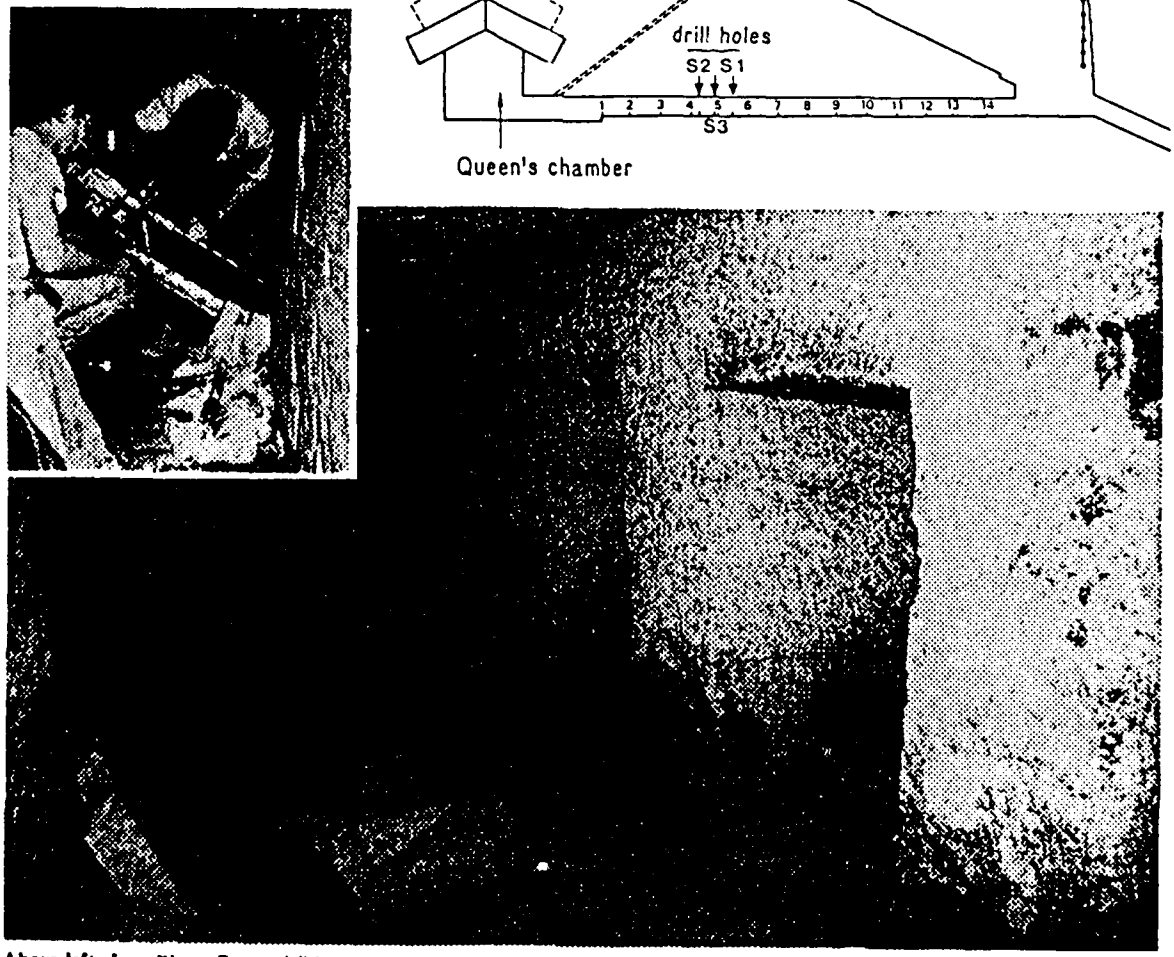

Above left: Jean-Pierre Baron drilling under supervision of Egyptian Department of Antiquities.
Above: An example from another pyramid of a "store" similar to the one we were looking for along the Queen's chamber access tunnel.

Microgravity surveys for caves. Microgravity surveys have been carried out by CPGF for several years — starting with the Paris-Lyon motorway (detection of karstic cavities) in November 1962 and in the city of Caen in Normandy (underground quarries) in December 1962. CPGF has, subsequently, carried out a number of microgravity surveys, involving a large number of stations. Traditional gravity surveys really became "microgravity" in 1968 when the firm of LaCoste & Romberg brought out the D-meter with a reading accuracy of one microgal. Various field procedures, processing techniques, and interpretation methods have been developed to utilize the higher sensitivity of microgravity surveys and some of them have recently been incorporated into conventional gravity surveys for oil.

Electricité de France is a major user of microgravity surveys — for preliminary site investigation of dams and nuclear power plants, for foundation quality control, and for fine microgravity gridding in the foundation excavation itself. The US Corps of Engineers has recently become interested in microgravity's potential and this year is studying the application of microgravity to the assessment of existing structures and structural foundations.

Station spacing ranges from 2 - 40 m in microgravity surveys. The usual depth of caves is of the same order. The gravity anomalies range from 15-300 μGals. In order to achieve maximum accuracy, field measurements are made with great care, in a semirandom sequence, with returns to base every 20-30 minutes. The instrumental drift curve is adjusted to take into account repeat stations, and to minimize time dependent anomalies. Work is often done at night when ambient noise conditions are quietest.

Final accuracy on repeats is in the order of 2-10 μGals when field conditions are good. When surveys are made in harsh urban conditions (for example, along the circular Paris freeway), repeat differences vary between 5 and 30 μGals. However, in the middle of large cities, microgravity is practically the only feasible geophysical technique.

The main geological targets in microgravity surveys are ancient underground quarries which occur frequently in chalk and limestone regions in Europe; World War I trenches and tunnels; sink holes and dissolved zones in gypsum, salt or limestone areas; and repeat surveys for controlling grouting operations.

Another novel application of microgravity is the measurement of absolute density of embankments by generalized Nettleton profiles. Conventional microgravity is often completed by vertical gradient profiles across major anomalies for more accurate depth evaluation. Gradient is measured between stations 1-1.5 m apart.

Microgravity survey in the pyramid of Cheops — preliminary modeling. Computer models were run, prior to the survey, in order to evaluate the type and size of cavities detectable by microgravity. These showed that by operating along accessible tunnels and chambers, cavities of around 10 - 40 cu m could be detected at distances reaching 10 m. A complete computer model of the pyramid was then run in order to compute the general effect *(P)* of the pyramid and the corrections *(C)* due to all the known existing chambers and tunnels.

Values of *P* range from $-2{,}500$ μGals in the Queen's chamber tunnel to $+1{,}700$ μGals at the highest decompression chamber with a gradient of around 96 μGals/m (for a density of 2.6 g/cu cm).

Values of *C* range from 0-280 μGals (for the same density) with the maximum values being on the floor of the King's chamber.

All of these corrections were made in advance so that the field crew could compute corrected Bouguer values on the site. Different models of unknown chambers were run in advance so that comparisons leading to immediate decisions could be made during the survey.

Field work in the pyramid (see Figure 2). During the May 1986 survey, a 2.1 × 2.1 m grid of 15 stations was set up on the floor of the King's chamber and on each of the five decompression chambers. In the September survey, scaffolding was put up and two extra levels were surveyed in the 6-m high King's chamber.

Jean-Claude Erling reading LaCoste & Romberg D-meter in the King's chamber.

Three stations were made close to the entry of the King's chamber in Caviglia's tunnel which was dug during the 19th century.

A 27-m profile with 15 stations (spaced 1-2 m) was made in May in the access tunnel to the Queen's chamber. Two other profiles were made in September on each side of the 1.1 × 1.1 m tunnel. Spacing between these three profiles is 0.5 m (which is probably a world record!) These two profiles include a total of 46 stations with spacing ranging from 0.5-2 m.

Interpretation procedure. The Pyramid's density was computed using an interpretation technique similar to that used in borehole gravity surveys. In fact, the measurement of gravity inside a finite body is a generalization of borehole gravity.

Measured free air gravity (*FA*) is the sum of:

- The general attraction *P* of a homogeneous theoretical pyramid, of density σ_p from which the effect *C* of known cavities is subtracted; *P-C* is the effect of the "pyramidoid," by analogy with the geoid.
- Regional effects on the pyramid due to external causes, either linear ($ax + by = C$) or of the second degree.
- Regional vertical gradient.
- Effect of local inhomogeneities inside the pyramid, such as unknown caves.

After computing *P-C* for an arbitrary density, a multivariable regression between *FA*, *P-C*, *x*, *y* and *z* should yield the correct average density σ_p. In fact, tests show that *P* being very strongly related to *z*, these two parameters cannot be easily separated. The regressions used were therefore based on equations of the type:

$$FA = \sigma_p' \frac{(P-C)}{2.6} + ax + by + c, \text{ or}$$

$$FA = \sigma_p' \frac{(P-C)}{2.6} + ax^2 + a'x + by^2 + b'y + c,$$

σ_p' being an apparent density, as in borehole gravity.

We also had to take into account the effect of granite slabs (2.65 g/cu cm) surrounding the King's chamber and the decompression chambers. This required an iterative procedure.

Tests were also made using a horizontally stratified, 3-layer pyramid density. Results yielded an average apparent density of the pyramid ranging from 1.88-1.95 g/cu cm (see Figure 3).

After computing σ_p', *a*, *b* and *c*, the theoretical free air gravity (*TFA*) was computed at each point, leading to a residual free air anomaly:

$$RFA = FA - TFA.$$

These residual values were then transformed into differential densities $\Delta\sigma$ by computing the vertical gradient ΔRFA inside a moving window. We (quite arbitrarily) suppose that ΔRFA is due to a local modification of the Pyramid's average density σ_p', inside a cylinder ΔZ meters high, and of a radius *R* meters.

The difference of free air attraction between the top and the bottom of a vertical cylinder is given by:

$$\Delta FA = \frac{80}{3} \cdot \pi \cdot \sigma \left[R + \Delta Z - \sqrt{R^2 + \Delta Z^2} \right],$$

which yields, setting $R = r\Delta Z$,

$$\Delta\sigma = \frac{1}{83.8} \frac{\Delta FA}{\Delta Z} \cdot \frac{1}{1 + r - \sqrt{1 + r^2}}$$

as compared to the usual borehole gravity formula

$$\sigma = \frac{1}{83.8} \frac{\Delta FA}{\Delta Z}.$$

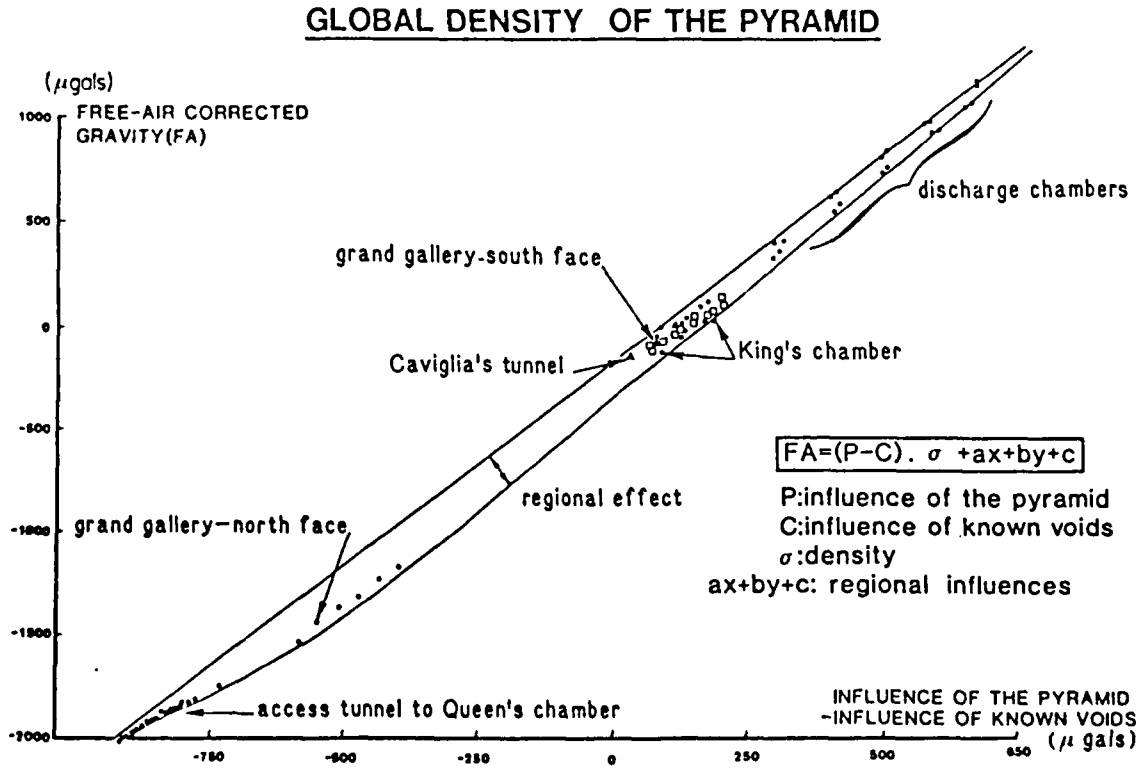

Figure 3. The slanted line represents apparent density of 1.95 g/cu cm. Corrected density is 2.05.

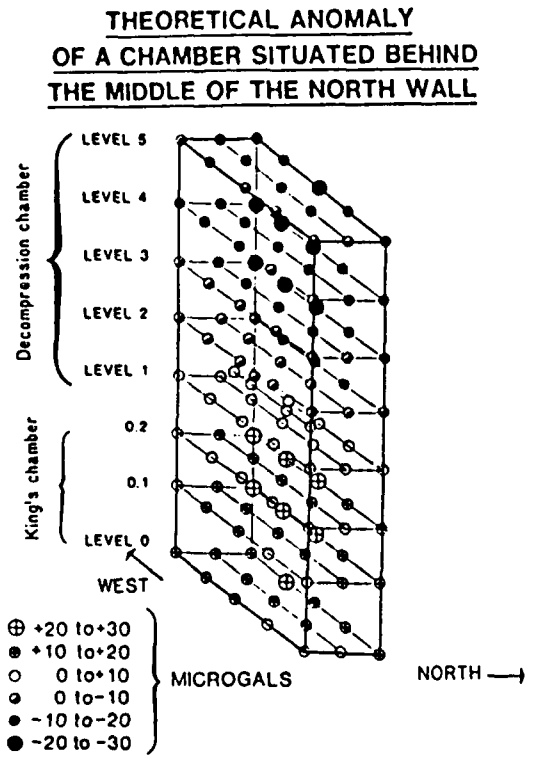

Figure 4.

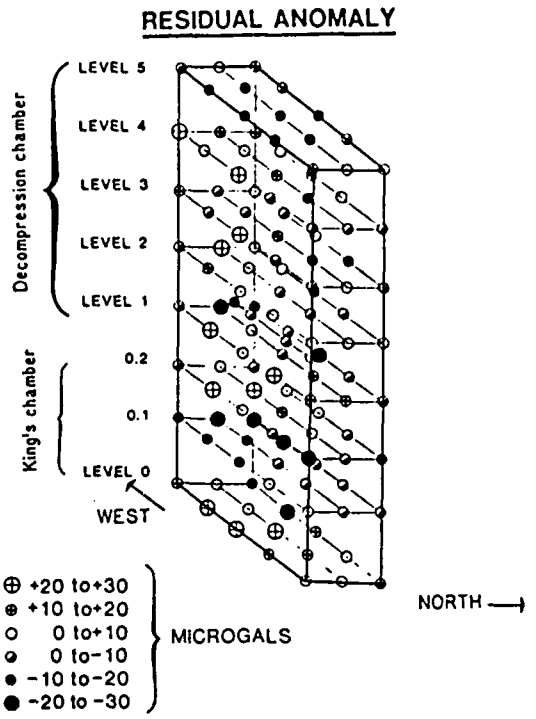

Figure 5.

When r = 5, we obtain $\Delta\sigma = \frac{1}{75.5}\frac{\Delta FA}{\Delta Z}$.

We can then compute an apparent density σ' at each point

$$\sigma' = \sigma_p' + \Delta\sigma.$$

Vertical gradients due to regional effects were then computed. The correction of the effect of a large gravity feature located 25 km NW of the pyramid increases the apparent density by 0.15 percent. The correction of the topographic effect of the Nile valley and of the effect of lower density quaternary sediments increases the apparent density by about 5 to 7 percent.

Average density and structure of the pyramid. Taking into account these corrections, the average density of the pyramid is very close to 2 g/cu cm. This figure should be compared to the known density of the materials of which the pyramid is (or could be) formed:

- TURA limestone, which covers all the access tunnels is 2.6 g/cu cm.
- Local paleogenic limestone is an average of 2.07 g/cu cm.
- Fill seen in Meidun Pyramid, but not yet seen in Cheops is 1.8 g/cu cm.

Pending further debates, we consider the hypothesis of a massive pyramid, mainly made of local limestone, without (or with very little) fill, to be the most coherent.

The results of more intricate models (3-layer, or with a second degree regional) make us suspect that this density of 2 g/cu cm is just an average. We feel that the lower southwest part of the pyramid could be heavier, but further measurements on the surface of the pyramid would be necessary.

Results in the King's chamber. The residual values range from

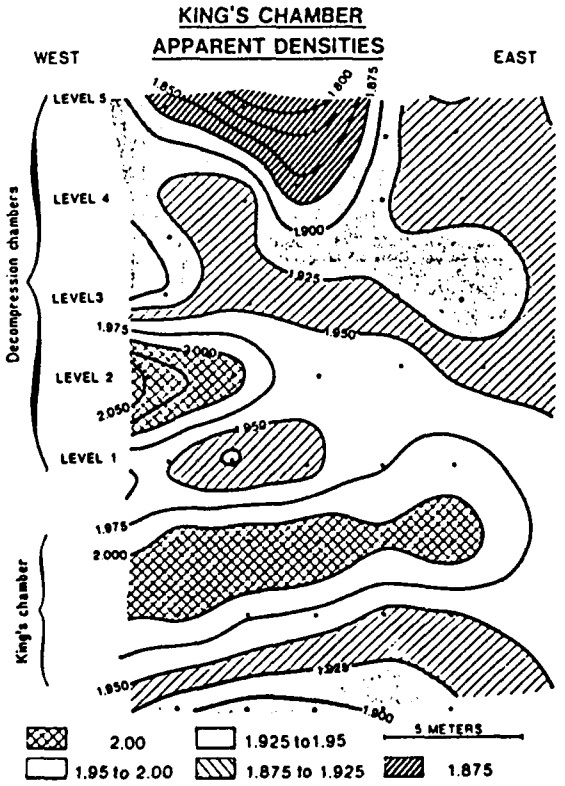

Figure 6.

−25 to +33 μGals. The main negative anomaly is located at the northwest corner of the King's chamber's floor. It corresponds to a small old investigation tunnel, leading out from below the stone coffin. A couple of small high frequency local anomalies show up and will be investigated later, but they have nothing to do with the anomaly computed from the presumed unknown tomb, which should have given a 5 m wide negative anomaly at decompression chambers 2 and 3 and a symmetrical positive anomaly of the two reading levels on the scaffoldings.

Figures 4 and 5 compare the theoretical gravity due to the suspected chamber and the real residuals and Figure 6 shows the apparent densities computed from these residuals corrected by 7 percent of the effect of regional vertical gradient.

The Queen's chamber access tunnel. This zone was only surveyed as a secondary target; however it was here that we had the most significant results.

Figure 7 is a residual anomaly map, showing the results of the three profiles after all corrections. Towards the entry of the tunnel, a positive zone (+20 μGals) shows up, while towards the Queen's chamber, a strong negative feature (−25 μGals) is visible, mainly on the western profile. The difference between the two zones, around −45 μGals, is a very significant, non-ambiguous anomaly.

Quantitative analysis is very difficult because data are only available along the three tightly spaced profiles. We made various interpretations with different hypotheses, supposing various positions and amplitudes of the maximum anomaly. The most prudent hypothesis supposes that the maximum is reached at the west profile, while one could suppose that this profile is in fact just on the edge of a larger anomaly (see Figure 8).

The different proposals yield various interpretations (either

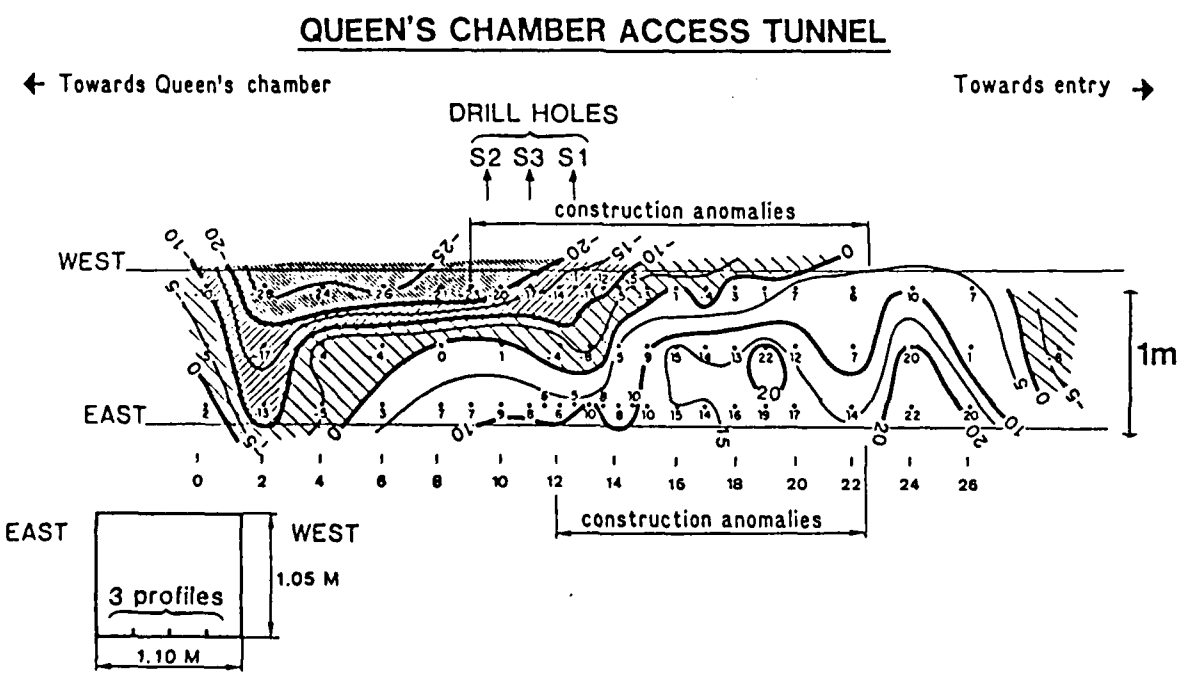

Figure 7.

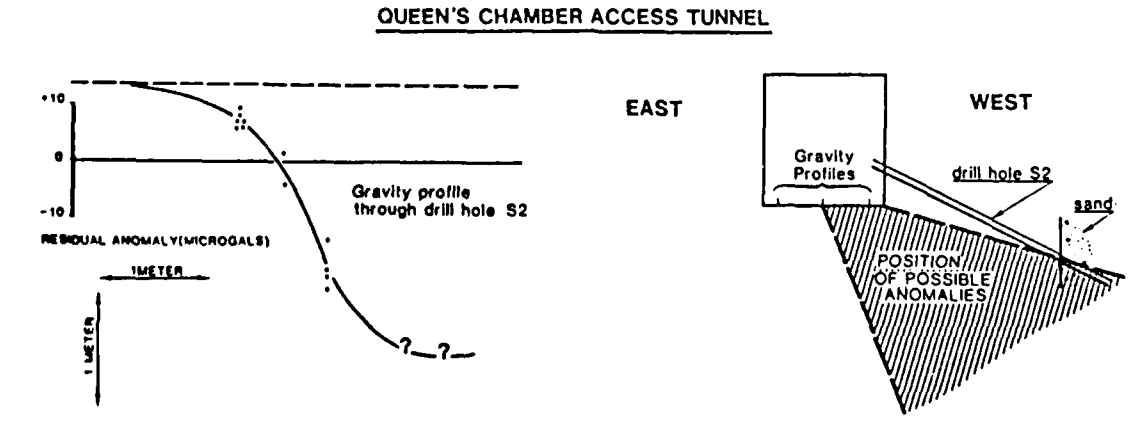

Figure 8.

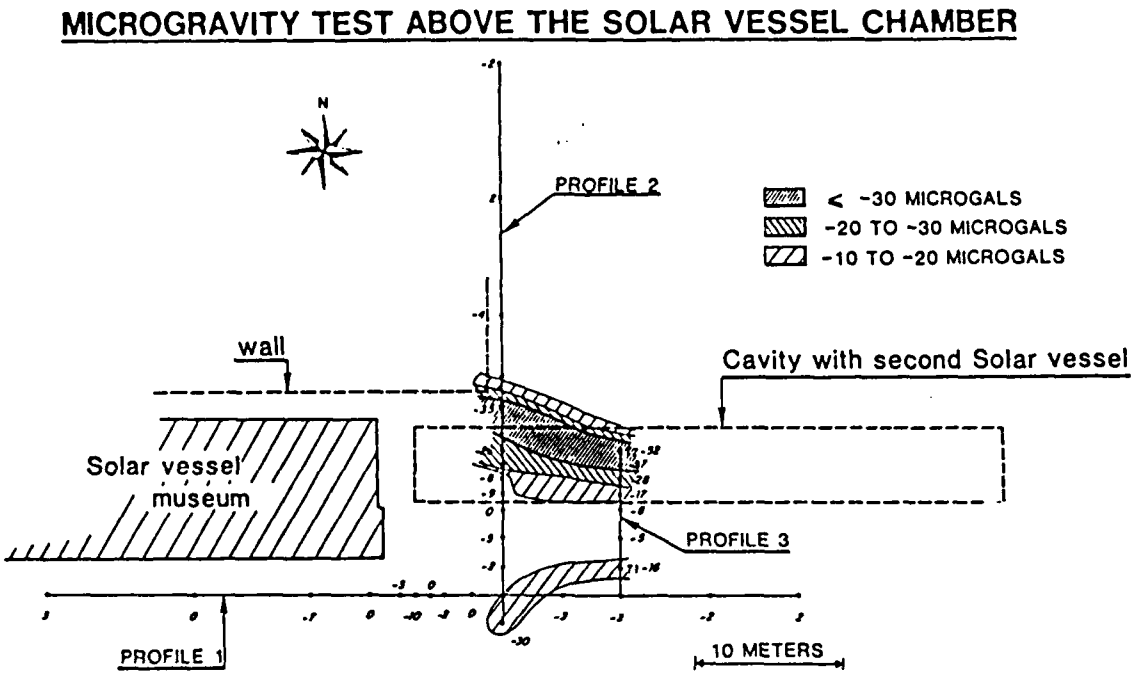

Figure 9.

for a horizontal cylinder or for a horizontal strip) all located in the hatched zone.

Of course, if one of these sources extended upward towards the side of the tunnel, the upper part (located on the same horizontal level as the measurements) would not create any anomaly at all on the vertical component of g, measured by the meter.

The position of this anomaly along the tunnel and its location on the west side coincide with a certain number of observations made by the architects. It was therefore decided to drill sideways, with holes tilted 30 degrees from the horizon, in order to locate possible "stores" as have been found in other pyramids.

The drill used was a small electric rotary drill with a 35-mm diameter. The Egyptian authorities made us carry out a preliminary test on large blocks outside the pyramid to avoid all risk of destroying valuable objects. The pyramid's building blocks are limestone and 53 cm thick. We were allowed to use water injection to flush out the sediments for the first 45 cm of drilling but we had to end the drilling in each block with dry diamond drilling.

Three holes, 2.6 m long, were drilled 1.5 m apart. After crossing about 2.1 m of limestone (four blocks), they all struck loose sand with pieces of mortar. The three holes were visually inspected using a Bodson endoscope. The edge of the sand was seen to be vertical in all three holes. This sand is very loose and we air-flushed out several liters with a small compressor. The architectural purpose of this sand is not known; however, the Egyptian Antiquities Department agrees that this discovery is a definite indication of an organized structure, probably related to new and unknown chambers.

Reverting to gravity interpretation, it is clear that if the anomaly was only due to sand, its volume would have to be very large — around 40 cu m for anomaly 4, for example.

Gravity test over the buried vessel chamber. A short gravity test was also carried out outside the pyramid, over a chamber where a buried vessel is suspected. A similar vessel has previously been discovered and reassembled in an adjacent museum.

The survey included 35 stations with spacings ranging from 1-6 m. The two profiles which cross the presumed vessel clearly show anomalies reaching -30 to -50 μGals. This short test showed how easily fine microgravity could be used for locating small underground chambers. Of course, all the sophisticated corrections made inside the pyramid were not necessary here.

We wish to put aside the "treasure hunt" and "curse of the Pharaoh" sides of the survey, which attracted 40 international journalists to the pyramid. We do not wish either to intervene in the present controversy between schools of Egyptologists as to the nature of the sand-filled cavities we have detected. However, the techniques used: microgravity with advanced correction and interpretation techniques, and microdrilling with endoscope visualization, are considered by all involved to be the best combination for surveying underground chambers, particularly when surveying inside structures like the pyramid.

Egyptian and French authorities are now discussing the best follow-up courses. One debate is between the use of a larger, more powerful drill or the construction of an investigation tunnel.

More gravity surveys are anticipated along uninvestigated tunnels (particularly the Grand Gallery) and on the outside faces of the pyramid. A complete 3-D gravity model "weighing" the pyramid could yield more information on both the possibility of other chambers and on the geotechnical features of the pyramid itself. Several observations (particularly in the decompression chambers) suggest that stability problems exist in the pyramid. Such an investigation could be a useful test for developing techniques for the assessment of other larger existing structures, such as earth dams. LE

(Oral versions of this article were presented at a seminar at the Colorado School of Mines in September and at SEG's Annual International Meeting in November 1986.)

APPENDIX A - PAPER A3

SOCIETY OF PROFESSIONAL WELL LOG ANALYSTS
Second International Symposium on Borehole Geophysics
For Minerals, Geotechnical, and Ground Water Applications
October 6-8, 1987 - Golden, Colorado

CURVED RAY SEISMIC TOMOGRAPHY - 17 YEARS EXPERIENCE FROM ZAIRE (1970) TO KENYA (1987)

Yves Bertrand(1), Alan T. Herring(2)
Jacques Lakshmanan(1), Manuel Sanchez(1)

(1) Compagnie de Prospection Géophysique Française, 20 rue des Pavillons - 92800 Puteaux (France)

(2) EDCON, Inc. 171 So. Van Gordon, Denver, Colorado 80228 (USA)

ABSTRACT

Nearly 20 years ago, the late Maurice LaPorte developed a very sophisticated technique for inverting well-to-well seismic travel times. For its initial purpose : the detailed investigation of oil fields, this technique came in too early, and was nearly forgotten. Now, several teams around the world have taken up the subject for oil exploration, on an even more ambitious line.

In the meantime, CPGF in France had started testing the algorithm in the field, for dams and other public works. During the last 17 years more than 50 surveys have been carried out and many developments have been made.

CPGF has also added, since 1980, two down-hole tools :
- the Sheargun, a down-hole mechanical hammer
- the Sismopressiomètre, a down-hole, three component geophone, with high pressure radial clamping.

The paper illustrates the advantages of curved ray tomography, as opposed to straight line tomography. The advantages of high power, clamped mechanical sources, such as the Sheargun, are also shown. Typical examples of seismic tomographies include :
- Survey of an underground power station in a horizontal plane, between 3 adits at Busanga dam, Zaire,
- Survey of an existing nuclear power plant at Doel, Belgium,
- Survey of an underground power station at the Grand'Maison dam in the Alps, in a vertical plane,
- Location of faults at a dam site, in Vendée, France,
- Structural study of limestone-marl sequence for a nuclear power project at Cruas, France,
- Location of a buried lava flow at the Grand Etang dam site, Reunion Island,
- Location of karstic zones along a large urban sewage tunnel in Bordeaux, France,
- Survey of the 150 m cliffs forming the foundations of the Turkwel dam site, Kenya,
- Location of fractured zones in chalk for the nuclear power plant of Nogent-sur-Seine, France,
- Location of karsts for the nuclear power plant of Civaux, France : tomography between ground surface and a deviated bore hole.

1. INTRODUCTION

Nearly 20 years ago, the late Maurice LaPorte developed a very sophisticated technique for inverting well-to-well seismic travel times, and tested it once at the Lacq oil field (*Bois et al, 1971*). *LaPorte's technique supposes* the iterative adjustment of velocities at a set of around a hundred nodes. Between the nodes, velocities are supposed to vary continuously. For its initial purpose : the detailed investigation of oil fields, this technique came in too early, and was nearly forgotten until the eighties. Now, several teams around the world and particularly in the U.S. (at the M.I.T. with Toksoz) and in France (with Tarantola) have taken up the subject for oil exploration, on an even more ambitious line, including full wave inversion, but without any field experience.

In the meantime, CPGF in France, who had maintained a neighbourhood relationship with Maurice LaPorte and the I.F.P., had started testing the algorithm in the field, for dams and other public works.

During the last 17 years, more than 50 surveys have been carried out in a vast variety of geological conditions, for many types of works and many developments have been made at CPGF, both for acquisition and processing.

In addition, CPGF has added, since 1980, two down-hole tools, to improve acquisition conditions :

- the Sheargun, a down-hole mechanical hammer
- the Sismopressiomètre, a down-hole, three component geophone, with high pressure radial clamping.

Now, quite a few groups have started working on seismic tomography applied to civil engineering, some with continuous sources (J. Wong et al, 1987), others with simplified straight line inversion.

In chapter IV, we will illustrate the advantages of curved ray tomography, as opposed to straight line tomography. In chapter VII, we will show the advantage of high power, clamped mechanical sources, such as the Sheargun.

II. EXAMPLES OF SEISMIC TOMOGRAPHIES

Typical examples of seismic tomographies include :

- Survey of an underground power station in a horizontal plane, between 3 adits at Busanga dam, Zaire (M. LaPorte, J. Lakshmanan, M. Lavergne, C. Willm, 1973), as described in chapter III,
- Survey of an existing nuclear power plant at Doel, Belgium (F. Henning, J. Jacquemart, J. Lakshmanan, J. Rougé, 1981), with tomography under the existing structure, and P- and S-wave measurements, using the Sheargun as described in chapter V,
- Survey of an underground power station at the Grand'Maison dam in the Alps, in a vertical plane, between 2 adits (A. Martinet, G. Akermann, J. Lakshmanan, F. Lantier, (1982), with P- and S-waves, leading to Young's modulus and Poisson's ratio maps,
- Location of faults at a dam site, in Vendée, France (J. Lakshmanan, 1982),
- Structural study of limestone-marl sequence for a nuclear power project at Cruas, France (J. Lakshmanan, Y. Bertrand, M. Bichara, Y. Lemoine, 1982),
- Location of a buried lava flow at the Grand Etang dam site, Reunion Island (J.F. Cottin et al, 1986), as detailed in chapter IV,
- Location of a buried cliff for the Marseille metro (unpublished CPGF report, 1985),
- Location of karstic zones along a large urban sewage tunnel in Bordeaux, France (J.C. Erling, Y. Bertrand, E. Kutkan, 1987).
- Survey of the 150 m cliffs forming the foundations of the Turkwel dam site, Kenya (unpublished CPGF reports, 1986-1987), as described in chapter VI,
- Location of fractured zones in chalk for the nuclear power plant of Nogent-sur-Seine, 9 tomographies, 40 m depth (CPGF unpublished report, 1982),
- Location of karsts for the nuclear power plant of Civaux : tomography between ground surface and a deviated bore hole (CPGF unpublished report, 1987).

III. BUSANGA DAM, ZAIRE

Near the 130 m arch dam project at Busanga, Zaire, an underground power plant was planned in primary schists and quartzophyllades, quite strongly faulted and located near the Lualaba river gorge, around 100 meters below the surface. The power plant site had already been surveyed by 2 adits G3 and G4 (see figure 1).

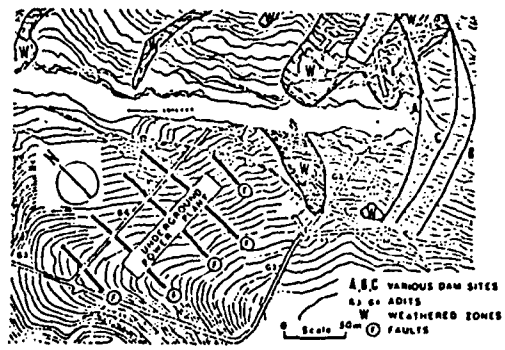

Figure 1. Location of Busanga power station

The purpose of the seismic tomography carried out in the horizontal plane G3, G4, was to locate the optimum position of the power plant. Along the sides of G3 and G4, during a preliminary survey, conventional seismic measurements had been made with 60 m, 12 geophone spreads. Compressional velocities obtained are shown on figure 2, with lower velocities near the adit entries (3600 and 4300 m/s) as well as in two interior zones (4300 and 4800 m/s) while the general rock mass velocity is around 5000 - 5400 m/s.

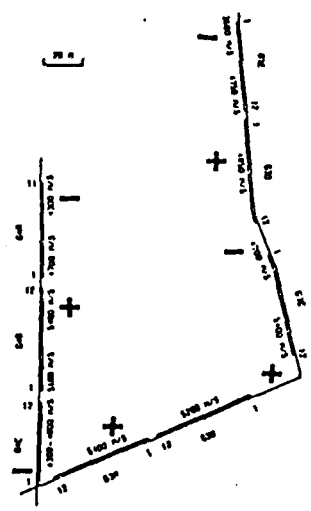

Figure 2. Velocity measurements at Busanga

5 transmitter points were used for the seismic tomography, while 21 among the 96 conventional receiver points were selected. The tomography panel is about 120 x 150 metres (see figure 3). After the first (straight line) iteration, the mean square difference between measured and computed travel times is 0.67 milliseconds (2.2 %), while after 3 iterations, it is 0.43 milliseconds (1.4 %). The computed velocity map compares well with the conventional survey, most of the maximums and the minimums coincide. In fact, we could have included the travel times along the adits in the inversion procedure. Here, they were kept apart.

The Busanga dam project is presently abandoned. It if were taken up again, comparison of figures 1 and 4 suggests that the plant be pushed 30 m south and slightly rotated.

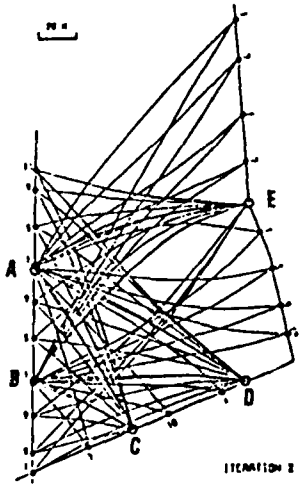

Figure 3. Shot points (A to E), receivers and raypaths at Busanga.

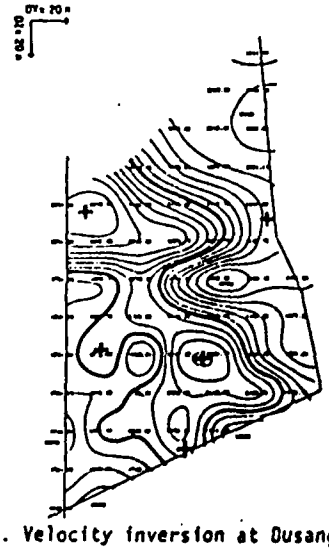

Figure 4. Velocity inversion at Busanga

IV. GRAND ETANG DAM, REUNION ISLAND

This dam is planned in a volcanic environment where previous drilling had detected a basaltic flow 5-30 m thick covered by 20-40 m silt and pervious scoria, filling an ancient valley.

In order to complete an impervious cutoff reaching the basalt, it was necessary to check the continuity of this impervious layer, and its link with older basalts forming the edges of the ancient valley. 12 seismic tomographies were run between 13 drill holes 50 m deep, and 50 m apart. Two of these tomographies, run together, are shown on figures 5 and 6. Central drill hole SS3 had the particularity of having met two layers of basalt, separated by silts, while the lateral drill holes SP2 and SD1 (like all the other ones) had only met a single basalt layer.

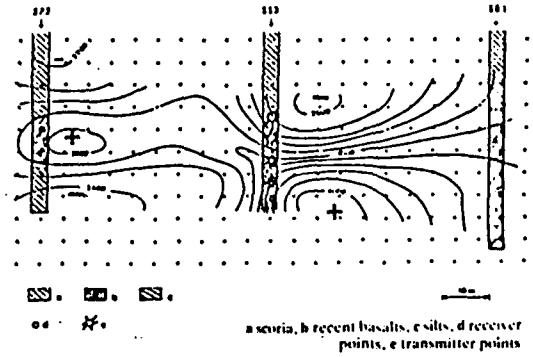

Figure 5. Grand Etang dam, velocity inversion (1st iteration).

After the first iteration, corresponding to a straight line tomography, the link between the high velocity zones on each side is not clear. After 5 iterations, it becomes clear that the upper basalt met by SS3 is related to the basalt of drill hole SP2, while the lower one is connected to basalt of SD1, with an evident low velocity separation between both layers.

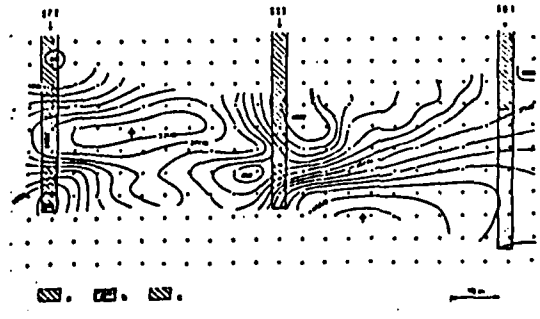

Figure 6. Grand Etang dam, velocity inversion (5th iteration)

The raypath construction corresponding to the last velocity distribution is shown on figure 7. Here too, the low velocity separation shows out clearly.

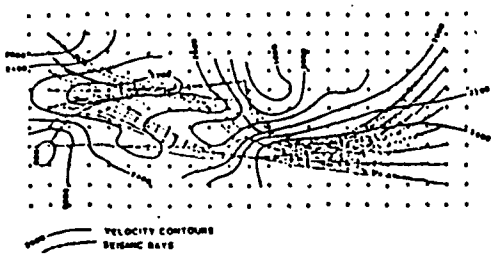

Figure 7. Grand Etang dam, raypaths

Figure 8 shows a synthetic cross-section with the 13 drill holes and the 12 tomographies. It seems clear that the recent basalt flow is continuous, except :
- close to SS3 as described above
- at each end, where it does not connect with the older basalts.

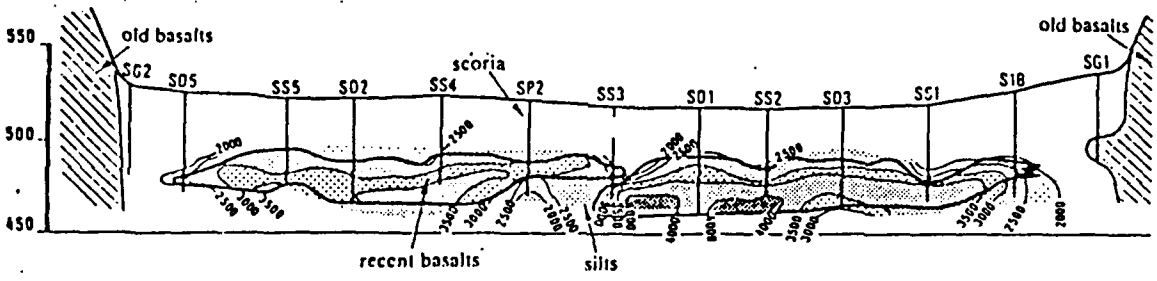

Figure 8. Grand Etang dam. 12 tomographies

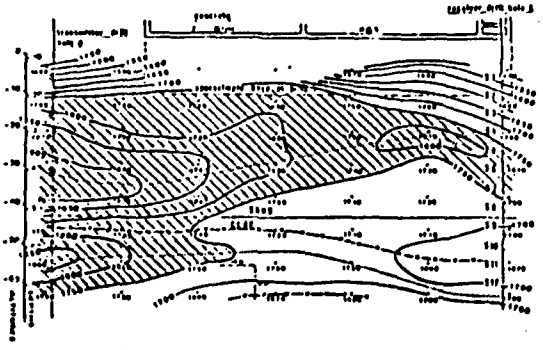

Figure 9. Doel nuclear plant, compressional velocities

5. DOEL NUCLEAR POWER PLANT, BELGIUM

Dynamic soil properties were studies after the concrete structure had been built. Therefore, in addition to two sets of conventional cross- and down-hole tests carried out in an accessible area outside the plant, a seismic tomography was made between two 60 m holes drilled on each side of the reactor, 120 m apart ; with 12 transmitter points (caps) on one side, and 12 receivers (hydrophones) on the other.

Figure 9 shows the results of the inversion of compressional velocities, with velocities less than 1700 m/s up to a depth of 20 metres (loose quaternary formations), then 1750-1900 m/s in the tertiary sands on which the pile foundation is built, and then 1700-1850 m/s in the Flandrian clays. Figure 10 shows the shear moduli in the same panel with moduli of 1500-2500, 2000-3500 and 2200 megapascals in the same 3 formations.
The increase of dynamic properties due to compaction under the weight of the structure is shown on figure 11, where the velocities in the "interior" columns are divided by the velocities of the 4 "exterior" columns.

50 m

It shows that the velocities in the sand layer are about 5 % higher under the middle of the reactor than under the edges. When comparing with measurements made in the "free field" outside the reactor, this ratio is close to 10 %. The corresponding increase in Young's modulus is around 20 %.

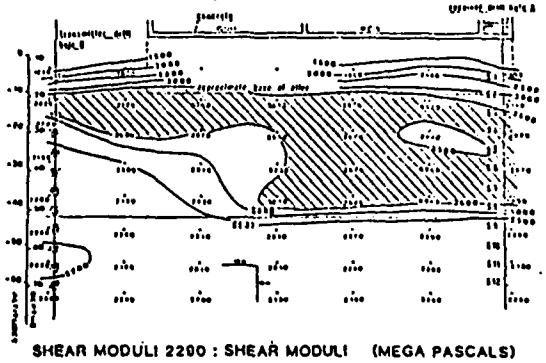

Figure 10. Doel nuclear plant, shear moduli

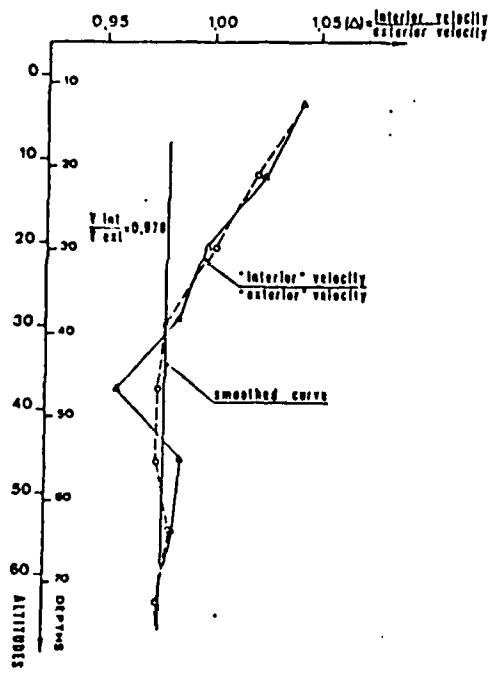

Figure 11. Doel nuclear plant, velocities

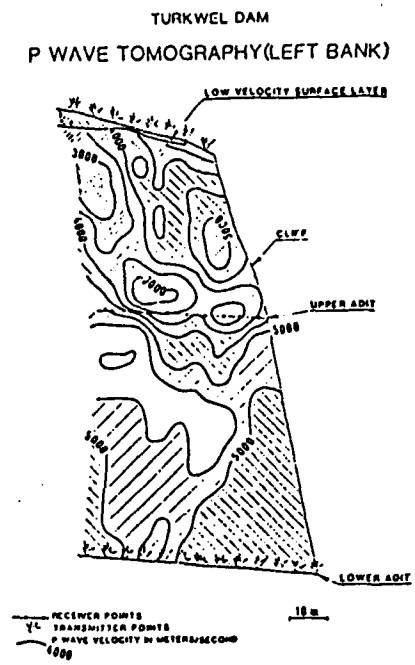

Figure 12. Turkwel dam, P wave tomography (left bank)

6. TURKWEL DAM

The general aim of this survey was the determination of geotechnical rock quality of the cliff abutments. This was done by seismic tomographies between two adits and between ground surface and adits on both banks. 4 tomographies were run with both P waves and S waves.

Maps of P and S wave velocities, E and G moduli and of Poisson's ratio were supplied. Examples of these maps are shown (figures 12, 13 and 14)

P wave velocities range from 1000 to 3700 m/s.
S wave velocities range from 2500 to 6100 m/s.

These values yield very high moduli which are not abnormal for such a gneissic or granitic rock mass.

A certain anisotropy seems to exist, particularly on the left bank, where vertical velocities can be 20 % higher than the horizontal ones. So, processing was rerun, taking into account this anisotropy by modifying the curvature of the rays. Results are very similar to those obtained without anisotropy.

It should be noted that the computed travel time can be compared to measured travel times. An example is shown on the following table (right bank, P waves).

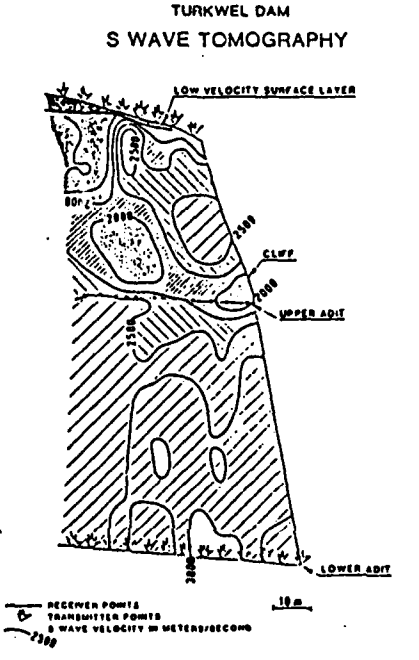

Figure 13. Turkwel dam, S wave tomography (left bank)

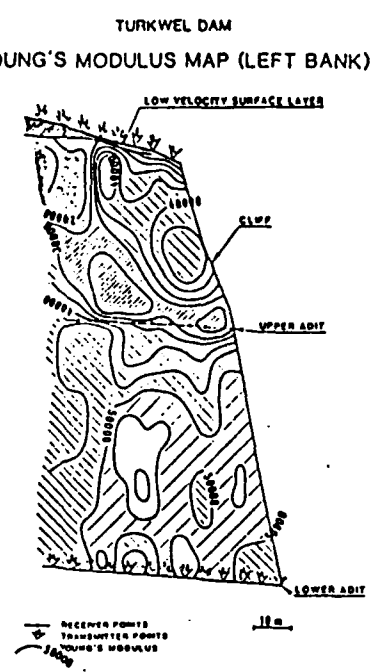

Figure 14. Turkwel dam, Young's moduli (left bank)

We can see that the mean quadratic difference between measured and computed times becomes steady after 3 iterations. Average travel time was about 12 milliseconds.

EXAMPLE OF INVERSION IMPROVEMENT

Right bank, P waves

Anisotropy = 1

Iteration	At quad. (quadratic average) milliseconds	At max milliseconds
1	0.995	2.302
2	0.353	1.453
3	0.288	1.202
4	0.281	1.161
5	0.278	1.159
6	0.276	1.153
Extra iterations after slight adjustment of the model		
7	0.303	1.153
8	0.277	1.148
9	0.273	1.143
10	0.270	1.138

Comparison with in situ static dilatometer "Hederatec" tests show quite good agreement between dynamic E moduli and static E moduli. Mean values measured at (or close to) the Hederatec measurement locations are :

static E 16500 MPa
dynamic E 26400 MPa

7. THE SHEARGUN AND THE ADVANTAGES OF STRAIGHTFORWARD TIMEBREAK PICKING

In order to obtain clear S wave components, it has been shown for several years that mechanical devices, both on the surface and in drill holes, are much more efficient than explosives, caps, sparkers or piezoelectrical sources. In fact, the original down-hole shear wave source for cross-hole testing was a hammer striking the top of a drill rod. In this case, very clear S waves were obtained, but the P wave component was very poor.

CPGF has developed since 1981, in collaboration with Techniques Louis Ménard (the inventors of the Pressiomètre®, the world famous in-situ geotechnical device) a down-hole hammer called the Sheargun® (Y. Bertrand, P. Bozetto, J. Lakshmanan, 1986). This system includes a pneumatical, radially clamped anvil which is in fact a Pressiomètre® included in its Ménard split tube. A spring actuated hammer, driven by air, strikes the top of the anvil (figure 15).

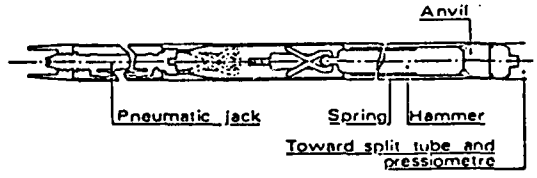

schematic of the sheargun

Figure 15. Schematic of the Sheargun

The receiver is a Sismopressiomètre®, which is a 3 component geophone clamped to the hole through a Ménard pressiomètre.

Tests in soft formations have shown that when the Pressiomètre® puts the soil back into its initial state of stress (see figure 16), the received signals are of much higher quality than when the geophone is just applied against the hole wall by an arm (total force applied by the Sismopressiomètre is around 50 tons, instead of 200 times less with a usual down-hole geophone). Depth range of both tools in the standard 63 mm version is around 200 metres.

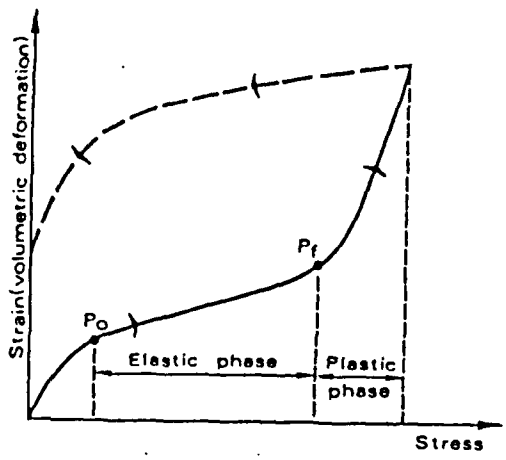

Figure 16. Pressiometric stress-strain curve

Signals transmitted by the Sheargun® and received by the Sismopressiomètre® are quite striking, and show remarkable frequency separation between P and S waves. Figure 17 shows the results of a cross-hole test with a horizontal separation of 20 m. On the left of the figure, the actual recordings are shown with the 2 horizontal geophones, and at the bottom left, with the vertical geophone, the most sensitive to the Sv waves created by the Sheargun® . The amplitude spectra on the right (normalized vertical scale) show the distinct frequency separation between P waves (1350 Hz) and S waves (120 Hz). The recording was made at Creys-Malville super-breeder nuclear power plant in France, in a clayey sandstone formation.

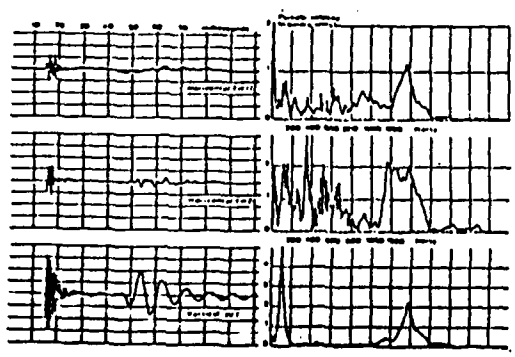

Figure 17. P and S waves observed on a 3-D receiver (signals to the left, amplitude spectra to the right)

Particularly, it can be noted that the P wave break can be measured with an accuracy of up to 0.02 milliseconds (using another time scale and, if necessary, an oscilloscope instead of digital seismic recorder) and the S wave with an accuracy of around 0.05 milliseconds. These figures seem surprising when looking at the frequency content of the whole signal. However, this controversy between time and frequency domains should be definitely settled in favour of time domain. When the seismograph (or the seismologist) gets the break, it does not care about the rest of the signal to come!

Time-break picking precision depends on the rise time which is not only related to the frequency content of the signal, but to the energy carried by it. Therefore, a powerful source like the Sheargun®, even with a limited frequency content (2000 Hz for the Sheargun) can yield breaks with an accuracy better than the actual sampling rate of the recorder itself ; 0.1 millisecond is not a problem.

When distances increase, an arithmetic stack is used, and the 63 mm tool can thus reach distances around 60 metres. For greater distances, CPGF has developed a 135 mm Sheargun®, for use in 6" holes. Tests carried for Elf Aquitaine have shown that this tool, which produces an energy of 500 joules (instead of 90 joules) can reach distances close to 300 metres, and can operate up to depths of 500 m.

8. CONCLUSIONS

CPGF's long practical experience in seismic tomography has shown the following features :

- curved ray processing strongly improves the resolution,
- the use of S waves increases the contrast between compact rock and fractured zones,
- high quality records, and therefore, strong sources are necessary to obtain good inversions.

Improvements presently being made concern the inversion of the quality factor. In the future, tomography will have to take into account the full wave form.

REFERENCES

Bois, P., LaPorte, M., Lavergne, M., Thomas, G. (1971). Essai de détermination automatique des vitesses sismiques par mesures entre puits. Geophysical Prospecting, 19, 42-83.

La Porte, M., Lavergne, M., Lakshmanan, J., Willm, C. (1973). Mesures sismiques par transmission, application au génie civil. Geophysical Prospecting, Vol. 21, 146-158.

Henning, F., Jacquemart, J., Lakshmanan, J., Rougé, J. (1981). Campagne géosismique sur le site nucléaire de Doel pour la détermination des paramètres dynamiques du sol. Influence de la présence des constructions. National Colloquy of the Belgian Committee of Engineering Geology, Gand.

Lakshmanan, J., Lantier, F., Martinet, G., Akerman, G. (1982). Aménagement de Grand' Maison. Usine souterraine du Verney. Symposium of Int. Soc. on Rock Mechanics, Aachen.

National French Committee on Large Dams - Workshop (Chairman : J. Lakshmanan). (1982). Nouvelles techniques de reconnaissance. 14th Congress on Large Dams, Rio de Janeiro.

Cottin, J.F., Deletie, P., Jacquet-Francillon, H., Lakshmanan, J., Lemoine, Y. (1986). Curved ray seismic tomography. Application to the Grand Etang dam (Reunion Island). The First Break, vol. 4, no. 7, 25-30.

Erling, J.C., Bertrand, Y., Kutkan, E. (1987). Prospection détaillée du sous-sol urbain en vue de travaux souterrains. International meeting AFTES, Bordeaux.

Lakshmanan, J., Bertrand, Y., Bichara, M., Lemoine, Y. (1982). Utilisation de diverses méthodes et mesures géophysiques pour l'étude de formations géologiques favorables à l'évacuation des déchets radioactifs. OECD seminar on geophysical prospecting applied to the storage of nuclear wastes in rock mass, Ottawa.

Wong, J., Bregman, N., West, G., Hurley, P. (1987). Cross-hole seismic scanning and tomography. The Leading Edge, 6-1, pp. 36-41.

Cote, P. Seismic imagery, velocity and quality factor inversion of sonic measurements between drill-holes. Thesis, Grenoble University.

AUTOMATIC DECONVOLUTION OF GRAVIMETRIC ANOMALIES*

BY

M. BICHARA and J. LAKSHMANAN**

ABSTRACT

BICHARA, M., and LAKSHMANAN, J., 1979, Automatic Deconvolution of Gravimetric Anomalies, Geophysical Prospecting 27, 798-807.

Existing techniques of deconvolution of gravity anomalies are principally based on upward and downward continuation of measured fields. It can be shown that a unique set of linear filters, depending only on geometrical parameters, relates density distribution at a given depth to gravity measured on the surface. A method to compute the filter coefficients is developed. Very accurate reconstitution of theoretical models of intricate shape, prove the validity of the linear relationship. One of these sets of linear filters is applied to a field case of underground quarries.

I – LINEARITY OF THE RELATIONSHIP BETWEEN GRAVITY AND DENSITY DISTRIBUTIONS

I.1 – *LA PORTE method*:

La Porte (1963) established an iterative method for the reconstruction of an underground geological structure from the gravity field on the surface of the ground.

In the first step the field is continued upwards:

$$g(x, y, +z) = \frac{z}{2\pi} \int_{-\infty}^{+\infty} \int_{-\infty}^{+\infty} \frac{g(x, y, 0)}{(x^2 + y^2 + z^2)^{3/2}}\, dx\, dy \qquad (1)$$

Next the field is continued downward by:

$$g(x, y, -z) = -g(x, y, +z) + 2g(x, y, 0) + z^2 \frac{\partial_g^2}{\partial_z^2}(x, y, 0) + 2 \sum_{i=2}^{\infty} \frac{z^{2i}}{(2i)!} \frac{\partial_g^{2i}}{\partial z^{2i}}(x, y, 0) \,. \qquad (2)$$

* Received September 1977

** Compagnie de Prospection Géophysique Française, Rueil Malmaison, France.

Finally, La Porte calculates a surface density distribution at depth z from

$$\sigma(x, y, -z) = \frac{3g(x, y, -z)}{4\pi} \tag{3}$$

or a volume density distribution from

$$\delta(x, y, -z) = \frac{3g(x, y, -z)}{4\pi e}, \tag{4}$$

where e is the thickness of the layer at depth $-z$.

Equation (4) and (5) suppose that the variation of the gravity field are due to the density variations within *one layer* at depth $-z$.

The La Porte method is very interesting and justifies itself by equations (1) to (3). It has been used by us for several problems. Nevertheless, it is a costly method needing many computations (see equations (1) and (2)). Furthermore, problems due to the discretisation of equation (2) often arise. These problems were already discussed in detail in La Porte (1963).

I.2 – *Relationship between gravity and density distribution*:

From equations (1), (2), and (3) one notes that, for a given depth $-z$, σ, and δ are linear in $g(x, y, 0)$. Therefore, there exists a transformation with the following properties: $\sigma = \mathfrak{F}(g)$
if $\sigma_1 = \mathfrak{F}(g1)$ and $\sigma_2 = \mathfrak{F}(g2)$, then $\sigma_1 + \sigma_2 = \mathfrak{F}(g_1 + g_2)$; λ is a scalar, then $\lambda\sigma = \mathfrak{F}(\lambda g)$.

This follows from the fact that:

$g(x, y, +z)$ is linear in $g(x, y, 0)$ (see equation(1))

$\frac{\partial^{2l} g(x, y, 0)}{\partial z^{2l}}$ is linear in $g(x, y, +z)$ at $z = 0$, thus $g(x, y, -z)$ is linear in $g(x, y, 0)$, and consequently from equation (3) the existence of function $\mathfrak{F}$ is demonstrated.

According to Schwartz's theorem (see Yosida 1968) $\mathfrak{F}$ could be represented by convolution with a kernel function K. We can write

$$\sigma(x_0, y_0, -z) = \int_{-\infty}^{+\infty} \int_{-\infty}^{+\infty} K(x - x_0, y - y_0, z)\, g(x, y)\, dxdy. \tag{5}$$

From equation (3) it is evident that $\delta(x_0, y_0, z)$ can be expressed by an integral equation similar to (5).

Discretization and limitation of equation (4) gives the equation:

$$\Delta\sigma(i, j, -z, e) = \sum_{k=-M}^{+M} \sum_{k=-N}^{+N} \alpha_{kl}\, g(i - k, j - l) \tag{6}$$

where the α_{kl} depend on the grid dimension, the depth z, and the thickness e.

The value z_{kl} is referred to as the filter coefficient. This denomination follows from a more general idea for the discretization of a convolution integral. For more informations the reader is referred to Ghosh (1971) or Bichara and Lakshmanan (1976).

The idea is the following:

There is theoretical reason for the existence of a filter (z_{kl}) realizing equation (6). This filter has been calculated and tested on various theoretical cases. We found that it was efficient and quite adapted to a density reconstitution at a given depth z.

II – Calculation of the Filter Coefficients

Proposed method

If equation (6) is valid, it follows that the coefficients α_{kl} depend only on geometric factors (grid, depth, and thickness of the source layer). Therefore they are unique and can be computed by considering the effect of any sort of source, for example a right prism.

Let us consider the effect of a right prism of length a_x, height e, situated at a depth z, and with a density contrast of 1, centered on point (m, n) on a grid of dimensions $(2m-1)\,a_x$, $(2n-1)\,a_y$; let $g(i, j)$ denote the gravity effect of that prism at point (i, j). The gravity anomaly is given by

$$\Delta g = \frac{2}{3}\Delta\sigma\, e \left\{ \operatorname{arctg} \frac{(i+1-m)(j+1-n)\,a_x a_y}{z\sqrt{(i+1-m)^2 a_x^2 + (j+1-n)^2 a_y^2 + z^2}} \right.$$
$$+ \operatorname{arctg} \frac{(i-m)(j-n)\,a_x a_y}{z\sqrt{(i-m)^2 a x_x^2 + (j-n)^2 a_y^2 + z^2}}$$
$$- \operatorname{arctg} \frac{(i+1-m)(j-)\,n a_x a_y}{z\sqrt{(i+1-m)^2 a_x^2 + (j-n)^2 a_y^2 + z^2}}$$
$$\left. - \operatorname{arctg} \frac{(i-m)(j+1-n)\,a_x a_y}{z\sqrt{(i-m)^2 a_x^2 + (j+1-n)^2 a_y^2 + z_2}} \right\} \tag{6}$$

Actually, the more accurate equations by Nagy (1966) were used.

We can then write a system of $(m \times n)$ equations

$$\sum_{k=-m}^{+m} \sum_{l=-n}^{+n} a_{kl}\, g(i-k, j-l) = 0 \qquad \forall (i, j) \neq (m, n) \tag{7}$$

$$\sum_{k=-m}^{+m} \sum_{l=-n}^{+n} \alpha_{kl}\, g(m-k, n-l) = \Delta\sigma, \text{ with the } \alpha_{kl} \tag{8}$$

as the $m \times n$ unknowns.

Solving these linear equations, we can compute $m \times n$ filter coefficients valid for a given set of values of a_x, a_y, e, and z.

The filter size ($m \times n$) and the grid size $(2m-1) \times (2n-1)$ should in theory be infinitely large. However, we have found empirically that the filter size is correct if outside the complete grid $(2m-1) \times (2n-1)$ the gravity anomaly is less than a hundredth of the maximum anomaly.

II.2 – *Experimental results*

For a right prism with

$a_x = a_y = 10$ m
overburden $z = 10$ m
height $e = 3$ m

density contrast 1 g cm^{-3} we obtain the anomaly shown in fig. 1.

For a grid of dimensions $2m-1 = 2n-1 = 13$ $(m = n = 7)$; the filter coefficients are given on figure 2.

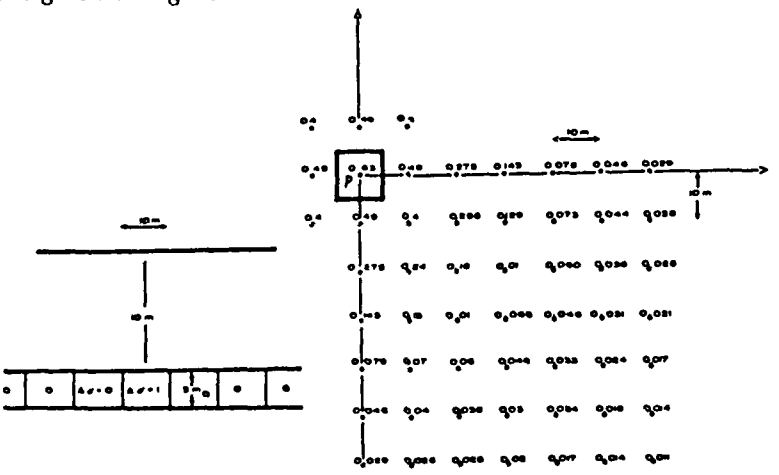

Fig. 1. Anomaly due to a square right prism, 3 m high, 10 m large, at 10 m depth (point P is center of symmetry).

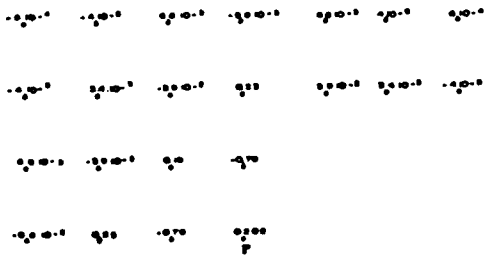

Fig. 2. Filter coefficients (point P is the center of symmetry).

We have

$\sum' \alpha_{kl} = 0.07968$ instead of the theoretical value $0.07974 = \frac{3}{4\pi} \cdot \frac{1}{e}$. This theoretical value follows from the equation (4) applied to a layer of constant thickness and contrast:

for $\Delta\sigma = \frac{3\Delta g}{4\pi e}$;

with $e = 3$ m and Δg in 0.01 mgal,

$\Delta\sigma = 0.07974\ \Delta g$. Application of the filter of fig. 2 gives

$\Delta\sigma = (\Sigma\alpha_{kl})\Delta g = 0.07968\Delta g$.

The close agreement confirms elegantly our theoretical assumptions.

III – Experimental results

The following examples concern mathematical control of the accuracy of the filters used. Figure 3 gives the theoretical density distribution: 7 blocks 10 m × 10 m and 3 m height along a line, at 10 m depth with a density contrast of 2 g cm^{-3}. Figure 4 gives the gravity anomaly of this model and figure 5

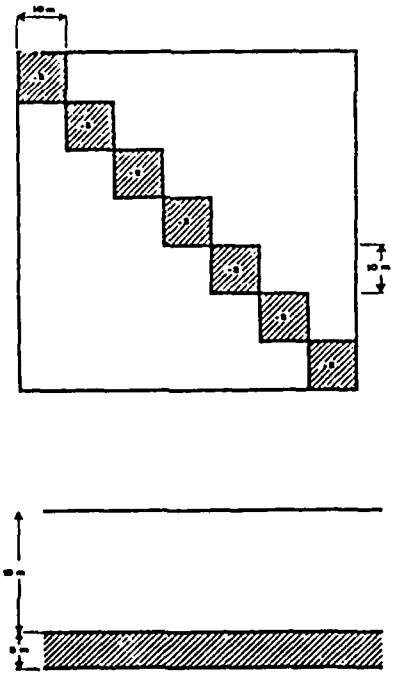

Fig. 3. Model 1.

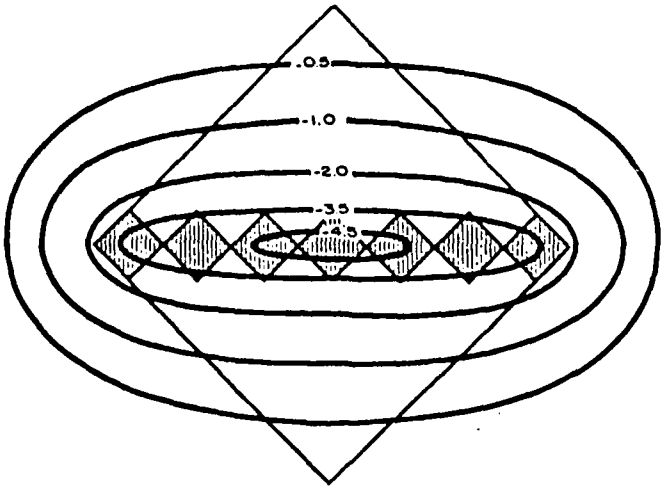

Fig. 4. Anomaly due to model 1 (contours in 0.01 mgal).

-2.005	-.003	-.003	.007	.056	.031	.002
-.003	-2.000	-.000	.001	.021	.066	.031
-.003	-.000	-2.001	-.001	-.000	.021	.056
.007	.001	-001	-2.000	-.001	.001	.007
.056	.021	-.000	-.001	-2.001	-.000	-.003
.031	.066	.021	.001	-.000	-2.000	-.003
.002	.031	.056	.007	-.003	-.003	-2.006

Fig. 5. Model 1 computed by linear filter.
Standard deviation of densities 0.004 g/cm³.
Standard deviation of recomputed anomaly 0.0006 mGal

gives the reconstructed model. The standard deviation on the density is 0.004 g cm^{-3} (maximum .056). The standard deviation of the gravity anomaly due to this structure compared with the original one is 0.06. 10^{-2} mgal for an average anomaly of 1.60 . 10^{-2} mgal.

The second model is more complicated (figure 6): it consists of 24 little blocks with density contrast -2 g cm^{-3} separated by 25 blocks with density contrast 0.

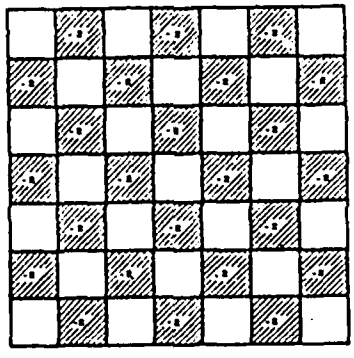

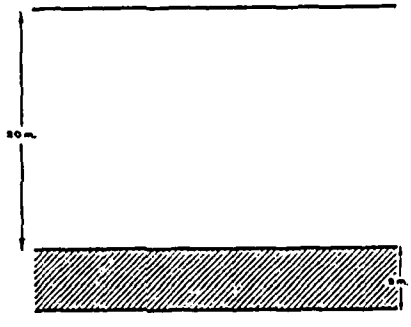

Fig. 6. Model 2.

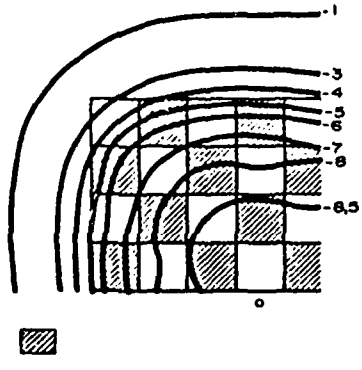

Fig. 7. Anomaly due to model 2 (contours 0.01 mgal).
Point o is center of symmetry.

Figure 7 shows a quarter of the anomaly due to this model. The combined effect of the 49 blocks is practically equivalent to that at a single big block with density contrast -1 g cm^{-3}.

The filter result is quite spectacular (figure 8). The mean square difference on the density is .052 g cm^{-3}, the largest difference being. 065 g cm^{-3}. The mean square difference on the reconstructed gravity anomaly is .16 $\cdot 10^{-2}$ mgal for an average of 6.0 $\cdot 10^{-2}$ mgal.

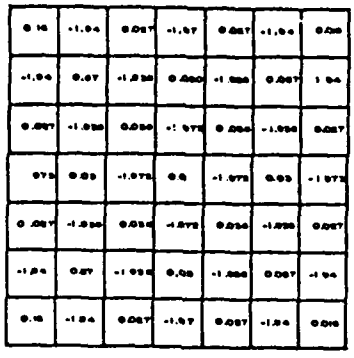

Fig. 8. Model 2 computed by linear filter.
Standard deviation of densities 0.025 g/cm^3.
Standard deviation of recomputed anomaly 0.0016 mGal.

Field results

Of course, these quite extraordinary results were obtained on theoretical models, and the reader would be quite justified in asking for practical results. Some of these were presented at the 1974 Hanover Symposium on Engineering Geology and have been controled by drilling. The studies presented at this symposium concerned detection of sinkhole areas in gypsum, 45 m deep.

More recent work has been carried out by CPGF in the Caen area (Normandy, France) where large underground limestone quarries are found. These quarries are approximately 4 m high and have very variable horizontal extension.

Figure 9 shows the map of such a quarry located by a gravity survery, and gives the reconstituted density of prisms 14 m × 14 m × 4 m.

The close correlation can be appreciated by computing percentage of quarried surface inside each 14 m × 14 m square (5) and comparing this percentage with the reconstituted densities D.

Figure 10 gives this correlation. We have $S = -0.385\ (D + 0.75) + 0.383$ or, admitting a least squares relationship passing through the origin $S = -0.405\ D$. This means that the average limestone density contrast for $S = 1$ would be $D = -1/0.405 = -2{,}15$ gcm^{-3}, which seems to be a correct density for this Jurassic limestone.

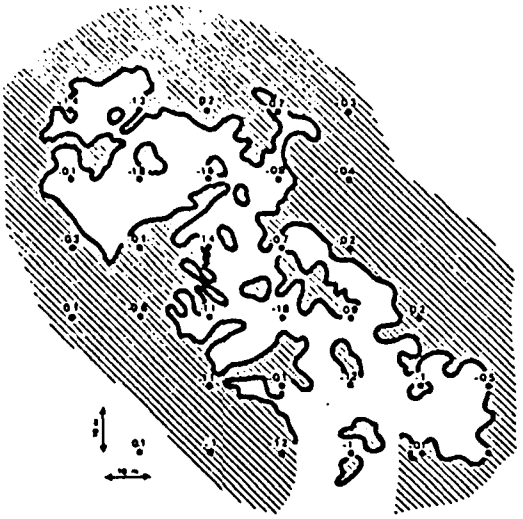

Fig. 9. Comparison between quarry map and densities computed by Filt program.

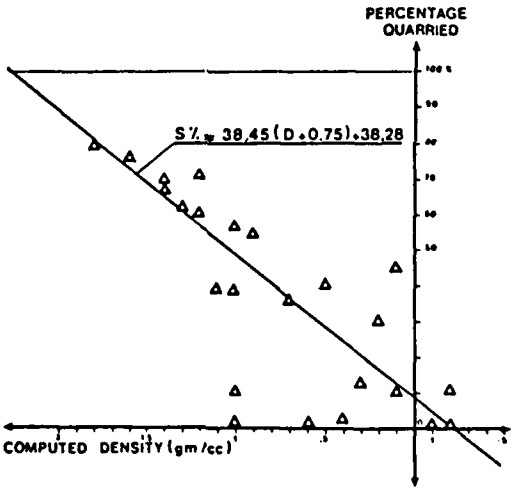

Fig. 10. Correlation between computed density and surface of quarries.

Conclusions

The described work has been carried out by the Compagnie de Prospection Géophysique Française, on a French Government research grant (Délégation Générale à la Recherche Scientifique et Technique). Further work is now being done for systematic use of several filters, to start with a preselected main layer, and building up (or down) density distribution from the residual difference between reconstituted and measured gravity.

References

Bichara, M., and Lakshmanan, J., 1970, Fast automatic processing of resistivity soundings, Geophysical Prospecting 24, 354-360.

Ghosh, D. P., 1971, The application of linear filter theory to the direct interpretation of geoelectrical resistivity sounding measurements, Geophysical Prospecting 19, 192-217.

Lakshmanan, J., 1973, Gravity and gamma-gamma mapping of sink-hole areas in Lutetian Gypsum, North East of Paris, I.A.E.G. Symp. on Eng. Geology, Hanover, September 1973.

La Porte, M., 1963, Calcul de la forme d'une structure homogène à partir de son champ gravimétrique, Geophysical Prospecting 11 1271-291.

Nagy, D., 1966, The gravitational attraction of a right rectangular prism, Geophysics 31, 362-371.

Yosida, K., 1968, Functional analysis, 2nd edition, P 168, Berlin, Heidelberg, New-York.

Variable density Bouguer processing of gravity data from Herault, France

Francine Rimbert*, Jean-Claude Erling† & Jacques Lakshmanan†

The Herault permit for oil is located in the south of France in very hilly terrain between Mount Aigoual (1500 m) and the sea at Sete. In the preliminary stage of exploration, it was decided that new Bouguer maps, including a variable density one, and a surface density map should be produced.

France is covered by a national gravity map published by BRGM on a scale of 1:80000. It was decided that the original data should be recovered and new data acquired to infill the blanks in order to get stations on an average grid of 1.2 by 1.2 km. The existing data had been acquired along roads with a station spacing of 800 to 1200 m, but the road lines were 3 to 6 km apart. Very detailed mining gravity data were also available from the area around Lodeve. After appropriate sampling of the latter data set, 2041 old stations were retained and 619 new stations were planned (Fig. 1). In most of the permit, the new stations were located along tracks or footpaths over the hills, whereas the old grid was located mainly in the valleys.

With 2660 stations in total, the number of stations per 100 km^2 varies between 60 and 70, and the largest remaining blanks in very inaccessible areas are about 3 by 3 km in size. The data from these stations were processed using a generalised Nettleton method. After isostatic corrections, structures show up much better on the variable density Bouguer anomaly map, facilitating interpretation. The surface density map shows the low density of the granites, and the high density of the Permian and Jurassic dolomites.

Generalised Nettleton corrections

Nettleton's (1940) method for estimating the near-surface density along a gravity profile is to calculate the Bouguer anomaly along the profile assuming a range of different values for the density in computing the Bouguer and terrain corrections, and then to choose the anomaly profile which correlates least with the topography: the corresponding value of density is the best estimate. Parasnis (1972) has summarised published variations on Nettleton's method. The generalised Nettleton procedure developed by CPGF (Lakshmanan 1985) was originally used for microgravity surveys, and in 1981 was used in a large gravity survey for oil in very hilly terrain in Morocco. In addition to applying the method to an areal array of stations, the particular feature of this procedure is the use of residual values of Bouguer anomalies and elevations, instead of raw values. This allows the effect of the near-surface density distribution to be removed without introducing any regional bias.

The topography is first smoothed with a moving window: a two-dimensional convolution operator is applied to the surface topography $z_0(x,y)$. The resultant is smoothly adjusted to yield a surface that lies just below

Fig. 1. Example of old and new gravity gridding.

*Total CFP, CEDEX 47, 92069 Paris La Défense, France.
†Compagnie de Prospection Géophysique Française, 20, rue des Pavillons, 92800 Puteaux, France.

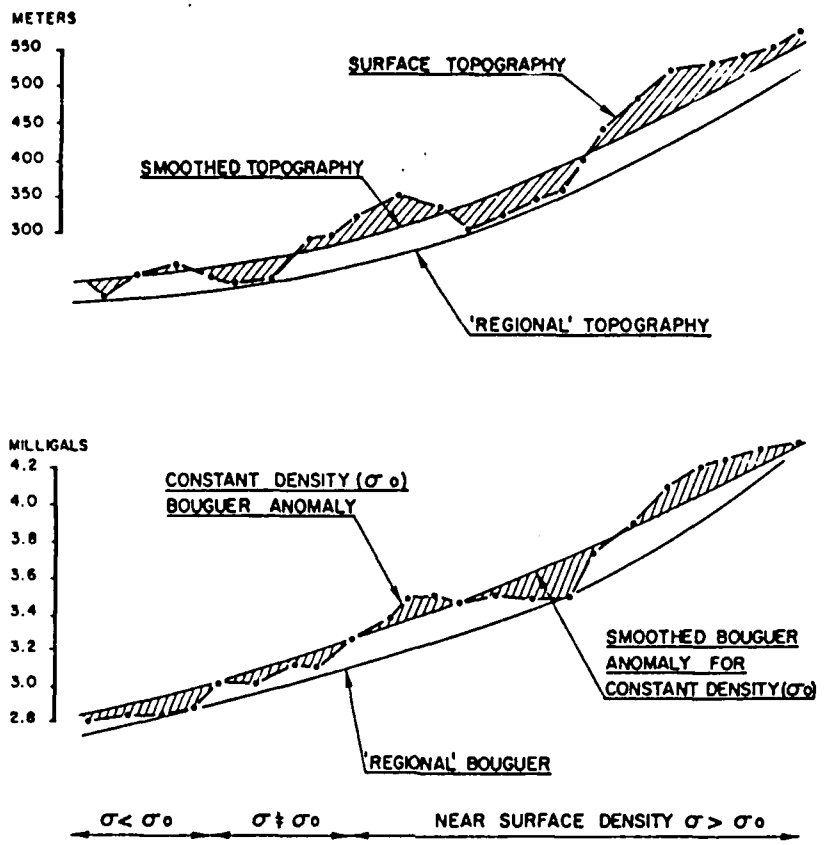

Fig. 2. Basis of generalised Nettleton technique. The regional topography is smoothed and chosen to pass below the surface topography everywhere. The density above the regional topography is adjusted by nulling the covariance between the residual topography and the residual Bouguer anomaly over a moving window. The variation in this near surface density is indicated at the bottom of the figure.

the low points in the topography throughout the area. We call this surface (Fig. 2) the regional topography $z_R(x,y)$. It is assumed that the density has a constant value σ_o below the regional topography.

Let us consider the Bouguer anomaly for two different density distributions between the surface topography and the regional topography: first that it has the same constant value σ_o everywhere, and secondly that it has an unknown constant value σ within a fixed radius of the station point and the original constant value σ_o beyond this radius. The Bouguer anomaly for the first case is the conventional one, which may be written as

$$\delta g_{Bo} = \delta g_{FA} + 2\pi G\sigma_o z_o - T\sigma_o.$$

Let the Bouguer anomaly for the second case be δg_B. It will differ from δg_{Bo} in both the Bouguer correction term and in the terrain correction term, and may be readily calculated as a function of σ.

The Bouguer anomaly δg_B is smoothed over the whole area using the same moving window and the same function that were used to produce the regional topography. The result is the regional Bouguer anomaly δg_{BR} which is also a function of σ.

We now consider the residual topography and the residual Bouguer anomaly, expressed as a function of σ, given by

$$z_r(x,y) = z_o(x,y) - z_R(x,y), \text{ and}$$
$$\delta g_{BR} = \delta g_B - \delta g_{BR}.$$

The best estimate of σ is obtained by setting the covariance between $z_r(x,y)$ and δg_{BR} equal to zero. This is done over a moving window. A better estimate of the Bouguer anomaly can then be computed from the density distribution found for the near surface on the first iteration, and an improved density distribution found by setting the covariance between the residual new Bouguer anomaly and the residual topography equal to zero. This second iteration is usually sufficiently accurate for the production of a map of the surface density distribution and the final calculation of the variable density Bouguer anomaly map.

Careful selection of the radii of the moving windows for regionalisation and for correlation is necessary. The value selected for σ_o is not too critical, and any reasonable constant value of density can be selected for the first iteration.

The Herault survey

Surveying. In order to reduce acquisition costs, it was decided to make do without optical levelling, which costs nearly as much as gravity acquisition. As many stations as possible were located on physical bench marks (60 stations) or on stereo-topographic elevation points (498 stations) marked on the regular 1:25000 topography maps published by the Institut Géographique National (IGN). The former have an accuracy of 0.02 m, while the latter have an accuracy of 1–2 m. Only 61 stations had to be located away from such topographic points. Their elevations were measured, and those of the stereo-topographic points checked, using two Paulin microaltimeters (one moving, one base). The mean square difference between barometric measurements and the published values of stereo-topographic elevation points was 1.62 m or, after excluding 9% of the microaltimeter readings taken during bad weather, 1.02 m. Finally, apart from a few points where the IGN stereo-topographic altitudes were incorrect, the IGN values were retained.

Terrain corrections. These were calculated in the standard manner, with the appropriate modifications to allow for the variable density. Long distance corrections were made up to a radius of about 50 km. The average terrain correction is 0.69 mgal, but they are much higher in the northwest half of the permit, where they exceed 5 mgal at 25 stations (maximum 14.38 mgal). The accuracy of the terrain corrections is estimated to be around 10%.

Quality control. The first control was the fit between the old BRGM stations and the new ones. After a certain number of repeats and base ties, no significant differences were found. In some areas, apparent differences between adjacent stations were due to the fact that the BRGM stations were located on deep valleys, while the CPGF stations were on the wooded plateaux, 300 to 500 m above. After variable density corrections, these apparent differences disappeared.

This improvement was confirmed by computing a 'local' residual by comparing the Bouguer anomaly at an individual station with the smoothed anomaly computed by averaging the Bouguer anomalies at nearby stations within a fixed radius of 2 km. With variable density, the percentage of points with residuals exceeding 3 mgal was 1.0 instead of 2.3 with a fixed 2.3 g cm^{-3} density. Final accuracy on the Bouguer anomaly was evaluated at 0.3–0.4 mgal.

The variable density Bouguer anomaly map for part of the permit is plotted in Fig. 3 with the surface topography for the same area plotted in Fig. 4.

Isostasy-corrected Bouguer

The Bouguer anomaly shows an important regional gradient decreasing from the sea towards the northwest. In order to remove this important gradient, isostatic corrections were carried out. Isostatic corrections were made at eight points surrounding the survey area, which is sufficient, taking into account the large radius of curvature of equal isostatic correction curves. The Pratt 30-km hypothesis was adopted (30 km is the depth to the isostatic compensation surface). Corrections were made with the Lejoy–Coron tables supplied by the International Gravimetric Bureau. For each of the eight stations, average altitudes are evaluated for each of the Hammer–Bouguer zones and corrections read in the tables; negative corrections were applied to oceanic compartments and positive ones to the terrestrial compartments.

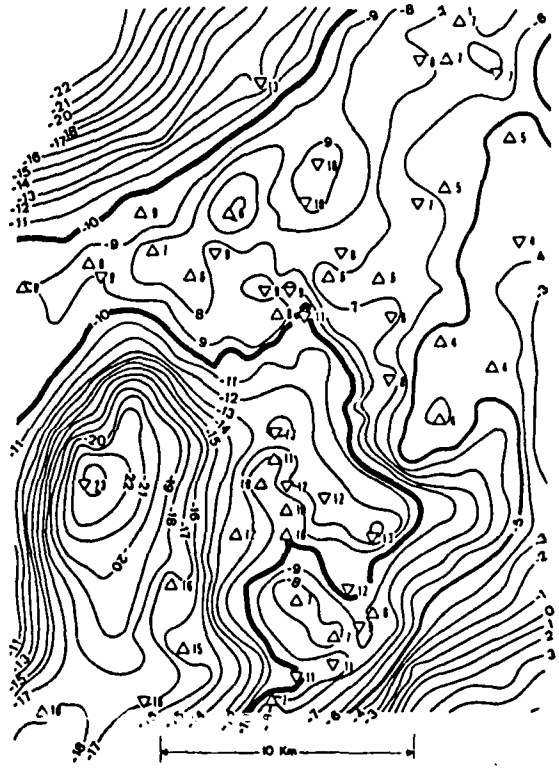

Fig. 3. Detail of Bouguer anomaly with variable density (values in milligals).

After isostatic corrections, the regional gradient is, to a large extent, removed. Figures 5 and 6 show the isostasy-corrected Bouguer for a part of the permit; Fig. 5 with only the old data and a constant 2.5 g cm^{-3} density, Fig. 6 with all data and a variable density. The effect of more regular gridding and of pseudo-static Nettleton corrections shows up clearly in the northeastern half of these maps. The elongated shapes of three Tertiary basins corresponding to 'lows' oriented NNE–SSW are clearly revealed on the variable density map, while on the old map, these structures are much more 'pseudopodic'.

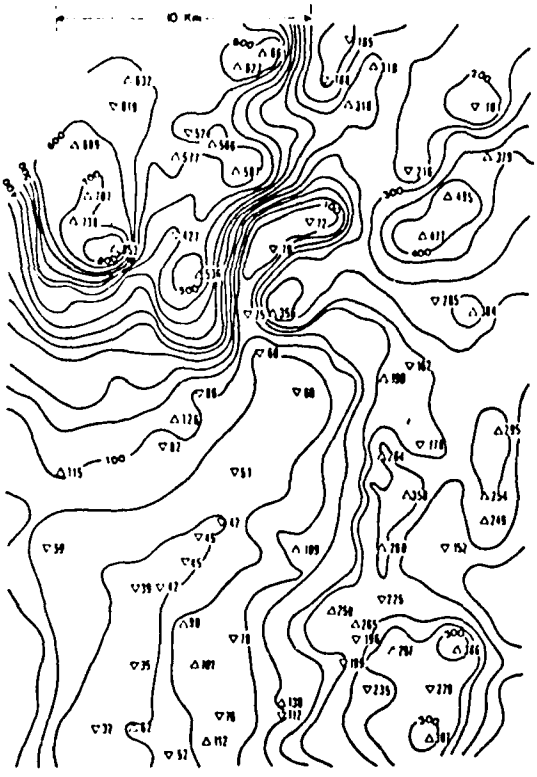

Fig. 4. Detail of elevation map (values in metres).

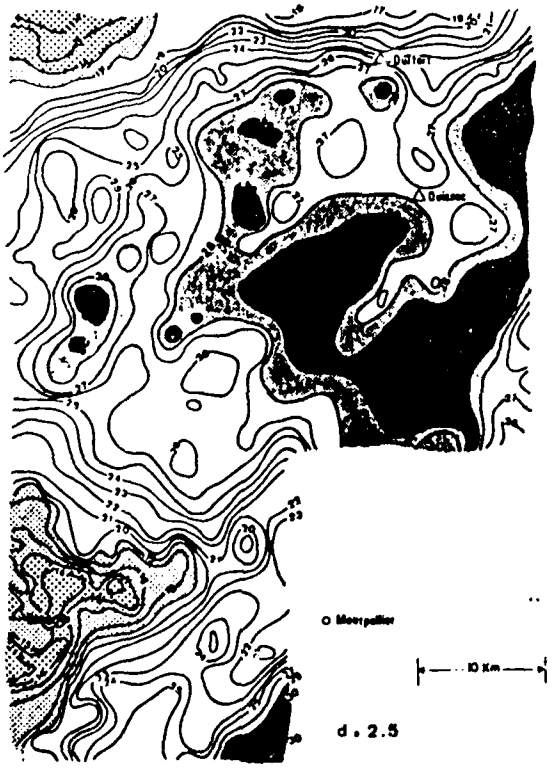

Fig. 5. Isostasy-corrected Bouguer anomaly map, for a constant 2.5 g cm^{-3} density, including old stations only (values in milligals).

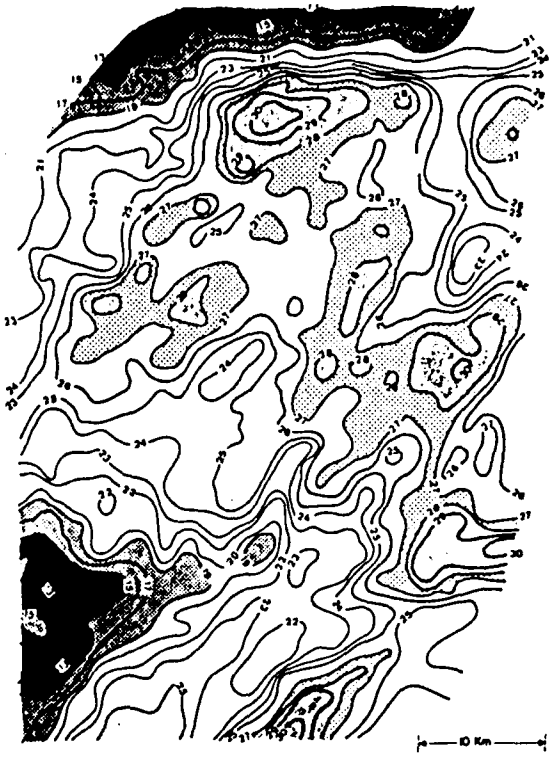

Fig. 6. Isostasy-corrected Bouguer anomaly map, for variable surface density, with old and new stations (values in milligals).

Surface density map

Figure 7 shows the surface densities over the whole permit, obtained by the generalised Nettleton procedure. In fact, these values are not significant over the valleys, but these are generally very narrow.

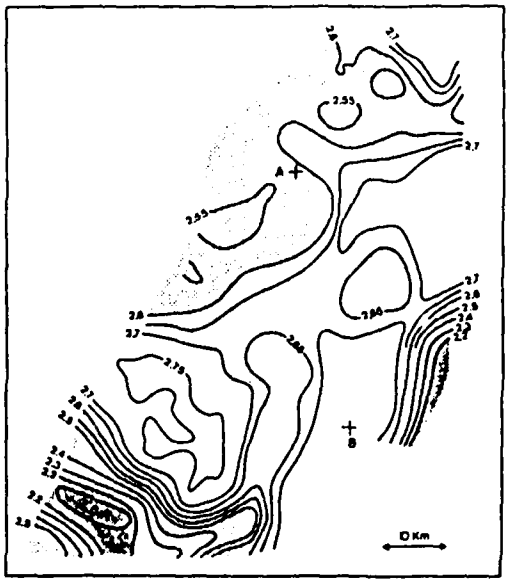

Fig. 7. Surface density map.

Fig. 8. Regional geology: (a) Tertiary; (b) Cretaceous; (c) Jurassic; (d) Permo-Triassic; (e) Palaeozoic; (f) gneiss and granite.

Compared to general geology (see Fig. 8), this surface density map shows, with all values in g cm^{-3}:

(i) medium-low densities (2.5–2.6) over the granite in the north,
(ii) high density (2.7) over the northern Palaeozoic rocks,
(iii) medium-low densities (2.5–2.6) over the Jurassic rocks along the northwestern edges of the permit,
(iv) high densities (2.7) over the Cretaceous and Jurassic rocks along the northeastern edge of the permit, probably due to the Jurassic hills,
(v) high densities (2.7–2.8) over the Jurassic dolomites of the La Gardiole hills, continuing the previous zone (iv) to the south,
(vi) low densities (2.2–2.5) in the southeast corner (Tertiary coastal plains),
(vii) high densities (2.7–2.8) in the centre/southwest coinciding with the Palaeozoic rocks, but extending eastwards from the outcrops,
(viii) low densities (2.2–2.5) in the southwest corner (Tertiary plains),
(ix) medium-low density (2.5–2.6) axis separating high density zones (v) and (vii), corresponding to the eastern border of the Tertiary basin located between the Jurassic (v) and the Palaeozoic (vii).

Conclusions

By infilling blanks of an old gravity survey (619 new and 2041 old stations), and using microaltimeter-controlled stereo-topographic points as gravity stations, an updated gravity map was obtained at 15% of the cost of a complete new survey. The generalised Nettleton technique gives a variable density Bouguer anomaly, pseudo-statically corrected. Accuracy of the new Bouguer values is aroung 0.3–0.4 mgal, quite sufficient for the large (4 to 15 mgal) anomalies of the permit.

Finally, isostatic corrections have removed a large gradient dipping from the sea towards the northwest. The new Bouguer map is now ready for further interpretation and modelling.

Received 27 March 1986; accepted 22 September 1986.

References

LAKSHMANAN, J. 1985. Corrections généralisées de Nettleton. Potential Fields in Rugged Topography. Symposium of the University of Lausanne, *IGL Bulletin no. 7, paper 2.5.*

NETTLETON, L.L. 1940. Geophysical prospecting for oil. McGraw-Hill, New York.

PARASNIS, D.S. 1972. Principles of applied geophysics. 2nd edn, Methuen, London.

END

DATED

FILM

9-88

DTIC